STUDY OF OPTICAL AND ELECTRICAL PROPERTIES OF $BaWO_4/CaWO_4$ NANOCOMPOSITES

A THESIS SUBMITTED IN PARTIAL FULFILLMENT FOR THE DEGREE OF

DOCTOR OF PHILOSOPHY

IN **PHYSICS**

SCHOOL OF PHYSICAL AND APPLIED SCIENCES

GOA UNIVERSITY

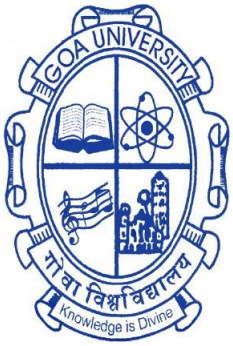

BY

PRASAD NARAYAN PATIL
SCHOOL OF PHYSICAL AND APPLIED SCIENCES
GOA UNIVERSITY, GOA

December 2021

DECLARATION

I, **Mr. Prasad Narayan Patil** hereby declare that this thesis represents work which has been carried out by me and that it has not been submitted, either in part or full, to any other University or Institution for the award of any research degree.

Place: Taleigao Plateau **Mr. Prasad Narayan Patil**

Date: 31/12 /2021

CERTIFICATE

I hereby certify that the above Declaration of the candidate, **Mr. Prasad Narayan Patil** is true and the work was carried out under my/our supervision.

Prof. Uma Subramanian(Retired)
(Research Guide)
School of Physical and Applied Sciences
Goa University, Goa
Taleigao Plateau
Goa.India. 403206

Dr. Rajeshkumar Shankar Hyam
(Research Co-Guide)
School of Physical and Applied Sciences
Goa University, Goa
Taleigao Plateau
Goa.India. 403206

ACKNOWLEDGEMENT

I bow before Goddess"**Shri JYOTIBA & MAHALAKSHMI**",the most Gracious and Merciful, for his/her blessings and for giving me the courage and fortitude tocomplete the research work.

I take the opportunity to acknowledge all those who have helped me directly or indirectly throughout my Ph.D.research work in the Department of Physics, School of Physical and Applied Sciences, Goa University.

I have been very fortunate to be guided by **Prof.Uma Subramanian,** Department of Physics, School of Physical and Applied Sciences, Goa University, for her decisive advice and valuable guidance, motivation and encouragement throughout my Ph.D.tenure.

I would also like to extend my sincere thanks to my co-guide **Dr.Rajeshkumar Shankar Hyam** for his patience, comments, suggestions and discussions with him helped me to reach next level of understanding and also valuable comments during the Department Research Committee (DRC) meetings.

Special thanks to the members **Prof.K.R.S.Priolkar (**Dean, School of Physical and Applied Sciences) and **Prof.B.R.Srinivasan** (Former Vice-dean, School of Chemical Sciences) for their constructive suggestions during Department Research Committee (DRC) meetings and annual presentations.

I also thank Dr.Sudhir Cherukulappurath, Dr.Bholanath Pahari & Dr.Venktesha Hathwar Department of Physics, School of Physical and Applied Sciences, Goa University for their presence during Pre-Synopsis presentation giving valuable comments, useful discussions and suggestions.

I wish to express my thanks to **Prof. R.V. Pai,** Former Head, Department of Physics, **Prof. R. B. Tangsali,** Former Head,Department of Physics, Goa University for their support and providing experimental facilities in the Department of Physics during my Ph.D research work.

I also thank **Prof. J. A. Erwin Desa** (Former Head of the Department of Physics and Former Dean of Faculty of Natural Sciences, Goa University) for his kind help, useful discussions and suggestions as and when it was needed.

I strongly acknowledge **Prof.C.K.Jayasankar**, Departmentof Physics, S.V.University, Tirupati, India to check the consistency of PL spectra with Edingburgh FLS-980 spectrometer through his MoU-DAE-BRNS Project (No.2009/34/36/BRNS/3174) and extending the experimental facility.

I express my deep gratitude to **Mr. Girish Prabhu,** NIO-Goa, for XRD measurements, **Mr. Madhusudan Lanjewar,** USIC, Goa University, for SEM measurements.

I am grateful to **Prof.V.M.S.Vernekar** and research scholar **Mr.Pratik Asogekar,** School of chemical sciences, Goa University, Goa for extending immense help in dielectric measurements.

I thank **Department of Botany** for helping me for providing distilled water for my Ph.D. work.
I am grateful to my senior research colleague **Dr.M.Jeyakanthan** for his valuable support during my period of Ph.D.research work.

I am thankful to the Management, specially the **Ganpat Parsekar College of Education, Harmal-Goa** for permitting me to carry out research and full support.

I am thankful to **Shri. Prasad Lolayekar, Director, Higher Education, Government of Goa** for sanctioning study leave for one year to complete Ph.D. research work.

I take the opportunity to acknowledge all those Ph.D.students who have helped me directly or indirectly throughout my Ph.D. research work in the Department of Physics, School of Physical and Applied Sciences, Goa University, Goa.

I extend my heartfelt thanks to all the teaching faculty and non-teaching staff of the Department of Physics, Goa University for extending co-operation and facilities throughout my research Work.

DEDICATED TO MY FAMILY MEMBERS

CONTENTS

List of Tables

List of Figures

CHAPTER 1

GENERAL INTRODUCTION AND LITERATURE REVIEW

1.1. Introduction

Owing to the increase in global demand for solid-state lighting appliances, energy-saving light sources are evaluated together with the performance of the phosphors used in them. In the interest of reducing the energy demand of these appliances, extensive research has been carried out in search of alternative light sources. In recent years, researchers have explored methods for the preparation of new ceramic luminescent phosphors and the improvement of their luminescence properties through various experimental techniques.Because,luminescent phosphors also known as 'light-bearing materials' are widely used in various potential applications such as WLEDs, display devices, imaging systems, monitor screens, optoelectronics, therapeutics, lumino-magnetic applications, and biological labeling, its demand increases day-by-day as novel devices keep emerging **[1-6]**. In the last decade, many synthesis methods have been explored for ceramic nanophosphors to improve the emission intensity as well as other properties such as magnetic, electrical, and thermoelectric properties. Type I band alignment in nanocomposites with the interface of two semiconductors is one of the best methods to improve emission intensity. In this chapter, the importance of nanocomposites, types of band alignment, the basic phenomenon of luminescence and energy transfer processes involved in tungstates, introduction to DC and AC electrical conductivity, Dielectric properties (dielectric constant and loss tangent) and thermoelectric properties, and brief review of the literature on the studied system, motivation of the problem and scope of the thesis are discussed.

1.2. Introduction to Nanocomposites

Nanocomposites is a multiphase solid material where one of the phases has one, two, or three dimensions of less than 100 nanometers (nm) or structures having nanoscale repeat distances between the different phases that make up the material **[7]**. The idea behind nanocomposites is to use building blocks with dimensions in the nanometer range to design and create new materials with unprecedented flexibility and improvement in their physical properties. Also, reducing the size of materials leads to a significant increase in optical, electrical, magnetic, and thermoelectric properties. The properties of nanocomposites are not only dependent on their individual properties of different phases but also their combined nature such as surface morphology and interfacial characteristics **[8]**. Some advantages of nanocomposites are summarized below:

- Improvement in tensile strength, flexibility, ductile strength, modulus, and stability of dimension all related to mechanical properties
- Enhanced thermal stability and heat distortion temperature
- Enhanced chemical and radiation hardness
- Enhanced electrical conductivity
- Enhanced thermoelectric power factor
- Enhanced photocatalytic and Photoluminescence

Generally, the nanocomposites are classified into three different categories: ceramic matrix nanocomposites, metal matrix nanocomposites, and polymer matrix nanocomposites **[9]**. Ceramic matrix nanocomposites consisting of a ceramic matrix combined with a ceramic (oxides, carbides) dispersed phase. Metal matrix nanocomposites refer to materials consisting of metal matrix nanocomposites (MMNCs) comprised of metal as the matrix and ceramic as the reinforcement. Polymer nanocomposites are materials in which a combination of polymer matrix (which could be thermosetting or thermoplastic) with some kind of nanomaterial. The Energy of the surface/interface essentially controls the properties of materials. Interfaces provide inhomogeneity in solid materials and this causes a significant change in their thermal, optical, electrical, magnetic, and mechanical properties of the materials. Particular mixing of two similar phases (homophase interface) of materials with different morphology as well as the high percentage of interface area lead to materials with enhanced properties **[10]**.

1.3. Ceramic nanocomposites

For the first concept of ceramic nanocomposites was reported in 1991 by Niihara et al. **[11]**.Ceramic nanocomposites are classified into four categories: intragranular, intergranular, hybrid, and nano/nanocomposites. Except in the case of nano/nano composites, the matrix phase can be a microstructure ceramic or glass while the reinforced phase can be nanoparticle, nanotube, nanoplatelets, and hybrid of these materials. In nano/nanocomposites both the matrix and reinforced phase are composed of nano dimensions. The nano/nanocomposites are further divided by their material combination into two categories; semiconductor – semiconductor nanocomposites, semiconductor – metal nanocomposites.Conjoining two or more semiconductors in single composite material with adjustable band alignment leads to develop a new degree of multifunctional nanocomposites. According to the band alignments, the semiconductor-semiconductor nanocomposites are divided into three types as shown in **Figure 1.1 [12]**:

1. Type I band alignment,

2. Type II band alignment and

3. Type III band alignment

Nanocomposites with Type I band alignment nanosystems occur byadjacent domains of two semiconductors having different band gap values and appropriately chosen band offsets could be used to trap electron–hole pairs in specific regions of another semiconductor thus forcing them to recombine therein with high efficiency. In this type I band alignment electrons and holes get accumulated in conduction and valence band position within the band gap of another semiconductor material leading to more recombination. Alternatively, nanocomposites with a type II band alignment of material bandgaps, constructed in such a way that band edges of one domain lie lower in energy than the corresponding band edges of the other, facilitate spatial separation of electron–hole pairs (excitons) between different parts of the composite nanostructure, which can be harnessed for the development of photo-voltaic and photo-catalytic materials.Type III is identical to type II except for the much more difference in the valence band and conduction band positions which gives a higher driving force for charge transfer **[13-15]**.

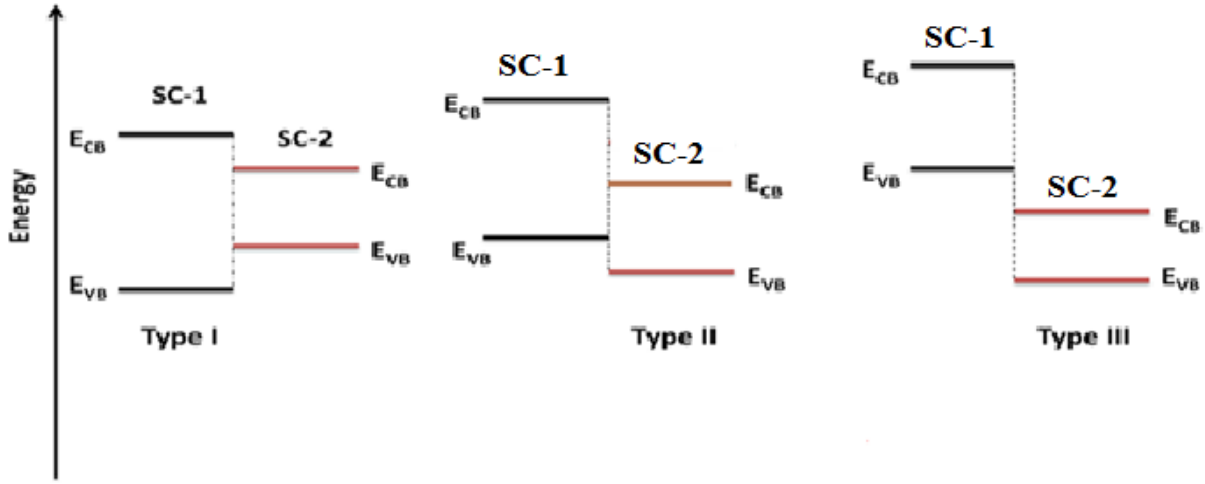

Figure 1.1: Band alignments of the semiconductor – semiconductor nanocomposites. **SC-1, SC-2, E_{VB}, E_{CB}** in figure represents the semiconductor 1, semiconductor 2, valence band position and conduction band position respectively.

1.4. Introduction to Luminescence

Naturally, the generation of light can be evolved depending on the source of occurrence, light can be classified in two ways, one is incandescence and the other is luminescence.

CHAPTER 1

Incandescence is the light glow caused by the heating of the object materials, and a bright light is produced. Example is electric bulbs. Luminescence is a collective term for different phenomena where a substance emits light without being strongly heated, i.e., the emission is not simply thermal radiation. This definition is also reflected by the term "cold light". The word luminescence was first used by a German physicist, 1888, Eilhardt Wiedemann, in Latin 'Lumen' means 'light' **[16]**. The materials exhibiting this phenomenon are known as 'Luminescent materials' or 'Phosphors' meaning 'light bearer' in Greek. The term phosphor was coined in17th century by an Italian alchemist named Vincentinusm Casciarolon of Bologona **[17]**. The phenomenon of luminescence can be classified into various categories depending on the mode of excitation (the prefix before the term luminescence is the mode of excitation in most of the cases).

- Photoluminescence, when the excitation is by electromagnetic radiation/photons, is a less specific term which embraces both fluorescence and phosphorescence.
- Cathodoluminescence, when the excitation is caused by energetic electrons or cathode rays.
- Electroluminescence is light emission triggered by electric influences.
- Radioluminescence, when the excitation is caused by high-energy X-rays or γ -rays.
- Sonoluminescence, when the excitation is caused by ultrasonic waves.
- Triboluminescence can occur when a material is mechanically treated, e.g.Fractured or polished.
- Chemiluminescence is light emitted during chemical reactions.
- Bioluminescence is a form of Chemiluminescence from living organisms.
- Thermoluminescence, also known as thermally stimulated luminescence, is the luminescence activated thermally after initial irradiation by other means such as α, β, γ, UV or X-rays. It is not to be confused with thermal radiation; the thermal excitation only triggers the release of stored energy.

Each process mentioned above has its significance and advantage in the field of science and technology. The emphasis in the present work has been given to study the photoluminescence (PL) of phosphors that exhibit strong emission in the visible region. However, before going into detail, it is important to know the procedure leading to luminescence and its various characteristics.

1.4.1. Photoluminescence

Vincenzo Cascariolo is the first identified luminescent emission from the mineral barite on exposure to sunlight known as 'photoluminescence' (PL), a material photoluminesces when excited by monochromatic light or by UV radiation with a spectrum broad enough to overlap the ion absorption bands. Photoluminescence (PL) spectroscopy is a contactless, non-destructive, and highly sensitive method. Generally, the energy of an emitted photon is lower than the exciting photon **[18]**.Photoluminescence can be either fluorescence in which emission of light during excitation or phosphorescence in which emission of light after removal of excitation happens. Photoluminescence (PL) spectra of the molecular species are different from photoluminescence (PL) spectra of the atomic species. There are several possibilities of the electrons returning from the excited state to the ground state. The processes competing in luminescence are radiative and non-radiative transitions [**19, 20**].

1.4.2. Radiative transition

There are several possibilities of returning an electron to the ground state. **Figure 1.2** shows the configurational coordinate diagram in a broad band emission.This radiative transition can be explained through Franck-Condon principle.

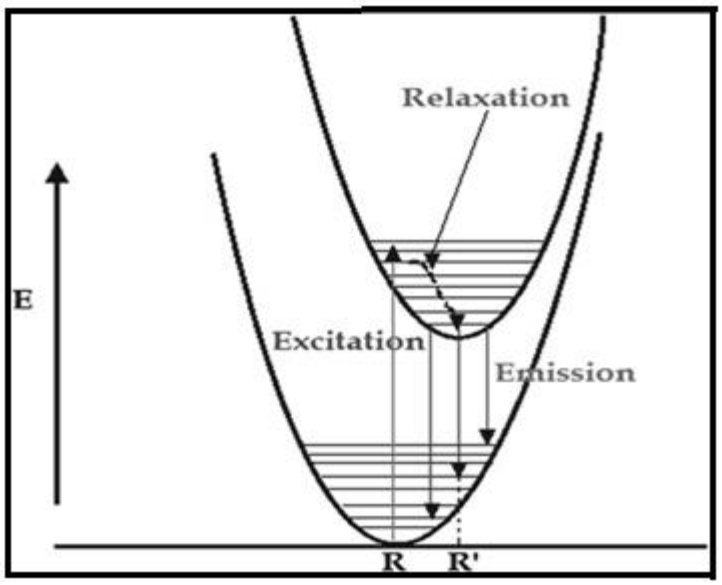

Figure1.2: Radiative transition (**From:***Kartik N.Shinde, S.J.Dhoble, H.C.swart and Kyeongsoon Park (2012), Basic Mechanism of Photoluminescence. In: Phosphate Phosphors for solid – state Lighting. Springer Series in materials Science, Springer, Berlin*.)

The Assumption is made on an offset between the parabolas of the ground state and the excited state. Upon excitation, the electron is excited in a broad optical band and brought in a higher vibrational level of the excited state and then relaxes to the lowest vibrational level of the excited state and gives up the excess energy to the vicinity. This relaxation process usually occurs non-radiative. From the lowest vibrational level of the excited state, the electrons return to the ground state through photon emission. Therefore, the emission wavelength is longer than the excitation wavelength.Therefore, the difference in energy between the maximum of the excitation band and that of the emission band is found which is called Stoke shift **[18]**.

1.4.3. Non-radiative transition

The energy absorbed by the luminescent materials which is not emitted as radiation and, is dissipated to the crystal lattice is called non-radiative transition. The non-radiative transition is also explained by the configurational coordinated diagram as shown in **Figure 1.3**. From **Figure 1.3 (a)** there is a Stoke shift between the ground state and the excited state. The relaxed excited state may reach the crossing of the parabolas by adjusting the temperature to be higher **[18]**. So the excited electron can return to the ground state through the crossing in a non-radiative manner. The excitation energy is transferred as heat to the lattice during the non-radiative process. In **Figure 1.3(b)** the parabolas of the ground state and excited state are parallel if the energy difference is equal to or less than four to five times the higher vibrational frequency of the surrounding lattice, so a few of the high energy vibrations are excited and are therefore lost in the radiation of phonons.This is called multiphonon emission. In three-parabola diagram,both radiative and non-radiative possible phenomena are shown in **Figure 1.3(c)**.The parallel parabolas (solid lines) from the same configuration are crossed by a third parabola originated from a different configuration. The transition from the ground state to the lower excited state (solid lines) is optically forbidden, but it is allowed to transit to the upper excited state (dash line).Excitation to the transition allowed parabola then relaxes to the relaxed excited state of the second excited parabola .Thereafter emission occurs from it **[21]**.

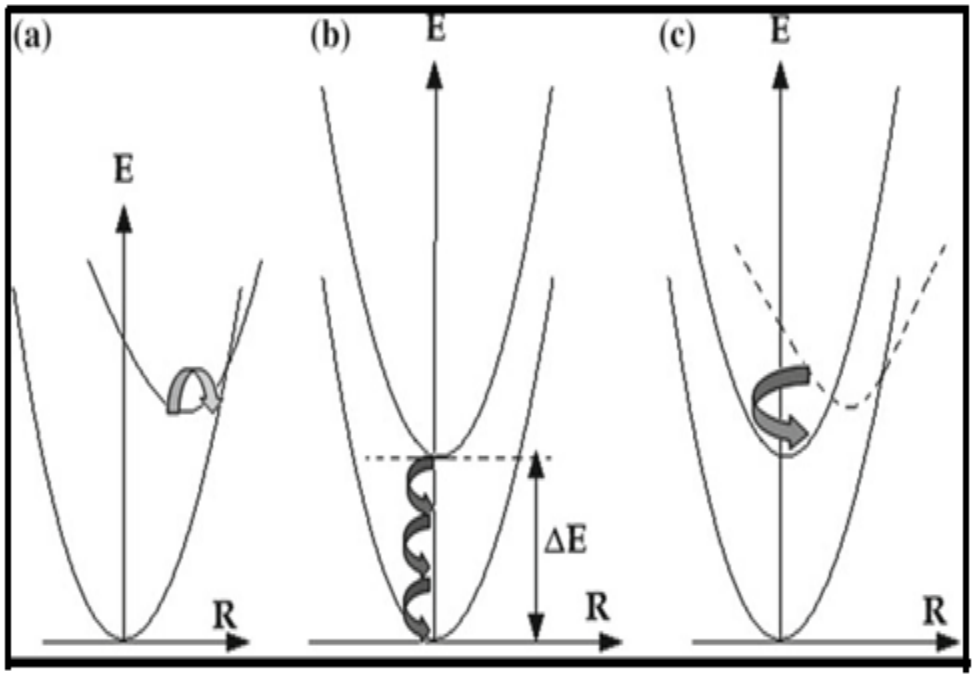

Figure 1.3: Non-radiative transition (**From:***Kartik N.Shinde, S.J.Dhoble, H.C.swart and Kyeongsoon Park (2012), Basic Mechanisms of Photoluminescence in: Phosphate Phosphors for solid – state Lighting. Springer Series in Materials Science, Springer, Berlin*.)

1.5. Introduction to the Tungstates

Tungstates are class of ternary oxides and self-activating luminescence materials. Other ternary oxides such as molybdates, vanadates are also self- activators **[22-24]**. Among important classes, metal tungstates are considered great self-activated luminescent materials and good host material for rare-earth doping for luminescence applications **[25-28]**.Tungstates two structures crystallize on their cationic radii,i.e.,Wolframite ($r \leq 0.77$Å) and Scheelite ($r \geq 0.90$Å) **[29, 30]**.

In Scheelite structure, "W" ion is coordinated with four oxygen atoms forming tetrahedral coordination while bivalent cation is coordinated with eight oxygen atoms forming polyhedral coordination as shown in **Figure 1.4**.$CaWO_4$,$SrWO_4$,$BaWO_4$,$PbWO_4$, etc. are examples of Scheelite type tungstates.The intrinsic luminescence of Scheelite arises due to the annihilation of the self-trapped exciton(STE),which forms excited $[WO_4]^{2-}$ complexes respectively **[31]**.The divalent transition metal tungstate shows wide-gained commercial interest in lasers and fluorescent lamps **[23,32]**.

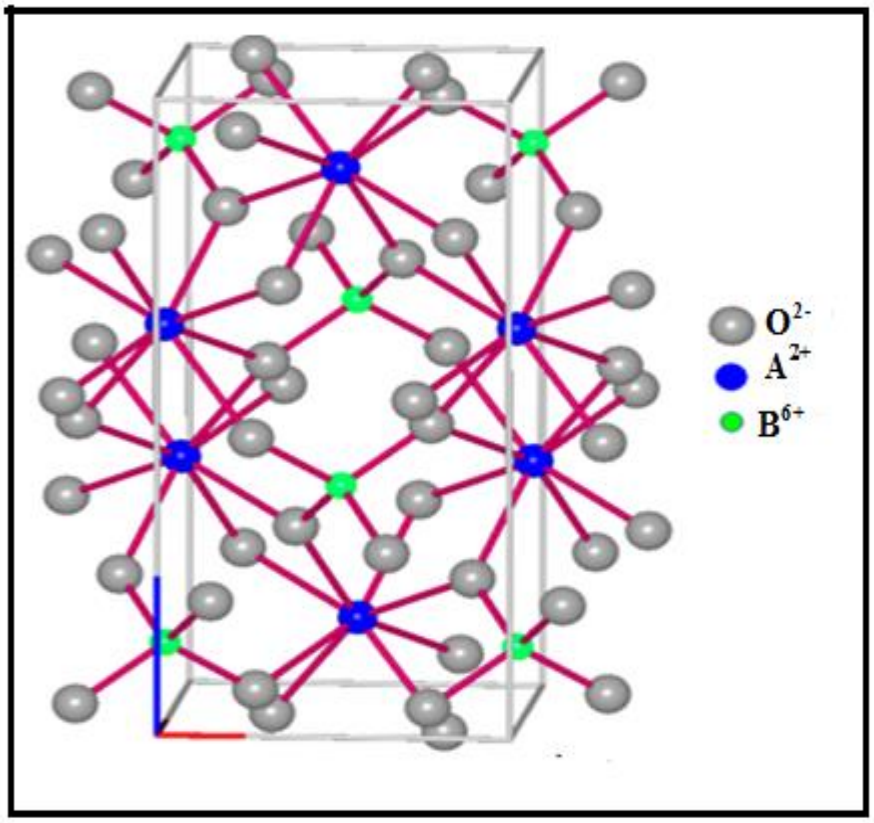

Figure 1.4: The conventional unit cell of Scheelite structure, where A, B and O are the metal cations, tungsten and oxygen respectively. [**From**: *https//shodhganga.inflibnet.ac.in/bitstream/10603/4722/11/11_chapter%201.pdf*].

1.6. Excitonic emission

An exciton is a bound electron-hole pair in which an excited electron is interacting with a hole. As the exciton moves through the crystal, carries some energy, and the electron and hole recombine to produce luminescence. There are three kinds of excitons. Frenkel exciton, Wannier-Mott exciton and charge transfer exciton **[33]**. Frenkel excitons are localized and resemble an atomic excited state. Wannier–Mott excitons extend over many lattice constants and are free to move through the lattice, while Frenkel excitons have a radius comparable to the interatomic distance. The Wannier exciton is composed of an electron in the conduction band and a hole in the valence band bound together. Charge transfer (CT) excitons are formed when an electron and a hole occupy adjacent molecules. They occur primarily in organic and molecular crystals; in this case, unlike Frenkel and Wannier excitons, charge transfer (CT) excitons display a static electric

dipole moment. The energy level diagrams of the Scheelite structure are given in **Figure 1.5** below.

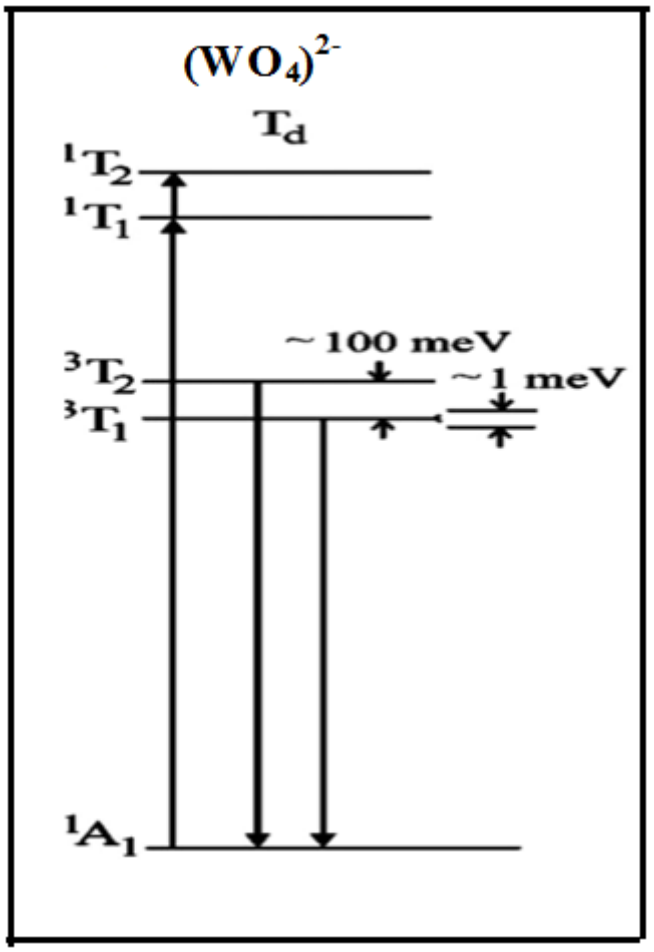

Figure 1.5: Energy level diagram of Scheelite structure.

1.7. Self-trapped exciton

In the intrinsic luminescence self-trapped excitons play an important role in the tungstates **[31, 34]**. In semiconductors and insulators, the excitons interact with phonons. If the interaction is strong enough, the exciton will be covered with clouds of phonons which would strongly diminish the movement of excitons across the crystal.This process is called self-trapping of the exciton. When the interaction is strong, the corresponding intrinsic luminescence spectrum will be very broad. Exciton self-trapping process can be explained in the following way: the translational movement of the exciton is driven by its hole. The movement of the heavy hole is then very slow. Therefore, the hole strongly polarizes the surrounding lattice thereby further slowing down, resulting in the overall positioning of the hole close to some atoms constituting

the host lattice. A light electron accompanying the hole will then describe its orbit in the close vicinity.

1.8. Charge transfer luminescence

In tungstate materials, charge transfer luminescence plays an important role. In the case of charge transfer, the optical transition occurs between different kinds of orbitals or between electronic states of different ions. In this process charge distribution on the optical center and chemical bonding also changes significantly **[35-37]**. Owing to these very broad emission spectra are expected. Very well-known examples are Scheelite type tungstates such as $CaWO_4$, $PbWO_4$, and $BaWO_4$. These materials are used for decades of the detection of X-rays, scintillators, and fluorescent lamps which show luminescence originating from the $[WO_4]^{2-}$ groups. The transition involves charge transfer of oxygen ions to empty d-levels of the tungsten ion. In these materials, no intentional dopants are introduced, so it is also called a self-activating material.

There are two types of charge transfer mechanisms involved in metal tungstates: Metal to ligand (MLCT) charge transfer and ligand to metal charge transfer (LMCT) **[38]**which is shown in**Figure 1.6(a-b)**. In Scheelite tungstates $[WO_4]^{2-}$ anion has a characteristic ligand to metal charge transfer (LMCT) **[39]**. In this transition, an electron is transferred from the highest occupied molecular orbital (HOMO) which has oxygen 2p non-bonding orbital character of the lowest unoccupied molecular orbital (LUMO), which is an anti-bonding orbital with W 5d orbital. Charge transfer of metal to ligand originates from the transition to electrons from molecular orbitals with metal-like characteristics to molecular orbitals with ligand-like characteristics. Furthermore, the presence of cation with partially filled d-orbital of transition metal tungstates leads to familiar d-d transition. A third possibility is the transfer of electrons from the partially filled d-orbital's of the cation to the empty molecular orbital's based of W 5d on the tungstate group. There is an effectively a transfer of an electron from the A^{2+} cation to the W^{6+} ion, this transition can be labeled as metal to metal charged transfer (MMCT) **[38]**.

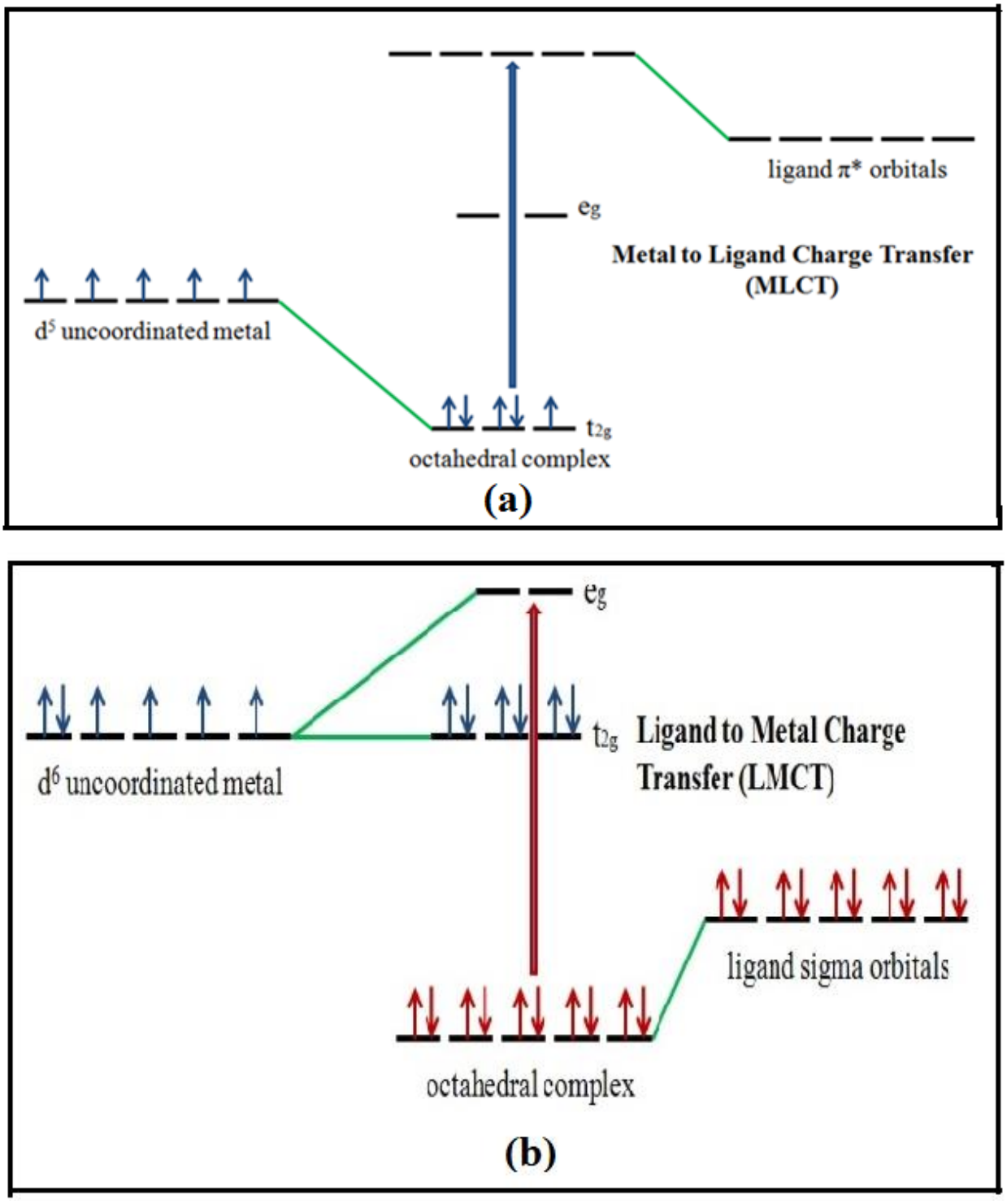

Figure 1.6(a-b): (a) Metal to ligand charge transfer **(MLCT)** (**b)** Ligand to metal charge transfer **(LMCT)**

1.9. Introduction to DC electrical conductivity

Well-known nanostructured materials have attracted considerable attention because of the nanoscale materials showing novel electric properties that are markedly different from those of the conventional bulk counterparts due to their quantum-size effects, small-size effects, and a large fraction of grain boundaries (GBs) **[40]**.The electrical conductivity is the material property that represents the ease with which a current of charge carriers can flow under an applied potential. Or in simple form, it is amount of electrical current a material can conduct called electrical conductivity (σ). P.K.L.Drude was first person to explain in solids electrical conduction and consider as sea of electrons or an electron gas in metals. Semiconductor Metal Oxides (SMO) are interesting materials due to their non-linear electrical response, making their use possible in many technological applications, such as light and gas sensors, electro-optical devices, photovoltaic cells, and electrical transient suppressors (varistors), responsible for acting as an energy drain **[41]**.This characteristic is due to the polycrystalline nature of ceramic varistors and the effective potential barriers at the grain boundaries that enable a non-linear relationship between the voltage and the current. This non-ohmic behavior of ceramics has been defined by the empirical **equation1.1 [42]**.

$$J = KE^{\alpha} \qquad (1.1)$$

Where (J) is the current density, (E) the electric field intensity and (K) constant related to the microstructure of the material and (α) is the non-linear coefficient. The larger the value of (α), the more useful as the varistor.

In varistor materials, one of the most important parameters is the non-linearity coefficient (α). The value of (α) defines how fast the change is from the high resistive to the low resistive state, allowing the excess current to flow through the ground.

The ratio of the current density (J) to the electric field strength (E) is defined as electrical conductivity, i.e. $\sigma = \frac{J}{A}$ **(1.2)**

Since current density, $J = \frac{I}{A}$, and electric field, $E = -\frac{dV}{dX}$, where (I) is the current, (A) is the cross section of the sample, and (X) is length. The inverse of conductivity (σ) is electrical resistivity (ρ), and defined as: $\rho = \frac{1}{\sigma}$. For a wire of cross-sectional area (A) having length (L) with resistance (R), the resistivity **(ρ)** is given by: $\rho = \frac{RA}{L}$ **(1.3)**

DC conductivity & non-linearity coefficients (α),Number of grain boundaries (n),Grain boundary voltage (V_{gb}),Breakdown field (E_B) of the samples were calculated by the following **equation (1.4)-(1.8) [43]**.

$$\sigma_{dc} = \frac{L}{RA} \quad (1.4)$$

Where (L), (R) and (A) is the thickness, resistance and area of the pellets respectively

$$\alpha = \frac{\log(J_2/J_1)}{\log(E_2/E_1)} \quad (1.5)$$

$$\text{Number of grain Boundaries (n)} = \frac{D}{d} \quad (1.6)$$

$$\text{Grain Boundary Voltage } (V_{gb}) = \frac{VB}{n} \quad (1.7)$$

$$\text{Breakdown field, } E_B = \frac{Vgb}{d} \quad (1.8)$$

Where (V_B) is the breakdown voltage (breakdown voltage is the voltage at which the varistor switches from a highly resistive state to a highly conductive state), (V_{gb}) is the average breakdown voltage per grain boundaries, (d) is the sample thickness and (E_1) and (E_2) are the electric fields measured at the current densities respectively.

1.9.1 DC electrical conductivity mechanism

Some theoretical models have been proposed that explain grain-grain conduction and other varistor phenomena with reasonable credibility **[44-53]**.These models are based on the double depletion layer concept for the region of closest grain-grain contact, and this is the generally accepted starting point for any physical model of the varistor junction. The origin of the double depletions layer can be understood by considering the formation of a grain boundary when two identical semiconducting grains are joined. The grain boundary is assumed to be comprised the same semiconducting material as the grain but also contains defects and dopants.As a result, its fermi level is different from that of the two grains, and it also has additional electronic states because of the defects and dopants within the bandgap. Electrons flow to the grain boundary, where they are trapped by the defects and dopants. The result of this electron flow is that the electrons trapped at the grain boundary act like a sheet of negative charge at the boundary, leaving behind a layer of positively charged donor sites on either side with the boundary thereby creating an electrostatic field with a barrier at the boundary. The boundary of each grain and its neighbor controls the current according to the applied voltage and allows current to flow in two directions. The mass of randomly oriented grains is electrically equivalent

to a network of back-to-back diode pairs, each pair in parallel with many other pairs. Varistor action is controlled by depletioning layers situated within the grains of the grain–grain interfaces. As the non-linear electrical behavior occurs to the boundary of each semiconducting grain, the varistor can be defined as a multi-junction device composed of series and parallel connections between grain boundaries. An ideal varistor should consist only of homogeneously distributed grains of highly resistive grain boundaries without secondary phases.Varistor system presents two phases or two kinds of similar (grain-grain) grain boundaries one thin (called type I), and the other thick dissimilar (grain-grain) (called type II), and the type I grain boundary is considered desirable to obtain good varistor properties **[54]**.The formation of the potential barrier in type I grain boundaries should present effective barriers for electron transport, whereas type II grain boundaries resultin loss of electrical properties.

1.10. Introduction to dielectric properties

The dielectric property of ceramics indicates the quality of the materials for a wide range of applications. All the tungstates are insulators. It is well known that the dielectric properties of ceramic materials depend on their composition, structure, and experimental conditions **[55]**. This section presents a brief description of dielectric materials and its mechanism. The crystalline dielectric materials are classified into two major categories **[56]:**

- Polar (dipole) dielectrics
- Non-polar (neutral) dielectrics

In polar dielectrics, permanent polarization (P_s) exists even without an external electric field. Whereas no permanent polarization (P_s) was observed in non-polar dielectrics **[57]**. Dielectric materials are generally known as an insulator. A dielectric (or dielectric material) is an electrical insulator that can be polarized by an applied electric field.The dielectric response arises from the short-range motion of charge carriers under the influence of an externally applied electric field while **Capacitance** is the ratio of the amount of electric charge **(Q)** stored on a conductor to a difference in electric potential**(V)**. The capacitance C is given as:

$$\mathbf{C = \frac{Q}{V}} \qquad \mathbf{(1.9)}$$

For a dielectric material placed between the plates of a capacitor, it may be shown that: The capacitance of the capacitor without the dielectric is given by:

$$\mathbf{C_0 = \frac{\varepsilon_o A}{L}} \qquad \mathbf{(1.10)}$$

The capacitance of the capacitor with dielectrics is termed as:

$$\mathbf{C = \frac{\varepsilon A}{L}} \qquad \mathbf{(1.11)}$$

Where (ε), (L) and (C) are permittivity or dielectric constant, thickness and area of the dielectric materials respectively.

1.10.1. Dielectric relaxation

In dielectric material, the change of polarization is a time-dependent process and given by the **equation (1.12)**:

$$\mathbf{P\ (t) = P_0\ [1\text{-}exp\ (\text{-}t/t)]} \qquad \mathbf{(1.12)}$$

Where (P_0) is a maximum polarization and (t) is the relaxation time of the polarization (dielectric relaxation). The time varies for different polarization processes. The space charge polarization occurs at very low frequencies less than 10^2 Hz. It refers to the diffusion of metal ions over several inter-atomic spacing. It also appears in machines having frequencies between 50 to 60 Hz. It is one of the slowest processes as compared to other types of polarization. It is very small and is negligible as compared to other types of polarization. The orientation polarization appears in the polar molecules under the application of the ac field. Its mechanism is faster than space charge polarization but slower than the ionic and electronic polarization. Its frequency range is less than 10^7 Hz. The ionic polarization exists in ionic molecules having a frequency of less than 10^{13} Hz. Ionic polarization cannot appear in optical frequencies (~10^{15} Hz) as the ionic molecules require a time of about 100 times greater than the frequency of the applied field. Ionic polarization is faster than space charge and orientation polarization but slower than electronic polarization. Electronic polarization is the fastest polarization and appears immediately after the supply is switched on. It occurs even at optical frequencies **[58]**.The frequency-dependent of the polarization is shown in **Figure 1.7**.

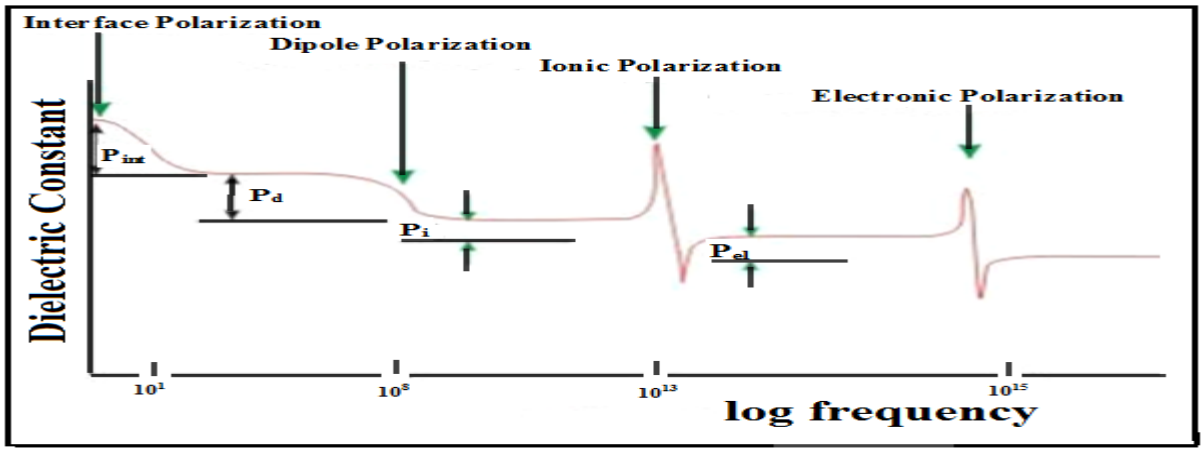

Figure 1.7: Variation of polarization with frequency.

1.10.2. Maxwell - Wagner polarization effect

The Maxwell–Wagner effect shows charge accumulation at the two-material interface based on the difference between charge carrier relaxation times for these two materials. This effect is based on charge carrier relaxation times for two materials and is commonly known as the interfacial charging effect. This effect occurs especially to low frequencies. The real and imaginary part of the capacitor is given by Maxwell - Wagner polarization model as following equations:

$$\varepsilon'(\omega) = \frac{1}{C_0(R_i+R_b)} \frac{\tau_i+\tau_b-\tau+\omega^2\tau_i\omega_b\tau}{1+\omega^2\tau^2} \qquad (1.13)$$

$$\varepsilon''(\omega) = \frac{1}{\omega C_0(R_i+R_b)} \frac{1-\omega^2\tau_i\tau_b+\omega^2\tau(\tau_i+\tau_b)}{1+\omega^2\tau^2} \qquad (1.14)$$

Where $\tau_i = C_i R_i$

$\tau_b = C_b R_b$

$$\tau = \frac{\tau_i R_b+\tau_b R_i}{R_i+R_b} \qquad (1.15)$$

where τ_i, τ_b, C_i, C_b, R_i, R_b are relaxation times, capacitance, resistance respectively and subscript i and b refers to the interfacial-like and bulk like layers, respectively.

1.11. Space charge layer (SCL) in nanocomposites

In nanocomposites, crystalline symmetry is broken at interfaces of two similar phases (homophase interface) between two grains or between two different phases (heterophase interface), resulting in a local space charge region due to the redistribution of ionic and electronic defects **[10]**. Ionic defects from the bulk phases adjacent to the interface are depleted in the space charge region, while those with opposite charge are accumulated **[59]**. In the case of oxygen-ion conductor having Frenkel equilibrium for the anionic sublattice, segregation of interstitial oxygen ions at the phase boundary increases the concentration of oppositely charged point defects (oxygen vacancy) in the space charge region. The fundamental concept is that ions can be trapped at the interface core. The counter species, in general a trapped ion vacancy, is then accumulated in the adjacent space charge regions. The chemical affinity of a second phase to the trapped ion gives rise to a driving force.

1.12. Introduction to Thermoelectricity

Thermoelectrics is the conversion ofheat toelectricity. Since thermoelectrics is thermodynamically reversible, so it can directly convert thermal energy into electrical energy or vice versa. In 1821, Thomas J. Seebeck discovered that an electromotive force or a potential difference could be produced by a circuit made from two dissimilar wires, when one of the junctions was heated. This is called the Seebeck effect.

1.12.1. Seebeck effect

"**Seebeck effect**, production of an electromotive force (emf) and consequently an electric current in a loop of material consisting of at least two dissimilar conductors when two junctions are maintained at different temperatures".

Voltge will be developed, when a temperature difference is established between the hot and cold ends of p-type and n-type semiconductors. Charge carriers (electrons or holes) at the hot side have more thermal energy than the carriers at the cold side of the materials; they start to diffuse to the cold side, causing accumulation of charge carriers at the cold end leading to the formation of an electric field, which opposes the further diffusion of charge carriers under the temperature difference. Then equilibrium will be established when the rate at which carriers move from the hot side to the cold side due to diffusion is balanced by the rate at which carriers move from the cold side to the hot side due to the established electric field which occurs in open circuit mode which is called Seebeck voltage, and amount of voltage developed per unit temperature gradient is called the Seebeck coefficient(S).

For a good thermoelectric material should have high values of both electrical conductivity (σ) and Seebeck coefficient (S), but needs to have low thermal conductivity (κ).The high electrical conductivity (σ) reduces the joule heating ($P=I^2R$) and increases the thermoelectric voltage (ΔV) generated, while the low thermal conductivity (κ) reduces transfer of heat of the junctions. The sign of Seebeck coefficient(S) depends on **(i)** sign of the charge carriers, unlike electrical and thermal conductivities (depends on the magnitude of the charge), and **(ii)** energy dependence on the momentum relaxation time of the scattering mechanism at Fermi energy.The physical factors that determine Seebeck coefficient(S) are two contributions tocharge-carrier diffusion (S_d) and phonon drag (S_p), which gives total Seebeck coefficient (S), $\mathbf{S=S_d+S_p}$. Under a temperature gradient, diffusion of electrons through the samples leads to set up an electric field, while a state of equilibrium is established between electrons under the temperature gradient and electrostatic repulsion due to the excess charge at the cold end arises due to flow of phonon wind dragging electrons due to electron-phonon coupling from the hot end to the cold end.

1.12.2. Thermoelectric power factor

Thermoelectric power factor (PF or P) defined as the multiplication of squared thermopower (S^2) with DC electrical conductivity (σ_{dc}) and is given by **equation (1.16)**:

$$\mathbf{P = S^2\sigma_{dc}\ (W/mK^2)} \qquad \mathbf{(1.16)}$$

Thermoelectric materials with a higher power factor are able to generate more energy (move more heat or extract more energy from that temperature difference) this is only true of a thermoelectric device with fixed geometry and unlimited heat source and cooling.The efficiency of the thermoelectric materials is given as figure of merit (ZT) given by the **equation (1.17):**

$$\mathbf{ZT = \frac{S^2\sigma dcT}{\kappa}}$$

$$\mathbf{ZT = \frac{PT}{\kappa}} \qquad \mathbf{(1.17)}$$

The higher value of power factor (PF or P) and low value of thermal conductivity (κ) leads to maximum efficiency of thermoelectric (TE) materials as well as devices.Thermoelectric materials are characterized by Figure of Merit (ZT), that is, they show high Seebeck coefficient(S), high conductivity and low thermal conductivity at the same time. Such three parameters are functions of carrier concentration that are difficult to be satisfied, which cannot be tuned independently. The Seebeck coefficient (S) decreases from increasing carrier concentration, while electrical

conductivity (σ) increases. As a consequence, the carrier concentration takes an optimum value of maximizing the power factor ($\mathbf{S^2\sigma_{dc}}$). A good balance between conductivity and Seebeck coefficient(S) is required to obtain a maximum power factor ($\mathbf{S^2\sigma_{dc}}$). In other words, conventional metals have small Seebeck coefficient(S), while semiconductors have low conductivity. Optimum carrier concentration to be evaluated 10^{19}–10^{21} cm^3 for a typical carrier concentration of semiconductors. Once the carrier concentration is set to be the optimum value, the only way to maximize the conductivity is to maximize the mobility.

1.12.3. Charge Carrier Scattering Mechanisms

Literature proves that, nanoinclusions and grain boundaries in composites scatters phonons and charge carriers thus reducing charge carrier mobility **[60, 61]**. However, it may be possible to enhance phonon scattering while simultaneously preserving the electrical conductivity with the optimum amount of nanoinclusions or grain boundaries **[62]**. The major carriers of heat called Acoustic phonons having spectrum of wavelengths and mean free paths (MFP**) [63]**. They contribute differently to thermal conductivity depending on their wavelengths.In order to scatter short wavelength phonons atomic defects are needed while large particles scatter mid and long wavelength phonons. The grain boundaries present in nanocomposites can act as large particles and are very efficient in scattering mid and longer-wavelength phonons. While dpending on the states available when phonons incident at the interfaces, they generate multiple phonons of longer wavelengths beyond the grain boundaries. If the nanostructures are smaller than the phonon mean free path (MFP), but greater than charge carrier mean free path (MFP), phonons are more strongly scattered by the interfaces than the charge carriers, resulting in reduced thermal conductivity but not changing the mobility of the charge carrier**[64]**. Another approach to arrest the coherent propagation of heat carrying acoustic waves without affecting the electrical conductivity and Seebeck coefficient is to incorporate chemically and physically inert nanoparticles into bulk thermoelectric power materials **[63, 65]**.When the dimensions of the nanoinclusions or grain boundaries are comparable to the mean free path (MFP), the phonons will be scattered, reducing lattice thermal conductivity (κ_l).

1.13. Literature review on the studied system

Tungstate materials have aroused much interest because of their, structural properties and potential applications in the fields of luminescence, microwave, electrical, optical, scintillating,

magnetic, photo-catalytic and humidity sensing. In Scheelite tungstates: As a self-activating phosphor, tungstate has some advantages, **e.g.,** high chemical stability, high X-ray absorption coefficient, high light to yield, and low afterglow to luminescence. Its luminescence originates due to the intrinsic structure which resulted in the charge transfer of excited 2p orbits of O^{2-} to the empty orbits of the central W^{6+} ions, and due to the structural defects. This section explores the brief review of the studied system $BaWO_4$ and $CaWO_4$ nanomaterials.

Calcium tungstate with the chemical formula $CaWO_4$ is the first compound of this class, which was first discovered in the year 1821 for an occurrence of Bispbergs Klack iron mine, Säter, Dalarna, Sweden, and it was named as Scheelite after the Swedish chemist Carl Wilhelm Scheele (1742-1786). Among the Scheelite structure tungstates, Barium tungstate, Calcium tungstate ($BaWO_4$, $CaWO_4$) aroused much attention in the electrical, optical and photo-catalytic applications. In Scheelite structure, $BaWO_4$ and $CaWO_4$ containing Ba^{2+} and Ca^{2+} ions and $[WO_4]^{2-}$ anion, bivalent cation coordinated by eight oxygen atom forming polyhedral coordination and"W" ion has coordinated by four oxygen atom forming tetrahedral coordination is considered to be highly functional nanomaterial due to its intrigue luminescent properties**[66]**.

Barium tungstate, $BaWO_4$ (BWO) has attracted interests in several research groups of its applications as a radiation detector, solid-state laser host, Raman shifters etc. **[31, 67-69]**. Luminescent properties of $BaWO_4$ (BWO) were investigated in the past for samples taken in the form of either sintered powders **[70-72]** or nano-crystallites **[73]**. Experiments on milled powder and theoretical calculations have shown that structural disorder in the lattice is an important condition to generate an intense and broad photoluminescence (PL) band at room temperature **[72]**.$BaWO_4$ (BWO) nanocrystals with different morphologies, such as whiskers, octahedral, fishbone-like, penniform, hollow, rod, wire, etc. have been successfully prepared and characterized as recent years **[72]**. In a recent study concerning the excitons emission from AWO_4 materials, the photoluminescence (PL) spectra of BWO single crystal were also reported.

As a blue phosphor and host material, $CaWO_4$ has been used in X-ray intensified screens, lasers, fluorescence lamps and scintillators. In 1947 luminescence studied of bulk tungstates and molybdates of Calcium, Strontium, and Magnesium was reported by F.A.Kroger **[74]**.Calcium tungstate material prepared by the stoichiometric mixture heating of CaO or $CaCO_3$ and tungstic acid was first reported by Kroger et al. **[74]**. Early first reported observation of faint absorption lines of the yellow region of the spectrum (~585 nm) from naturally occurring $CaWO_4$ crystals

that contained trace impurities of Nd perhaps prompted the use of Nd: $CaWO_4$ for the generation of second harmonics of a laser radiation **[75,76]**. In powder form, Calcium tungstate is a well-known blue-emitting phosphor **[77]**. Recently, highly crystallized thin films of $CaWO_4$ was prepared by an electrochemical method of room temperature and observed blue emission (456 nm) with excitation light of 254 nm was reported by Woo-Seok Cho et al. **[78]**. Enhanced Blue emission from $CaWO_4$ originated from recombination of self-trapped excitons due to removal of hydroxyl ions from surface of $CaWO_4$ after annealing reported by Basu et al. **[79]**. Bi^{3+}doped $CaWO_4$ decreases the photoluminescence (PL) emission intensity of $CaWO_4$ reported by Kang et al. **[80]**.

$CaWO_4$ micro - and nanocrystals were obtained by the microwave-assisted hydrothermal/solvothermal method at 160^0C for 30 minutes. The maximum photoluminescence (PL) emissionsof 491 nm and 484 nm for the $CaWO_4$ micro- and nanocrystals were attributed to the CCCT mechanism involved in the electronic transitions **[81]**. Luminescence of Bi^{3+} and Bi^{3+}+ Eu^{3+} in calcium tungstate powder prepared by the solid state diffusion method has been reported. The increase in the intensity of Eu^{3+} emission of $CaWO_4$: Bi^{3+}; Eu^{3+}. This enhances the Eu^{3+} emission intensity by 60 times compared to $CaWO_4$: Eu^{3+} (1 mol %) **[82]**. Undoped and Eu^{3+} doped MWO_4 (M=Ca, Sr, Ba) nanomaterials were prepared at room temperature (RT) by co-precipitation method. Strong red emission has been observed from Eu^{3+}doped MWO_4 nanomaterials and the emission intensity decreases from increase in ionic size of M^{2+} **[83]**. Single crystals of $CaWO_4$ and $CaMoO_4$ doped with Tb^{3+} have been grown by the flux growth method and measured luminescence spectra and emission decay profiles in different experimental conditions at temperatures ranging from 10 to 600K **[84]**. Scheelite-type Calcium tungstate ($CaWO_4$) nanophosphors with different phase purity were synthesized by a wet chemistry method and the phase transition, optical, and photoluminescence properties of as-prepared samples were systematically studied. The intensity of the emission peaked at 428 nm increases first and then decreases from the increasing of calcining temperature. The emission peaks at 428 and 386 nm can be ascribed to the $^1T_2$ to $^1A_1$ optical transition of electrons within $[WO_4]^{2-}$ anions and the defect or carbon skeleton, respectively **[85]**.By a combination method of sol-gel process and electrospinning one-dimensional $CaWO_4$ and $CaWO_4$:Tb^{3+} nanowires, and nanotubes have been prepared,under ultraviolet and low-voltage electron beams excitation, the $CaWO_4$ samples gives blue emission higest intensity at 416 nm wavelength which originates from $[WO_4]^{2-}$groups,while

the $CaWO_4:Tb^{3+}$ samples show the characteristic emission of Tb^{3+} related to $^5D_4–^7F_{6,5,4,3}$ transitions owing to an efficient energy transfer from $[WO_4]^{2-}$ to Tb^{3+} **[86]**.This paper reports on the synthesis of $Ca_{(1-x)}WO_4 : Ag_x$ ($0 \leq x \leq 0.05$ mol %) powder phosphors by a hydrothermal method and followed by calcinations, the emission spectrum shows a broad emission from the wavelength ranges of 360-550 nm revealing a peak position of 420 nm due to the $[WO_4]^{2-}$ ion **[87]**. Nanocrystalline $CaWO_4$ has been synthesized by a sol-gel method using tungsten (VI) oxide, WO_3, and calcium nitrate tetra hydrate, $Ca(NO_3)_2.4H_2O$ as starting materials.The $CaWO_4$ particles ranged from 350 to 850 nm in size and reported emission from the blue region **[88]**. A solid-state metathetic (SSM) route assisted by cyclic microwave irradiation was used to synthesize Calcium tungstate ($CaWO_4$) particles.$CaWO_4$ well-crystallized particles were formed into 600ºC for 3 hours,showing an excellent and homogeneous morphology with sizes of 1-2 μm **[89]**.

Metal oxide semiconductor nanocomposites have enhanced photo-catalytic properties **[90]**.There are numerous reports on nanoscale heterostructures incorporating tungstate compounds, such as $ZnWO_4$/BiOI, Bi_2WO_6/TiO_2, $CaWO_4/Bi_2WO_6$, and SnO_2/WO_3, which were generated with a goal towards developing novel photo-catalytic and field emission properties **[91-94]**. $BaWO_4$/ $PrWO_4$ enhances the $BaWO_4$, photoluminescence (PL) and photo-catalytic reported by Cavalcante et al. **[95]**. $BaWO_4$/ $CdMoO_4$ nanocomposites studied photo-catalytic performance under visible light reported by Eghbali-Arani et al. **[96]**.Visible photoluminescence (PL) emission from room temperature in $Ca_xSr_{1-x}WO_4$ having structural order emitted more greener lights and disorder structure emitted stronger red and yellow light was first reported by V.M.Longo et al.**[97]**. Later sintered at 600^0C,$Ca_xSr_{1-x}WO_4$ sample reported (600nm peak showing broad emission) maximum PL emission which was not structurally highly ordered or disordered and explained the role of disorder and charge transfer between WO_4 and WO_3 clusters in $CaWO_4$ lattice for improved photoluminescence (PL) intensity reported by S.L.Porto et al. **[98]**. The PANI/$CaWO_4$ nanocomposites were successfully synthesized in-situ chemical oxidative polymerization method and Raman studies revealed electronic interaction between PANI and $CaWO_4$ nanoparticles.The photoluminescence (PL) spectra for the nanocomposite sample exhibited very large intensity emission **[99]**. $Sr_{1–x}Ca_xWO_4$ ceramics prepared by the solid state reaction route, shows broad blue photoluminescence (PL) emission at room temperature when excited with 250 nm wavelength **[100]**. The micro/nano-structured $CaWO_4/Bi_2WO_6$ composites

were successfully synthesized by a one-step hydrothermal route without using any templates or surfactants. The mechanism of enhanced photo-catalytic activity for the micro/nano-structured $CaWO_4/Bi_2WO_6$ composite can be attributed to the effective separation of electron–hole pairs **[94]**.Prasad Narayan Patil et al. reported enhanced blue emission of $CaWO_4$ in $BaWO_4/CaWO_4$ nanocomposites.The mechanism of enhanced photoluminescence (PL) emission of $xBaWO_4/(1-x)CaWO_4$ nanocomposites can be due to the excitonic charge transfer from $BaWO_4$ phase to $CaWO_4$ phase because of their Type I band alignment and interface occurring between them. More excitons in the $CaWO_4$ phase lead to an increase in the number of recombination processes which increases emission intensity from the $[WO_4]^{2-}$ anions of the $CaWO_4$ phase of the sample **[101]**.

In Polycrystalline Pb $(Cd_{1/2}W_{1/2})O_3$ samples both ac and dc conductivity have been studied over a wide range of temperature, current–voltage (I–V) characteristics of the compound studied at different temperatures reveal that the compound has excellent varistor behavior**[102]**. Ceramic varistors based ZnO with lead zinc borosilicate glass instead of Bi_20_3 were prepared. The obtained zinc borate phase at the grain boundary of ZnO-glass samples enhances the non-ohmic characteristics of the ceramic varistors **[103]**. Polycrystalline Pb $(Mn_{1/2}W_{1/2})$ O_3 samples were prepared by the high-temperature solid state reaction technique, the current density field strength (J-E) characteristics of the compound studied at different temperatures revealed that the compound has excellent varistor behavior **[104]**. Current-voltage characteristics and non-linear coefficients of the ZnO/Polypyrrole nanocomposites thin disks were studied in direct current mode. Results showed good varistor behavior of prepared ZnO/Polypyrrole nanocomposites **[105]**. In Ca, Ta-doped TiO_2 varistors with high non-linear coefficients are obtained by a ceramic sintering. The effects of Ta and, the non-linear electrical behavior of the TiO_2 system is explained by analogy between a grain-boundary atomic defect model **[106]**.The morphological and the electrical properties in Nb_2O_5-doped SnO_2-MnO_2 varistor systems were studied, the results showed that the increase of Nb_2O_5 contents in the SnO_2-MnO_2 Matrix have led to an increase in the varistor properties **[107]**. The electrical properties of (Sc, Ta) doped TiO_2 varistor ceramics have been investigated, the results revealed Schottky type barrier, is responsible for the varistor behavior **[108]**.The non-linear properties of ZBMCCS-based varistors are studied in relation to sintering temperature, in the range of 1280–1350^0C, and the effect of sintering temperature on the

microstructure and electrical properties of the ZBMCCS-based varistors are studied & reported **[109]**.The effect of composition controls the microstructure and electrical properties of the ZnO varistors doped with Ho_2O_3. The relation between the electrical characteristics of the Bi_2O_3-based ZnO varistor ceramics with various Ho_2O_3 content was investigated and the results are analyzed **[43]**.ZnO–V_2O_5–MnO_2–Nb_2O_5–Bi_2O_3 varistor ceramics low-temperature sintering effect on microstructure and electrical properties were investigated, and surprisingly high non-linear coefficient and noticeably lower leakage current ware attained by a proper sintering temperature **[110]**. The microstructure and non-ohmic behavior of ZnO-V_2O_5 ceramics is reported. The typical Schottky barrier controlled current behavior and the non-linearity characteristics were in response to the grain boundary barrier layer **[111]**.

Microwave dielectric characteristics of AWO_4 (A = Mg, Zn, Mn, Ca, Sr, Ba) compounds and their relations to structure have been investigated as a function of (A) cations and reported on the size of (A) cations permittivity decreased and with unit cell volume temperature coefficient of resonant frequency was correlated **[112]**.The Scheelite ceramics, with the general formula MWO_4 (M= Ca, Sr and Ba), are regarded as promising materials for microwave substrate applications, and studied the stability of the scheelites under the influence of a humid atmosphere and water. Also, influence of alkaline-containing (Na, Li) impurities on the sintering of scheelites and their susceptibility to humidity is presented **[113]**.$CaWO_4$-based ceramics reported as a new low-temperature co-fired ceramic (LTCC) material **[114]**.Nanocrystalline samples of $CaWO_4$ were prepared for room temperature by simple chemical precipitation. Very low dielectric loss in nanocrystalline $CaWO_4$ powder was observed at high frequencies. The values of ac electrical conductivity calculated from the permittivity studies were found to increase as frequency increased, conforming to small polaron hopping **[115]**.Nanostructured calcium tungstate ($CaWO_4$) of different(13nm & 26nm) grain sizes were synthesized using controlled chemical precipitation technique the dc electrical conductivity of compacts of nanocrystalline $CaWO_4$ wasreported as a function of temperature. The variation in DC electrical conductivity with chamber pressure, grain size and low temperature annealing was studied **[116]**. Microwave dielectric properties of A^{2+} B^{6+} O_4 (**A^{2+}**: Ca, Pb, Ba; **B^{6+}**: Mo, W) ceramics were investigated as a function of packing fraction and bond valence **[117]**.The electrical conductivity of $CaWO_4$ was studied at 900-1300°C and partial pressures of oxygen from 10^{-9} to 10^{-14}atm and reveals the

tungstate was found to be an a n-type semiconductor and its defect structure was interpreted in terms of oxygen vacancies and interstitials was reported by Ringdon and Grace **[118]**.

Microwave dielectric properties of $Ba_{1-x}Sr_xWO_4$ ceramics prepared by solid state reaction route and studied microwave dielectric constant, temperature coefficient of resonant frequency (τ_f), quality factors were measured with Hakkie-Coleman technique **[119]**.Optical and microwave dielectric properties of $Sr_{1-x}Ca_xWO_4$ ceramics prepared by the solid state reaction route, the permittivity was found to increase from the increase in Ca content in agreement with the Clausius–Mosotti relation **[100]**.Microwave dielectric properties of $(1-x)CaWO_4–xTiO_2$ prepared for conventional solid-state route in order to tune the dielectric properties, and were prepared for different values of x. In particular, at x = 2.6, showed good microwave dielectric properties **[120]**. $(1-x)CaWO_4-xTiO_2$ (CWT) ceramics was fabricated by conventional solid-state sintering method of 1200 °C for 4 hours. When x = 0.15, the sample achieves the optimum dielectric properties **[121**]. $(1-x)CaWO_4-xLaNbO_4$ ($0.0 \leq x \leq 0.5$) ceramics was investigated to control [TCF] of $CaWO_4$ based materials and results discussed the microwave dielectric properties of these $CaWO_4$–based materials the bond valence and atomic packing was also discussed **[122]**. Sintered at low temperature 900^0C of $Ba_5Nb_4O_{15}$-$BaWO_4$and $Ba_3(VO_4)_2$-$BaWO_4$composites and studied its dielectric properties for LTCC application were reported by Zhuang et al. **[123-125]**.

It was found that all Pr-doped $PbWO_4$ tungstates show the sign change of thermoelectric power around the temperature of 366K suggesting the p-n transition due to the existence of vacancy acceptor and donor levels **[126]**.Thermoelectric power of $CrVO_4$ in the temperature range 300-1000K exhibiting extrinsic conduction polaron hopping mechanism resulting in p-type semiconductor material up to 750K & normal band types showing intrinsic conduction above 750K**[127]**.Thermoelectric power of Palladium Sulfide (PdS) by Raman Scattering Spectroscopy is used to investigate the thermal transport properties of material over a wide range of temperatures**[128]**. Seebeck effects was observed by intramolecular charge-transfer states in n-type IIDT and p-type IIDDT devices based on vertical architecture of conductor/polymer/conductor design the results show that Seebeck coefficient is essentially determined by the combination of two Seebeck effects driven by polarization and entropy divergences**[129]**. Enhanced Seebeck coefficient observed through energy-barrier scattering in PbTe nanocomposites **[130]**. BTO/BST composite materials have been prepared by the

combination of ultrasonic dispersion and SPS, and the TE performance was systematically investigated in the temperature range of 300 K to 500 K. The results indicated that appropriate adding of BTO can improve the Seebeck coefficient by adjusting the carrier concentration and energy filtering effect to maintain a high power factor values **[131]**.Bi_2Te_3 nanocomposites samples have been prepared by incorporating nanostructures into the bulk matrix phase, the composite system have the theoretical potential to benefit from both quantum confinement effects and grain boundary scattering of phonons, resulting in enhanced thermopower and lowered thermal conductivity, respectively**[132]**.The Al_2O_3/Bi_2Te_3 nanocomposites sintered from the composite powders exhibit improved Figure of Merit (ZT) value at room temperature compared to that of pure Bi_2Te_3 due to reduced thermal conductivity caused by active phonon and carrier scattering at the newly formed Al_2O_3/Bi_2Te_3 interface**[133]**.Based on the concept of band bending to metal/semiconductor interfaces as an energy filter for electrons, present a theory about enhancement of the thermoelectric properties of semiconductor materials with metallic nanoinclusions**[134]**.Enhance thermoelectric performance of $Cu_2Se/Bi_{0.4}Sb_{1.6}Te_3$ nanocomposites at elevated temperatures due to elevated energy filtering out carriers andinhibition of minority transport besides enhanced phonon blocking from scattering at interfaces **[135]**. Alternatively, composite thermoelectric materials containing several phases may enhance the performance of thermoelectric materials by conserving a relatively high electrical conductivity while introducing more interfaces leading to a decrease in the thermal conductivity. Although several reports on the synthesis of composite thermoelectric materials have been published **[136-144]**.

1.14. Motivation, scope and objective of the present work

1.14.1. Motivation

Enhancing the photoluminescence (PL) emission intensity of phosphors along with multifunctional properties is a great challenge to the researchers. Tungstate nanomaterials are important inorganic materials for their vast applications of many technological fields.Because of easy charge separation behavior in tungstate materials; it is used in photo-catalytic and photoluminescent applications frequently.However, in $CaWO_4/CdSe$ nanocomposites, photoluminescence (PL) quenching and shortened photoluminescence (PL) lifetime were observed for the $CaWO_4$ phase due to $CaWO_4$ is transferring charge to CdSe phase and it was reported by Han et al. **[145**]. In another study, prepared $Ca_{(1-x)}Zn_xWO_4$ nano-crystals at room temperature based on solution chemistry and characterized their structural and optical properties.

It is observed that iso-valent substitution of Ca^{2+} by Zn^{2+} in $CaWO_4$ lattice leads to quenching of intrinsic blue emission **[146]**.From the brief review on schellite type tetragonal $CaWO_4$, in particular, $CaWO_4$ is a material of special interest, because of its intriguing and superior luminescence properties as a 'self-activated' luminescent material, whose optical properties are defined to a large degree by its intrinsic structural properties **[147-149]**. Specifically, upon UV excitation in the spectral range of 235- 260 nm, a strong blue emission near 420 nm can be observed and can be attributed to electronic transitions associated with charge transfer between oxygen and tungstate moieties within the WO_4 group **[150,148,151]**.We came to know that there is no report on the nanocomposites of $CaWO_4$ with scheelite type tungstates.The inspiration behind research problem came from the reported research papers entitled visible photoluminescence (PL) emission from room temperature(RT) in $Ca_xSr_{1-x}WO_4$ having structural ordered emitted more greener light and disordered structure emitted stronger red and yellow light which was first reported by Longo et al. [**97**]. Later reported maximum photoluminescence (PL) emission (broad emission with peak around 600 nm) intensity for $Ca_xSr_{1-x}WO_4$ sample sintered at 600°C which was not structurally highly ordered or disordered and well explained the role of disorder and charge transfer between WO_4 and WO_3 clusters in $CaWO_4$ lattice for improved photoluminescence (PL) intensity by Porto et al. [**98**].Also, we have synthesized Mixed $Ba_xCa_{1-x}WO_4$ nanopowder samples which did not give enhanced 420 nm emission in comparison with $CaWO_4$ emission from sintered (400^0,200^0C) and unsintered mixed samples. So it was decided to synthesize and characterize the $CaWO_4$ in $xBaWO_4/ (1-x) CaWO_4$nanocomposites.

Interfaces play an important role in oxide hetero-structure nanocomposites. In oxide heterostructure thin films interfacial effects have been studied widely **[152]**. It is observed that crystalline symmetry is broken at interfaces between two grains (homophase interface) or between two different phases (heterophase interface), resulting in a local space charge region due to the redistribution of ionic and electronic defects in ionic solids **[10]**.In the space charge region, ionic defects from the bulk phase are depleted to the adjacent interface; while those with opposite charge are accumulated **[59]**.Heterostructures powder nanocomposites are demonstrated great potential owing to their enhanced ionic conductivity **[153]**.Challenging to have interfacial effects in oxide homostructure nanocomposites.In tungstates, oxygen vacancies are the major defects **[154]**. The creation of space charge layer (SCL) at the interface is the reason for enhancing the

DC and AC electrical properties in nanocomposites samples. The spirit of the DC electrical properties studies originated from the paper entitled "Structural, dielectric and electrical properties of lead cadmium tungstate ceramics" by R.N.P. Choudhary et al. **[104]**. In this paper reported current–voltage (I–V) characteristics of the compound studied at a wide range of temperatures reveals that the compound also has excellent varistor behavior. Another AC electrical properties study originated from the paper entitled "Admittance-Frequency Response in Zinc Oxide Varistor Ceramics" by Mohammad A. Alim et al. **[155]**.In this paper reported room temperature dielectric constant (ε′) &loss tangent (tan δ) of ZnO-Bi_2O_3 ceramics having Debye relaxation peaked at 300 KHz due to trapping of certain intrinsic defects within the grain boundaries.So in order to study interface effect on DC and AC electrical conductivity and dielectric properties [dielectric constant (ε′) and loss tangent (tan δ)] of $xBaWO_4/(1- x)CaWO_4$ nanocompositesat room temperature (RT).

At present many researchers are developing various novel thermoelectric (TE) power materials with low cost, high power factor and environmental safety. In thermoelectric materials higher thermal conductivity is the major disadvantages. There is a big challenge to improve the efficiency of energy conversion which can be characterized by the figure of merit (*ZT*). In the past two decades it is seen that nanomaterials showed enhanced figure of merit (ZT) **[156]**. Recently, more researchers are devoted to study the temperature dependences on the electrical conductivity (σ) and Seebeck coefficient (S) of the composites by enhanced lattice scattering effect leads to increase in Seebeck coefficient (S) in the low temperature range and then minority carrier increased significantly on account of intrinsic excitation tending to decline Seebeck coefficient as the temperature increases and also reduces the thermal conductivity in $BaTiO_3/Bi_{0.5}Sb_{1.5}Te_3$ composite Materials **[131]**, $Cu_2Se/Bi_{0.4}Sb_{1.6}Te_3$ nanocomposites **[135]**, $CrVO_4$ **[127]**. The focus on this review article is on examining the metal oxide potentials for TE power generation of an emphasis on materials with high power factor. Effective doping strategies in achieving high power factor are highlighted for various metal oxides, particularly, Na_xCoO_2 **[157]**, $Ca_3Co_4O_9$ **[158]**, BiCuSeO **[159]**, $CaMnO_3$ **[160]**, $SrTiO_3$**[161]**, ZnO-based **[162]**,SnO_2-based **[163]**, and In_2O_3-based **[164]** alloys.The inspiration to explore thermoelectric power study above room temperature (RT) highlighted when observed that the crystallite size doesn't change much when C0 ($CaWO_4$) &C4 ($BaWO_4$) nanosamples are sintered till 400^0C which is shown in [**Table 3.3**] and reported by us which confirms its smaller grain size than C4 ($BaWO_4$)

nanosamples respectively**[101,165**].So there was interest in exploring the thermoelectric power properties of $xBaWO_4/ (1-x) CaWO_4$ nanocomposites above room temperature (RT).

1.14.2. Scope of the present work

Self-activated luminescent metal tungstates act as host for rare earth elements for luminescence applications **[24-27]**.The metal tungstates crystallizes into two structures based on their cationic radii **[28, 29]**.The intrinsic luminescence of Scheelite arises due to annihilation of the self-trapped exciton (STE), which forms excited $[WO_4]^{2-}$ complexes.These materials are found to be suitable applications for scintillation counters, lasers and optical fibers. Divalent transition metal tungstates showed commercial interest in lasers and fluorescent lamps, while some are of special importance due to their electrical conductivity and thermoelectric properties. Additionally, these materials also find applications as catalysts and humidity sensors **[166]**.

Among the Alkaline earth metal tungstates,$CaWO_4$ plays an important role and can be produced at low cost. It is used as an opto-electrical, laser host materials in quantum electronics, scintillators in medical devices, with properties giving blue luminescence at room temperature (RT) **[148,167-169]**. The optical properties of $CaWO_4$ nanomaterials have been studied and listed in literature survey. However, a very little work has been reported on luminescence study of $CaWO_4$ nanomaterials. The luminescence properties of $CaWO_4$ can be enhanced by doping various rare-earth ions which result in broad and intense absorption bands. Several papers on the luminescent properties of $CaWO_4$ doped with rare earth ions have been published **[168,170, 79]**. However, there are no reports on the efficient phosphors with thermally stable blue emissions from white light LED's based on $CaWO_4$ host matrix. In the recent years, intense effort has been witnessed in the preparation of nanomaterials thanks to their markedly different physical and chemical properties as compared to bulk materials **[171,172]**. At room temperature (RT), the photoluminescence (PL) intensity of $CaWO_4$ shows intense blue luminescence with microsecond decay than that of $CaWO_4$ bulk material **[173]**.

There are reports available with ceramic-ceramic nanocomposites for improving electrical properties **[174,175]**. Many approaches such as doping [**176-178]**, sintering **[179,180]** and different preparation methods **[181,167,182]** have been done to revive the conductivity of oxides semiconductors. In the reported studies of nanocrystalline cerium oxide, predominantly electronic conductivity was observed under conditions at which microcrystalline cerium oxide exhibits ionic conductivity materials. The most significant aspect regarding the electrical conductivity reported

to the microcrystalline and nanocrystalline cerium oxide is the change from impurity controlled ionic to electronic conductivity controlled by the external equilibrium **[183]**.The researcher found that nanocomposites with space charge layer (SCL) formation also raised the electrical conductivity of metal oxides **[184,152,185]**. The tungstate was found to be n-type semiconductor and its defect structure was interpreted in terms of oxygen vacancies and interstitials. The conductivity mechanisms in tungstates are largely unexplored and very few reports are found in the literature. In our literature study, we found that $CaWO_4$ sintered at 1100^0 C for 3 hours and showed good microwave dielectric properties(ε′) of 10, quality factor (Q·f) of 75000, which can be applicable to the materials for substrate and inductor in LTCC module. Also, reported that the sintering temperature of $CaWO_4$ ceramics could be effectively reduced from 1100 to 850^0C without degradation of dielectric properties by co-addition of Bi_2O_3- H_3BO_3**[186,187]**. The study of dielectric properties of samples as a function of frequency may help in identifying their potential applications **[188]**. The characterization of dielectric behavior is very important not only to the theory of the polarization mechanism but also from an application point of view, where knowledge of frequency dependence of dielectric constant is very important. The relative dielectric constant of the material determines its ability to store electrostatic energy.

Nanocomposites are materials with a nanoscale structure that improve the macroscopic properties of products.Until now, reported ceramic nanocomposites consist of ceramic nanophase in a ceramic matrix, a carbonaceous nanophase in a ceramic matrix or a ceramic nanophase in a polymer matrix. Experimental work has shown that all types and classes as nanocomposites materials lead to new and improved properties as compared to macrocomposites **[12]**. Therefore, nanocomposites promise new applications for many fields such as non-linear optics, nanowires, mechanically-reinforced lightweight components, battery cathodes and ionics, sensors and other systems **[189]**.

The properties of nanocomposites are not only dependent on their individual properties of different phases but also on their combined nature such as surface morphology and interfacial characteristics **[8]**. Therefore, the drawbacks of using inorganic nanostructure materials can be overcome by fabricating nanocomposites with interface **[11]**.The interfacing with nanocomposites can provide high-performance novel materials that find applications for various fields such as photoluminescent, photo-catalytic, photo-voltaic,electrochemical and thermoelectric.In nanocomposites accumulation of electrons and holes in one of the phases due to

charge transfer increases the number of recombinations in that phase. This process enhances the photoluminescence (PL) intensity of that phase. The formation of a space charge layer (SCL) at the interface enhances the dielectric properties (dielectric constant and loss tangent) and conductivity (AC and DC) of the nanocomposites. As in the case of thermoelectric materials, the lattice scattering effect is an effective method to improve the thermoelectric performances.

By a simple co-precipitation method samples were prepared without using surfactants. Co-precipitation reactions involve instantaneous occurrence of nucleation, growth, coarsening and/or agglomeration processes. The co-precipitation method provides high yield, high product purity, the lack of necessity to use organic solvents, easily reproducible, and low cost **[190,191]**. Generally, a surfactant in co-precipitation method is used to disperse the nanoparticles. But in our work the non-use of surfactant and unsintering the samples resulted in Type I band alignment. Type I band alignment was found to support interfacing, thus enhancing optical and electrical conductivity and dielectric properties (dielectric constant and loss tangent) of $xBaWO_4/(1-x)CaWO_4$ nanocomposites. Also, possible risk of contamination of the samples is avoided by not using surfactants **[192]**.

In this thesis we report the photoluminescence (PL) 420nm intrinsic peak intensity emitted by all the samples (unsintered and sintered). Maximum photoluminescence (PL) 420nm intrinsic peak intensity was emitted by C2 ($0.5BaWO_4/0.5CaWO_4$) unsintered nanocomposites. This maximum 420nm photoluminescence (PL)emission intensity of C2($0.5BaWO_4/0.5CaWO_4$) nanocomposites could be due to the excitonic charge transfer from $BaWO_4$ phase to $CaWO_4$ phase because of their type I band alignment and interface occurring between them. More excitons in the $CaWO_4$ phases lead to an increase in the number of recombination processes which increases emission intensity from the $[WO_4]^{2-}$ anions of the $CaWO_4$ phase of the sample. HRTEM image of C2 ($0.5BaWO_4/0.5CaWO_4$) nanocomposites also shows interfacing of $BaWO_4$ phase and $CaWO_4$ phase. The C2 ($0.5BaWO_4/0.5CaWO_4$) nanocomposites emission has maximum lifetime as compared to other samples which are approximately 13% more than the emission lifetime of C0 ($CaWO_4$) single phases respectively. This may be attributed to the recombination through non-radiative process introduced into the migration of charge from the conduction band (CB) of $BaWO_4$ phase to the conduction band (CB) of $CaWO_4$ phases. Due to the charge transfer mechanism this nanocomposite could be a host material to get enhanced

dopant (PL) emissions. Mixed $Ba_xCa_{1-x}WO_4$ nanopowder samples did not give enhanced 420 nm emission in comparison with $CaWO_4$ emission.

DC electrical conductivity at room temperature (RT) from 8Volts or (27.5 Volts/cm) onwards is found to be maximum for C2 ($0.5BaWO_4$/ $0.5CaWO_4$) nanocomposites and is approximately **40times** ($\sigma = 1.11x10^{-5}\ \Omega^{-1}\ cm^{-1}$) greater than that of C0($\sigma = 2.76x10^{-7}\ \Omega^{-1}\ cm^{-1}$) and **1008** times greater than that of C4 ($BaWO_4$) [$\sigma = 0.11x10^{-7}\Omega^{-1}\ cm^{-1}$] single phase samples. It is observed that the non linear coefficient alpha (**α)** for nanocomposites are less than the single phase C4($BaWO_4$) and C0($CaWO_4$) samples and is maximum for C4($BaWO_4$) sample.The calculated non-linearity coefficient (α)values lie in the range of 3.44 to 4.70 for the samples.This non-linearity current density (J) [A/cm^2]–electric field (E) [V/cm] characteristics arise in the samples due to the presence of insulating layer between the grain boundaries.The space charge layer (SCL) formation is a suitable mechanism to explain high conductivity and lower non-linearity in the C2 ($0.5BaWO_4/0.5CaWO_4$) nanocomposites.Also Type I band alignment interface occurring between the two phases of the nanocomposites promote easy charge transfer from $BaWO_4$ phase to $CaWO_4$ phase resulting in maximum conductivity of C2($0.5BaWO_4/0.5CaWO_4$) nanocomposites. The dielectric constant (ε′) at 20Hz frequency of C2 ($0.5BaWO_4/0.5CaWO_4$) nanocomposites is approximately **3 times** & **8 times** more than that of C0 ($CaWO_4$) & C4 ($BaWO_4$) single phase respectively.This maximum dielectric constant (ε′) of C2 ($0.5BaWO_4/0.5CaWO_4$) nanocomposites could be due to the type I band alignment and maximum interfacing occurring between the two phases in the samlpe. The total polarization of dielectric materials at lower frequency (20Hz) are due to electrode effect and the combination of electronic, ionic, orientation and interfacial polarization. Therefore interface plays an important role in increasing dielectric constant (ε′) in the nanocomposites.Interfaces between the two phases of the nanocomposite samples increase the accumulation of dipoles on the surface leading to increased surface charge polarizationand increasing the dielectric constant (ε′) of the C2 ($0.5BaWO_4/0.5CaWO_4$) nanocomposites. All the samples give the signature of single relaxation peak (Debye relaxation peak).Loss tangents (tan δ) peak of C2($0.5BaWO_4/0.5CaWO_4$) nanocomposites is more than that of other samples except the C3($0.75BaWO_4/0.25CaWO_4$) and also occurs at higher frequency. Higher (tan δ) at relaxation peak and shift towards the higher frequency side for C2 ($0.5BaWO_4/0.5CaWO_4$) nanocomposites shows decrease in relaxation time due to maximum additional collection of defects (electrons and holes) at the interface. The

relaxation time [τ =130µsec] at loss tangents (tanδ) peak of C2 ($0.5BaWO_4/0.5CaWO_4$) nanocomposites is **3 & 10 times less than** C0 ($CaWO_4$)[τ =410µsecond] & C4 ($BaWO_4$) [τ=1340µsecond] single phases respectively and ac conductivity ($\sigma_{ac}=52.2x10^{-7}\ \Omega^{-1}cm^{-1}$) at loss tangents (tanδ) peaks at particular frequency (1218Hz) of C2 ($0.5BaWO_4/0.5CaWO_4$) nanocomposites is **4 & 19 times** higher than C0 ($CaWO_4$) & C4 ($BaWO_4$) single phases respectively.

Seebeck coefficient(S) gives the confirmation of n-type semiconductors at room temperature (RT). The Seebeck coefficient (S) at inflexion point peak (I_p) of C3 ($0.75BaWO_4/0.25CaWO_4$) [0.52 µV/K] is greater than that of all other samples. Enhanced Seebeck coefficient(S) at inflexion point peak (I_p) and power factor (PF) ($698pWcm^{-1}K^{-2}$**)** of C3 ($0.75BaWO_4/0.25CaWO_4$) nanocomposites are due to higher lattice scattering effect resulting from optimal atomic ratio (Ba/Ca=3), grain size which support a good balance between electrical conductivity and Seebeck coefficient(S).

1.14.3. Objectives of the present work

- Synthesis of $xBaWO_4/\ (1-x)\ CaWO_4$ nanocomposites at room temperature (RT) using co-precipitation method without using any surfactant, optimizing the Ba/Ca atomic ratio and sintering temperature to get the possible interface.
- Room temperature XRD characterization to find the phase purity, crystallite size, lattice strain and lattice constant.
- Characterization by SEM, HRTEM, EDS and FTIR at room temperature (RT) to check the surface morphology, particle size, elemental composition, agglomeration, stretching vibrations and elemental oxidation states respectively of the prepared samples.
- UV-Vis Diffuse reflectance spectra to calculate the band gap energy and band positions of $BaWO_4$ and $CaWO_4$ phases and check the band alignment between the two phases.
- Recording of photoluminescence (PL) emission spectra and photoluminescence (PL) lifetime measurements at room temperature (RT) to check the effect of $BaWO_4$ phase on the photoluminescence (PL) emission and photoluminescence (PL) lifetime of $CaWO_4$ phase.

- DC electrical measurements done at room temperature (RT) to study the non-linearity characteristics behavior and its interfacial effects in $xBaWO_4/(1-x)CaWO_4$ nanocomposites.
- AC electrical measurements done at room temperature (RT) in the frequency range of 20Hz to 3MHz to study the interfacial effects on the electrical properties [dielectric constant (ε′), loss tangent (tanδ) and AC conductivity (σ_{ac})] of the $xBaWO_4/(1-x)\ CaWO_4$ nanocomposites.
- Thermoelectric power study in the temperature range of 300K to 773K to study the lattice scattering effect of the $xBaWO_4/\ (1-x)\ CaWO_4$ nanocomposites.

1.15. Organization of chapters in the thesis

- **Chapter 2**: Lists the various instruments used to characterize the $xBaWO_4/(1-x)CaWO_4$ nanocomposites.
- **Chapter 3**: Explains the Co-precipitation synthesis of $xBaWO_4/(1-x)CaWO_4$ nanocomposites and initial characterization of the prepared nanocomposites.
- **Chapter 4:** Showcases the optical study and mechanism behind the enhanced PL Intensity of $xBaWO_4/(1-x)CaWO_4$ nanocomposites.
- **Chapter 5:** Covers the DC, AC electrical Conductivity, dielectric properties (dielectric constant & dielectric loss), and thermoelectric properties of $xBaWO_4/(1-x)CaWO_4$ nanocomposites.
- **Chapter 6**: Summary of the results, overall conclusions and future scope within the area of research are presented.

References

[1] Li K, Geng D, Shang M, Zhang Y, Lian H and Lin J, Color-tunable Luminescence and energy transfer properties of $Ca_9Mg(PO_4)_6F_2:Eu^{2+}$, Mn^{2+} phosphors for UV-LEDs, J. Phys. Chem. C, **118**:11026-11034 **(2014)**.

[2] Krishnan R, Thirumalai J, Banu I. B. S and Chandramohan R, Influence of Eu^{3+} ions in $Na_{0.5}La_{0.5}MoO_4$: structural and optical investigation, J. Mater.Sci: Mater Electron., Vol. **24**:4774–4781**(2013)**.

[3] Zhang L, Lu Z, Han P, Wang L and Zhang Q, Synthesis and photoluminescence of Eu^{3+} - activated double perovskite NaGdMg (W, Mo) O_6^- a potential red phosphor for solid state lighting, J. Mater. Chem. C, **1**:54-57**(2013)**.

[4] Krishnan R, Thirumalai J, Thomas S and Gowri M, Luminescence and magnetic behavior of almond like ($Na_{0.5}La_{0.5}$) MoO_4:RE^{3+} (RE = Eu, Tb, Dy) nanostructures, J. Alloys and Compd., **604**:20–30**(2014)**.

[5]KrishnanR and Thirumalai J, Up/down-conversion luminescence properties of ($Na_{0.5}Gd_{0.5}$)MoO_4:Ln^{3+} (Ln = Eu, Tb, Dy, Yb/Er, Yb/Tm, and Yb/Ho) microstructures: Synthesis, morphology, structural and magnetic investigation, New J. Chem., **38**: 3480-3491**(2014)**.

[6] Krishnan R, Thirumalai J and Kathiravan A, Luminescence and magnetic properties of novel nanoparticle-sheathed 3D micro-architectures of $Fe_{0.5}R_{0.5}(MoO_4)_{1.5}$:$Ln^{3+}$ (R = Gd^{3+},La^{3+}), (Ln = Eu, Tb, Dy) for bi-functional application, Electron. Mater. Lett., **11**: 24-33**(2015)**.

[7] Pedro Henrique Cury Camargo, Kestur Gundappa Satyanarayana, and Fernando Wypych, Nanocomposites: Synthesis, Structure, Properties and New Application Opportunities Mater. Res., **12**:1-39 **(2009)**.

[8] R. Bogue, Nanocomposites: A review of technology & applications, Assem. Autom.,**31:**106-112 **(2011)**.

[9]J.Njuguna,F.Ansari,S. Sachse, H. Zhu, and V. M. Rodriguez, in Health &EnvironmentalSafety of Nanomaterials, *Polymer Nancomposites & Other Materials Containing Nanoparticles*, pp. 3–27. (Woodhead Publishing Limited, UK, **2014**).

[10]Maier J, Nanoionics: Ion transport and electrochemical storage in confined systems Nature Materials, **4**:805-815 **(2005)**.

[11] Koichi Niihara, New design concept of structural ceramics-Ceramic nanocomposites Ceram. Soc. Japan, **99**(10)**:**974-982 **(1991)**.

[12]M. Zamkov and C. S. S. R. Kumar, *UV-VIS and Photoluminescence Spectroscopy for Nanomaterials Characterization* (Springer Heidelberg New York Dordrecht London, **2013**).

[13]L.Wei,C.Shifu,Z. Huaye, and Y. Xiaoling, Preparation, characterisation of p–nheterojunction photocatalyst $CuBi_2O_4/Bi_2WO_6$ and its photocatalytic activities J. Exp. Nanosci.,**6**:102-120 **(2011)**.

[14]F. Ansari, A. Sobhani, and M. Salavati-Niasari, Simple sol-gel synthesis and characterization of new $CoTiO_3/CoFe_2O_4$ nanocomposite by using liquid glucose, maltose and starch as fuel, capping and reducing agents J. Colloid Interface Sci.,**514:**723 **(2018)**.

[15]A.Hamrouni,N. Moussa, A. Di Paola, L. Palmisano, A. Houas, and F. Parrino**,** Photocatalytic activity of binary and ternary SnO_2–ZnO–$ZnWO_4$ nanocomposites J. Photochem. Photobiol. A Chem., **309**:47-54 **(2015)**.

[16] S. Shionoya, W. Yen, *Phosphor Handbook*, CRC Press, Boca Raton, **(1999)**.

[17] M.H.V. Werts,*Making sense of Lanthanide Luminescence*,Science Progress, **88**(2):101–131**(2005)**.

[18] G. Blasse and B. C. Grabmaier, *Luminescent Materials*(Springer.VerJag Berlin Heidelberg, VerJag Berlin Heidelberg **1994**).

[19] A. Kitai, *Luminescent Materials and Applications* (John Wiley & Sons Ltd, West Sussex, England, **2008**).

[20] J. R. Lakowicz, *Principles of Fluorescence Spectroscopy*, 3rd Edition (New York, **2006**).

[21] R. Liu, Phosphors, *Up Conversion Nano Particles, Quantum Dots and Their Applications* (Springer Science+Business, Singapore, **2016**).

[22] V. N. Shevchuk and I. V. Kayun**,** Dipole effects in AWO_4 (A=Pb, Cd) luminescent crystalsRadiat. Meas., **42**:847-850**(2007)**.

[23] M. Guzik, E. Tomaszewicz, Y. Guyot, J. Legendziewicz, and G. Boulon, Structural and spectroscopic characterizations of two promising Nd-doped monoclinic or tetragonal laser tungstates,J. Mater. Chem., **22**:14896-14906**(2012)**.

[24] A. A. Annenkov, M. V. Korzhik, and P. Lecoq, Lead tungstate scintillation material,Nuclear Instruments and Methods in Physics Research Section A: Accelerators, Spectrometers, Detectors and Associated Equipment,**490 (1-2)**:30-50**(2002)**.

[25]I. M. Pinatti, I. C. Nogueira, W. S. Pereira, P. F. S. Pereira, R. F. Gonçalves, J. A. Varela, E. Longo, I. L. V. Rosa, Structural and photoluminescence properties of Eu^{3+} doped α-Ag_2WO_4 synthesized by the green co precipitation methodology, Dalt. Trans., **44**:17673-17685 **(2015)**.

[26] J. Liao, B. Qiu, H. Wen, W. You, Photoluminescence green in microspheres of $CaWO_4$:Tb^{3+} processed in conventional hydrothermal, Opt. Mater. (Amst), **31**:1513-1516 **(2009)**.

[27]L.Lv,J.Wang,W.Wang, L. Han,Microstructure control by Y^{3+} ions doping in $CaMoO_4$:Eu^{3+}: Tunable optical and luminescent performance,J. Alloys Compd.,**635**:25 **(2015)**.

[28] K. G. Sharma and N. R. Singh, Synthesis of $CaWO_4$: Eu^{3+} phosphor powders via ethylene glycol route and its optical properties,J. Rare Earths,**30**:310-314 **(2012)**.

[29] S. J. NAIK, *CATALYTIC AND SOLID STATE STUDIES OF METAL TUNGSTATES AND MOLYBDATES*, Ph.D.Thesis, Goa University, **(2010)**.

[30]J. Macavei and H. Schulz, The crystal structure of wolframite type tungstates at high pressure Zeitschrift Fiir Krist., **207**:193-208 **(1993)**.

[31]M.Nikl,P. Bohacek, E. Mihokova, M. Kobayashi, M. Ishii, Y. Usuki, V. Babin, A. Stolovich, S. Zazubovich, and M. Bacci, Excitonic emission of scheelite tungstates AWO_4 (A=Pb, Ca, Ba, Sr),J. Lumin., **87**:1136-1139**(2000)**.

[32] S. Ye, F. Xiao, Y. X. Pan, Y. Y. Ma, and Q. Y. Zhang, Phosphors in phosphor-converted white light-emitting diodes: Recent advances in materials, techniques and properties, Mater. Sci. Eng. R Reports, **71**:1-34 **(2010)**.

[33]K.W. Böer and U. W. Pohl, *Exciton. In: Semiconductor Physics* (Springer, Switzerland, **2015**).

[34]V. V. Laguta, M. Nikl, and S. Zazubovich, Luminescence and decay of excitons in lead tungstate crystals Radiat. Meas., **42**:515-520 **(2007)**.

[35] E. Sreeja, S. Gopi, V. Vidyadharan, P. Remya Mohan, C. Joseph, N. V. Unnikrishnan, and P. R. Biju, Luminescence properties and charge transfer mechanism of host sensitized Ba_2CaWO_6: Eu^{3+} phosphor Powder Technol.,**323**:445-453 **(2018)**.

[36] G. Blasse, Luminescence of the tungstate group in Scheelite and Fergusonite, Philips Res. Repts.,**25**:231-236 **(1970)**.

[37] Toshihiro Yamase and M. Sugeta, Charge-transfer photoluminescence of polyoxo-tungstates and molybdates, J. Chem. Soc. Dalt. Trans., **20:759**-765 **(1993)**.

[38] S. Dey, R. A. Ricciardo, H. L. Cuthbert, and P. M. Woodward, Metal-to-Metal Charge Transfer in AWO_4(A = Mg, Mn, Co, Ni, Cu, orZn) Compounds with the Wolframite Structure, Inorg. Chem.,**53**:4394-4399 **(2014)**.

[39] S. M. M. Zawawi, R. Yahya, A. Hassan, H. N. M. E. Mahmud, and M. N. Daud, Structural and optical characterization of metaltungstates (MWO_4; M=Ni, Ba, Bi) synthesized by a sucrose-templated method, Chemistry Central Journal,**7**(1):80 **(2013)**.

[40] Hong Zeng, Ying Wu, Jiuxing Zhang, Chunjiang Kuang, Ming Yue, Shaoxiong Zhou, Grain size-dependent electrical resistivity of bulk nanocrystalline Gd metals, Progress in Natural Science: Materials International,**23**(1):18-22**(2013)**.

[41] Levinson LM, Philipp HR. The physics of metal oxide varistors, Journal of Applied Physics, **46**(3):1332-1341**(1975)**.

[42]Mateus Gallucci Masteghin, Marcelo Ornaghi Orlandi, Grain-Boundary Resistance and Nonlinear Coefficient Correlation for SnO_2-Based Varistors, Materials Research,**19**(6):1286-1291 **(2016)**.

[43] M.A. Ashraf, A.H. Bhuiyan, M.A. Hakim, M.T. Hossain, Microstructure and electrical properties of Ho_2O_3 doped Bi_2O_3-based ZnO varistor ceramics,Physica B-Condensed Matter,**405**:3770–3774**(2010)**.

[44]W.G.Morris,Physical properties of the electrical barriers in varistors, Journal, Vac.Sci.Technol.,**13**:926-931**(1976)**.

[45] J. D. Levine, Theory of varistor electronic properties, Crit. Rev. Solid State Sci., **5**:597 **(1975)**.

[46] J. Bernasconi, H. P. Klein, B. Knecht, and S. Strassler, Investigation of various models for metal oxide varistors J. Electron. Mater., **5**:473-495 **(1976)**.

[47] G. D. Mahan, L. M. Levinson, and H. R. Philipp, Theory of Conduction in ZnO Varistors,J. Appl. Phys., **50**:2799-2812 **(1980)**.

[48]J. Bernasconi, S. Strassler, B. Knecht, H. P. Klein, and A. Menth**,** Zinc oxide based varistors: A possible mechanism Solid State Commun., **21**:867-870 **(1977)**.

[49]P. R. Emtage, The physics of zinc oxide varistors J. Appl. Phys., 48:4372-4384 **(1977)**.

[50] P. L. Hower and T. K. Gupta, A barrier model for ZnO varistors J. Appl. Phys., **50**:4847-4855**(1979)** .

[51] G. E. Pike, Electronic properties of ZnO varistors: a new model, in: Grain Boundaries in Semiconductors, Eds. G.E. Pike, C.H. Seager, H.J. Leamy, Vol. Mater. Res. Soc. Proc.,**5**:369-379 **(1982)**.

[52] F. Greuter, G. Blatter, M. Rossinelli, and F. Stucki, in Ceramic Transactions: Advances in Varistor Technology, L. M. Levinson, eds., American Ceramic Society,Columbus, Ohio,**3**:31 **(1989)**.

[53]F.Greuter, and G. Blatter, Electrical properties of grain boundaries in polycrystalline compound semiconductorsSemicond. Sci. Technol, **5:111**-137**(1990)**.

[54]Bueno P.R., Orlandi M.O., Simões L.G.P., Leite E.R., Longo E., Cerri J.A., Nonohmic behavior ofSnO_2-MnO polycrystalline ceramics. I. Correlations between microstructural morphologyand nonohmic features. Journal of Applied Physics,**96**(5):2693-2700 **(2004)**.

[55] J. K. Nelson and Y. Hu, Nanocomposite dielectrics-properties and implications J. Phys. D. Appl. Phys.,**38**:213-222**(2005)**.

[56]S.Devi and A. K. Jha, Dielectric and complex impedance studies of $BaTi_{0\cdot85}W_{0\cdot15}O_{3+\delta}$ ferroelectric ceramics, Bull. Mater. Sci., **33**:683-690 **(2010)**.

[57] C. E. Ciomaga, A. M. Neagu, M. V. Pop, M. Airimioaei, S. Tascu, G. Schileo, C. Galassi, and L. Mitoseriu, Ferroelectric and dielectric properties of ferrite-ferroelectric ceramic composites J. Appl. Phys.,**113**:074103**(2013)**.

[58] V. Rajendran and A. Marikani, *Materials Science*, Tata Mc-Graw-Hill Publishing Company Limited, New Delhi **(2004)**.

[59]Maier Joachim, Defect chemistry and ion transport in nanostructured materials: Part II. Aspects of nanoionics, Solid State Ion., **157**(1-4): 327-334 (**2003)**.

[60]P. Alboni, X. Ji, J. He, N. Gothard, T.M. Tritt, Thermoelectric properties of $La_{0.9}CoFe_3Sb_{12}$–$CoSb_3$ skutterudite nanocomposites,Journal of Appl. Phys. **103**(11):113707(1-5)**(2008)**.

[61]J.Li,Q.Tan,J.F.Li,D.W.Liu, F. Li, Z.Y. Li, M. Zou, K. Wang, BiSbTe-Based Nanocomposites with High ZT : The Effect of SiC Nano dispersion on Thermoelectric Properties Adv. Funct. Mater., **23:4317**-4323**(2013)**.

[62]Y. Lan, A.J. Minnich, G. Chen, Z. Ren, Enhancement of Thermoelectric Figure-of-Merit by a Bulk Nanostructuring Approach,Adv. Funct. Mater.,**20**:357-376**(2010)**.

[63]D. Rowe, C. Bhandari,Effect of grain size on the thermoelectric conversion efficiency of semiconductor alloys at high temperature,Applied Energy,**6**:347-351 **(1980)**.

[64]A. Minnich, M. Dresselhaus, Z. Ren, G. Chen, Bulk nanostructured thermoelectric materials: current research and future prospects, Energy&Environmental Science,**2**:466-479 **(2009)**.

[65]C.J. Vineis, A. Shakouri, A. Majumdar, M.G. Kanatzidis, Nanostructured Thermoelectrics: Big Efficiency Gains from Small Features,*Adv. Mater.*,**22**:3970-3980.**(2010)**.

[66]A. Katelnikovas, L. Grigorjeva, D. Millers, V. Pankratov, A. Kareiva, Sol Gel Preparation of Nanocrystalline $CaWO_4$, Lithuanian J. Phys.,**47**(1):63-68**(2007)**.

[67]T.T. Basiev, A.A. Sobol, P.G. Zverev, L.I. Ivleva, V.V. Osiko, R.C. Powell, Raman spectroscopy of crystals for stimulated Raman scattering,Opt. Mater., **11**:307-314**(1999)**.

[68] P. Cerny, H. Jelinkova, T.T. Basiev and P.G. Zverev, Highly efficient picosecond Raman generators based on the $BaWO_4$ crystal in the near infrared, visible, and ultraviolet, J. IEEE, Quantum Electron., **38**:1471-1478 **(2002)**.

[69]A.I. Vodchits, V.A. Orlovich, P.A. Apanasevich, T.T. Basiev and P.G. Zverev, Nonlinear optical properties of $BaWO_4$ crystal, Optical Materials, **29**(12):1616-1619**(2007)**.

[70]F.A.Kroger,*Some Aspects of the Luminescence of Solids*, Elsevier's Publishing Co., Amsterdam, **(1948)**.

[71]G. Blasse and W.J. Schipper, Low-Temperature Photoluminescence of Strontium and Barium Tungstate Phys. Stat. Solidi (a),**25**:K163-K165 **(1974)**.

[72]R.C. Lima, M. Anicete-Santos, E. Orhan, M.A. Maurera, A.G. Souza, P.S. Pizani, E.R. Leite, J.A. Varela and E. Longo, Photoluminescent property of mechanically milled $BaWO_4$ powderJ. Lumin.,**126**:741-746 **(2007)**.

[73]J.H. Ryu, J.W. Yoon and K.B. Shim, Blue-luminescence of nanocrystalline MWO_4 (M = Ca, Sr, Ba, Pb) phosphors synthesized via a citrate complex route assisted by microwave irradiation Electrochem. Solid State Lett.,**8**: D15-D18 **(2005)**.

[74] F.A. Kroger, *Fluorescence of tungstates and molybdates*. Nature, **159**:674 **(1947)**.

[75]L.F. Johnson, K. Nassau, Infrared fluorescence and stimulated emission of Nd^{3+} in $CaWO_4$ Proc. IRE, **49**:1704-1706**(1961)**.

[76] L. F. Johnson, Optical Maser Characteristics of Rare Earth Ions in Crystals J. Appl. Phys., **34**:897-909 **(1963)**.

[77] C. Ropp, *Luminescence and the Solid State*, Volume 21,2nd edition (Elsevier, Amsterdam, **2004**).

[78]Woo-Seok Cho, Masatomo Yashima, and Masato Kakihana, Room-temperature preparation of the highly crystallized luminescent $CaWO_4$ film by an electrochemical method, Appl. Phys. Lett., **66**:1027**(1995)**.

[79]S.Basu,B.S.Naidu,B.Viswanadh,V. Sudarsan,S.N. Jha, D. Bhattacharya, R.K. Vatsa, Nature of WO_4 tetrahedra in blue light emitting $CaWO_4$ probed through the EXAFS technique. RSC Advances, **4**:15606–15612**(2014)**.

[80] F. Kang, M. Peng, A new study on the energy transfer in the color tunable phosphor $CaWO_4$: Bi. Dalton Trans., **43**:277–284 **(2014)**.

[81]L.S.Cavalcante,V. M. Longo, J. C. Sczancoski, M. A. P. Almeida, A. A. Batista, J. A. Varela, M. O. Orlandi, E. Longo, and M. Siu Li, Electronic structure, growth mechanism and photoluminescence of $CaWO_4$ crystals, CrystEngComm,, **14**:853-868**(2012)**.

[82] R. B. Pode and S. J. Dhoble, Photoluminescence in $CaWO_4:Bi^{3+}$; Eu^{3+} Material, Physica Status Solidi (b), **203**(2): 571-577**(1997)**.

[83] B.S. Naidu, B. Vishwanadh, V. Sudarsan and R.K. Vatsa, Room temperature synthesis of $MWO_4:Eu^{3+}$ (M = Ca, Sr, Ba) nanomaterials, BARC Newsletters, Founder's Day Special Issue, **313(October 2011)**.

[84]Enrico Cavalli, Philippe Boutinaud,Rachid Mahiou,Marco Bettinelli,and Pieter Dorenbos, Luminescence Dynamics in Tb^{3+}-Doped $CaWO_4$and $CaMoO_4$Crystals, Inorg. Chem., **49**:4916–4921**(2010)**.

[85] Shifa Wang, Huajing Gao, Guangzhuang Sun, Yanwu Li, Yong Wang, Hufeng Liu, Chaoli Chen,Liang Yang,Structure characterization, optical and photoluminescence properties of Scheelite-type $CaWO_4$ nanophosphors:Effects of calcination temperature and carbon skeleton,Optical Materials,**99**:109562 **(2020)**.

[86]Zhiyao Hou, Chunxia Li, Jun Yang, Hongzhou Lian, Piaoping Yang, Ruitao Chai, Ziyong Chenga and Jun Lin, One-dimensional $CaWO_4$ and $CaWO_4:Tb^{3+}$ nanowires and nanotubes: electrospinning preparation and luminescent properties, J. Mater. Chem., **19**:2737–2746, (**2009)**.

[87]U. Rambabu, N. R. Munirathnam, T. L. Prakash, Synthesis and characterization of Ag doped $CaWO_4$ powder phosphors for optical blue emission, Journal of Optoelectronics & Advanced Materials, **11**(11):1841–1842 **(2009**).

[88]A. Katelnikovas,L.Grigorjeva,D.Millers,V. Pankratov, A. Kareiva,Sol.Gel Preparation of Nanocrystalline $CaWO_4$, Lithuanian Journal of Physics, **47**(1):63-68 **(2007)**.

[89]Won-Chun Oh, Chong Yeon Park, Jeong Won Jeon and Chang Sung Lim, Solid-State Metathetic Synthesis and Photoluminescence of Calcium Tungstate Particles Assisted by Cyclic Microwave Irradiation,Asian Journal of Chemistry, **24**(8):3319-3322 **(2012)**.

[90]F.Sun,X.Qiao,F.Tan,W.Wang,X.Qiu,One-step microwave synthesis of Ag/ZnO nanocomposites with enhanced photo catalytic performance, J. Mater. Sci. **47**:7262–7268 **(2012)**.

[91]Li, P., Zhao, X., Jia, C.-j., Sun, H., Sun, L., Cheng, X., Liu, L., Fan, W., $ZnWO_4$/BiOI heterostructures with highly efficient visible light photocatalytic activity: the case of interface lattice and energy level match,Journal of Materials Chemistry A,**1**(10):3421-3429**(2013)**.

[92]Shang, M., Wang, W., Zhang, L., Sun, S., Wang, L., Zhou, L., 3D Bi_2WO_6/TiO_2 hierarchical heterostructure: controllable synthesis and enhanced visible photocatalytic degradation performances. The Journal of Physical Chemistry C,**113**(33):14727-14731 **(2009)**.

[93] Lee, S. H., Deshpande, R., Parilla, P. A., Jones, K. M.,To, B., Mahan, A. H., Dillon, A. C., Crystalline WO_3 nanoparticles for highly improved electrochromic applications,Advanced Materials,**18**(6):763-766**(2006)**.

[94] Guo, Y., Zhang, G., Gan, H., Zhang, Y., Micro/nano-structured $CaWO_4/Bi_2WO_6$ composite: synthesis, characterization and photocatalytic properties for degradation of organic contaminants. Dalton Transactions,**41**(41):12697-12703 **(2012)**.

[95]L.S.Cavalcante,F.M.C. Batista, M.A.P. Almeida, A.C. Rabelo, D.I.C. Nogueira, N.C. Batista, J.A. Varela, A.M.R.M.C. Santos, E. Longobd, M. Siu Li, Structural refinement, growth process, photoluminescence and photo catalytic properties of $(Ba_{1-x}\,Pr_{2x/3})\,WO_4$ crystals synthesized by the co precipitation method. RSC Adv., **2**:6438–6454 **(2012)**.

[96] M.Eghbali-Arani, S. Pourmasoud, F. Ahmadi, M. Rahimi-Nasrabadi, V. Ameri, A. Sobhani-Nasab, Optimization and detailed stability study on coupling of $CdMoO_4$ into $BaWO_4$ for enhanced photodegradation and removal of organic contaminant. Arabian Journal of Chem., **13**(1):2425-2438 **(2020)**.

[97]V.M. Longo, E. Orhan, L.S. Cavalcante, S.L. Porto, J.W.M. Espinosa, J.A. Varela, E. Longo, Understanding the origin of photoluminescence in disordered $Ca_{0.60}Sr_{0.40}WO_4$. Chem. Phys., **334**:180–188 **(2007)**.

[98]L. Porto, E. Longo, P.S. Pizani, T.M. Boschi, L.G.P. Simoes, S.J.G. Lima, J.M. Ferreira, L.E.B. Soledade, J.W.M. Espinoza, M.R. Cassia-Santos, M.A.M.A. Maurera, C.A. Paskocimas,

I.M.G. Santos, A.G. Souza, Photoluminescence in the $Ca_xSr_{1-x}WO_4$ system at room temperature. J. Solid State Chem., **181**:1876–1881 **(2008)**.

[99]N. Aloysius Sabu, Xavier Francis, Jose Anjaly, S. Sankararaman, and Thomas Varghese, Enhanced structural and optical properties of the polyaniline-calcium tungstate (PANI-$CaWO_4$) nanocomposite for electronics applications, Eur. Phys. J. Plus,**132**(6): 290 **(2017)**.

[100]Nidhi Khobragade, Ela Sinha, S.K. Routa,, Manoranjan Kar, Structural, optical and microwave dielectric properties of $Sr_{1-x}Ca_xWO_4$ceramics prepared by the solid state reaction route, Ceramics International, **39**:9627–9635**(2013)**.

[101]Prasad Narayan Patil, Uma Subramanian, M. Jeyakanthan, Enhanced blue emission of $CaWO_4$ in $BaWO_4/CaWO_4$ nanocomposite, Journal of Materials Science: Materials in Electronics, **31**(9):7260-7275 (**2020)**.

[102]R.N.P. Choudhary, Ratnakar Palai, S. Sharma, Structural, dielectric and electrical properties of lead cadmium tungstate ceramics, Materials Science and Engineering B,**77:**235–240 **(2000)**.

[103] Yih-Shing Lee and Tseung-Yuen Tseng, Phase Identification and Electrical Properties in ZnO-Glass Varistors, Journal of American Ceramic Society, **75**(6):1636-1640 **(1992)**.

[104]R.N.P.Choudhary, Ratnakar Palai, Seema Sharma, Studies of dielectric and varistor behavior of lead manganese tungstate ceramics, Journal of Materials Science: Materials in Electronics,**11**:685- 689**(2000)**.

[105]Ali Olad, Sahar Shakoori, Sajedeh Mohammadi Aref, Investigation of nonlinear electrical properties of ZnO/PPy nanocomposite and its application as a low-voltage varistor,Physica B: Condensed Matter, **550**:127–135**(2018)**.

[106]W.Y. Wang, D.F. Zhang, T. Xu, Y.P. Xu, T. Zhou, B.Q. Hu, C.Y. Wang, L.S. Wu, X.L. Chen, Nonlinear electrical characteristics and dielectric properties of Ca, Ta-doped TiO_2 varistors, Appl. Phys. A **76**:71–75 **(2003)**.

[107]Mateus Gallucci Masteghin, Marcelo Ornaghi Orlandi, Grain-Boundary Resistance and Nonlinear Coefficient Correlation for SnO_2-Based Varistors, Materials Research. **19**(6):1286-1291 **(2016)**.

[108]Wenbin Su, Jinfeng Wang, Hongcun Chen, Guozhong Zang, Peng Qi and Chunming Wang, Nonlinear Electrical Properties of (Sc,Ta) Doped TiO_2 Varistor Ceramics, Key Engineering Materials,**280-283**:289-292**(2005)**.

[109]Ahmed Bouchekhlal, and Farida Hobar, Effect of sintering temperature on microstructure and nonlinear electrical characteristics of ZnO varistor, Journal of Advanced Dielectrics, **8**(2):1850014 (5 pages) **(2018)**.

[110]Choon-W. Nahm, Low-temperature sintering effect on varistor properties of $ZnO–V_2O_5–MnO_2–Nb_2O_5–Bi_2O_3$ ceramics,Ceramics International, **39**:2117–2121**(2013)**.

[111] YhKuang Tsai and TaiBor Wu, Non-ohmic characteristics of $ZnO\text{-}V_2O_5$ ceramics, Journal of Applied Physics, **76**:4817 **(1994)**.

[112]Sung Hun Yoon, Dong-Wan Kim, Seo-Yong Cho, Kug Sun Hong, Investigation of the relations between structure and microwave dielectric properties of divalent metal tungstate compounds, Journal of the European Ceramic Society, **26**:2051–2054 **(2006)**.

[113]Marjeta Macek Krmmanc, Manca Logar, Bojan Budic, and Danilo Suvorov, Dielectric and Microstructural Study of the $SrWO_4$, $BaWO_4$, and $CaWO_4$ Scheelite Ceramics, Journal of American Ceramic Society, **94** (8):2464–2472 **(2011)**.

[114] E. S. Kim, S. H. Kim, and B. I. Lee, Low-Temperature Sintering and Microwave Dielectric Properties of $CaWO_4$ Ceramics for LTCC Applications, J. Eur. Ceram. Soc., **26**: 2101– 2104 **(2006)**.

[115]N.Aloysius,M.S.Rintu,E. M. Muhammed, T. Varghese,Dielectric studies of nanocrystalline calcium tungstate, Nanosystems: Physics, Chemistry, and Mathematics, **7**(4): 599–603 **(2016)**.

[116] Ananda Kumar V M, DC conductivity of nanocrystalline calcium tungstate,International Journal of Scientific Research and Reviews, **8**(2):1605-1621**(2019)**.

[117]Eung Soo Kim, Byung Sam Chun,Robert freer,R.J.cernik, Effects of packing fraction and bond valence on microwave dielectric properties of A^{2+} B^{6+} O_4 (A^{2+} : Ca, Pb, Ba; B^{6+} : Mo, W) ceramics, Journal of the European Ceramic Society, **30(7)**:1731–1736**(2010)**.

[118] M. A. Rigdon and R. E. Grace, Electrical Charge Transport in Single Crystal $CaWO_4$ J. Amer. Ceram. Soc., **56**:475 **(1973)**.

[119]Ammu Priya, Ela Sinha, S.K. Rout, Structural, optical and microwave dielectric properties of $Ba_{1-x}Sr_xWO_4$ ceramics prepared by solid state reaction route,Solid State Sciences, **20**:40-45 **(2013)**.

[120]Sung Hun Yoon, Geun-Kyu Choi, Dong-Wan Kim, Seo-Yong Cho, Kug Sun Hong, Mixture behavior and microwave dielectric properties of $(1-x)\ CaWO_4–xTiO_2$, Journal of the European Ceramic Society,**27**:3087–3091**(2007)**.

[121] Jiqing Lv, En-cai Xiao, Xue-hui Li, Xianlin Dong, Ying Chen, Zhenxing Yue, Feng Shi,Crystal structures, dielectric properties, and lattice vibrational characteristics of (1-x)$CaWO_4$-xTiO_2 composite ceramics.Ceramics International, **46**(3):3715-3724**(2020)**.

[122] Eung Soo Kim,Soon Ho Kim,effects of structural characteristics on microwave dielectric properties of (1-x)$CaWO_4$-x$LaNbO_4$ ceramics J.Electroceram., **17**:471-477**(2006)**.

[123]H. Zhuang, Z. Yue, F. Zhao, and L. Li, Low-temperature sintering and microwave dielectric properties of $Ba_5Nb_4O_{15}$- $BaWO_4$composite ceramics for LTCC applications, Journal ofthe American Ceramic Society, **91**(10):3275–3279**(2008)**.

[124]H. Zhuang, Z. Yue, F. Zhao, J. Pei, and L. Li, Microstructure and microwave dielectric properties of $Ba_5Nb_4O_{15}$-$BaWO_4$ composite ceramics,Journal of Alloys and Compounds, **472**(1-2):411–415**(2009)**.

[125]H. Zhuang, Z. Yue, S. Meng, F. Zhao, and L. Li, Low-temperature sintering and microwave dielectric properties of $Ba_3(VO_4)_2$-$BaWO_4$ ceramic composites,Journal of the American Ceramic Society, **91**(11):3738–3741**(2008)**.

[126]Tadeusz Gron, Magdalena Piatkowska, Elzbieta Tomaszewicz, Bogdan Sawicki, Piotr Urbanowicz, Henryk Duda, Electrical and optical properties of new Pr^{3+}- doped $PbWO_4$ ceramics, Materials Science-Poland, **36**(4):530-536**(2018)**.

[127]Shubha Gupta, Y. P. Yadava, and R. A. Singh, Electrical Transport Properties of Polycrystalline Chromium Vanadate, Z. Naturforsch.,**42a**:577-581 **(1987)**.

[128]Liu-Cheng Chen, Zi-Yu Cao, Hao Yu, Bin-Bin Jiang, Lei Su, Xun Shi, Li-Dong Chen, and Xiao-Jia Chen,Phonon anharmonicity in thermoelectric palladium sulfide by Raman spectroscopy, Applied Physics Letters, **113**:022105 **(2018)**.

[129] Dehua Hu, Qing Liu, Jeremy Tisdale, Ting Lei, Jian Pei, Hsin Wang, Augustine Urbas, and Bin Hu, Seebeck Effects in N‑Type and P‑Type Polymers Driven Simultaneously by Surface Polarization and Entropy Differences Based on Conductor/Polymer/Conductor Thin-Film Devices, American Chemical Society Nano, Vol. XXX' No. XX**(2015)**.

[130]J. Martin, Li Wang, Lidong Chen, and G. S. Nolas, Enhanced Seebeck coefficient through energy-barrier scattering in PbTe nanocomposites, Physical Review B **79**:115311 **(2009)**.

[131]Zhengang Zhang, Weiwei zhao, Wanting Zhu, SHIFANG Ma, Cuncheng Li, Xin Mu, Ping Wei, Xiaolei Nie, Qingjie Zhang, and Wenyu Zhao, Preparation and Thermoelectric Performance

of $BaTiO_3/Bi_{0.5}Sb_{1.5}Te_3$ Composite Materials, Journal of Electronic Materials,**49**:2794-2801**(2019)**.

[132]N. Gothard, X. Ji, J. He, and Terry M. Tritt, Thermoelectric and transport properties of n-type nanocomposites, J. Appl. Phys., **103**:054314 **(2008)**.

[133]Kyung Tae Kim, Hye Young Koo, Gil-Geun Lee, Gook Hyun Ha, Synthesis of alumina nanoparticle-embedded-bismuth telluride matrix thermoelectric composite powders, Materials Letters, **82**:141–144 **(2012)**.

[134]Sergey V. Faleev and François Léonard,Theory of enhancement of thermoelectric properties of materials with nanoinclusions, Physical Review B, **77**: 214304**(2008)**.

[135]Y. Y. Li, X. Y. Qin, D. Li, J. Zhang, C. Li, Y. F. Liu, C. J. Song, H. X. Xin, and H. F. Guo,Enhanced thermoelectric performance of $Cu_2Se/Bi_{0.4}Sb_{1.6}Te_3$ nanocomposites at elevated temperatures, Applied Physics Letters, **108**:062104 **(2016)**.

[136]J.Martin,L.Wang, L. Chen, and G. S. Nolas, Enhanced Seebeck coefficient through energy-barrier scattering in PbTe nanocomposites,Physical Review B,**79**(11-15),115311,**(2009)**.

[137] T. M. Tritta, N. Gothard, X. Ji, and J. He, Thermoelectric and transport properties of n-type Bi_2Te_3 nanocomposites, Journal of Applied Physics, **103**:054314**(2008)**.

[138] Z. H. Zheng, P. Fan, J. T. Luo, G. X. Liang, and D. P. Zhang, Enhanced Thermoelectric Properties of Antimony Telluride Thin Films with Preferred Orientation Prepared by Sputtering a Fan-Shaped Binary Composite Target, Journal of Electronic Materials,**42**:3421-3425**(2013)**.

[139] G. J. Tan, Y. Zheng, and X. F. Tang, High thermoelectric performance of non-equilibrium synthesized $CeFe_4Sb_{12}$ composite with multi-scaled nanostructures,Applied Physics Letters,**103**:183904**(2013)**.

[140] J. Liu, X. G. Wang, and L. M. Peng, Effect of annealing on thermoelectric properties of eutectic PbTe-Sb_2Te_3 composite with self-assembled lamellar structure, Intermetallics,**41**:63-69**(2013)**.

[141]H. Xu and W. Wang, Electrodeposition of MWNT/Bi_2Te_3 Composite Thermoelectric Films, Journal of Electronic Materials,**42**:1936-1945**(2013)**.

[142]Y. Du, K. F. F. Cai, S. Z. Shen, B. J. An, Z. Qin, and P. S. Casey, Influence of sintering temperature on thermoelectric properties of Bi_2Te_3/Polythiophene composite materials, Journal of Materials Science-Materials in Electronics,**23**:870-876**(2012)**.

[143] K. C. Kim, W. C. Choi, H. J. Kim, H. K. Lyeo, J. S. Kim, and C. Park, Thermoelectric Properties of Bi_2Te_3-In_2Se_3 Composite Thin Films Prepared by Co-Sputtering, Journal of Nanoscience and Nanotechnology,**12**:3633-3636**(2012)**.

[144]Y.Y.Wang,K.F.Cai,J.L.Yin,B.J.An,Y.Du,and X. Yao, In situ fabrication and thermoelectric properties of PbTe-polyaniline composite nanostructures, Journal of Nanoparticle Research,**13**:533-539**(2011)**.

[145] J. Han, C. McBean, L. Wang, J. Hoy, C. Jaye, H. Liu, Z.Q. Li, M.Y. Sfeir, D.A. Fischer, G.T. Taylor, J.A. Misewich, S.S. Wong, Probing structure-induced optical behavior in a new class of self-activated luminescent 0D/1D $CaWO_4$ metal Oxide − CdSe nanocrystal composite heterostructures. Chem. Mater., **27**:778– 792 **(2015)**.

[146]W. Hu, W. Tong, L. Li, J. Zheng and G. Li,Cation non-stoichiometry in multi-component oxidenanoparticles by solution chemistry: a case study on $CaWO_4$ for tailored structural properties Phys. Chem. Chem. Phys., **13**:11634-11643 **(2011)**.

[147]Treadaway, M. J.; Powell, R. C., Luminescence of calcium tungstate crystals. The Journal of Chemical Physics,**61**(10):4003-4011**(1974)**.

[148] Grasser, R.; Scharmann, A.; Strack, K.-R., On the intrinsic nature of the blue luminescence in $CaWO_4$. Journal of Luminescence,**27**(3):263-272 **(1982)**.

[149]Zhang Y., Holzwarth N.,Williams R., Electronic band structures of the scheelite materials $CaMoO_4$, $CaWO_4$, $PbMoO_4$, and $PbWO_4$. Physical Review B,**57**(20):12738 **(1998)**.

[150]Errandonea, D.; Manjón, F. J., Pressure effects on the structural and electronic properties of ABX_4 scintillating crystals. Progress in Materials Science,**53**(4):711-773**(2008)**.

[151] Mikhailik, V., Kraus, H., Miller, G., Mykhaylyk, M., Wahl, D., Luminescence of $CaWO_4$, $CaMoO_4$, and $ZnWO_4$ scintillating crystals under different excitations. Journal of Applied Physics, **97**(8):083523 **(2005)**.

[152] E. Fabbri, D. Pergolesi, E. Traversa,Ionic conductivity in oxide heterostructures: the role of interfaces, Science and Technology of Advanced Materials, **11** (9pp):054503**(2010)**.

[153]S. Takai, K. Sugiura, and T. Esaka, Ionic Conduction Properties of $Pb_{1-x}M_xWO_{4+d}$ (M=Pr, Tb) Mater. Res. Bull.,**234**:193-202 **(1999)**.

[154]Y. Li, Z. Wang, L. Sun, Z. Wang, S. Wang, X. Liu, and Y. Wang, Investigation of oxygen vacancy and photoluminescence in calcium tungstate nanophosphors with different particle sizes, Mater. Res. Bull., **50**:36-41**(2014)**.

[155] Mohammad A. Alim, Admittance-Frequency Response in Zinc Oxide Varistor Ceramics, J. Am. Ceram. Soc., **72** (l):28-32 **(1989)**.

[156]E.M.M.Ibrahim,A.M.Abu-Dief,A. Elshafaie, and A. M. Ahmed, Electrical, thermoelectrical and magnetic properties of approximately 20-nm Ni-Co-O nanoparticles and investigation of their conduction phenomena,Mater. Chem. Phys.,**192**:41-47**(2017)**.

[157]Lee M Liliana Viciu, Lu Li, Yayu Wang, M. L. Foo, S. Watauchi, R. A. Pascal Jr, R. J. Cava & N. P. Ong Large enhancement of the thermo power in Na_xCoO_2 at high Na doping, Nat. Mater., **5**:537–540**(2006)**.

[158]Ohta H, Sugiura K, Koumoto K Recent progress in oxide thermoelectric materials: p-type $Ca_3Co_4O_9$ and n-type $SrTiO_3^-$, Inorg. Chem., **47**:8429–8436 **(2008)**.

[159]Pei Y L, Wu H, Wu D, Zheng F, He J High thermoelectric performance realized in a BiCuSeO system by improving carrier mobility through 3D modulation doping. J Am. Chem. Soc., **136**:13902–13908 **(2014)**.

[160]Funahashi, A. Kosuga, N. Miyasou,E. Takeuchi, S. Urata, K. Lee, H. Ohta, and K. Koumoto Thermoelectric properties of $CaMnO_3$ system. Int. Conf. Thermoelectric, pp.124–128 (**2008)**.

[161]Koumoto K, Wang YF, Zhang RZ, Kosuga A, Funahashi R, Oxide thermoelectric materials: a nanostructuring approach. Annu. Rev. Mater. Res., **40**:363–394**(2010)**.

[162]Kucukgok B, Hussain B, Zhou CL, Ferguson IT, Lu N Thermoelectric properties of ZnO thin film grown by metal organic chemical vapor deposition. MRS Online Proceedings Library. Cambridge University Press, Cambridge, pp.1805 **(2015)**.

[163]Yanagiya S, Nong N, Sonne M, Pryds N Thermoelectric properties of SnO_2-based ceramics doped with Nd, Hf and Bi. AIP Conference Proceedings,**1449**:327 **(2012)**.

[164]Lan J L, Lin Y H, Liu Y, Xu SL, Nan CW High thermoelectric performance of nanostructured In_2O_3-based ceramics. J. Am. Ceram. Soc., **95**:2465–2469 **(2012)**.

[165]Chang Sung Lim,Cyclic Microwave Synthesis and Photoluminescence of Barium Tungstate Particles Assisted by A Solid-State Metathetic Reaction,Asian Journal of Chemistry; **25**(1)63-66**(2013)**.

[166]L. Zhang, C. Lu, Y. Wang, and Y. Cheng, Hydrothermal synthesis and characterization of $MnWO_4$ nanoplates and their ionic conductivity Mater. Chem. Phys., **103**:433-436**(2007)**.

[167]L. S. Cavalcante, F. M. C. Batista, M. A. P. Almeida, A. C. Rabelo, I. C. Nogueira, N. C. Batista, J. A. Varela, M. R. M. C. Santos, E. Longo, M. S.Li,Structural refinement, growth process, photoluminescence and photocatalytic properties of $(Ba_{1-x}Pr_{2x/3})WO_4$ crystals synthesized by the co-precipitation method,RSC Adv.,**2**:6438-6454 **(2012)**.

[168] X. Lou, D. Chen, Synthesis of $CaWO_4:Eu^{3+}$ phosphor powders via a combustion process and its optical propertiesMater. Lett.,**62**:1681-1684 **(2008)**.

[169]V. Nagirnyi, E. Feldbach, L. Jonsson, M. Kirm, A. Lushchik, C. Lushchik, L.L. Nagornaya, V.D. Ryzhikov, F. Savikhiu, G. Svensson, and I.A. Tupitsina, Excitonic and recombination processes in $CaWO_4$ and $CdWO_4$ scintillators under synchrotron irradiation, Radiat. Meas., **29**:247–250 **(1998)**.

[170]Z. Hou, C. Li, J. Yang, H. Lian, P. Yang, R. Chai, Z. Cheng, J. Lin,One-dimensional $CaWO_4$ and $CaWO_4:Tb^{3+}$nanowires and nanotubes: electrospinning preparation and luminescent properties J. Mater. Chem.,**19**:2737-2746 **(2009)**.

[171]D.J. Norris, D.E. Arlinghaus, L. Meng, R. Heiny, and L.E. Scriven, Opaline photonic crystals: How does self-assembly work? Adv. Mater., **16**:1393–1399 **(2004)**.

[172]M. Remskar, Inorganic nanotubes, Adv. Mater., **16**:1497–1504 **(2004)**.

[173]Z. Lou, M. Cocivera**,** Cathodoluminescence of $CaWO_4$ and $SrWO_4$ thin films prepared by spray pyrolysis Materials Research Bulletin, **37**:1573**(2002)**.

[174]S.A. Salehizadeh, H.M. Chenari, M. Shabani, H.A. Ahangar, R. Zamiri, A. Rebelo, J. S. Kumar, M.P.F. Graça, J.M.F. Ferreira, Structural and impedance spectroscopy characteristics of $BaCO_3/BaSnO_3/SnO_2$ nanocomposite: observation of a non-monotonic relaxation behavior, RSC Adv., **8**:2100–2108 **(2018)**.

[175]L. Li, M. Xu, Q. Zhang, P. Chen, N. Wang, D. Xiong, B. Peng, L. Liu, Electrocaloric effect in La-doped BNT-6BT relaxor ferroelectric ceramics, Ceram. Int., **44**:343–350**(2018)**.

[176]M.A. Ahmed, E. Ateia, S.I. El-Dek, Rare earth doping effect on the structural and electrical properties of Mg-Ti ferrite, Mater. Lett., **57**:4256–4266 **(2003)**.

[177] Dewan, M. Tomar, R.P. Tandon, V. Gupta, Zn doping induced conductivity transformation in NiO films for realization of p-n homo junction diode, J. Appl. Phys.,**121**:215307**(2017)**.

[178] A.U. Rahman, M.A. Rafiq, M.U. Hasan, M. Khan, S. Karim, S.O. Cho, Enhancement of electrical conductivity and dielectric constant in Sn-doped nanocrystalline $CoFe_2O_4$, J. Nanoparticle Res., **15**:2–7 **(2013)**.

[179]Q.Q. Yang, B. Meng, Z.L. Lin, X.K. Zhu, F. Yang, S. Wu, Effect of sintering temperature on the elemental diffusion and electrical conductivity of $SrTiO_3$/YSZ composite ceramic, Ionics (Kiel), **23**:967–975 **(2017)**.

[180]Y.Jing, N. Luo, S. Wu, K. Han, X. Wang, L. Miao, Y. Wei, Remarkably improved electrical conductivity of ZnO ceramics by cold sintering and post-heat-treatment, Ceram. Int., **44**:20570–20574 **(2018)**.

[181]R.F. Shimanouchi, T. Tsuji, R. Yagi, Y. Matsumoto, H. Nishizawa, Hydrothermal synthesis and crystal structure of ionic conductive metal tungstates, IOP Conf. Ser. Mater. Sci. Eng., **18**:2–6**(2011)**.

[182] R.M. Sebastian, S. Xavier, E.M. Mohammed, Dielectric behavior and AC conductivity of Mg^{2+} doped zinc ferrite nanoparticles synthesized by sol-gel technique, Ferroelectrics,**481**:48–56 **(2015)**.

[183]A. Tschope, E. Sommer and R. Birringer, Grain size-dependent electrical conductivity of polycrystalline cerium oxide: I. ExperimentsSolid State Ionics, **139**(3-4): 255-265**(2001)**.

[184]S. Sanna, V. Esposito, J.W. Andreasen, J. Hjelm, W. Zhang, T. Kasama, S. B. Simonsen, M. Christensen, S. Linderoth, N. Pryds, Enhancement of the chemical stability in confined δ - Bi_2O_3, Nat. Mater.,**14**:500–504**(2015)**.

[185]E.S. Kim, B.S. Chun, J.D. Kim, and K.H. Yoon, Low-temperature sintering and microwave dielectric properties of $[Ca_{0.6}\ (Li_{0.5}Nd_{0.5})_{0.4}]_{0.45}Zn_{0.55}TiO_3$ ceramics Mater. Sci. & Eng. B, **99(1-3)**:243-246 **(2003)**.

[186]N.Pryds,V.Esposito, When two become one: an insight into 2D conductive oxide Interfaces, Journal of Electroceramics, **38**:1–23**(2017)**.

[187]Eung Soo Kim , Soon Ho Kim,Effects of structural characteristics on microwave dielectric properties of $(1-x)CaWO_4 - xLaNbO_4$ ceramics,J. Electroceram.,**17**:471–477 **(2006)**.

[188]Chi Kao K. *Dielectric phenomena in Solids*. Elsevier, New York, **(2004)**.

[189]B.G.Rao, D.Mukherjee, B. M. Reddy, Novel approaches for preparation of nanoparticles, in: Nanostructuresin Nov. Ther. Synth. Charact. Appl., 1–36 **(2017)**.

[190]N. Sivakumar, A. Narayanasamy, K. Shinoda, C. N. Chinnasamy, B. Jeyadevan, and J. M. Greneche, Electrical and magnetic properties of chemically derived nanocrystalline cobalt ferrite J. Appl. Phys.,**102**:013916 **(2007)**.

[191]L. S. Cavalcante, J. C. Sczancoski, L. F. Lima, J. W. M. Espinosa, P. S. Pizani, J. A.Varela, and E. Longo, Synthesis, Characterization, Anisotropic Growth and Photoluminescence of $BaWO_4$ Cryst. Growth Des., **9**:1002- 1012**(2009)**.

[192]A.V.Rane, K. Kanny, V. K. Abitha, and S. Thomas, *Methods for Synthesis of Nanoparticles and Fabrication of Nanocomposites* (Elsevier Ltd., **2018)**.

CHAPTER 2

INSTRUMENTATION TECHNIQUES

2.1. Introduction

In this chapter Instrumentation techniques have been discussed which include X-ray diffraction (XRD) techniques,Fourier Transform Infra-Red spectrometer (FTIR),scanning electron microscopy (SEM) and Energy Dispersive Spectroscopy (EDS), High Resolution Transmission Electron Microscope (HRTEM),UV-Vis diffuse reflectance spectrophotometer,DC conductivity two probe method, Dielectric conductivity measurement, thermoelectric power measurement.

2.2. X-ray diffraction techniques

XRD is a non-destructive technique used to study the crystal structure of solids, phase identification, crystal parameters such as lattice constants, crystallite size, shape of unit cell, identification of unknown materials, defects, stresses, etc **[1]**.Each crystalline solid has its unique characteristic X-ray powder pattern, which may be used as a "fingerprint" for its identification. When X-rays interact with a crystalline substance, one gets a diffraction pattern. A crystal might be regarded as a three dimensional diffractions grating for X-rays whose wavelength is comparable with the atomic spacing and hence the diffraction pattern provides information about the regular arrangements of atoms in the lattice. In context to nanocrystalline samples, the most important parameter that influences physical and chemical properties of the samples is average crystallite size. X-ray diffraction is the most convenient indirect method of the determination of average crystallite size of nanocrystalline samples **[2]**.

RIGAKU Ultima IV powdered X-ray diffractometer is shown in **Figure 2.1**.XRD patterns were recorded using RIGAKU Ultima IV powder X-ray diffractometer with Cu-Kα radiation (λ = 1.5418 Å). The measurement was recorded in the 2θ range of 20^o – 80^o with a step size of 0.02^o. X-ray source, a sample chamber and an X-ray detector are the three important components of X-ray diffractometer. **Figure 2.1(a-b)** shows the schematic diagram of computer controlled X-ray powder diffractometer. When X-ray beam (Cu-Kα) is incident on the crystal surface at an angle (θ) it gets reflected off the atomic planes. Constructive interference occurs to crystalline material, when the path difference between the reflected beams is an integral multiple of X-ray wavelength. This condition satisfies the Bragg's law of diffraction as given in equation ($2d\sin\theta=N\lambda$), where (N) is an integer, (d) is the lattice spacing, (θ) is the diffraction angle, and (λ)

is the wavelength of the incident X-ray beam. The sample is scanned at an angle of (2θ) in all the possible directions of the lattice because of the random orientation of the powdered sample. The XRD patterns were identified with comparing the experimental (2θ) values of the peak intensities to the Joint Commission Powder Diffraction (JCPDS) pattern files. UNITCELL-95 program is used to calculate lattice parameters of tetragonal phases in composite samples using least square refinement method by X-ray wavelength of 1.5418 Å. The calculated lattice parameters were compared with the Joint Commission Powder Diffraction (JCPDS).

2.2.1. Crystallite size (D)

The peak broadening in X-ray diffraction patterns of nanomaterials is due to their finite size effect.The average crystallite sizes of freshly prepared samples were calculated by substituting X-ray line broadening in Debye Scherrer formula given in **Equation 2.1**.

$$\mathbf{D=\frac{0.89\lambda}{\beta Cos\theta}} \qquad \mathbf{(2.1)}$$

Where (D) is crystallite size in nm,(λ) is X-ray wavelength in Å,(β)is line broadening at full width half maxima intensity (FWHM) in radians,0.89 is shape factor and (θ)is Bragg's angle **[3]**.

2.2.2. Micro-strain (ε)

It may be noted that in the above Debye Scherrer Equation, it was considered that broadening of XRD peak was only due to the small size of the crystallites. However, there exist two other contributions to the line broadening, **(i)** from instrumental factors (negligible) and **(ii)** strain in the crystallites **[4]**. Thus strain broadening of the diffraction peaks must also be taken into account for an unambiguous determination of crystallite size. This strain broadening is explained by Williamson-Hall method **[5]**. In this method it is assumed that the size and strain contributions to the line broadening are independent of each other and the observed line broadening full width half maximum (FWHM) is simply the sum of crystallite size broadening and strain induced broadening. In this method (β) (FWHM) is given by **equation 2.2.** Here, (ε) is the root mean square value of the micro-strain introduced and (D) is crystallite size. **Equation 2.3** is called as Williamson-Hall Equation.

$$\mathbf{\beta = \beta_D + \beta_\varepsilon}$$

$$\mathbf{Where\ \beta_D = \frac{0.89\lambda}{D\ Cos\theta} \quad and\ \beta_\varepsilon = 4\varepsilon\ tan\theta} \qquad \mathbf{(2.2)}$$

$$\therefore \beta\cos\theta = \frac{0.89\lambda}{D} + 4\varepsilon\sin\theta \qquad (2.3)$$

By plotting **equation 2.3,** the value of micro-strain **(ε)** may be estimated at the slope of the line and crystallite size (D) from the intersection with the y-axis. Micro-strain, i.e. strain that extends over a few lattices spacing in the crystallites is another important contribution to the X-ray diffraction line broadening. Thus strain contribution may be resolved from the particle size contribution by Williamson- Hall-method **[6]**.

2.2.3. Sample preparation for Powder X-ray diffraction

Finely ground powdered samples, weighted around 1gm each was used for obtaining X-ray diffraction patterns of nanocomposites.

Figure 2.1: RIGAKU Ultima IV powder X-ray diffractometer, NIO, Goa.

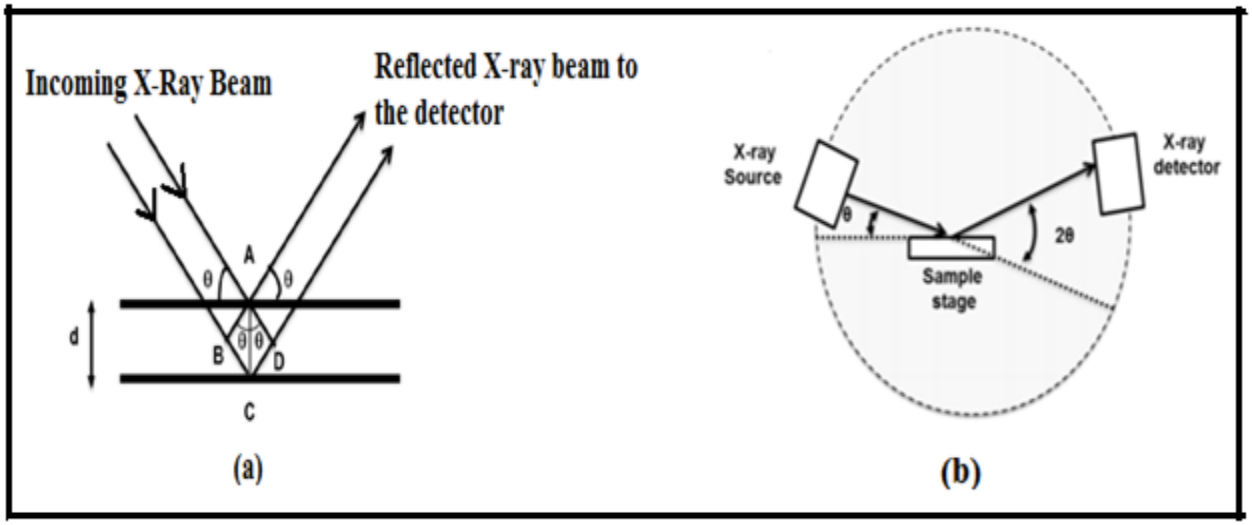

Figure 2.1(a-b): (a) Diffraction from two scattering planes. **(b)** Schematic diagram of X-ray diffractogram.

2.3. Fourier Transform Infrared (FTIR) Spectroscopy

Infrared (IR) spectroscopy gives information about the vibrational characteristics of chemical functional groups of a sample **[7]**.The term infrared covers the wavelength range of the electromagnetic spectrum between 0.78 and 1000 µm. In the context of infrared spectroscopy, wavelength is measured in wave numbers, which have the unit cm^{-1}. IR radiation does not have enough energy to induce electronic transitions and its absorption is restricted to compounds with small energy differences in the possible vibrational and rotational states. The major types of molecular vibrations are stretching and bending.Stretching (change in inter-atomic distance along the bond axis) can be symmetric or asymmetric.Bending (change in angle between two bonds) can be of rocking, scissoring, wagging or twisting type. In addition to these, interaction betweenvibrations can lead to vibrational coupling, if the vibrating bonds are joined to a single central atom. Infrared radiation is absorbed and the associated energy is converted into these types of motions. The absorption involves discrete and quantized energy levels. However, the individual vibrational motion is usually accompanied by other rotational motions. These combinations lead to the absorption bands and not the discrete lines of the IR spectrum.

IR region of electromagnetic spectrum could be classified into three different groups of the basis of their wave number as follows: **(a)** near infrared region (14000 cm^{-1} to 4000 cm^{-1}), **(b)** mid infrared region (4000 cm^{-1} to 400 cm^{-1}) and **(c)** far infrared region (400 cm^{-1} to 4 cm^{-1}) **[8,9]**.

The infrared (IR) spectrum of a sample is recorded by passing a beam of infrared light through the sample. When the vibrational frequency of a bond is same as frequency of the IR absorption occurs. For a molecule to absorb IR, the vibrations or rotations of a molecule must cause a net change in the dipole moment of the molecule. The alternating electrical field of the radiation interacts with fluctuations in the molecule dipole moment. If the frequency of the radiation matches the vibrational frequency of the molecule then the radiation will be absorbed, causing a change in the amplitude of molecular vibration. Analysis of the position, shape and intensity of peaks in this spectrum reveals details about the molecular structure of the sample.

2.3.1 Sample preparation and experimental work

To record the FTIR spectra of nanocomposites, we have used Shimadzu FTIR 8900 spectrophotometerwhich is shown in **Figure 2.2**. The wave number (IR) ranges is 4000 to 400 cm^{-1} with a resolution of 0.5 cm^{-1}. For FTIR measurements, 1mg of sample was mixed with 100mg of KBr and pelletized with a thickness of 1.5mm and radius of 6mm with 3 tons pressure for 5 minutes. 100mg KBr pellets were made with the same conditions and was used as a reference sample. Similar procedures were followed and pellets of all the samples were prepared for recording of FTIR spectra. This ensured that the final spectra were due to the vibrational modes present in the sample of study.

Figure 2.2: Shimadzu FTIR 8900 assembly, School of Physical and Applied Sciences, Goa University.

Specifications:

Model	: Shimadzu FTIR 8900
Wave number range	: 7800 cm^{-1} – 350 cm^{-1}
Detector	: High sensitivity pyroelectric detector
Accuracy	: 0.125 cm^{-1}
Resolution	: 0.5 cm^{-1}
S/N ratio	: 20000: 1

2.4. Scanning electron microscope (SEM) and Energy dispersive X-ray spectroscopy (EDS)

The SEM is widely used to generate high-resolution images of the shapes of objects, and show spatial variations in chemical compositions, acquire spot chemical analyses using EDS and identify phases based on qualitative chemical analysis and/or crystalline structure. It is used in materials evaluation such as grain size, surface roughness, porosity, particle size distributions, mechanical damages etc. The SEM has a large depth of field, which allows a large amount of the sample to be in focus at one time. Even the image resolution of an SEM is about an order for magnitude poorer than that of a TEM; its images rely on surface processes rather than transmission **[10]**. We have used CARL ZEISS EVO 18 special edition model for recording the SEM images of the samples. CARL ZEISS EVO 18 SEM model is shown in **Figure 2.3 (a)**.

SEM works on the basic principle of accelerated electrons. When accelerated electrons strike the sample, the electron energy is dissipated on the sample by electron-sample interaction and various signals are produced. These signals include secondary electrons that generate SEM images, the backscattered electrons and the generation of characteristic X-rays which are utilized for chemical composition analysis of the sample, continuum X-rays, visible light and heat. The equipment consists an electron gun that produces a monochromatic electron beam which is condensed and focused on the help of a set of magnetic condensing lenses. A set of coils is used for the beam scanning and the objective lensis used to focus the scanning beam on the desired sample area as shown in **Figure 2.3 (b)**. The electron beam striking the sample produces secondary electrons that is collected by a secondary detector and applied to the display unit after converting it into a voltage signal and amplifying the same. This gives rise to an intensity- related light spot on the screen. The ultimate image contains thousands of these types of light spots of

varying intensity on the display screen which corresponds to the samples morphology **[11-15]**.SEM micrograph shows two dimensional topographic views of the sample.

2.4.1 Sample preparation and experimental work

Small amount of sample was dissipated on a conductive carbon adhesive tape and then subjected to Au/Pd coating as shown in **Figure 2.3 (c)**. The coated samples were then exposed to an electron beam from CARL ZEISS EVO 18 special edition SEM model, and they were placed in the scanning electron microscope to study the morphology. Analysis of morphology, particle size and size distribution were done from the obtained images.

Figure 2.3(a): CARLZEISS EVO 18 SEM Special Edition, USIC, Goa University, Goa.

Specifications of CARL ZEISS EVO 18 SEM:

Filament	: Tungsten
Secondary e- image resolution	: 50 nm (depends on sample)
BSD detector	: Available
Magnification	: Upto 50X – 100KX (depends on sample)

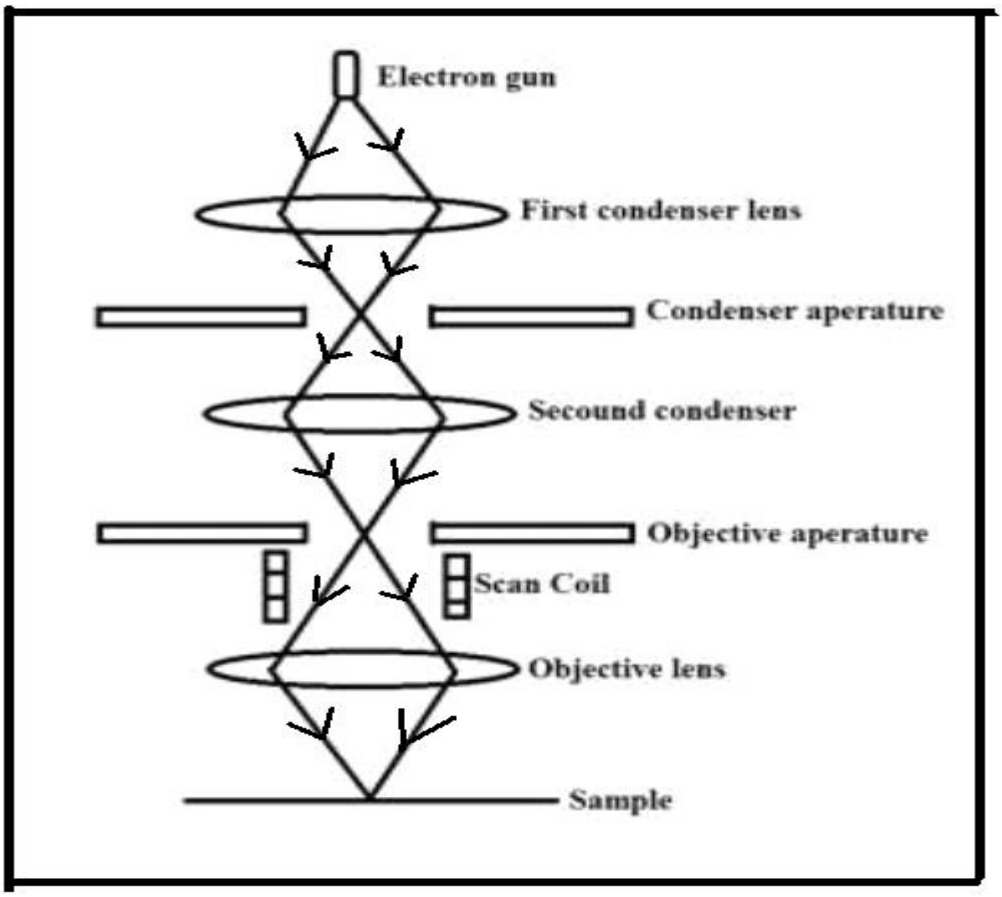

Figure 2.3(b): Basic assembly of Scanning Electron Microscope.

Figure 2.3(c): Sputtering process using sputtering unit.

2.4.2. Energy dispersive X-ray spectroscopy (EDS)

EDS analysis was carried out for prepared samples to find the elemental composition present in the samples. It was carried out by JEOL-JSM 5800 LV scanning electron microscope instrument. It involves a beam of X-rays, incident onto the sample which may elevate an electron to an excited state. The arrival of the electron to the ground state results in characteristic X-ray emission. These X-rays are then detected and utilized to give useful information about the constituent elements present in the compound **[16, 17]**.

Specifications of JEOL-JSM 5800 LV:

Magnification range : 18 to 300kX

Number elements mapping at a time : 32 elements

2.5. High Resolution Transmission electron microscopy (HRTEM)

The HRTEM is useful to get information about the morphology, crystal structure and defects. It is highly useful in resolving crystal phases, grain boundaries, interfaces, etc. with atomic scale resolution. The HRTEM is also capable of forming a focused electron probe, as small as 20 Å, which can be positioned on very fine features of the sample of micro diffraction information or analysis of X-rays for compositional information. In addition, the instrument can be used to produce electron-diffraction patterns, useful for analyzing the properties of a crystalline specimen. The HRTEM has been equally useful in the life sciences, for example, for examining plant and animal tissue, bacteria, and viruses. It provides very high magnification ranging from 50 to 10^6 and its ability to provide both image and diffraction information from a single sample.

The high resolution transmission electron microscopy technique, electrons are accelerated beyond 90 to 200 KeV and are projected onto the thin specimen by means of electromagnetic lenses. The transmitted beam after interaction with the specimen is used to form a magnified image of photographic film or on a fluorescent screen or is detected by a CCD camera which is a sensor. The four main parts of HRTEM system the source of electron, electromagnetic lens system, sample holder, and imaging system. The electron source is normally a tungsten filament which emits electrons when being heated. After leaving the electron source, the beam is then accelerated and is tightly focused using electromagnetic lens and metal apertures to pass through the specimen. The transmitted electrons are refocused using electromagnetic lens and enlarged image is projected onto a screen for the user to see as shown in **Figure 2.4 (a)[18, 19]**. In the

present study, HRTEM images were recorded using the instrument JEOL/JEM-2100 with an accelerating voltage 200KV which is shown in **Figure 2.4 (b)**.

2.5.1 Sample preparation and experimental work

An extremely small amount of material is suspended in water/ethanol (just enough to obtain slightly turbid solution). The solution is ultrasonicated to disperse the particles, a drop of the solution is then pippeted out and cast the drop on carbon-coated grids of 200 mesh.Then HRTEM images were recorded using the instrument JEOL/JEM-2100.Detailed calculations of particle size and size distribution of HRTEM images were carried out using image J software.

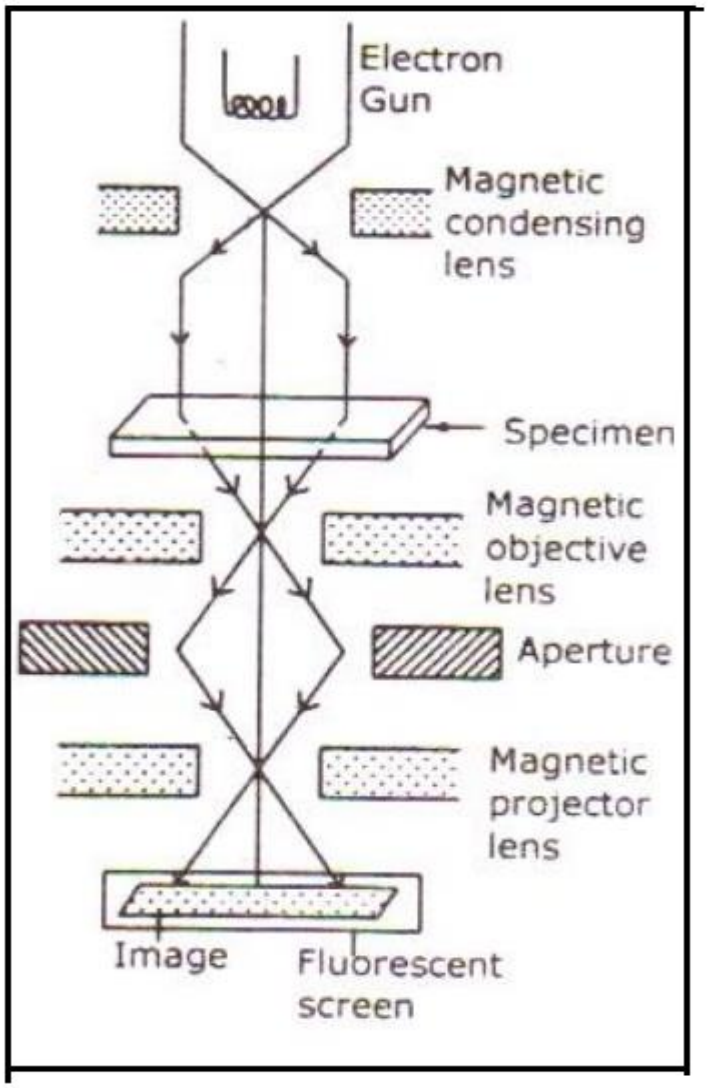

Figure 2.4(a): Basic assembly of High Resolution Transmission Electron Microscope (HRTEM).

Figure 2.4(b): HRTEM JEOL/JEM-2100, with an accelerating voltage 200KVDST-SAIF, Kochi.

Specifications of HRTEM JEOL/JEM-2100

Accelerating voltage	: 200kV
Filament	: LaB6 Electron gun
Point resolution	: 0.23 nm (depends on sample)
Lattice resolution	: 0.14nm

2.6. Ultraviolet - Visible Diffuse Reflectance Spectroscopy

Diffuse reflectance Ultraviolet -Visible Spectroscopy (UV-Vis) DRS is known to be a very sensitive and useful technique for the opaque samples. Ultraviolet and visible light have

sufficient energy to excite electrons to higher energy levels are usually applied to inorganic ions and molecules or composite materials **[20-23]**.Diffuse reflectance for the samples was carried out using SHIMADZU 2401 PC UV-Vis spectrophotometer is shown in **Figure 2.5(a)**.

Diffusive reflectance spectroscopy (DRS) is a powerful technique for the powdered materials. This technique gives vital information about the electron transition to the material. It is closely connected with the UV-Vis spectroscopy, because in both the techniques a visible light is utilized to excite the electrons the valence bands to the conduction band within the sample. The only difference is that, in UV-Vis spectroscopy, the relative change of transmittance of light, when it passes through a solution is recorded, while in diffusive reflectance technique a relative change in the amount of reflected light from the powdered sample surface is recorded. Light to get reflected off the surface of the opaque samples as shown in **Figure 2.5 (b-c)**. There are two types of reflections: Specular Reflection and Diffuse Reflection. If the incident light gets scattered in different directions it is called diffuse reflection, whereas symmetrical reflection with respect to the normal line is called specular reflection. The integrating sphere method is used to measure the diffuse reflectance spectra (DRS). The measurement is performed by placing the sample in front of the incident light window and the reflected light from the sample is concentrated on the detector using a sphere of ($BaSO_4$) coated into. **Figure 2.5 (d)** shows baseline compensation and sample measurement of DRS without including of specular reflection. The obtained reflectance light becomes relative reflectance with respect reference reflectance of the standard white board ($BaSO_4$). To avoid specular reflectance during the DRS measurements, the incident light is directed towards the sample at an angle of 0^0. As a result only diffuse reflected light is measured.

The most popular continuum theory describing the diffuse reflectance effect is Kubelka - Munk (K-M) theory and is given by the following **equation (2.4)**.

$$\mathbf{F(R)} = \frac{(1-R)^2}{2R} \qquad \mathbf{(2.4)}$$

Where (R) is the diffuse reflectance (DR) of the sample and F(R) is K-M factor and is proportional to absorption coefficient (α).

2.6.1 Sample preparation and experimental work

Nanocomposites were ground manually down a motor pestle. A sample quantity of 2-3 grams of powder is required to fill the sample holder. The powder was filled into the holder by

applying an adequate amount of pressure using a cylindrical crystal piece, so that the powder may not fall down. Then the holder containing the sample was mounted on the machine, and the required data was obtained in reflectance mode using Shimadzu 2401 PC UV Spectrophotometer.

Figure 2.5(a): SHIMADZU 2401 PC UV-Vis Spectrophotometer, School of Physical and Applied Sciences, Goa University.

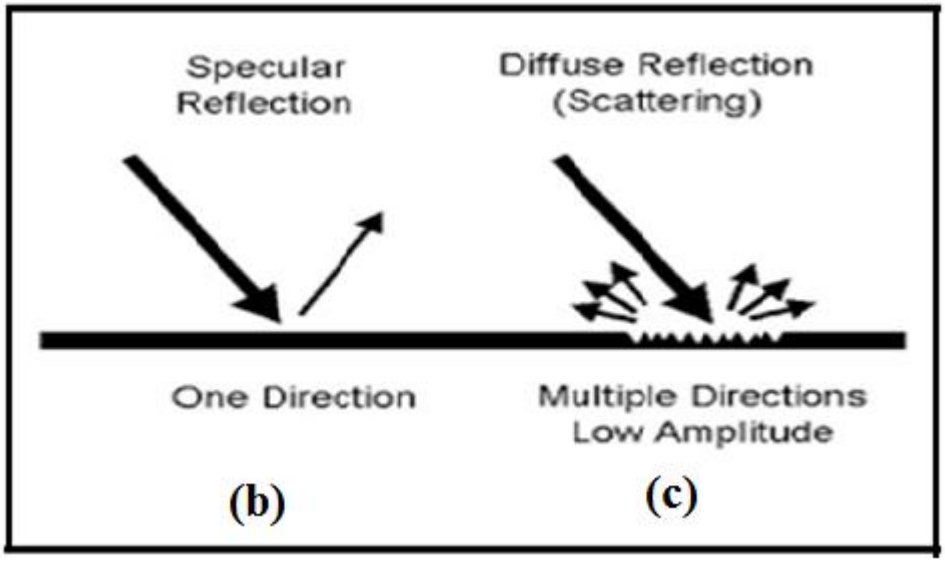

Figure 2.5(b-c): Schematic diagram of **(b)** Specular and **(c)** Diffuse reflection.

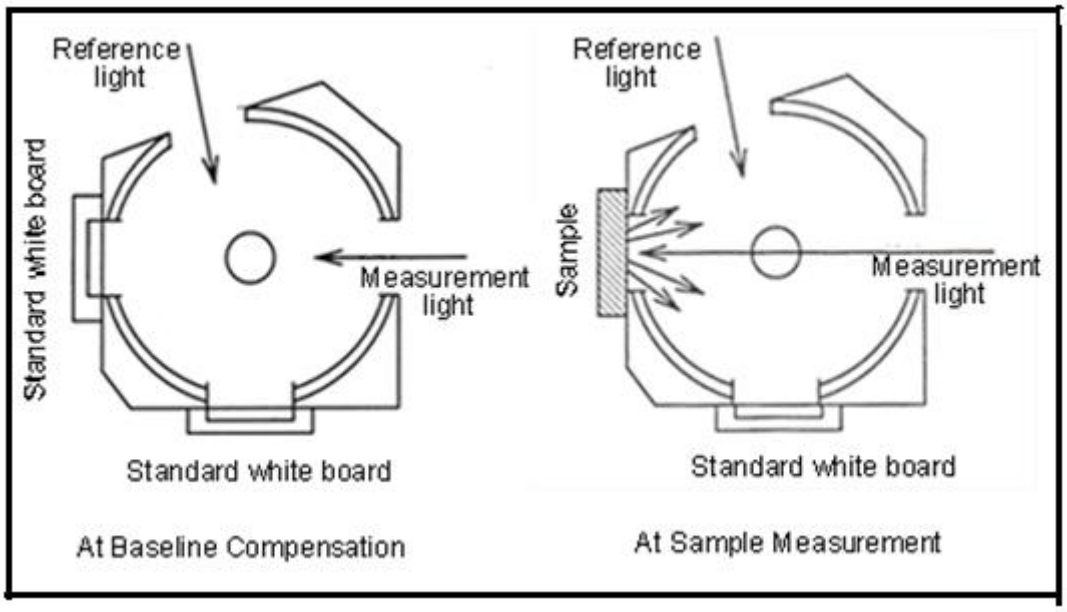

Figure 2.5(d): Measurement of diffuse reflection not including specular reflection using an integrated sphere.

Specifications:

Model	: SHIMADZU UV-2401PC
Lamp	: 50W halogen lamp, Deuterium (socket type)
Resolution	: 0.1nm
Detectors	: Photomultiplier R-928
Wavelength Range	: 190-800nm
Wavelength accuracy	: ± 0.3 nm

2.7. PL Spectroscopy

Photoluminescence (PL) emission is observed when spontaneous light is emitted by the material, under exact optical excitation. The excitation intensity and energy can be selected to analyze different types of excitations of the sample. The photoluminescence (PL) technique is nondestructive and this method requires very small sample quantity. Photoluminescence (PL) emission spectra and photoluminescence (PL) life-time decay curve of the samples were recorded using PTI QM-40 and QM-40Xe spectrofluorometer respectively controlled by FelixGX software. Cylindrical pellet of the samples was used to record the photoluminescence (PL) measurements.The emission spectra are measured by fixing the excitation wavelength and

scanning the emissions. The instrumental set up for the PTI QM-40/40Xe spectrofluorometer is shown in **Figure 2.6(a)** and a schematic diagram is shown in **Figure 2.6(b)**. The spectrum of Xenon arcs lamp and Xenon pulsed lamp is shown in **Figure 2.6(c) and (d)**.

2.7.1 Sample preparation and experimental work

Prepared nanocomposites was pressed for pellets of thickness ranging between 3 mm to 3.5 mm with diameter of 12 mm. Variation in intensity was recorded for all these samples of the wavelength range of 280 nm to 650nm with excitation wavelength of 260nm using PTI QM-40/40Xe spectrofluorometer.

Figure 2.6(a): PTI QM-40/40Xe spectrofluorometer, School of Physical and Applied Sciences, Goa University.

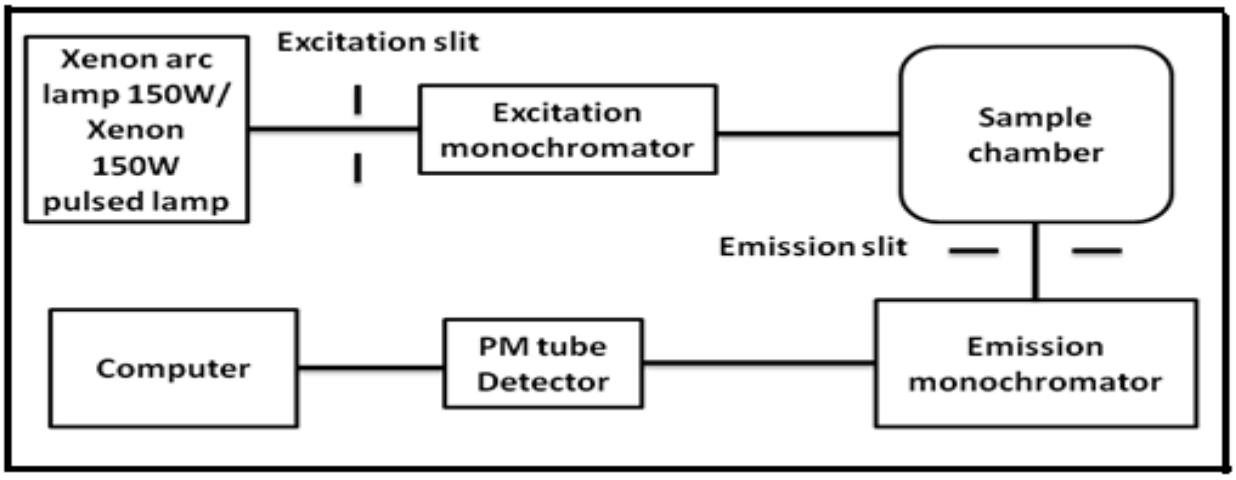

Figure 2.6(b): Schematic diagram of PTI QM-40/40Xe spectrofluorometer.

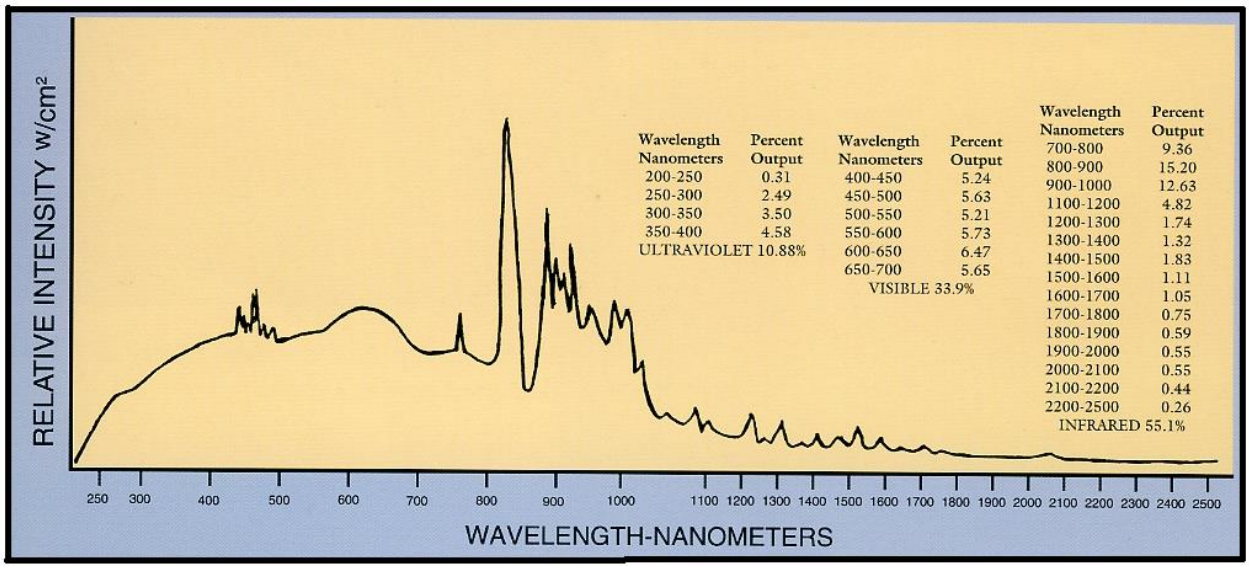

Figure 2.6(c): Spectral distribution of Xenon arc lamp.

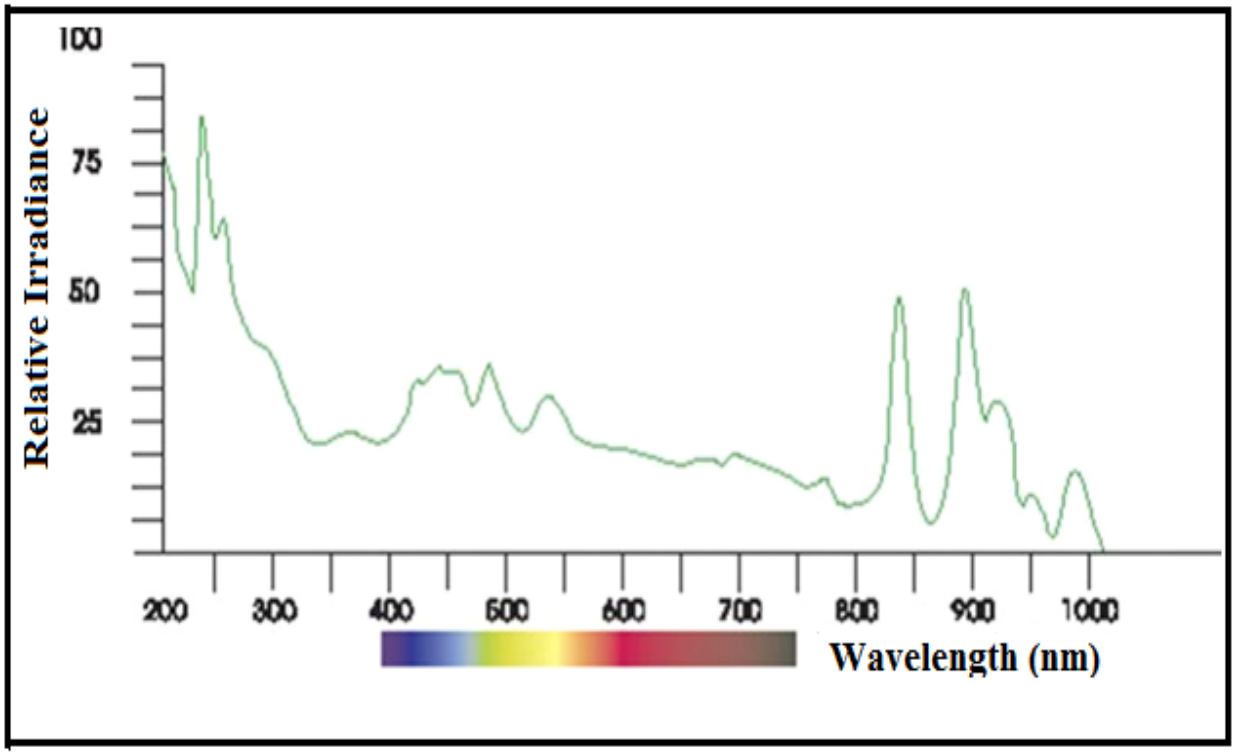

Figure 2.6(d): Spectral distribution of Xenon pulsed lamp.

Specifications:

Model : PTI QM-40/40Xe spectrofluorometer

Lamp : 150W Xenon arc lamp, 150W Xenon pulsed lamp for

Lifetime Signal to Noise Ratio : 10,000:1

Wavelength Accuracy	: +/- 0.5 nm
Wavelength Resolution	: 0.06 nm
Detection	: Photon counting/analog
PMT type	: R928
Lower limit for recording decay time	: 1μS

2.8. Dielectric Spectroscopy

A dielectrics material exhibits insulating nature having an important property of electrical polarization, which is a good feature. A dielectric material attains polarized when it is placed into an electric field. **Figure 2.7(a)** displays a dielectric material without any application of electric field while,**Figure 2.7 (b)** displays a dielectric material polarization with an application of electric field. This occurrence of polarization is known as dielectric polarization. Clausius **[24]** and Mossotti **[25]** have successfully interconnected the specific inductive capacity to microscopic structure of the material; a macroscopic feature of the insulator was studied by Faraday **[26]** which is now commonly termed as dielectric constant. In highly crystalline and well-structured materials the dielectric constant is sturdily dependent on applied field frequency. For the dielectric studies WAYNE KERR 6440B precision component analyzer has been used which is shown in **Figure 2.7(c)**. It is one of the powerful impedance analyzers in the field of dielectric spectroscopy and has great accuracy and sensitivity of the measured parameters.

2.8.1 Sample preparation and experimental work

Samples were pressed for pellets of thickness ranging between 1.5mm to 2.5mm and the diameter of 6mm. The pellets were silver painted on both sides of establishing good ohmic contacts with the electrodes. The values of capacitance and loss factor at room temperature were recorded for all the samples in the frequency range of 20 Hz to 3 MHz.

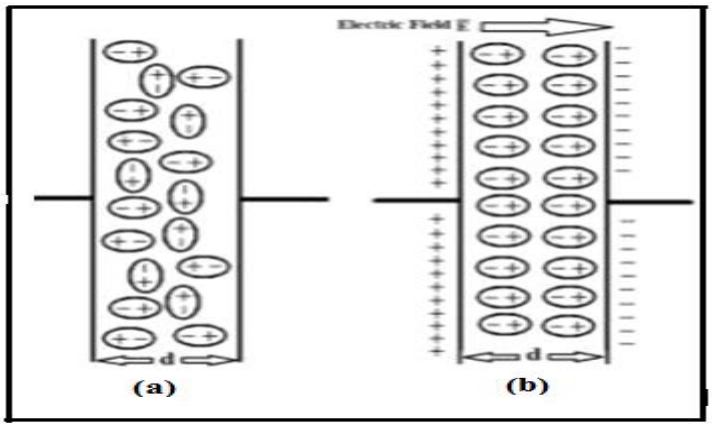

Figure 2.7(a-b): (a) Dielectric material in the absence of electric field. **(b)** Dielectric material in the presence of electric field.

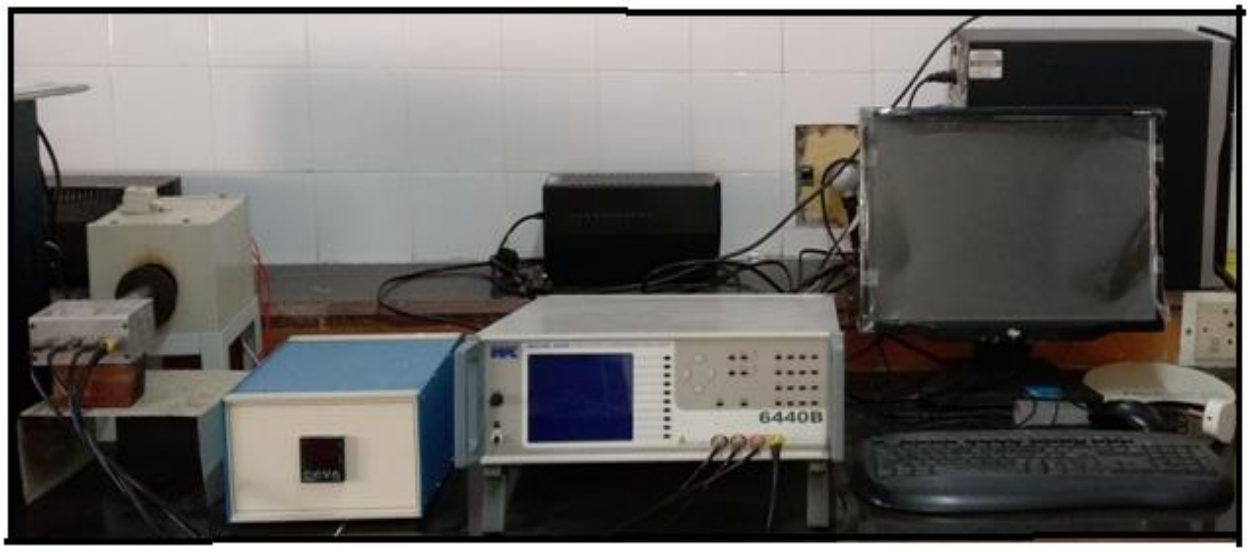

Figure 2.7(c):WAYNE KERR 6440B Precision component analyzer, School of Physical and Applied Sciences, Goa University, Goa.

2.9. DC conductivity measurement

DC conductivity of the samples was measured by two probes (two electrodes) method. It is one of the simplest and most cost-effective methods. The schematic diagram of the two probes (two electrodes) DC conductivity is shown in **Figure 2.8**.

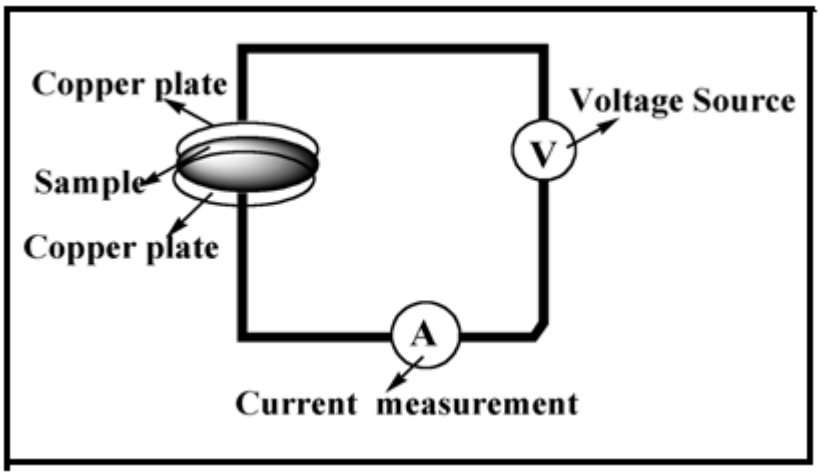

Figure 2.8: Block diagram of DC conductivity measurement set up.

2.9.1 Sample preparation and experimental work

Sample preparation for conductivity measurement is the same as the preparation done for dielectric measurements. DC conductivity measurements are carried out by measuring the current through a sample by different fixed voltage from 1-10Volts. Different fixed voltage 1-10Volts DC potential was applied to the sample and current measured using Keithley electrometer at room temperature.

2.10. Thermoelectric measurement setup

The temperature difference between the two ends of a semiconductor material produces an electromotive force (emf) known as thermo emf (V). Thermopower analysis is widely useful in understanding the conduction mechanism in the semiconductor material. The quantification of thermo-emf is very straightforward and its sign provides very important information about conduction mechanism whether the conduction in the material is due to electrons or holes and also explores the behavior of the material whether it is p-type or n-type. The experimental set-up of thermo-emf is displayed in **Figure 2.9**. It has upper point contacts probe that forms a hot junction and a bottom point contact which makes a cold junction when the sample is placed in between **[27-30]**.

2.10.1 Sample preparation and experimental work

The samples of investigation were pressed for pellets having thickness between 2.5mm to 3mm with the diameter of 12 mm. The pellets were painted with silver paste on both sides to

establish good ohmic contact. Thermoelectric power measurements were carried for all the samples of a temperature range of 300K to 773K.

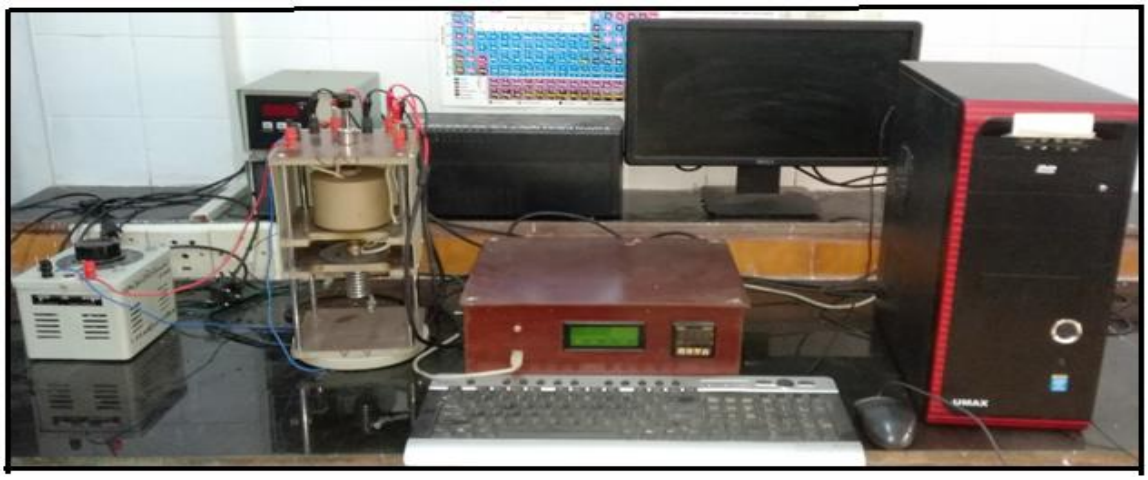

Figure 2.9: Thermopower setup, School of Physical and Applied Sciences, Goa University.

References

[1]B.D.Cullity, *Elements of X-Ray Diffraction*, 2nd Edition (ADDISON-WESLEY PUBLISHING COMPANY INC., Philippines, **1978**).

[2]C.B.Murray,C.R.Kagan, and M. G. Bawendi, Synthesis and Characterization of Monodisperse Nanocrystals and Close-Packed Nanocrystal Assemblies,Annual. Rev. Mater., Sci., **30**:545-550 **(2000)**.

[3]C. Kittel, *Introduction to Solid State Physics*,7th Edition, John Wiley & SonsInc., Singapore, **(1995)**.

[4] Yu. Rosenberg, V. S. Machavariani, A. Voronel, S. Garber, A. Rubshtein, A. I.Frenkel and E. A. Stern, Strain energy density in the x-ray powder diffraction from mixed crystals and alloys, Journal of Phys. Condens. Matter., **12**:8081-8084**(2000)**.

[5] J. A.Eastman,M.R.Fitzsimmons,L.J.Thompson,A.C. Lawson and R. A. Robinson, Diffraction studies of the thermal properties of nanocrystalline Pd and Cr, Nanostruct. Mater., **1**:465-470**(1992)**.

[6] D.Oleszak and P.H.Shingu, Nanocrystalline metals prepared by low energy ball milling. Appl. Phys., **79**:2975-2980**(1996)**.

[7] Q. Zhang, Q. Meng, and W. Sun, The concentration dependence of luminescent properties for Eu^{3+} doped $CaWO_4$ micron spherical phosphors Opt. Mater. (Amst).,**35**:915-922 **(2013)**.

[8] B. Stuart, *Infrared Spectroscopy: Fundamentals and Applications* Chichester: Wiley **(2004)**.

[9] H.Gunzler, H. U. Gremlich, *IR Spectroscopy: An Introduction* Weinheim: Wiley **(2002)**.

[10]J.Goldstein,*Scanning Electron Microscopy and X-ray microanalysis*,Kluwer Academic/Plenum Publishers, **689(2003)**.

[11] R. F. Egerton, *Physical Principles of Electron Microscopy: An Introduction to TEM, SEM*, and AEM, Springer: New York **(1986)**.

[12] J.Goldstein, D.Newbury, D. Joy, C. Lyman, C.; Echlin, P.; Lifshin, E.; Sawyer, L.; Michael, J. *Scanning Electron Microscopy and X-Ray Microanalysis*, 3rd Ed., Kluwer: New York **(2003).**

[13]M.T.Postek,K.S.Howard,A.H. Johnson and K.L. McMichael, *Scanning Electron Microscopy A Student's Handbook*, Ladd Research Ind., Inc.Williston, VT **(1980)**.

[14] C.E. Lyman, D.E. Newbury, J.I. Goldstein, D.B. Williams, A.D. Romig, J.T. Armstrong, P. Echlin, C.E. Fiori, D.C. Joy, E. Lifshin, Klaus-Ruediger Peters, *Scanning Electron Microscopy, X-Ray Microanalysis*, and Analytical Electron Microscopy Plenum Press. New York, N.Y. **(1990)**.

[15]J.I.Goldstein, H.Yakowitz, D.E.Newbury, E. Lifshin, J.W. Colby, J.W. Colby, J.R. Coleman, J.I. Goldstein and H. Yakowitz,*Practical Scanning Electron Microscopy: Electron and Ion Microprobe Analysis* Pelnum Press. New York, N.Y **(1975)**.

[16]B.Voutou and E. C. Stefanaki,*Electron Microscopy: The Basics, Physics of Advanced Materials* Winter School, **(2008)**.

[17] E. Suzuki,High-resolution scanning electron microscopy of immuno gold-labelled cells by the use of thin plasma coating of osmium, Journal of Microscopy, **208**(3):153-157**(2002)**.

[18] Thomas LaGrange, *Introduction: Basics of Transmission Electron Microscopy (TEM), TEM* Doctoral Course MS-**637(2016)**.

[19] S. J. B. Reed, *Electron Microprobe Analysis* Cambridge Univ. Press. 2nd Edition **(1993)**.

[20] D. A. Skoog, F. J. Holler, S. R. Crouch, *Principles of Instrumental Analysis*, 6th Edition. Thomson Brooks/Cole **(2007)**.

[21] J. P. Sibilia, *Materials Characterization and Chemical Analysis*, 2nd Edition. Wiley-VCH, New York **3 (1996)**.

[22] D. C. Harris, *Quantitative Chemical Analysis*, 7th Edition. Freeman, New York **(2007)**.

[23] G.R.Chatwal, S. K. Anand *Instrumental methods of chemical analysis*, Himalaya Publishing House **(1979)**.

[24] R.Clausius, *The mechanical Theory of Heat*, Vieweg Braunschweigh, Volume **2** (**1879)**.

[25] M. Faraday, Phil. Trans., **128**:1 79 265**(1837)**.

[26] O.F.Mossoti, Bibl. Univ. Modena., **6**:193**(1847)**.

[27]B.L.Gallagher and P. N. Butcher, *Handbook on semiconductors*, Amsterdam; Elsevier, **1:**721-816**(1992)**.

[28] C.M. Bandari and D.M. Rowe, *Thermal conduction in semiconductors*, Wiley Eastern Ltd, New Delhi **(1988)**.

[29] F.J. Blatt, P.A.Schroeder, C.L.Foiles and D. Greig, *Thermoelectric power of metals*, Plenum Press, New York, **(1976)**.

[30] S.M. Puri, and T.H. Geballe, *Semiconductors and Semimetals*, Eds. R. K. Willardson and A. C. Beer, Academic Press, New York **203(1966)**.

CHAPTER 3

SYNTHESIS AND CHARACTERIZATION OF$xBaWO_4/(1-x)CaWO_4$ NANOCOMPOSITES

3.1. Introduction

Nanocomposites had been studied enormously for enhancing the unique properties of metal oxide semiconductors**[1]**. Preparation of nanocomposites by wet chemical methods is used to make nanostructured materials with variable optical and electronic properties for the development of new multifunctional materials.Type I band alignment nanosystems are assembled by mixing two semiconductors in such a way that conduction and valence band positions of one semiconductor fall entirely within the band gap of another semiconductor creating an interface. In this type of alignment electrons and holes get accumulated in lower band gap material leading to more recombinations.Tungstate nanocomposites have been reported to possess interesting photoluminescent,photo-catalytic,electrochemical and thermoelectric applications**[2-5]**.In this work samples were prepared by co-precipitation method and characterized by various experimental techniques such as X-ray diffraction (XRD),Fourier transforms infrared spectroscopy (FTIR),Scanning electron microscope (SEM) and energy dispersive X- ray spectroscopy (EDS), high resolution transmission electron microscope (HRTEM). In this current chapter synthesis and characterization of $xBaWO_4/(1-x)CaWO_4$ nanocomposites have been briefly discussed.

3.2. Preparation of samples by co-precipitation method

The chemicals were purchased from Alfa Aesar and Sigma-Aldrich. They were of analytical grade and used without further purification. Calcium nitrate tetra hydrate: $Ca(NO_3)_2 \cdot 4H_2O$ (purity 99.0-103.0%), Sodium tungstate: $Na_2WO_4 \cdot 2H_2O$ (99.99%), Barium nitrate: $Ba(NO_3)_2$ (99.99%) were used for sample preparation.

$xBaWO_4/(1-x)\,CaWO_4$ where (x= 0, 0.25, 0.5, 0.75, 1) nanocomposites labeled as C0, C1, C2, C3 and C4, respectively, were prepared by co-precipitation method at room temperature in aqueous medium without any surfactant **[6]**. $Ba(NO_3)_2$, $Na_2WO_4.2H_2O$ and $Ca(NO_3)_2 .4H_2O$ were separately dissolved in distilled water to make aqueous solutions and named as A, B, and C respectively. The solutions A and B were mixed together and stirred for 20 minutes and then the solution C was slowly added to it. The final solution (A+B+C) was stirred for 3 hours and the

white colour precipitate was filtered out. The precursor was washed for several times of distilled water, dried at 100^0C and sintered at 200^0C,400^0C for 1 hour. Unless it is specified, C0, C1, C2, C3 and C4 labeling means unsintered samples. On the basis of cation percentage, compositions of different samples are given below.

$CaWO_4$ ----------C0

$0.25BaWO_4/0.75CaWO_4$----------C1

$0.5BaWO_4/0.5CaWO_4$----------C2

$0.75BaWO_4/0.25CaWO_4$----------C3

$BaWO_4$---------- C4

The chemical reaction equations are as follows **[6]:**

$Ba(NO_3)_{2(s)} + H_2O_{(aq)} \rightarrow Ba^{2+}_{(aq)} + 2NO_{3(aq)} + H_2O$ **Solution A**

$Na_2WO_4 .2H_2O_{(s)} + H_2O_{(aq)} \rightarrow 2Na^{2+}_{(aq)} + WO_4^{2-}{}_{(aq)} + 3H_2O$ **Solution B**

$Ca(NO_3)_2 .4H_2O_{(s)} + H_2O_{(aq)} \rightarrow Ca^{2+}_{(aq)} + 2NO_3^-{}_{(aq)} + 5H_2O$ **Solution C**

$Ca^{2+}_{(aq)} + 2NO_3^-{}_{(aq)} + 5H_2O + Ba^{2+}_{(aq)} + 2NO_{3(aq)} + H_2O + 4Na^{2+}_{(aq)} + 2WO_4^{2-}{}_{(aq)} + 6H_2O \rightarrow xBaWO_4/(1-x)\,CaWO_{4(s\downarrow)} + 4NaNO_{3(aq)}(\downarrow) + 12H_2O$

Graphical chart of the preparation method is shown in Figure 3.1.

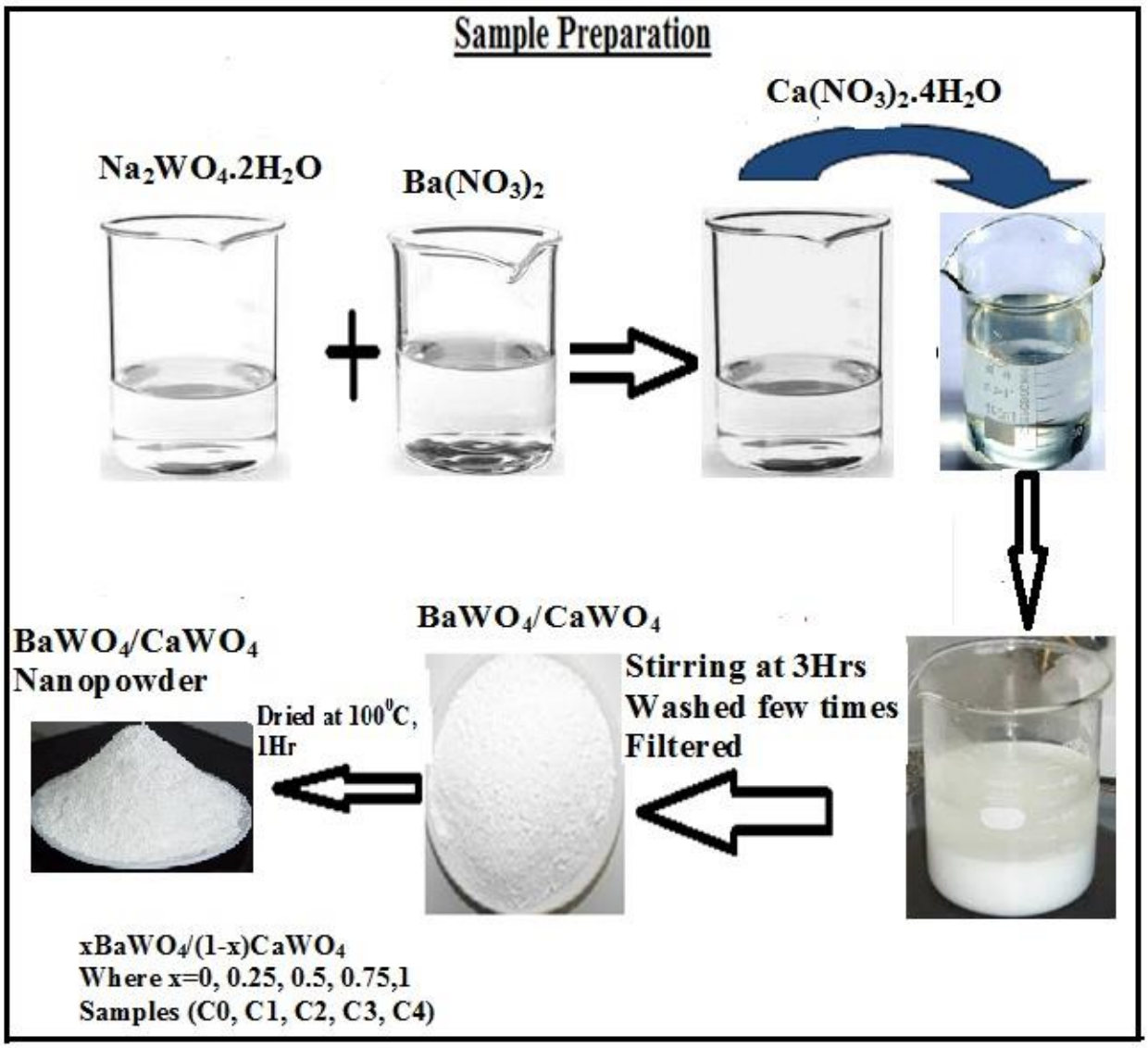

Figure 3.1: Schematic of sample preparation techniques.

3.3. Characterization of Nanocomposites

The XRD patterns of the samples were recorded by Rigaku X-ray diffractometer with Cu-K_α radiation. Fourier transform infrared spectroscopy (FTIR) spectra were recorded using SHIMADZU IR-800 Spectrometer.The morphologies of synthesized samples were analyzed by EVO-18 Carl Zeiss scanning electron microscope and elemental compositions of the samples were obtained by analyzing EDS recorded with JEOL-JSM 5800 LV scanning electron microscope.The high resolution transmission electron microscope (HRTEM) images of optimized samples were recorded using JEOL/JE-2100 with an accelerating voltage 200KV.

3.3.1. X-ray diffraction analyses

Powder XRD patterns of $xBaWO_4/ (1- x) CaWO_4$ unsintered nanocomposites are shown in **Figure 3.2(a-b)**.

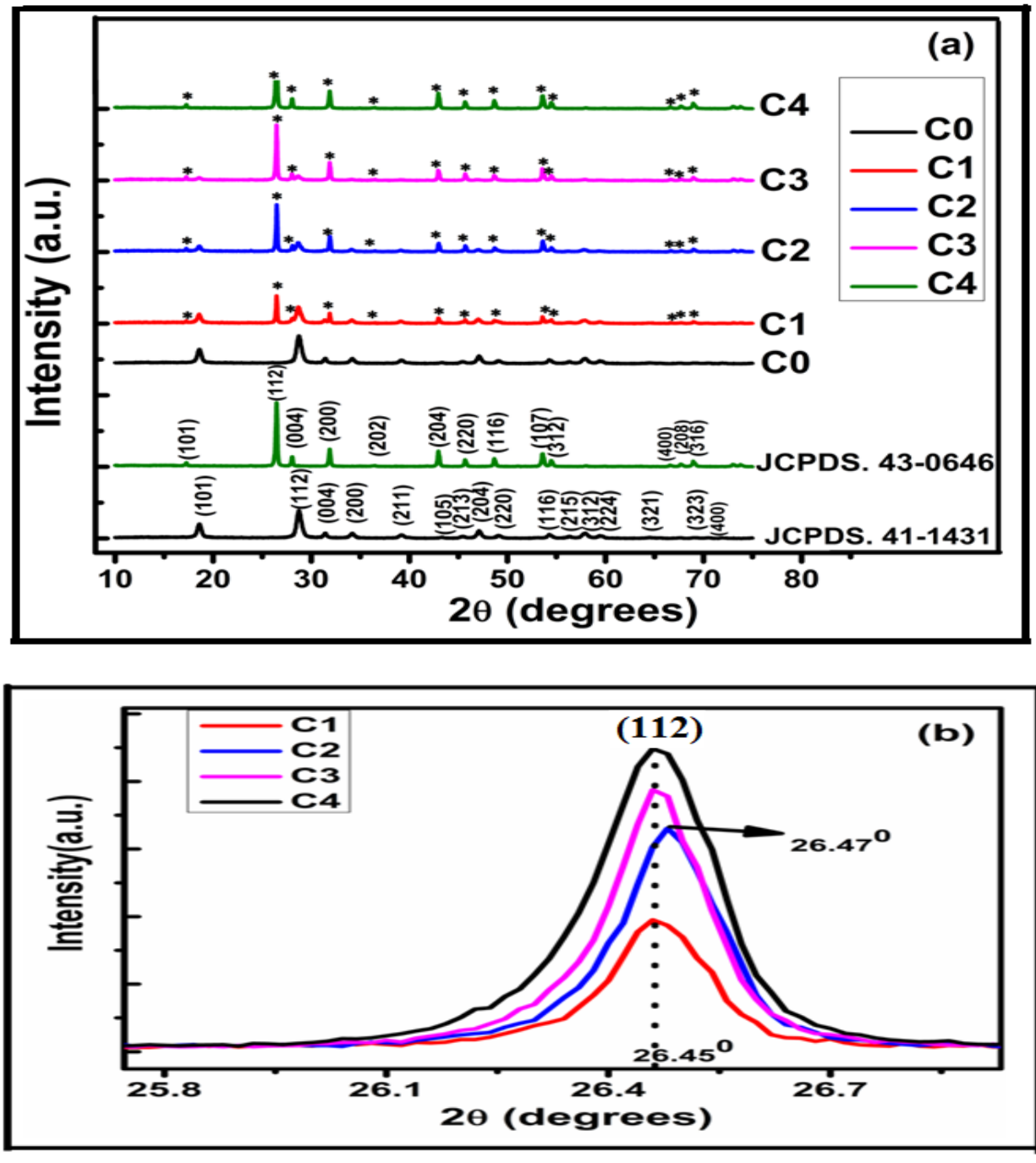

Figure 3.2(a-b): (a) XRD patterns where ('*') denotes $BaWO_4$ phase. (**b)** Intensity versus 2θ of (112) peak of nanocomposites samples.

XRD patterns of C0 ($CaWO_4$) and C4 ($BaWO_4$) single phase depict pure phase tetragonal structure of $CaWO_4$ and $BaWO_4$, and match with JCPDS: 41-1431 and JCPDS: 43-0646 **[7]**, respectively. All the composites samples show Scheelite-type tetragonal phases of $CaWO_4$ and $BaWO_4$ in accordance with JCPDS: 41-1431 and JCPDS: 43-0646, respectively **[7]**.The $BaWO_4$ phase is marked by (**'*'**) in the XRD patterns (17.26°, 27.95°, 31.68°, 36.23°, 42.79°, 45.57°, 48.60°, 53.41°, 66.56°, 67.82°, 68.83°) in **Figure 3.2(a)**. From **Figure 3.2(b)**, it is seen $BaWO_4$ phases that principle peak (112) plane intensity of C2 ($0.5BaWO_4/0.5CaWO_4$) nanocomposites alone shifts towards higher angle 2θ(26.45° to 26.47°), whereas that of C1 ($0.25BaWO_4/0.75CaWO_4$) and C3($0.75BaWO_4/0.25CaWO_4$) nanocomposites do not shift as compared to the C4($BaWO_4$) single phase respectively.This shift occurs in C2 ($0.5BaWO_4/0.5CaWO_4$) nanocomposite due to decrease in cell volume which confirms very small contraction of lattice parameters in $BaWO_4$ phase **[8]**. Also $CaWO_4$ phase has lower cell volume in comparison with $BaWO_4$ phase has higher cell volume **[9]**.This decrease in cell volume is attributed to the smaller ionic radius of Ca^{2+}(1.12Å) than that of Ba^{2+}(1.42Å**) [10]**.The lattice parameter does not change the tetragonal structure of $BaWO_4$ & $CaWO_4$ phase in nanocomposites samples.The lattice constants of $BaWO_4$ & $CaWO_4$ tetragonal phase in nanocomposites are tabulated in **Table 3.1(a-b)**.

3.3.2. Lattice parameters of $CaWO_4$ and $BaWO_4$ tetragonal phases in nanocomposites samples.

UNITCELL-95 program is used to calculate lattice parameters of $CaWO_4$ and $BaWO_4$ tetragonal phases in composite samples using least square refinement method by X-ray wavelength of 1.5418 Å. The calculated lattice parameters are shown in **Tables 3.1(a-b)** and matches well with the data onto JCPDS: 41-1431 (a = b = 5.243 **Å**, c = 11.373 **Å**) **[11]** and of JCPDS: 43- 0646 (a = b = 5.612 **Å**, c = 12.705 **Å**) **[12]**.

Table 3.1(a): Lattice constants of $CaWO_4$ tetragonal phase in nanocomposites samples

Samples	a = b(Å)	c (Å)	α =β = γ(°)	JCPDS: 41-1431 values a=b and c (Å) Ref. [11]
C0	5.4236±0.0014	11.9017±0.0010	90	
C1	5.4047±0.0049	11.3380±0.0027	90	**a = b = 5.243 and**
C2	5.4091±0.0049	11.3291±0.0027	90	**c = 11.373**
C3	5.4409±0.0060	11.3243±0.0032	90	

Table 3.1(b): Lattice constants of $BaWO_4$ tetragonal phase in nanocomposite samples

Samples	a= b (Å)	c (Å)	α = β = γ(°)	JCPDS: 43-0646 values a=b and c (Å) Ref. [12]
C1	5.7967±0.0026	12.8737±0.0021	90	
C2	5.6739±0.0025	12.7466±0.0019	90	**a = b =5.612 and**
C3	5.6895±0.0020	13.1333±0.0018	90	**c =12.705**
C4	5.5744±0.0006	12.8699±0.0004	90	

3.3.3. Crystallite size and lattice strain calculation

The Crystallite size and lattice strains of the $xBaWO_4/(1-x)CaWO_4$ unsintered nanocomposites were calculated using Debye Scherrer formula and Williamson-Hall methods **[13]** as given in **equations (3.1) and (3.2)** respectively and listed in **Table 3.2.**

$$\mathbf{D = \frac{K\lambda}{\beta \cos\theta}} \qquad \textbf{(3.1)}$$

$$\mathbf{\beta \cos\theta = \frac{K\lambda}{D} + 4\varepsilon \sin\theta} \qquad \textbf{(3.2)}$$

where (K) ~ 0.89 is a constant, (β) is the FWHM of the XRD peak in radians, (λ) is the X-ray wavelength (1.5418 Å), (D)is average crystallite size, (θ)is the Bragg angle and (ε) is the lattice strain respectively.

Figure 3.3 (a-d) is the plots of $BaWO_4$& $CaWO_4$ phase crystallite size and % lattice strain (calculated by Scherrer formula & Williamson–Hall equation) versus % Ba concentration of the samples. It is observed that the $BaWO_4$ phase crystallite sizes and $CaWO_4$ phase crystallite sizes of the composite samples match that of the $BaWO_4$ crystallite size and $CaWO_4$ crystallite

size respectively. Similarly the $BaWO_4$ phase % strain and $CaWO_4$ phase % strain of the composite samples match that of the $BaWO_4$ % strain and $CaWO_4$ % strain respectively. It means that the crystallite sizes and % lattice strain of the individual phases is not affected much in the composites. $BaWO_4$ and $BaWO_4$ phase crystallite sizes are large as compared to $CaWO_4$ crystallite size as seen in **Figure 3.3(a)**. $BaWO_4$ and $BaWO_4$ phase % lattice strain are less as compared to $CaWO_4$ % lattice strain as seen in **Figure 3.3(b)**. Whereas $CaWO_4$ and $CaWO_4$ phase crystallite sizes are less as compared to $BaWO_4$ crystallite size as seen in **Figure 3.3(c)** and $CaWO_4$ and $CaWO_4$ phase % lattice strain are large as compared to $BaWO_4$ % lattice strain as seen in **Figure 3.3 (d)**.

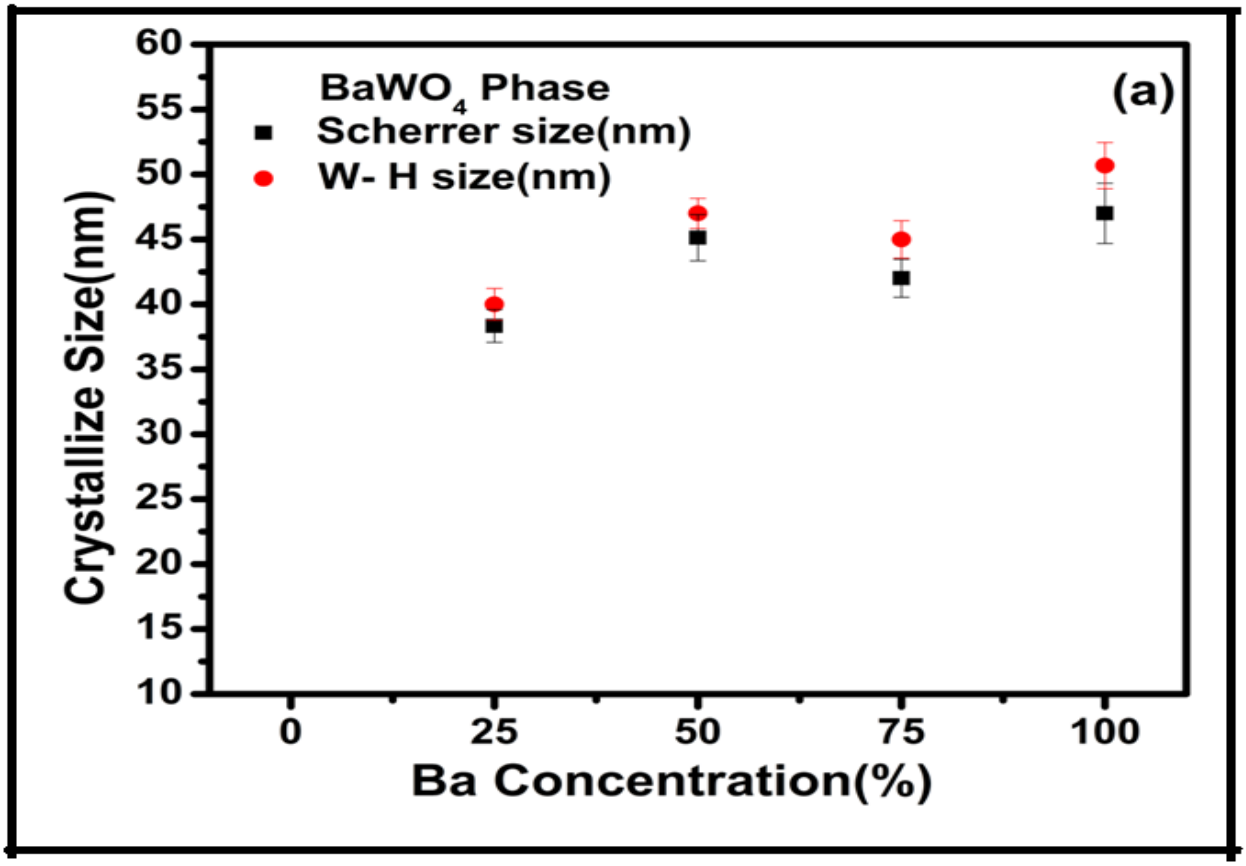

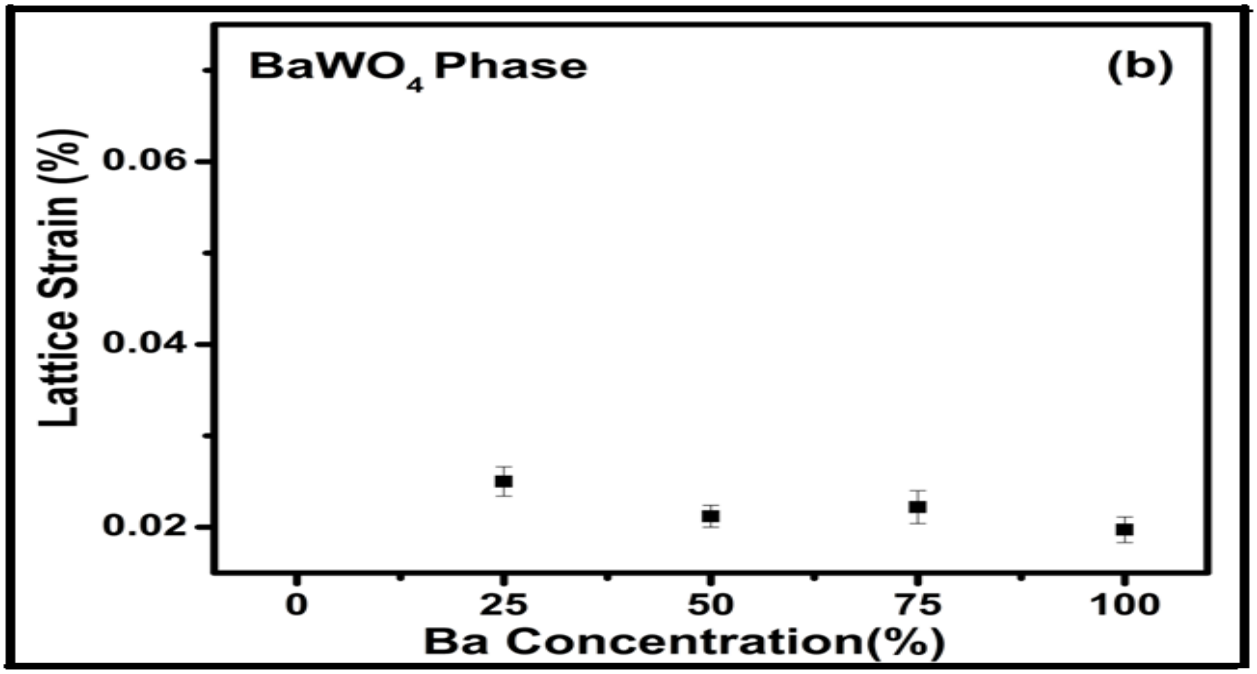
BaWO4 Phase
(b)
Lattice Strain (%)
0.06
0.04
0.02
0
25
50
75
100
Ba Concentration(%)

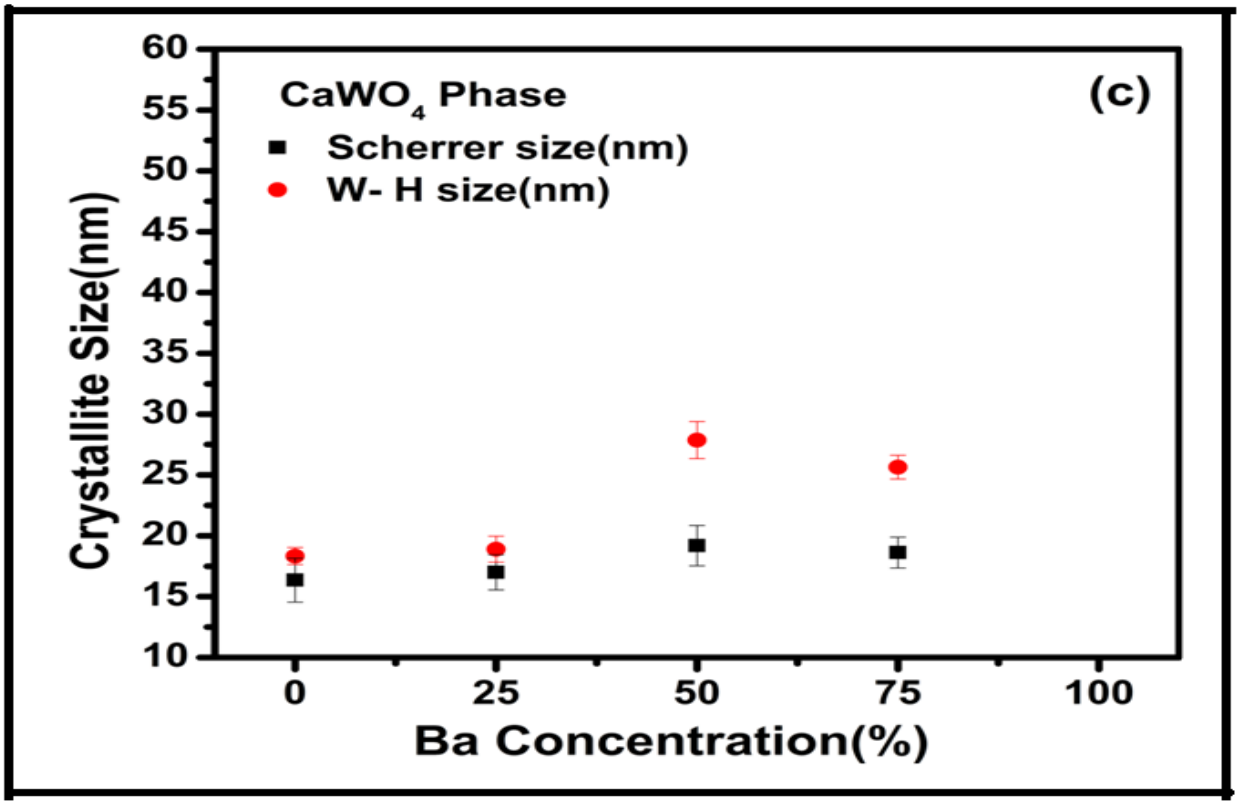
CaWO4 Phase
(c)
Scherrer size(nm)
W- H size(nm)
Crystallite Size(nm)
60
55
50
45
40
35
30
25
20
15
10
0
25
50
75
100
Ba Concentration(%)

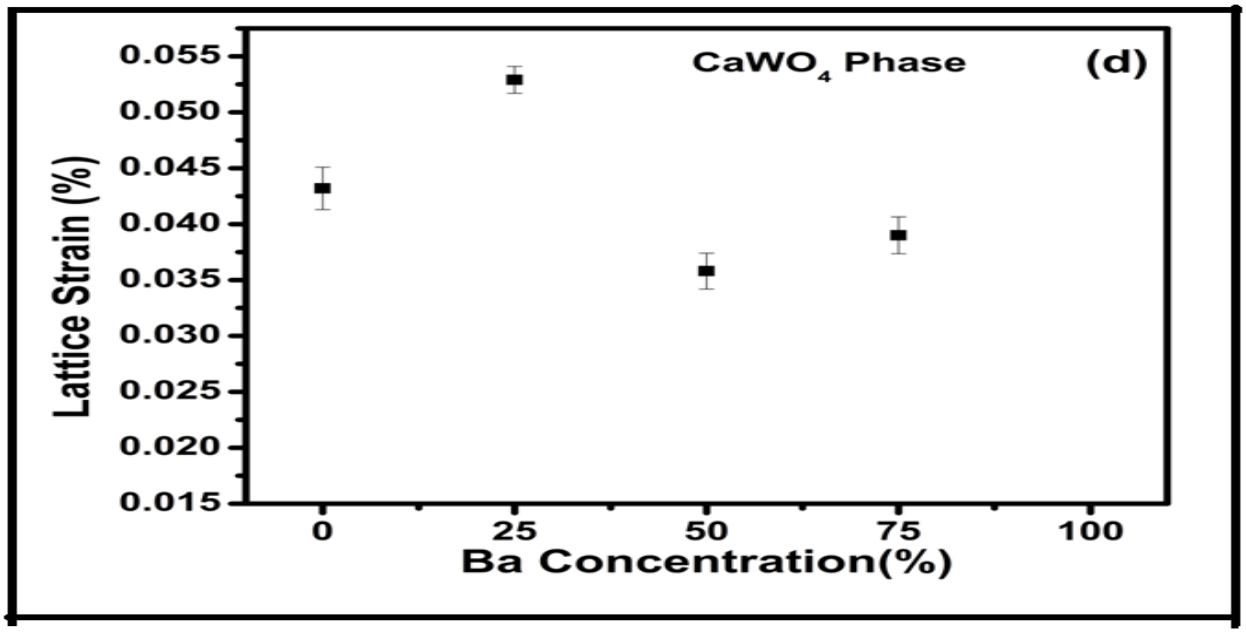

Figure 3.3(a-d):**(a-b)** Crystallite size (Scherrer formula & Williamson-Hall equation plot) & lattice strain (Williamson-Hall plot) versus % Ba concentration plots of $BaWO_4$ phase in nanocomposites. **(c-d)** Crystallite size (Scherrer formula & Williamson-Hall equation plot) & lattice strain (Williamson-Hall equation plot) versus % Ba concentration plots of $CaWO_4$ phase in nanocomposites.

Table 3.2: Crystallite size and % strain of $BaWO_4$ phase and $CaWO_4$ phase in nanocomposites samples.

Samples	Scherrer Formula		W-H Equation		W-H Equation	
	$BaWO_4$ phase Crystallite size (nm)	**$CaWO_4$ phase Crystallite size (nm)**	**$BaWO_4$ phase Crystallite size (nm)**	**$BaWO_4$ phase Strain (ε) (%)**	**$CaWO_4$ phase Crystallite size (nm)**	**$CaWO_4$ phase Strain (ε) (%)**
C0	-------	16.36±1.80	-------	-------	18.33±0.70	0.0432±0.0019
C1	38.34±1.26	17.00±1.44	40.00±1.22	0.025±0.0016	18.90±1.07	0.0529±0.0012
C2	45.13±1.78	19.19±1.66	47.00±1.16	0.0212±0.0012	27.86±1.52	0.0358±0.0016
C3	42.01±1.46	18.62±1.26	45.00±1.44	0.0222±0.0018	25.64±0.97	0.0390±0.00165
C4	47.00±2.32	-----	50.68±1.78	0.01973±0.0014	-------	------

3.3.4. Crystallite size and lattice strain calculation of $CaWO_4$ nanosample

Average crystallites sizes of $CaWO_4$ nanosamples sintered at different temperatures (100^0C,200^0C & 400^0C) are listed in the **Table 3.3**.The plots of the same are shown in **Figure 3.3(e)**. It is found that the crystallite size doesn't change much when the $CaWO_4$ nanosamples are sintered till 400^0C.

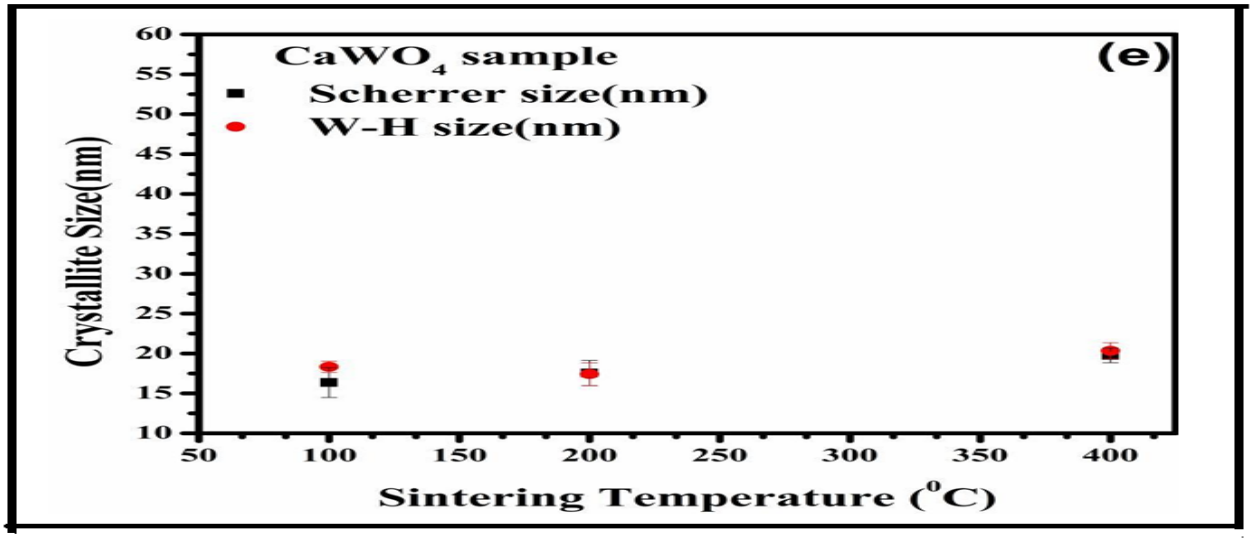

Figure 3.3(e): Crystallite size (Scherrer formula & Williamson-Hall equation) versus sintering temperature of $CaWO_4$ nanosamples.

Table 3.3: Crystallite size of $CaWO_4$ nanosamples sintered at different temperatures.

Sintering Temperature (^{0}C)	Scherrer Crystallite Size (nm)	W-H Crystallite Size (nm)
100	16.36±1.80	18.33±0.70
200	17.55±1.58	17.42±1.42
400	19.76±0.91	20.34±1.02

3.4. FTIR spectra studies and analyses

Figure 3.4 shows the FTIR transmittance spectra of the samples. Among the internal modes [ν_1(A1), ν_2(E), ν_3(F2) and ν_4(F2)] of $[WO_4]^{2-}$ specified as anti-symmetric stretching vibrations only ν_3(F2) and ν_4(F2) are IR active **[14]**.The weak peak of W–O bending band of ν_4 (F2) was detected at 445 cm^{-1}. The strong broad peak at 786-883 cm^{-1} is attributed to the anti-symmetric stretching vibration ν_3(F2) of O-W-O bond between $[WO_4]^{2-}$ tetrahedron in lattice

space. Sometimes they split into two bands; sometimes they do not **[15-17]**. Peak at 1385cm^{-1} is due to H-O-H stretching vibration.

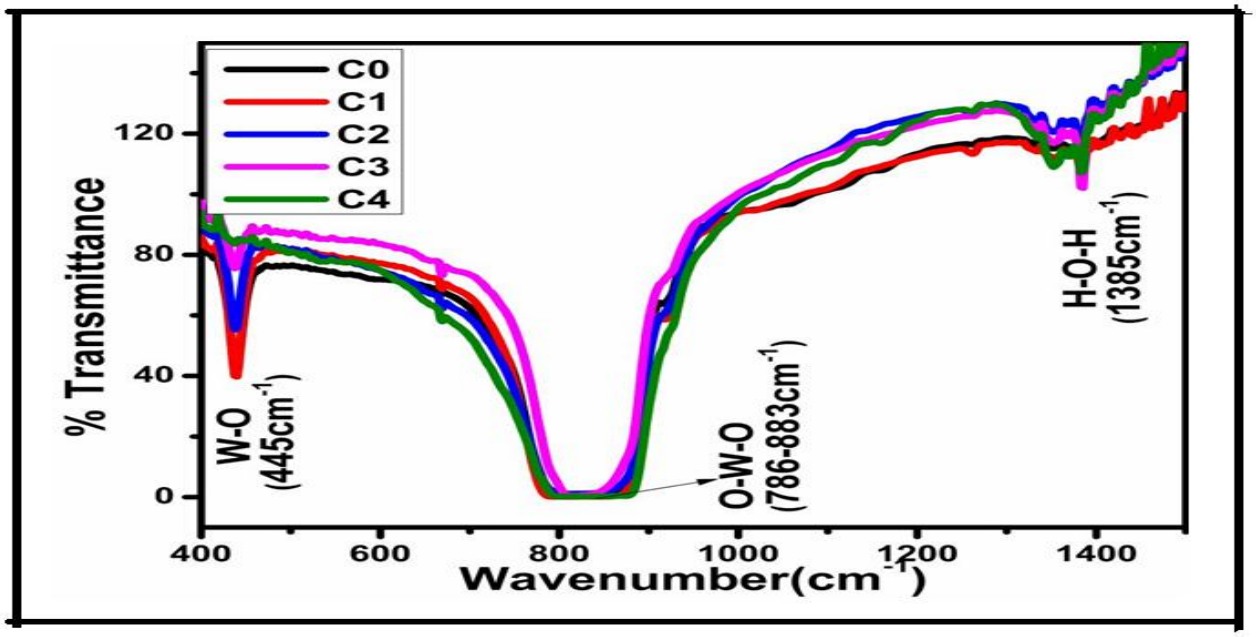

Figure 3.4:FTIR spectra of nanocomposites samples.

3.5. Surface morphology (SEM) and elemental (EDS) analyses

Shown in **Figure 3.5(a–e)** are the SEM pictures of $xBaWO_4$/ (1-x) $CaWO_4$ nanocomposites. The C0 ($CaWO_4$) sample shows small spherical shape crystallites. The C1 ($0.25BaWO_4/0.75CaWO_4$) nanocomposites shows bigger crystallites and smaller crystallites.C2 ($0.5BaWO_4/0.5CaWO_4$) nanocomposites shows bigger and smaller spherical crystallites. In C3 ($0.75BaWO_4/0.25CaWO_4$) nanocomposites few smaller crystallites and bigger crystallites are observed. The C4 ($BaWO_4$) sample shows bigger crystallites. Smaller and bigger crystallites correspond to $CaWO_4$ & $BaWO_4$ single phases respectively (crystallites sizes are calculated from XRD pattern).

EDS spectra of the samples are given in **Figure 3.6(a-e)**. Existence of Barium (Ba), Calcium (Ca), Tungsten (W) and Oxygen (O) elements without other impurity elements constitute the samples. Concentration of added Ba/Ca atomic ratios was calculated from these spectra. Observed elemental atomic percentages and Ba/Ca atomic ratio for the entire nanosamples tally with the calculated values within the limits of experimental errors.

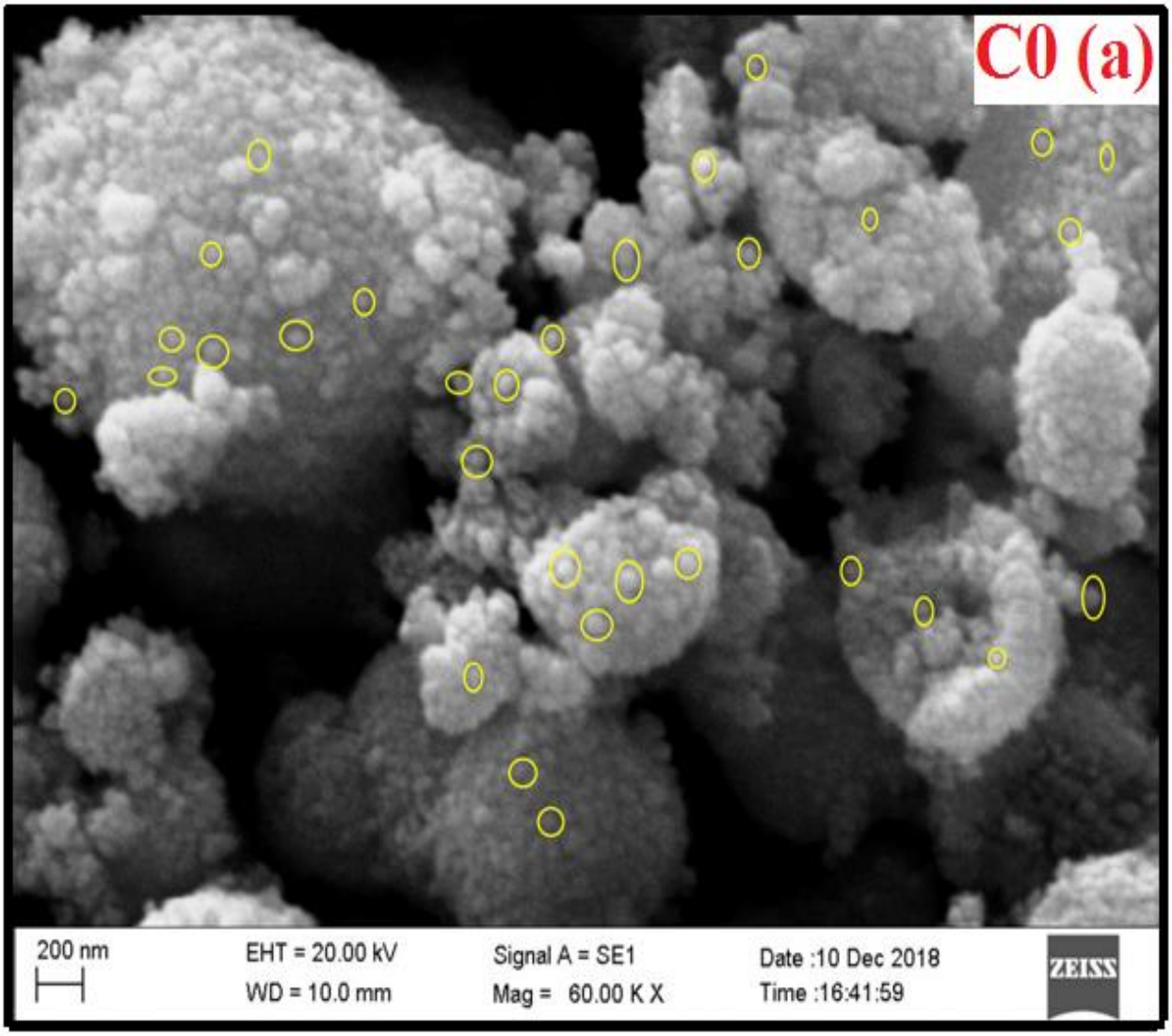
C0 (a)
200 nm
EHT = 20.00 kV
WD = 10.0 mm
Signal A = SE1
Mag = 60.00 K X
Date :10 Dec 2018
Time :16:41:59
ZEISS

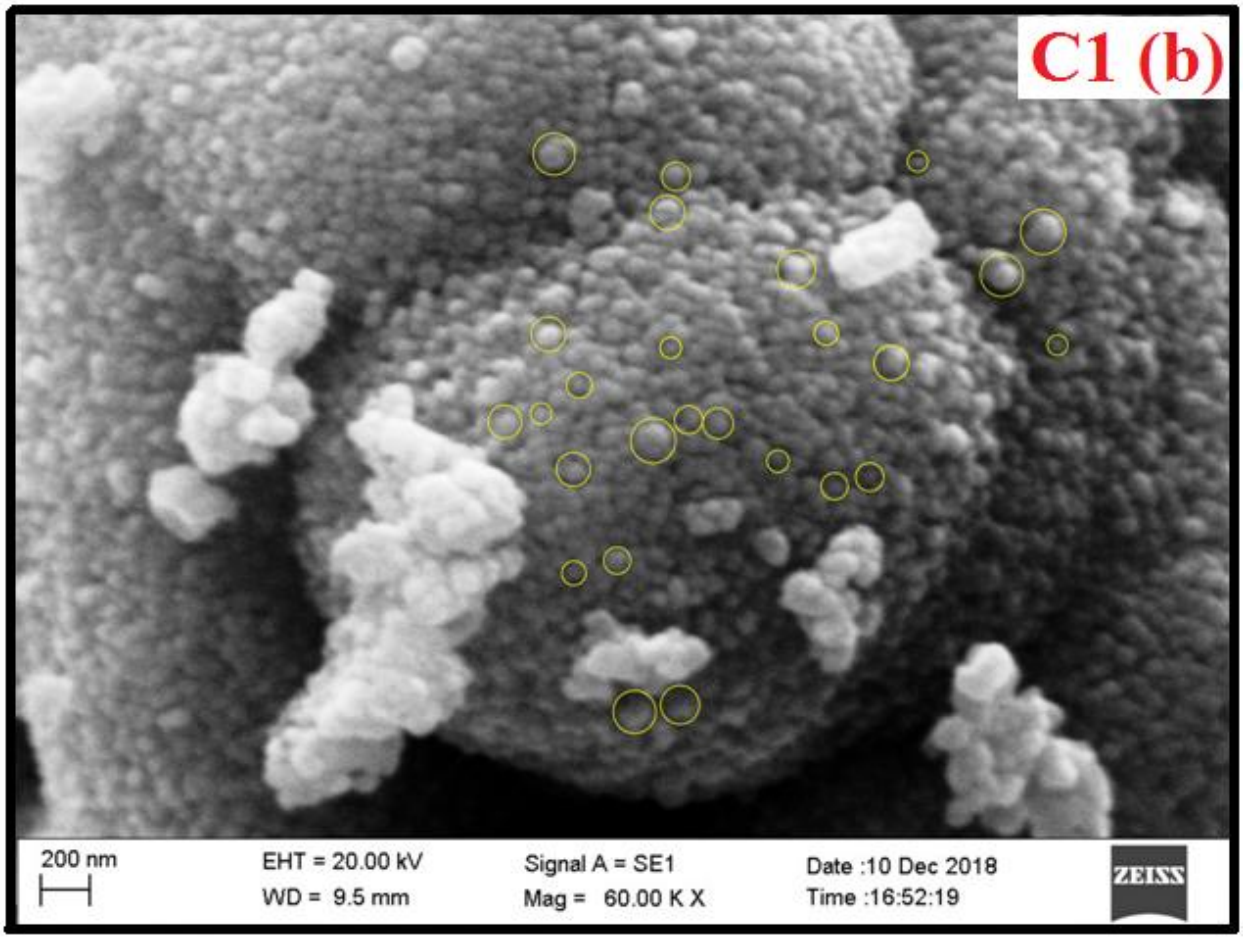
C1 (b)
200 nm
EHT = 20.00 kV
WD = 9.5 mm
Signal A = SE1
Mag = 60.00 K X
Date :10 Dec 2018
Time :16:52:19
ZEISS

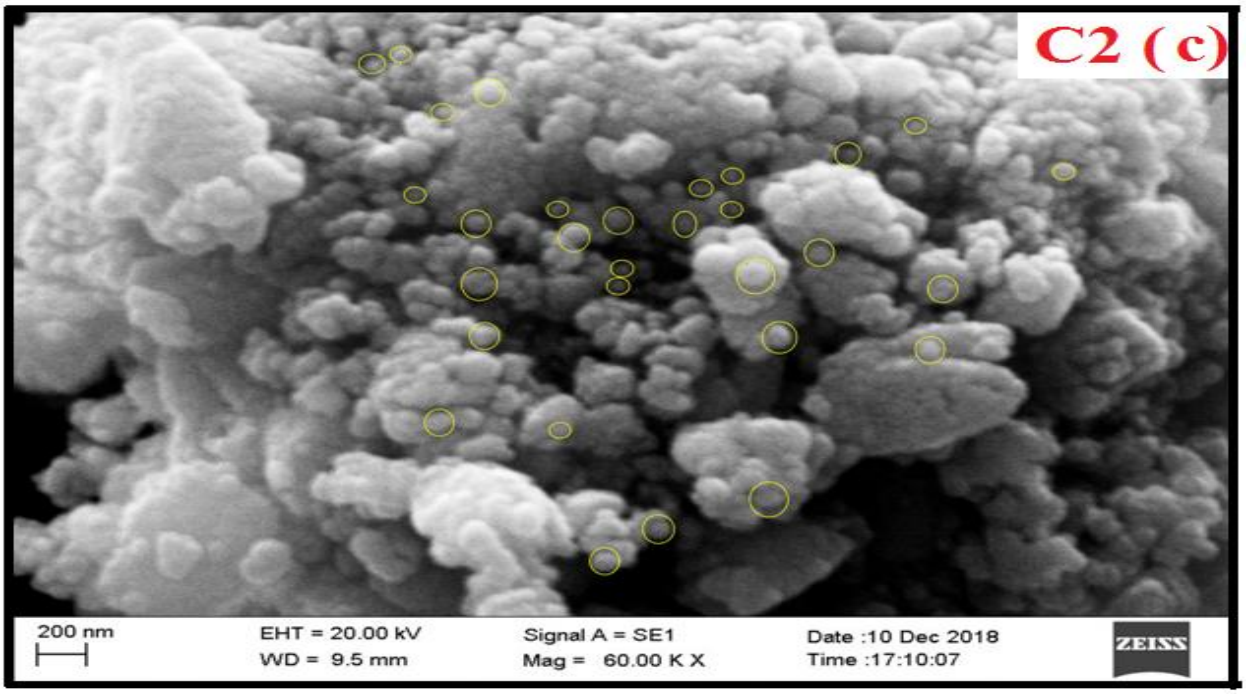
C2 (c)
200 nm
EHT = 20.00 kV
WD = 9.5 mm
Signal A = SE1
Mag = 60.00 K X
Date :10 Dec 2018
Time :17:10:07
ZEISS

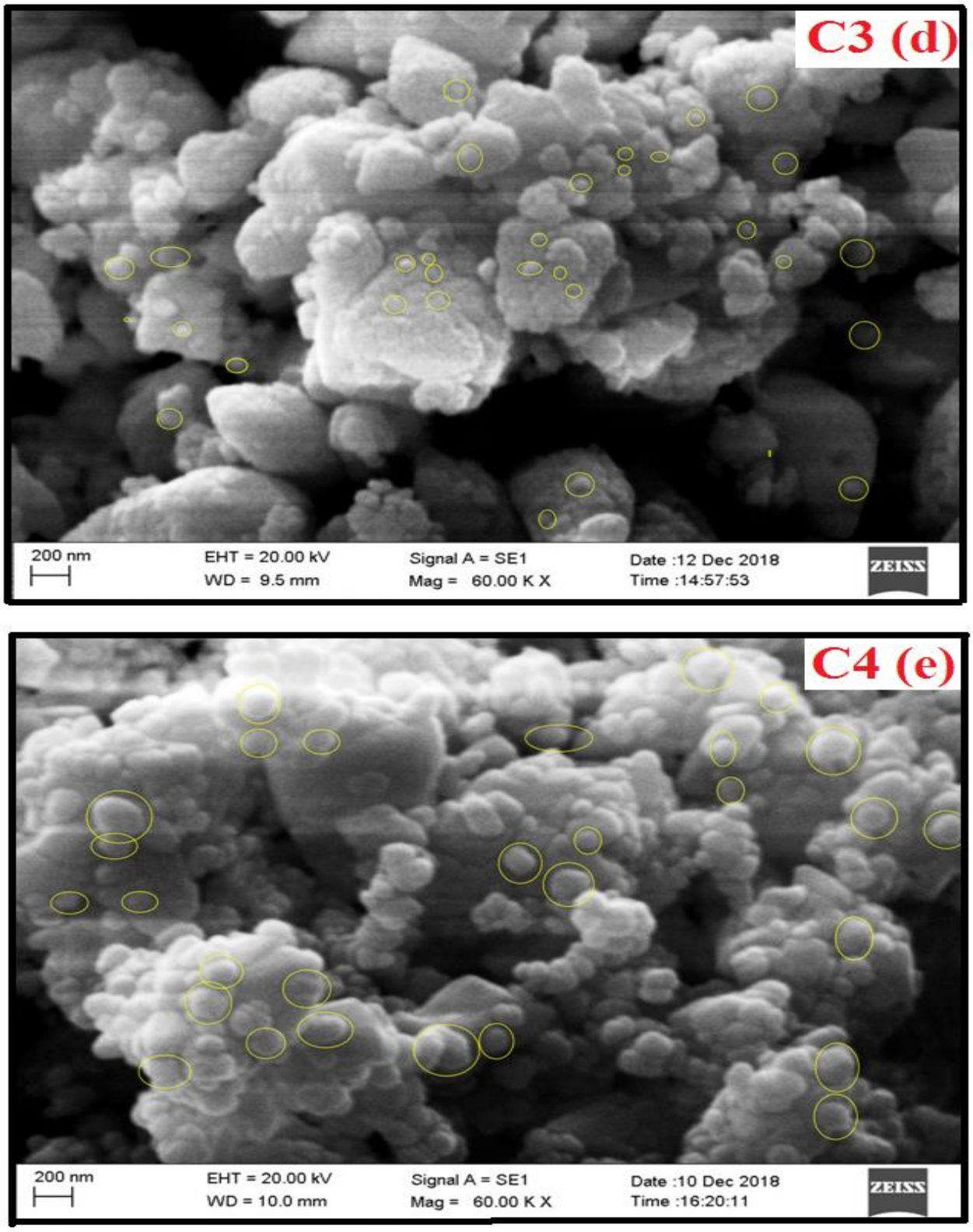

Figure 3.5(a-e): SEM pictures of nanocomposites samples.

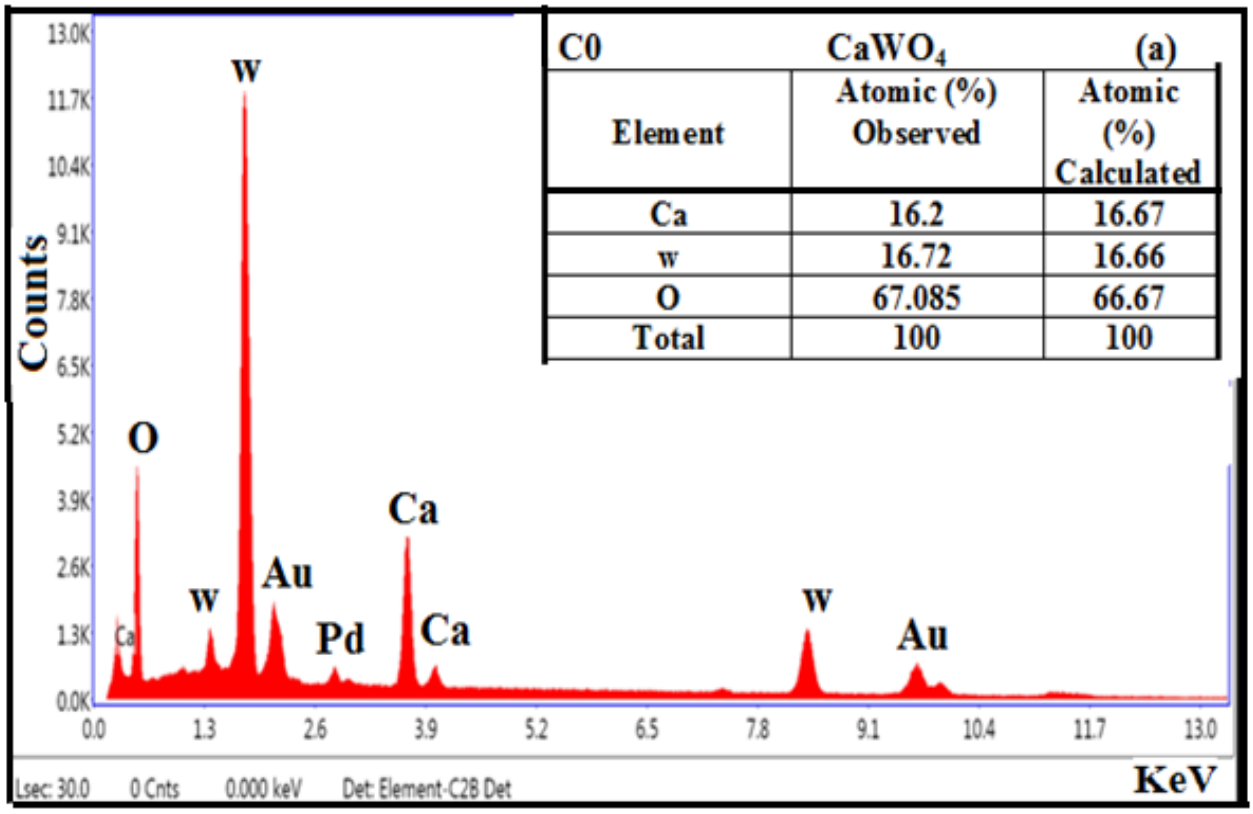

C0	$CaWO_4$	(a)
Element	Atomic (%) Observed	Atomic (%) Calculated
Ca	16.2	16.67
w	16.72	16.66
O	67.085	66.67
Total	100	100

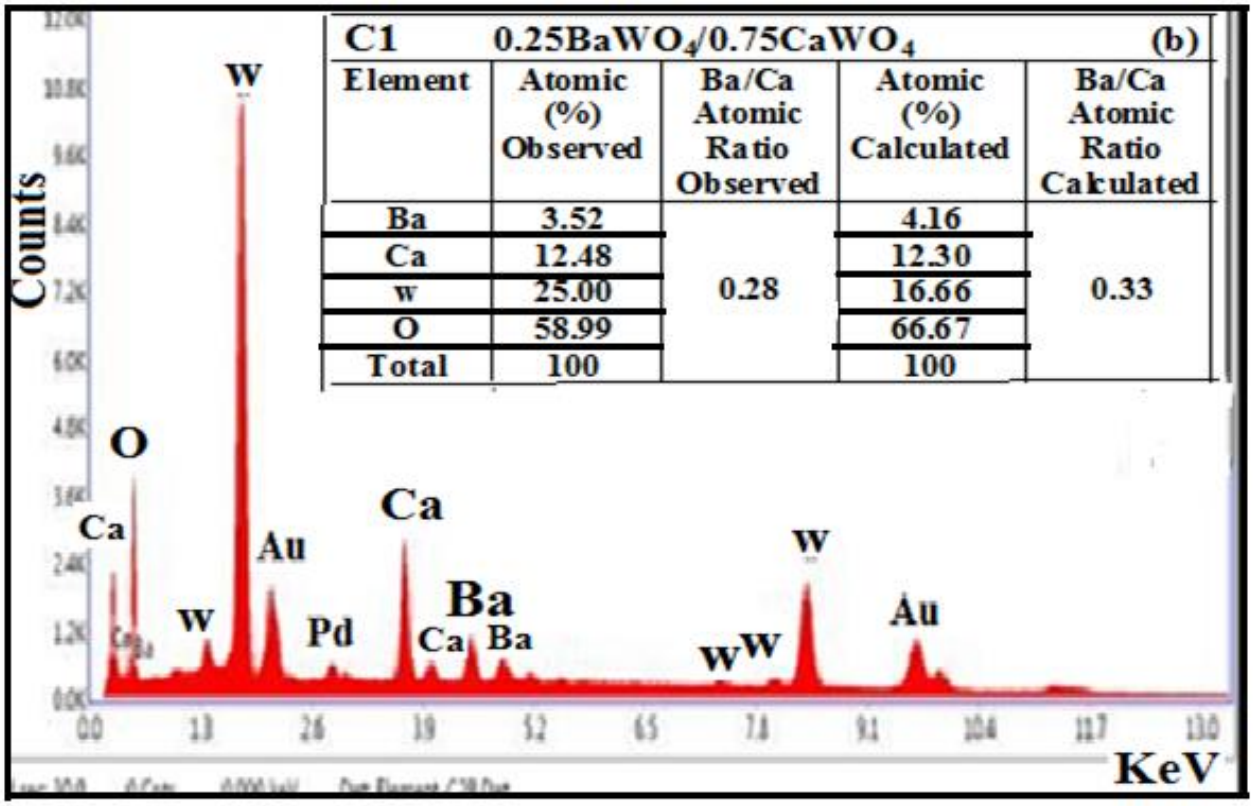

C1	$0.25BaWO_4/0.75CaWO_4$			(b)
Element	Atomic (%) Observed	Ba/Ca Atomic Ratio Observed	Atomic (%) Calculated	Ba/Ca Atomic Ratio Calculated
Ba	3.52	0.28	4.16	0.33
Ca	12.48		12.30	
w	25.00		16.66	
O	58.99		66.67	
Total	100		100	

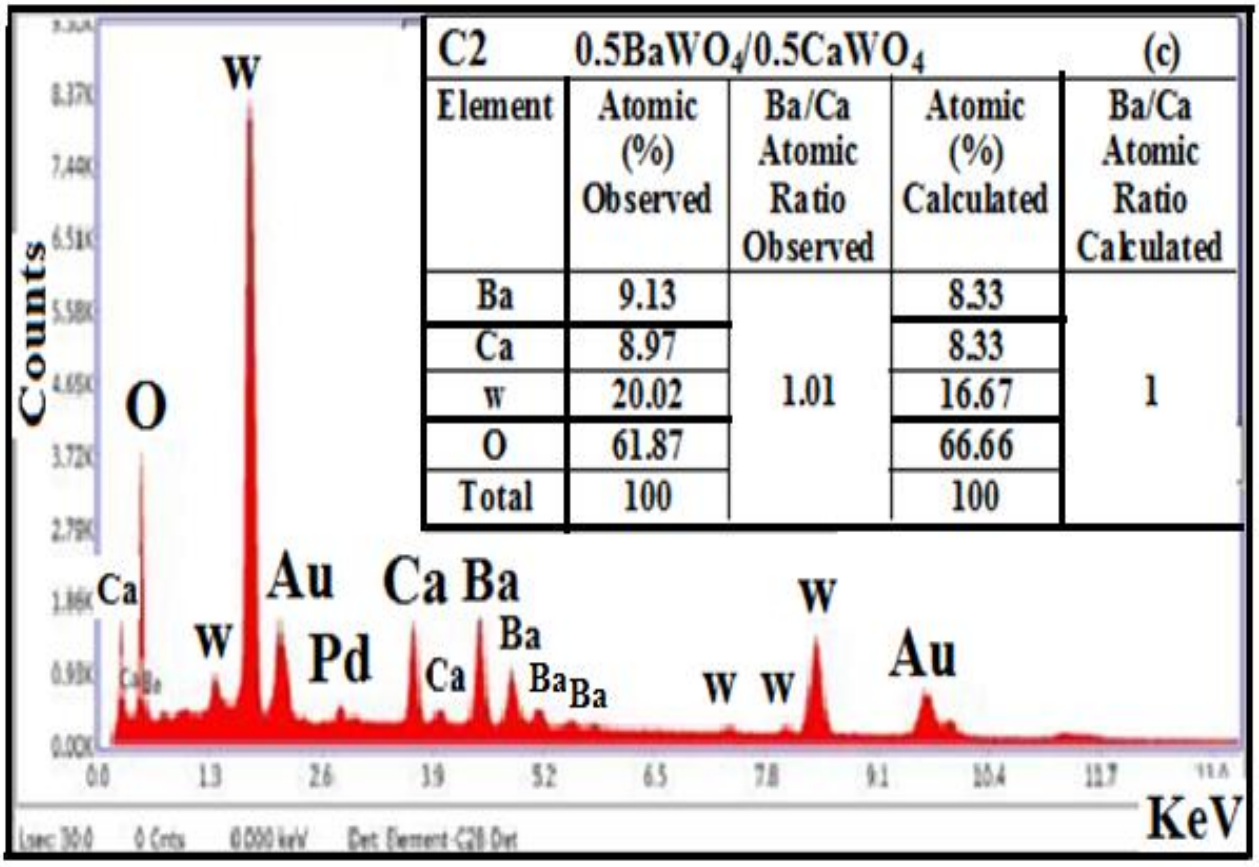

C2 $0.5BaWO_4/0.5CaWO_4$ (c)

Element	Atomic (%) Observed	Ba/Ca Atomic Ratio Observed	Atomic (%) Calculated	Ba/Ca Atomic Ratio Calculated
Ba	9.13	1.01	8.33	1
Ca	8.97		8.33	
W	20.02		16.67	
O	61.87		66.66	
Total	100		100	

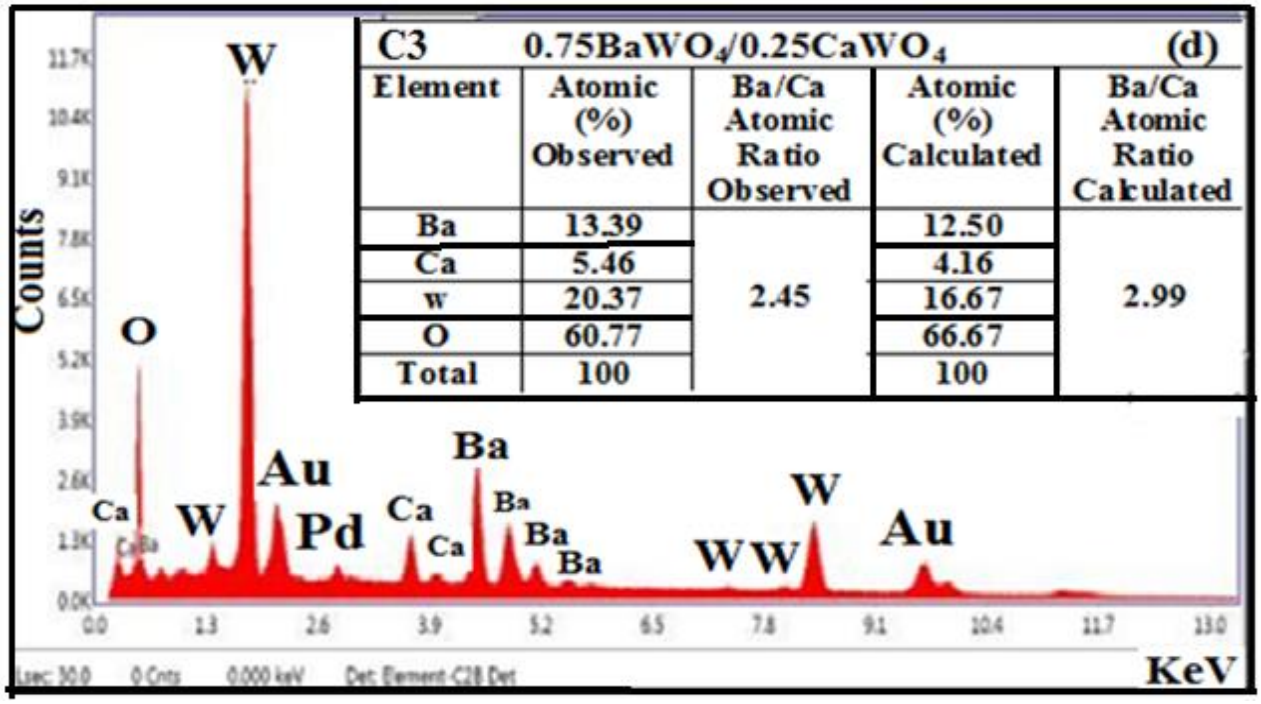

C3 $0.75BaWO_4/0.25CaWO_4$ (d)

Element	Atomic (%) Observed	Ba/Ca Atomic Ratio Observed	Atomic (%) Calculated	Ba/Ca Atomic Ratio Calculated
Ba	13.39	2.45	12.50	2.99
Ca	5.46		4.16	
W	20.37		16.67	
O	60.77		66.67	
Total	100		100	

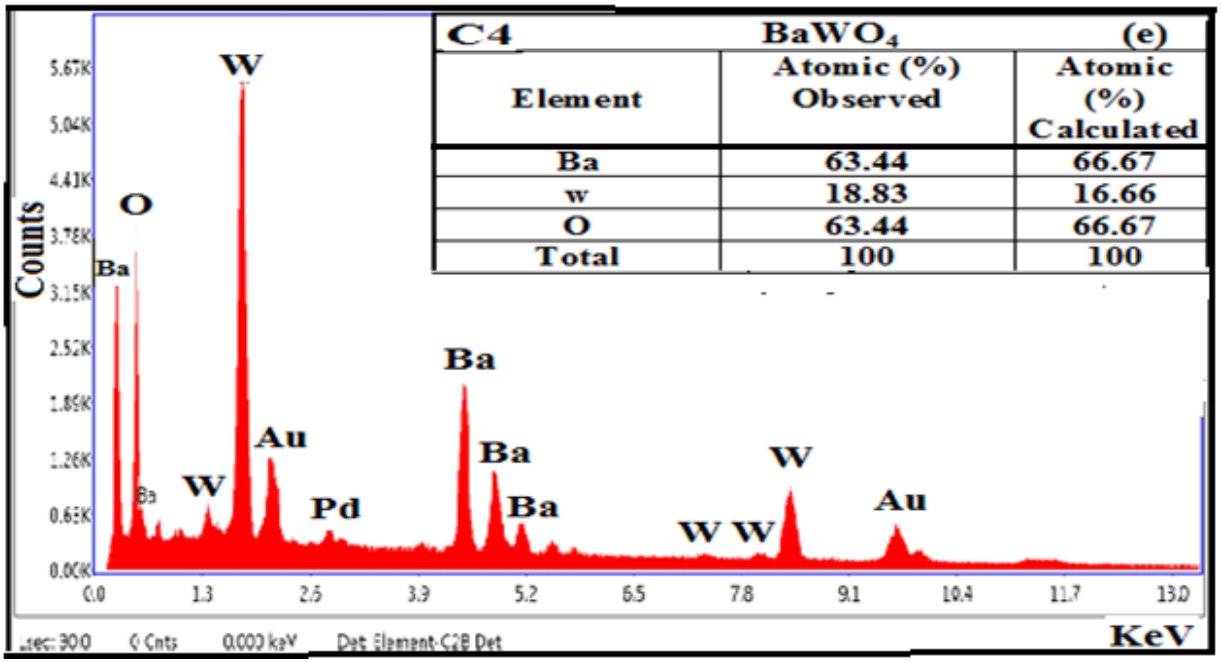

Figure 3.6(a-e): EDS spectra of nanocomposites.

3.6. High Resolution Transmission Electron Microscope (HRTEM)

Figure 3.7(a) shows HRTEM image of C2 ($0.5BaWO_4/0.5CaWO_4$) nanocomposites. Bigger and smaller particles are seen. Particle sizes are measured using Image J software. The distribution of particle size is given in **Figure 3.7(b)**.It is observed that maximum number of smaller particles have size between 20nm to 40nm and that of bigger particles from 50nm to 60nm**[7]**. It matches with the particle sizes calculated from XRD patterns as given in **Table 3.2.** HRTEM image of lattice planes & selected area diffraction (SAED) patterns are seen in **Figure 3.7(c-d**) showing nano-sized crystallites. Lattice planes shows that atomic planes are uniformly arranged in systematic array. The detected interplanar spaces correspond to (200), (112) planes for $CaWO_4$ and $BaWO_4$ respectively which matches calculated values of interplanar spaces (d) for C2($0.5BaWO_4/0.5CaWO_4$) nanocomposites and it is shown in **Table 3.4 (a-b)**.The selected area diffraction (SAED) pattern of C2($0.5BaWO_4/0.5CaWO_4$) nanocomposites appeared as concentric rings, due to the diffraction of electrons through the nano-sized particles. The interplanar (112) plane of $CaWO_4$ and (101) plane of $BaWO_4$were calculated from the diameters of the rings and, compared with those of the **JCPDS: 41-1431 & 43- 0646**, which confirmed its tetragonal crystal structure. This strongest intensities interplanar planes are well matching with those of the corresponding XRD spectra.

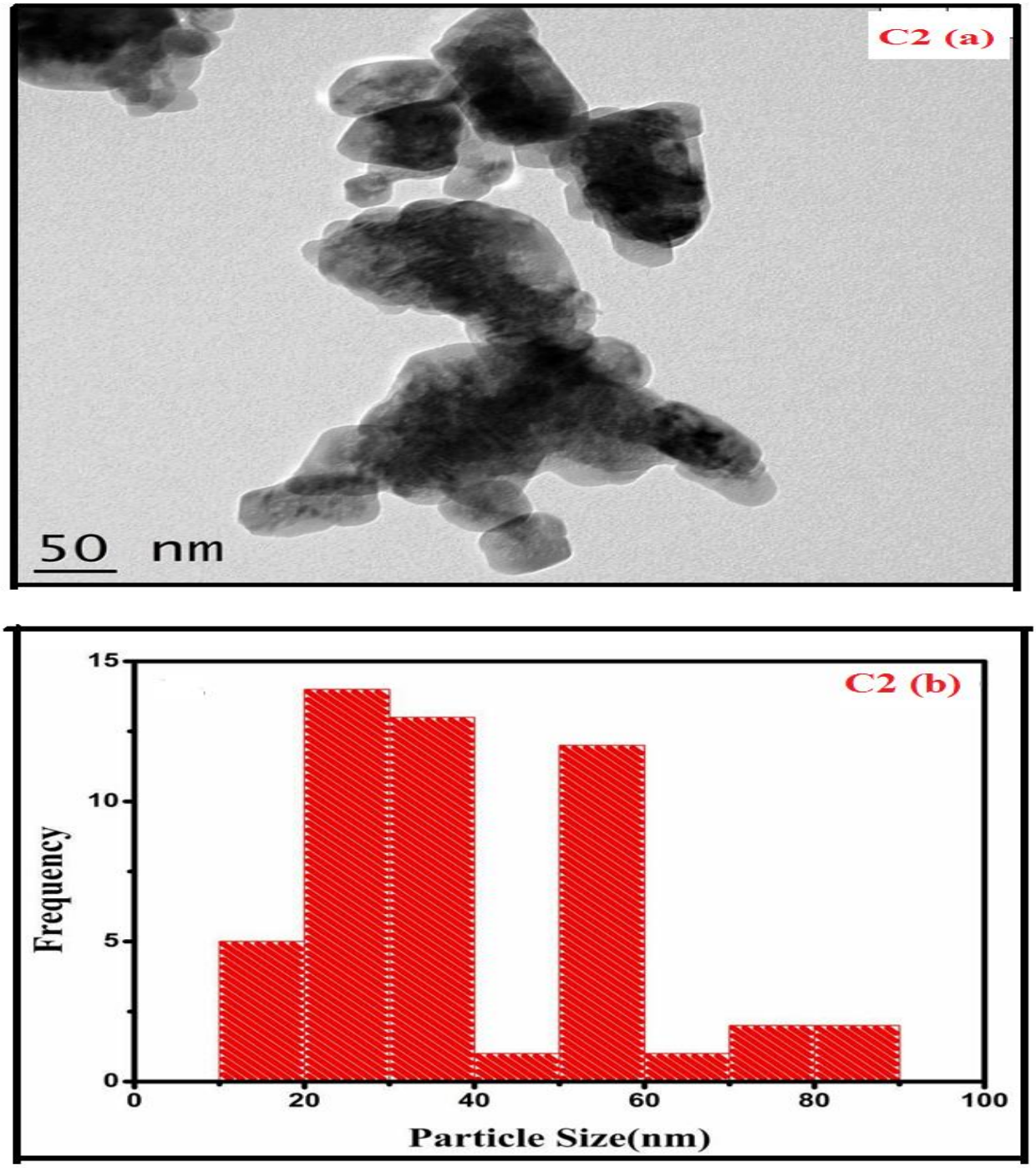

Figure 3.7(a-b): (a) HRTEM image & **(b)** particle size distributions of C2 ($0.5BaWO_4/0.5CaWO_4$) nanocomposites.

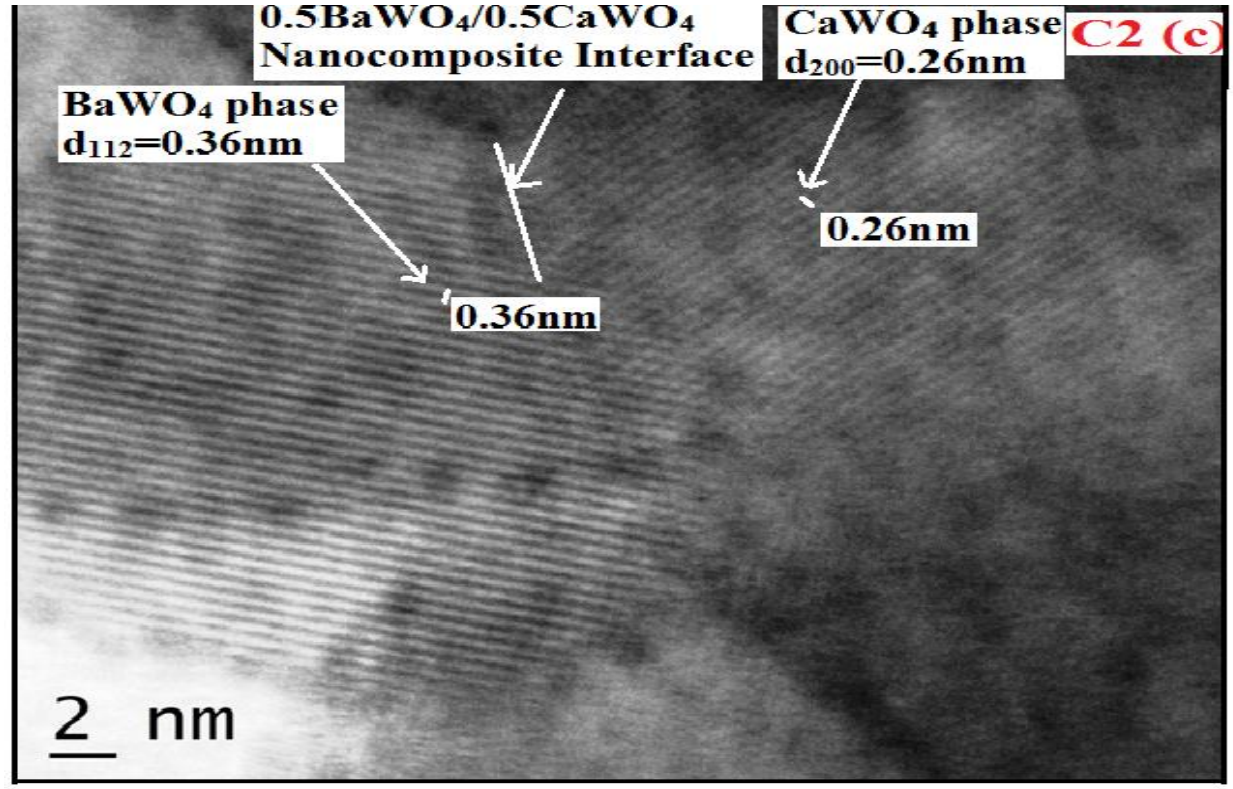

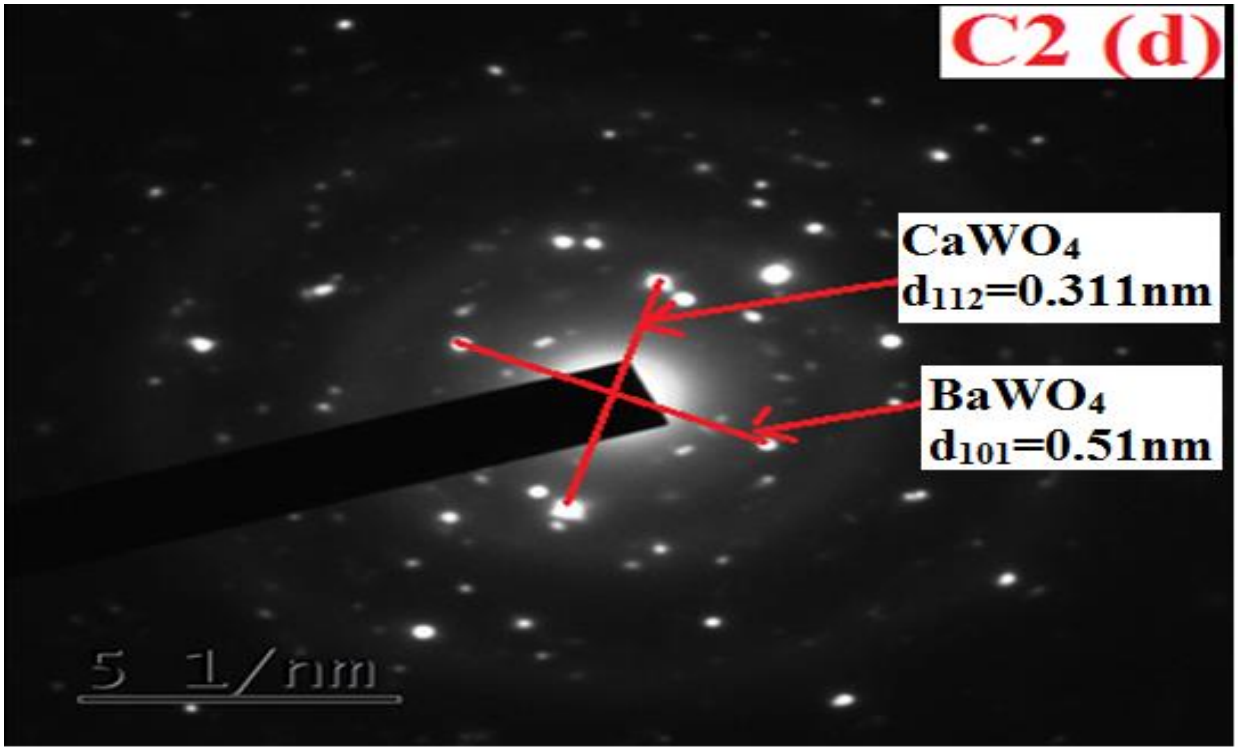

Figure 3.7(c-d): (c) HRTEM images of lattice planes & **(d)** SAED pattern of C2 ($0.5BaWO_4/0.5CaWO_4$) nanocomposites.

Table 3.4. (a): Interplanar distance (d) for $CaWO_4$ phase of C2 ($0.5BaWO_4/0.5CaWO_4$) nanocomposites.

2θ	Crystallographic plane	Interplanar distance d (nm) observed from XRD pattern	Interplanar distance d (nm) Literature [11]
18.57	101	0.47	0.47
28.69	112	0.311	0.310
28.08	004	0.31	0.28
34.12	200	0.26	0.26
39.12	211	0.23	0.22
47.04	204	0.19	0.19
57.83	312	0.15	0.15

Table 3.4. (b): Interplanar distance (d) for $BaWO_4$ phase of C2 ($0.5BaWO_4/0.5CaWO_4$) nanocomposites.

2θ	Crystallographic plane	Interplanar distance d (nm) observed from XRD pattern.	Interplanar distance d (nm)Literature [12]
17.26	101	0.51	0.51
26.47	112	0.33	0.33
31.89	004	0.28	0.31
36.50	202	0.24	0.25
45.73	213	0.19	0.21
48.75	116	0.18	0.18
53.64	312	0.17	0.17
54.50	215	0.16	0.17

3.7. Conclusions

For the first time $xBaWO_4/(1-x)CaWO_4$ nanocomposites were prepared by co-precipitation method and characterized. It is observed from (W-H equation) that $CaWO_4$ phase crystallite sizes lie between 18nm to 25nm and that of $BaWO_4$ phase crystallite sizes lie between 40nm to 50nm. XRD patterns of C0 ($CaWO_4$) and C4 ($BaWO_4$) single phases depict pure phase

tetragonal structure of $CaWO_4$ and $BaWO_4$ respectively and match with JCPDS: 41-1431 and JCPDS: 43-0646 respectively. All the nanocomposites show scheelite typed tetragonal phases of $CaWO_4$ and $BaWO_4$ in accordance with JCPDS: 41-1431 and JCPDS: 43-0646 respectively. It is seen that the principle peak (112) plane intensity of C2 ($0.5BaWO_4/0.5CaWO_4$) nanocomposites alone shifts towards higher angle (26.45^0 to 26.47^0) whereas that of C1 ($0.25BaWO_4/0.75CaWO_4$) and C3 ($0.75BaWO_4/0.25CaWO_4$) nanocomposites do not shift as compared to the C4 ($BaWO_4$) single phase. It is observed from distribution of particle size from HRTEM image that the maximum number of smaller particles have size of 20nm to 40nm and that of bigger particles from 50nm to 60nm. It matches with the particle sizes calculated from XRD patterns.HRTEM image of lattice planes & selected area diffraction (SAED) patterns are seen which shows nano-sized crystallites. The SEM pictures of $xBaWO_4$/ (1-x) $CaWO_4$ nanocomposites show smaller and bigger crystallites correspond to $CaWO_4$ & $BaWO_4$single phases respectively (crystallites sizes are calculated from XRD pattern). EDS spectral analysis confirms the presence of expected chemical elements and their atomic concentration. Characteristics vibrational bands of $BaWO_4$ and $CaWO_4$ were observed in the FTIR spectra of the samples. These initial characterizations show that the samples are prepared successfully.

References

[1] F. Sun, X. Qiao, F. Tan, W. Wang, and X. Qiu, One-step microwave synthesis of Ag/ZnO nanocomposites with enhanced photocatalytic performance, J. Mater. Sci.,**47**:7262-7268 **(2012)**.

[2] Q. Zhang, Q. Meng, and W. Sun**,** The concentration dependence of luminescent properties for Eu^{3+} doped $CaWO_4$ micron spherical phosphors**,**Opt. Mater. (Amst),**35**:915-922**(2013)**.

[3]M. Feng, D. An, H. Zhang, G. Ma, C. Zhang, and Z. Ma, Facile synthesis of cobalt/nickel tungstate and its application in hybrid supercapacitor,Int. J. Chem. Stud.,**5**:1954-1960 **(2017)**.

[4]V.B.Kumar and D.Mohanta, Formation of nanoscale tungsten oxide structures and colouration characteristics Bull. Mater. Sci., **34**:435-442 **(2011)**.

[5] F.Ahmadi, M. Rahimi-Nasrabadi, A. Fosooni, and M. Daneshmand, Synthesis and application of $CoWO_4$ nanoparticles for degradation of methyl orange, Journal Material Science: Materials in Electronics, **27**:9514-9519 **(2016)**.

[6]Titipun Thongtem, Anukorn Phuruangrat and Somchai Thongtem, Synthesis of $CaWO_4$, $SrWO_4$ and $BaWO_4$ with nanosized particles using cyclic microwave radiation, Journal of Ceramic Processing Research, **9**(3):258-261 **(2008)**.

[7] T. Thongtem, A. Phuruangrat, S. Thongtem, Characterization of $MeWO_4$ (Me = Ba, Sr and Ca) nanocrystallines prepared by sonochemical method, Appl. Surf. Sci., **254**:7581–7585 **(2008)**.

[8]Nidhi Khobragade, ElaSinha, S.K.Rout, ManoranjanKar, Structural, optical and microwave dielectric properties of $Sr_{1-x}Ca_xWO_4$ ceramics prepared by the solid state reaction route,Ceramics International,**39**:9627-9635 **(2013)**.

[9]C.Shivakumara , Rohit Saraf , Sukanti Behera , N. Dhananjaya , H. Nagabhushana, Scheelite-type MWO_4 (M = Ca, Sr and Ba) nanophosphors: Facile synthesis,structural characterization, photoluminescence and photocatalytic properties,Mater. Res.Bull., **61**: 422–432 **(2015).**

[10]R.Lacomba-Perales, J. Ruiz-Fuertes, D. Errandonea, D. Martinez-Garcia and A. Segura, Optical absorption of divalent metal tungstates: Correlation between the band-gap energy and the cation ionic radius,EPL (Europhysics Letters), **83**(3):37002 **(2008)**.

[11]W.Wang, W. Pan, Y. Dai, S. Gai, P. Yang, Uniform $CaWO_4$:Ln(Ln=Eu^{3+}, Dy^{3+}) phosphors: solvothermal synthesis and luminescent properties, Optoelectr. Adv. Mater., **4**(8):1078–1082 **(2010)**.

[12] L.S. Cavalcantea, J.C. Sczancoski, J.W.M. Espinosaa, J.A. Varela, P.S. Pizani, E. Longo, Photoluminescent behavior of $BaWO_4$ powders processed in microwave-hydrothermal, Journal of Alloys Compounds, **474**:195–200 **(2009)**.

[13] V.D. Mote, Y. Purushotham, B.N. Dole, Williamson-Hall analysis in estimation of lattice strain in nanometer-sized ZnO particles, Journal of Theoretical Applied Physics, **6**(6):1–8 **(2012)**.

[14]J.T.Kloprogge, M.L.Weier, L.V. Duong, R.L. Frost, Microwave assisted synthesis of divalent metal tungstate Minerals: Feberite, Hubnerite, Sanmartinite, Scheelite and Stolzite, Mater. Chem. Phys., **88**:438–443 **(2004)**.

[15]G.M.Clark, W.P.Doyle, Infra-red spectra of anhydrous molybdates and tungstates, Spectrochim,Acta.**22**:1441–1447 **(1966)**.

[16] G. Zhang, R. Jia, Q. Wu, Preparation, Structural & Optical properties of AWO_4 (A= Ca, Ba, Sr) nanofilms, Mater. Sci. Eng. B, **128**:254–259 **(2006)**.

[17] F.A. Miller, C.H. Wilkins, Infrared spectra & characteristic frequencies of inorganic ions, Anal. Chem., **24**:1253–1294**(1952)**.

CHAPTER 4

OPTICAL ABSORPTION AND ENHANCED PHOTOLUMINESCENCE OF $CaWO_4$ IN $xBaWO_4/ (1-x) CaWO_4$ NANOCOMPOSITES

4.1. Introduction

Enhancing the photoluminescence (PL) intensity is a challenging task for researchers. There are many ways to improve the photoluminescence (PL) intensity. In the last few decades nanocomposites have been studied extensively for enhancing the unique properties of metal oxide semiconductors. Fabricating nanocomposites with interface is one of the best methods to improve the photoluminescence (PL) intensity **[1]**. Metal tungstates are important inorganic ternary oxides and self-activated luminescent materials.Metal tungstates nanocomposites are reported extensively to photo-catalytic and electrochemical applications **[2-5]**. There are only few reports available for enhanced photoluminescence (PL) intensity of tungstates nanocomposites. For example, Yuri V. B. De Santana et al. reported the enhancement of the photoluminescence (PL) intensity in Silver tungstate and Silver molybdate nanocomposites **[6]**. Jian Ming Lin et al. reported the enhanced photoluminescence (PL) emission of ZnO nanorods in SnO/ZnO nanocomposites **[7]**.The enhanced photo-catalytic and photoluminescence (PL) emission of ZnO-$ZnWO_4$ nanocomposites has been reported **[3]**.Guo et al. reported that $CaWO_4$/ Bi_2WO_6 has enhanced photo-catalytic property **[8]**.Cavalcante et al. reported that $BaWO_4$/$PrWO_4$ enhanced the photoluminescence (PL) and photo-catalytic activity of $BaWO_4$ **[9]**. Eghbali-Arani et al. reported photo-catalytic performance of $BaWO_4$/$CdMoO_4$ nanocomposites studied under visible light **[10]**. However, in $CaWO_4$/CdSe nanocomposite photoluminescence (PL) quenching and shortened photoluminescence (PL) life-time was observed for the $CaWO_4$ phase.This is because in $CaWO_4$ /CdSe nanocomposite $CaWO_4$ is transferring charge to CdSe phase reported **[11]**. Instead of using single phase material coupling with other semiconductor has also been found to be an effective means to enhance the luminescence properties of oxide nanomaterials **[12, 13]**. $BaWO_4$ is a scheelite structured wide band semiconductor. Photoluminescence (PL) properties of $BaWO_4$ have been widely studied **[14-16]**.

In this chapter we have presented the results and discussion of optical absorption, photoluminescence (PL) and photoluminescence (PL) lifetime. Band gap energy, photoluminescence (PL) intensity and photoluminescence (PL) lifetime are controlled by the Ba/Ca atomic concentration ratio. The highest 420 nm photoluminescence (PL) emission from C2

($0.5BaWO_4/0.5CaWO_4$) nanocomposites could be due to the exciton charge transfer of $BaWO_4$ phase to $CaWO_4$ phase because of type I band alignment interface occurring between them. Due to the availability of additional excitons in the $CaWO_4$ phase more recombination processes can occur leading to enhancement of emissions from the $[WO_4]^{2-}$ anions of $CaWO_4$ phase. The intrinsic blue emission of $CaWO_4$ at 420nm was found to be maximum in C2 ($0.5BaWO_4/0.5CaWO_4$) nanocomposites for the optimized value of (**'x')** and unsintering temperature. The lifetime of this emission was also enhanced for the same nanocomposites. The mechanism for the enhanced photoluminescence (PL) emission intensity and life time is also discussed elaborately. Mixed $Ba_xCa_{1-x}WO_4$ nanopowder samples did not give enhanced 420 nm emission in comparison with $CaWO_4$ emission which is observed in photoluminescence (PL) peak intensity (420nm) versus % Ba concentration which is shown in **Figure 4.10 (a–c)**.

4.2. Results and discussion

4.2.1. Optical absorption study

Diffuse reflectance spectra of the samples were measured and converted to the absorption spectra by using Kubelka–Munk equation (K-M equation) **[17]**. Reflectance spectra of $xBaWO_4/(1-x)CaWO_4$ nanocomposites are shown in **Figure 4.1(a)**. Transfer of UV excited electrons from oxygen(O) 2p-states to tungsten(W) 5d-states of $[WO_4]^{2-}$ anion gives rise to the observed broad reflectance spectra from 200nm to 330nm and the hole (on the oxygen) and the electron (on the tungsten) due to their strong interactions form an exciton **[18]**. The reflectance spectra peak wavelength shifts from 248nm to 220nm and also the reflectance peak intensity gradually decreases as the % Ba concentration increases. Minimum reflectance peak intensity (maximum absorption) is for $BaWO_4$ sample and maximum reflectance (minimum absorption) peak intensity is for $CaWO_4$ sample. This is because the molecular photon- absorption cross section of $BaWO_4$ is larger than that of $CaWO_4$ **[19]**.

The optical band gap energy (E_g) was calculated by the method proposed by Kubelka and Munk **[20]**.This methodology is based on the transformation of diffuse reflectance measurements to estimate the E_g values with good accuracy **[21]**. Particularly, it can be well-employed in limited cases of infinitely thick sample layer. The Kubelka–Munk equation for any wavelength is described as**:**

$$\mathbf{F\,(R_\infty) = \frac{(1-R\infty)^2}{2R\infty} = \frac{k}{s}} \qquad \mathbf{(4.1)}$$

Where F (R_∞) is the Kubelka–Munk (K-M) functions or absolute reflectance of the sample. In our case, the Barium sulphate ($BaSO_4$) was the standard sample in the reflectance measurements. $R_\infty = R_{Sample}/R_{BaSO4}$ (R_∞ is the reflectance when the sample is infinitely thick), (k) is the molar absorption coefficient, and (s) is the scattering coefficient.

In a parabolic band structure, the optical band gap and absorption coefficient of semiconductor oxides **[22]** can be calculated by the following **equation (4.2):**

$$\mathbf{Ahv=A\ (hv-E_g)^n} \qquad \mathbf{(4.2)}$$

Where (h*)* is the Planck's constant, (A) is the constant; (α) is the absorption coefficient, (E_g) is the band gap energy and (ν) is the frequency of the incidence photon. The coefficient (n*)* can beassigned the values 0.5 and 2 for allowed direct and indirect transitions respectively. According to the literature, the tungstates (AWO_4; A = Ca, Sr, Ba) exhibit an optical absorption spectrum governed by direct electronic transitions **[23]**.In this phenomenon, after electronic absorption process, the electrons located in the maximum-energy states in the valence band fall back to the minimum-energy states in the conduction band of the same point in the Brillouin zone **[24]**. E_g of $BaWO_4$ and $CaWO_4$ were calculated using n= 0.5 in **equation (4.2)** and with the term k=2α and A_1 is a proportionality constant, we obtained modified Kubelka-Munk (K-M) equation indicated in **equation (4.3)**.

$$\mathbf{[F\ (R_\infty)\ hν]^2 = A_1\ (hν-E_g)} \qquad \mathbf{(4.3)}$$

Therefore, finding the F (R_∞) values from equation (3) and plotting a graph of $[F\ (R_\infty)\ hν]^2$ against hv, it was possible to determine the E_g of $CaWO_4$ and $BaWO_4$.Kubelka-Munk (K-M) plots **Figure 4.1(b)** were used to calculate band gap energies Eg of the samplesand aretabulated in **Table 4.1**.Calculated E_g values for $CaWO_4$ and $BaWO_4$ nanosamples match with literature values **[23]**.Variation in band gap energy versus % Ba concentration of the samples is plotted **Figure 4.1(c)**.E_g is enhanced with increase in % Ba concentration. This is because E_g of $BaWO_4$ is higher than that of $CaWO_4$ phase. Due to the larger radius of Ba^{2+} ion (1.42Å) as compared to that of Ca^{2+} ion (1.12Å) **[23]**.The energy of Ca 3p-states in $CaWO_4$ is lower than that of Ba 5p-states in $BaWO_4$. Hybridization between Ca 3p-states and O 2p-states will be there in $CaWO_4$ lowering its band gap. Whereas hybridization between Ba 5p-states and O 2p-states will not be there in $BaWO_4$ making its bandgap higher **[25]**.

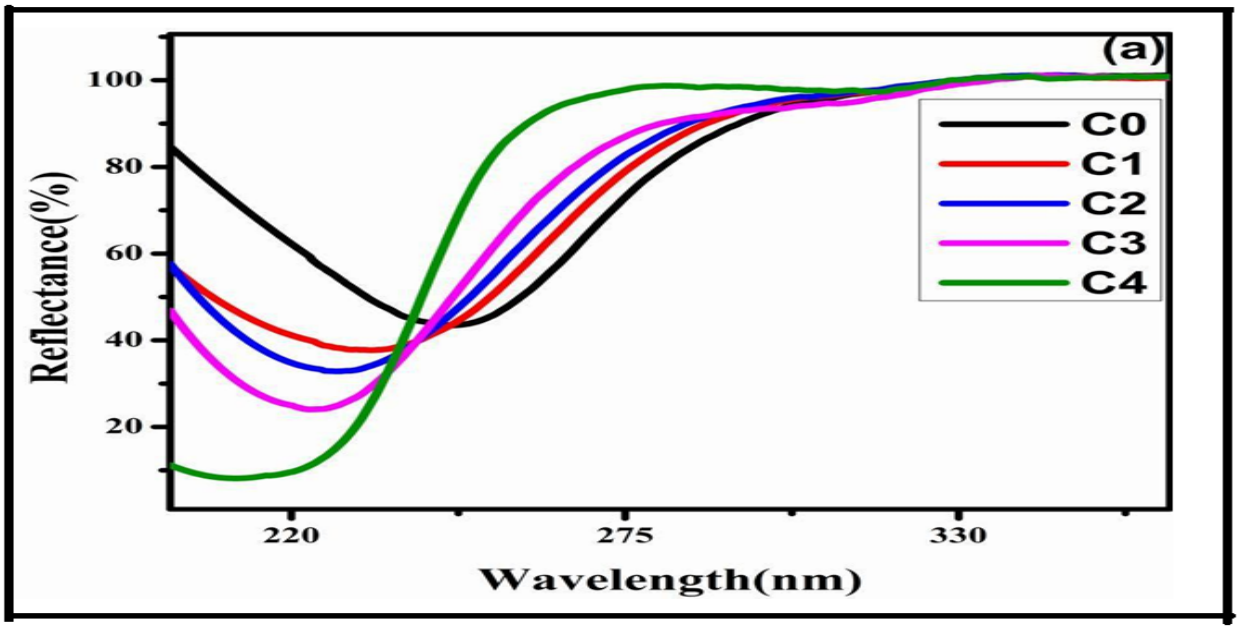
(a)
Reflectance(%)
100
80
60
40
20
220
275
330
Wavelength(nm)
C0
C1
C2
C3
C4

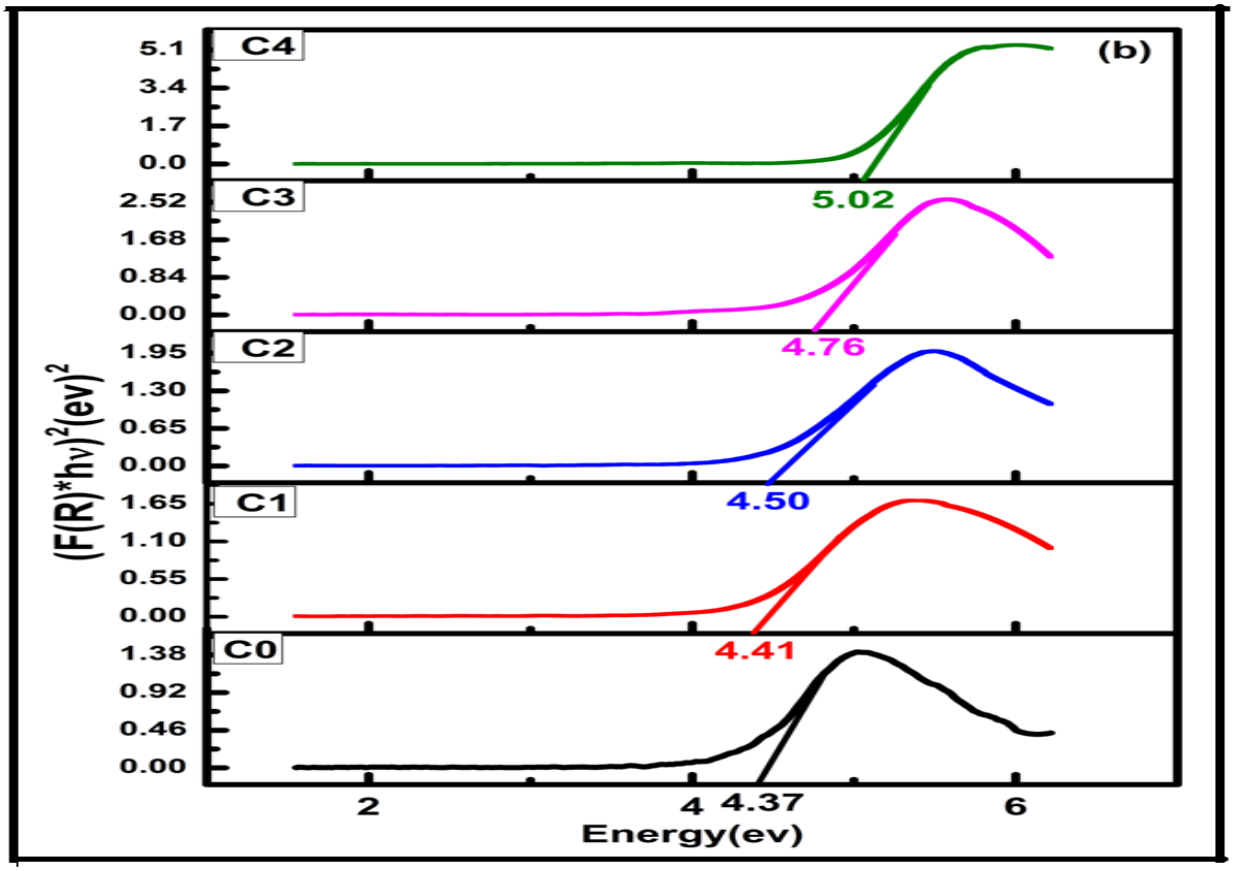
(b)
C4
C3
C2
C1
C0
5.02
4.76
4.50
4.41
4.37
(F(R)*hν)²(ev)²
Energy(ev)
2
4
6

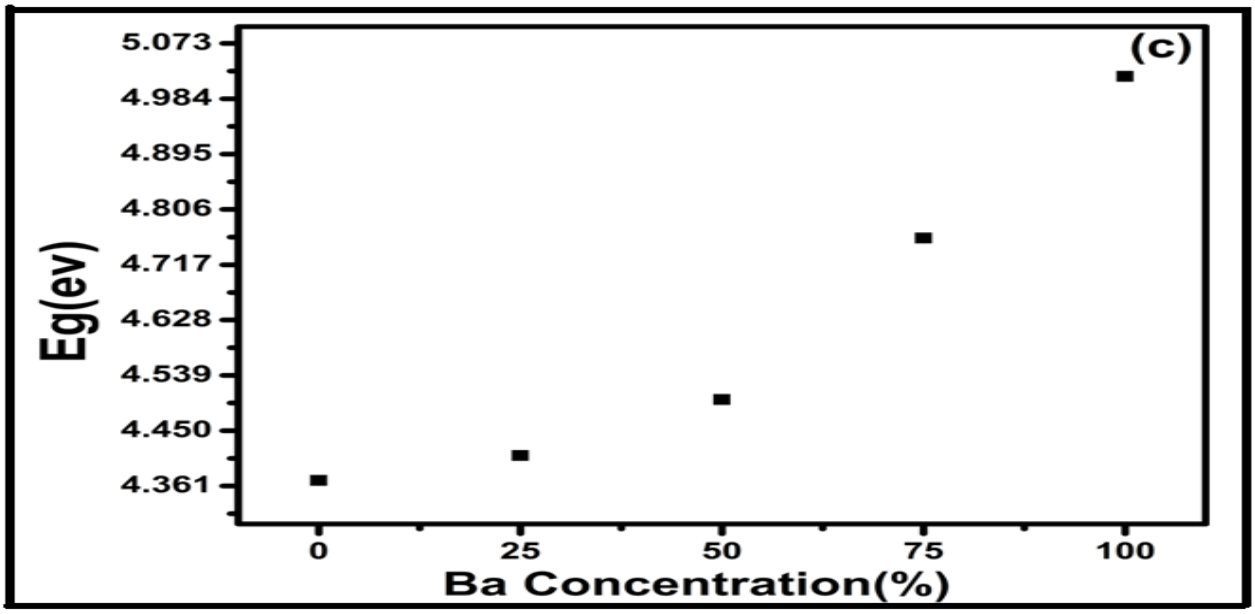

Figure 4.1(a-c): (a) DRS spectra of nanocomposites samples. **(b)** K-M plots of nanocomposites samples. **(c)** Eg versus % Ba concentration of nanocomposites samples.

Table 4.1: Bandgap energy of $xBaWO_4/ (1-x) CaWO_4$ nanocomposites.

Samples	K-M Bandgap energy Eg(eV)	Literature value Eg(eV)
C0	4.37±0.00153	4.94 **[23]**
C1	4.41±0.00156	-----
C2	4.50±0.00163	-----
C3	4.76±0.00182	-----
C4	5.02±0.00203	5.26 **[23]**

4.2.2. Photoluminescence (PL) study

4.2.2.1. PL spectral analyses

Excitation spectra measured for 420 nm emissionsof sintered (400^0C & 200^0C) and unsintered samplesare shown in **Figure 4.2(a-c)**. All the samples except $BaWO_4$ (C4) exhibit broad peaks centered around 260 nm because of transfer of UV excited electrons from oxygen O 2p-states to tungsten W 5d- states of $[WO_4]^{2-}$anion. **Figure 4.2 (d-f)** shows emission spectra for 260nm excitation for sintered (400^0C & 200^0C) and unsintered samples recorded from 280nm to 650nm. Intrinsic luminescence of $CaWO_4$ is due to the annihilation of self-trapped excitons

forming excited $[WO_4]^{2-}$ anions giving rise to the broad emission spectra peaking around 420nm. $xBaWO_4/ (1-x) CaWO_4$ nanocomposites altered the photoluminescence (PL) emission intensities of $CaWO_4$ but not the structure of the spectra. For 400 °C and 200 °C sintered samples $CaWO_4$ exhibit maximum photoluminescence (PL) intensity **Figure 4.2(d–e)**. For unsintered samples in **Figure 4.2(f)** emission intensity 420 nm is maximum for C2 ($0.5BaWO_4/0.5CaWO_4$) nanocomposites and is higher than the unsintered C0 ($CaWO_4$) single phase respectively. **Figure 4.2(g)** shows emission spectra for 260nm excitation of sintered and unsintered $CaWO_4$ samples along with emission of C2 ($0.5BaWO_4/0.5CaWO_4$)unsintered nanocomposites respectively.It is found that C2 ($0.5BaWO_4/0.5CaWO_4$) nanocomposites emission intensity is maximum. Log PL peak (420nm) intensity versus sintering temperature for $CaWO_4$ nanosamples is plotted in **Figure 4.3(a)**. PL peak (420nm) intensity for unsintered $CaWO_4$ sample is little more than sintered $CaWO_4$ nanosamples. **Figure 4.3 (b)** shows the plot of photoluminescence (PL) peak (420nm) intensity versus % Ba concentration of unsintered nanocomposites samples.Maximum photoluminescence (PL) peak (420nm) intensity is emitted by C2($0.5BaWO_4/0.5CaWO_4$) unsintered nanocomposites. Photoluminescence (PL) peak (420nm) intensity of $CaWO_4$ sample is much higher than that of $BaWO_4$ sample. This is because the radius of Ba^{2+} ions ($1.42A^0$) surrounding the tungstates ions is higher than that of Ca^{2+} ions ($1.12A^0$) and when $BaWO_4$ is excited with ultraviolet (UV) energy Ba^{2+} ions cannot counteract the expansion of $[WO_4]^{2-}$ anions. Then the offset between the excited state parabola and ground state parabola in the configuration coordinates system becomes large resulting in increase in non-radiative transitions, broader optical absorption and emission bands **[26]**.Whereas when $CaWO_4$ is ultraviolet (UV) excited Ca^{2+} ions can counteract the expansion of $[WO_4]^{2-}$ anions resulting in less non-radiative transitions. Therefore it is seen that among all the samples (sintered and unsintered), C2 ($0.5BaWO_4/0.5CaWO_4$) unsintered nanocomposites gives maximum 420nm intrinsic emission of $CaWO_4$. In tungstates with Scheelite structure the excited $[WO_4]^{2-}$ ions get relaxed by intrinsic emission due to recombination of self-trapped exciton (STE) **[27]**.**Figure 4.3 (c)** shows the log plot of photoluminescence **(**PL) peak (420nm) intensity versus % Ba concentration of unsintered Mixed $Ba_xCa_{1-x}WO_4$ nanopowder & nanocomposites samples. In unsintered Mixed $Ba_xCa_{1-x}WO_4$ nanopowder samples maximum photoluminescence (PL) peak (420nm) intensity is emitted by $CaWO_4$ sample,whereas incase of nanocomposites maximum photoluminescence (PL) peak (420nm) intensity is emitted by C2 ($0.5BaWO_4/0.5CaWO_4$) unsintered nanocomposites.

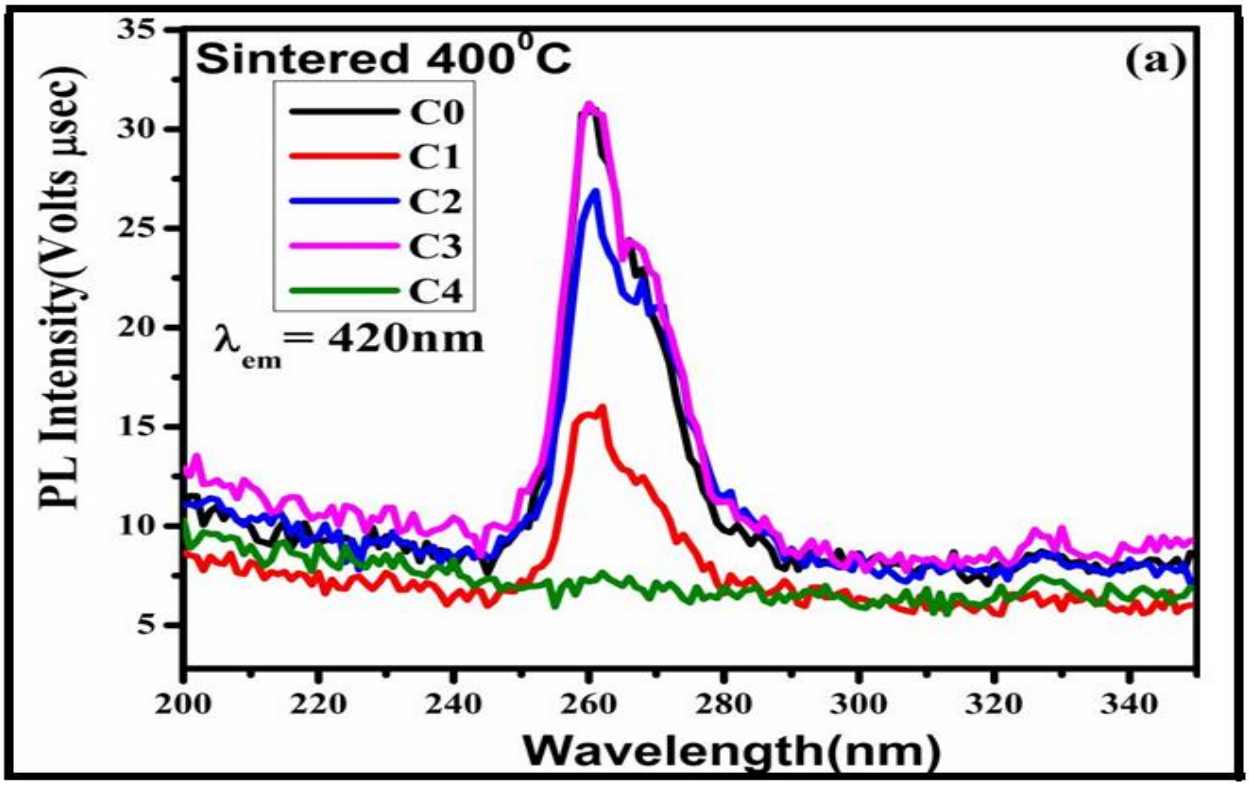
Sintered 400°C
(a)
C0
C1
C2
C3
C4
λem = 420nm
PL Intensity(Volts µsec)
Wavelength(nm)
35
30
25
20
15
10
5
200
220
240
260
280
300
320
340

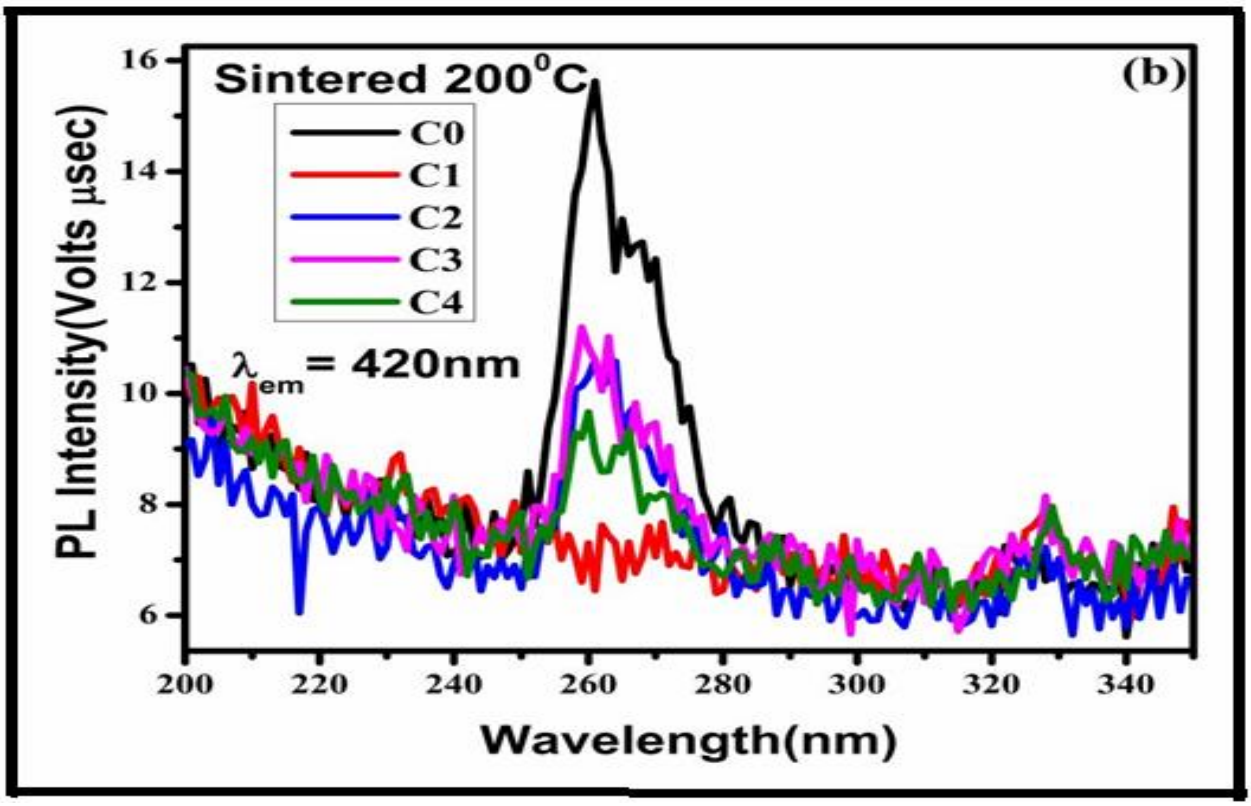
Sintered 200°C
(b)
C0
C1
C2
C3
C4
λem = 420nm
PL Intensity(Volts µsec)
Wavelength(nm)
16
14
12
10
8
6
200
220
240
260
280
300
320
340

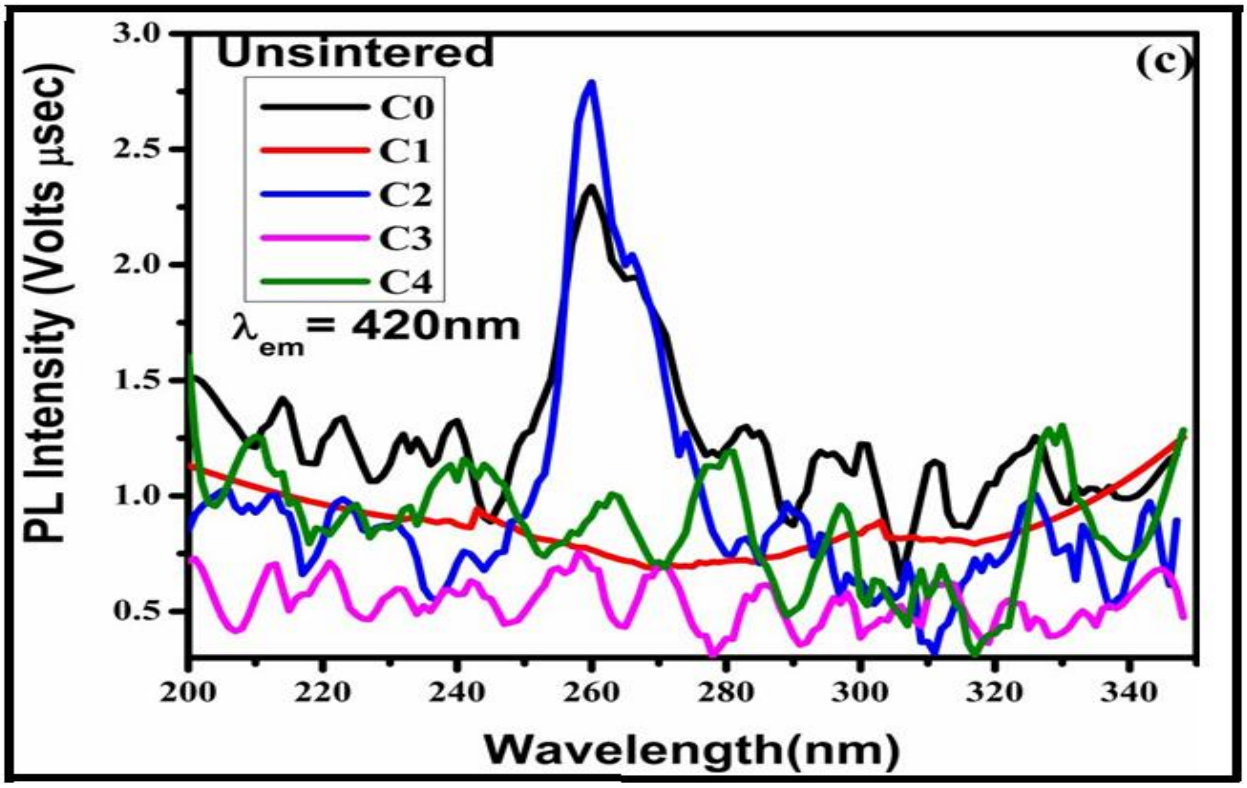

Figure 4.2(a-c): (a-c) Excitation spectra measured for 420 nm emission for sintered (400^0C & 200^0C) and unsintered nanocomposites samples.

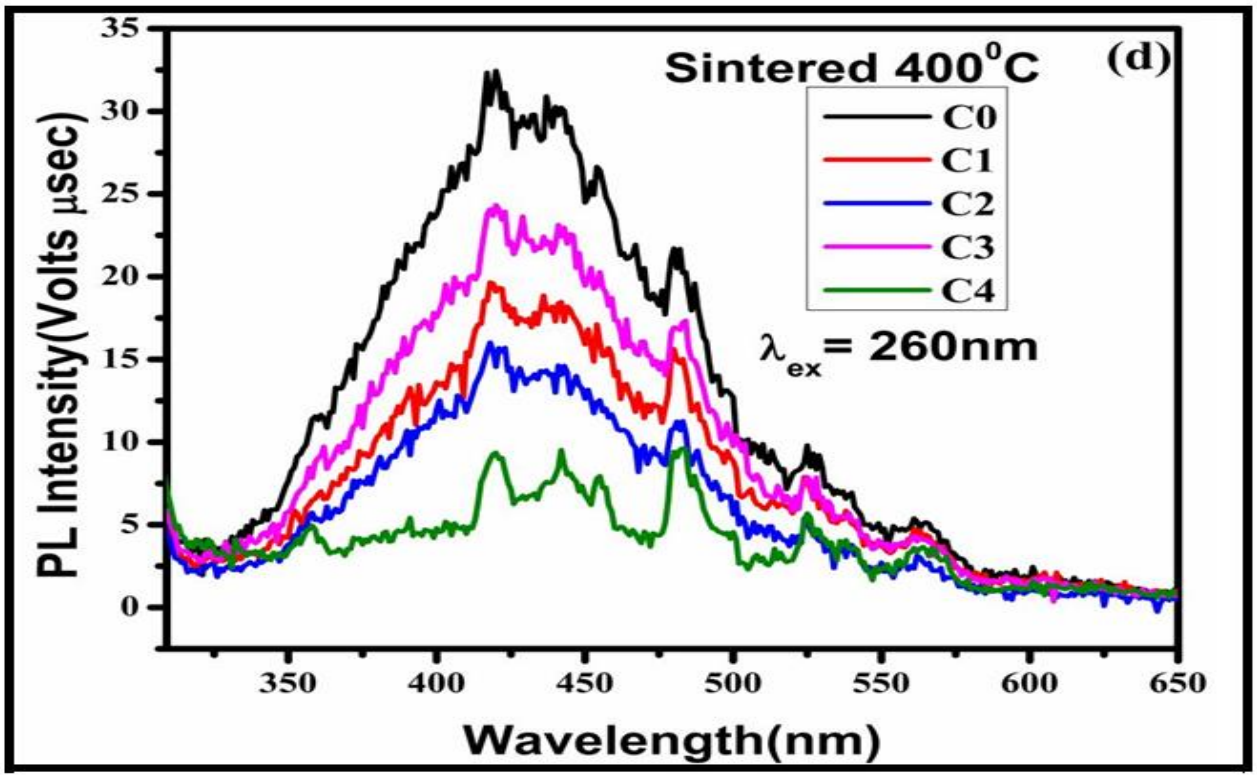

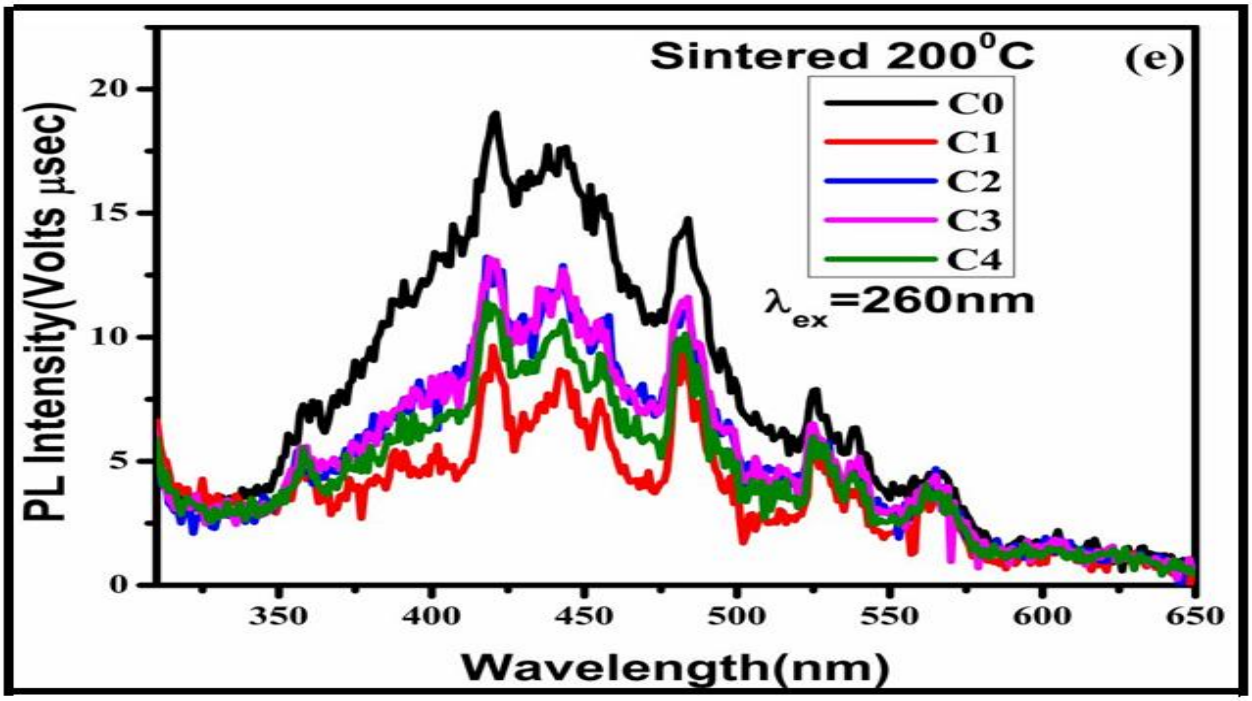
Sintered 200°C
(e)
C0
C1
C2
C3
C4
λex=260nm
PL Intensity(Volts μsec)
Wavelength(nm)
0
5
10
15
20
350
400
450
500
550
600
650

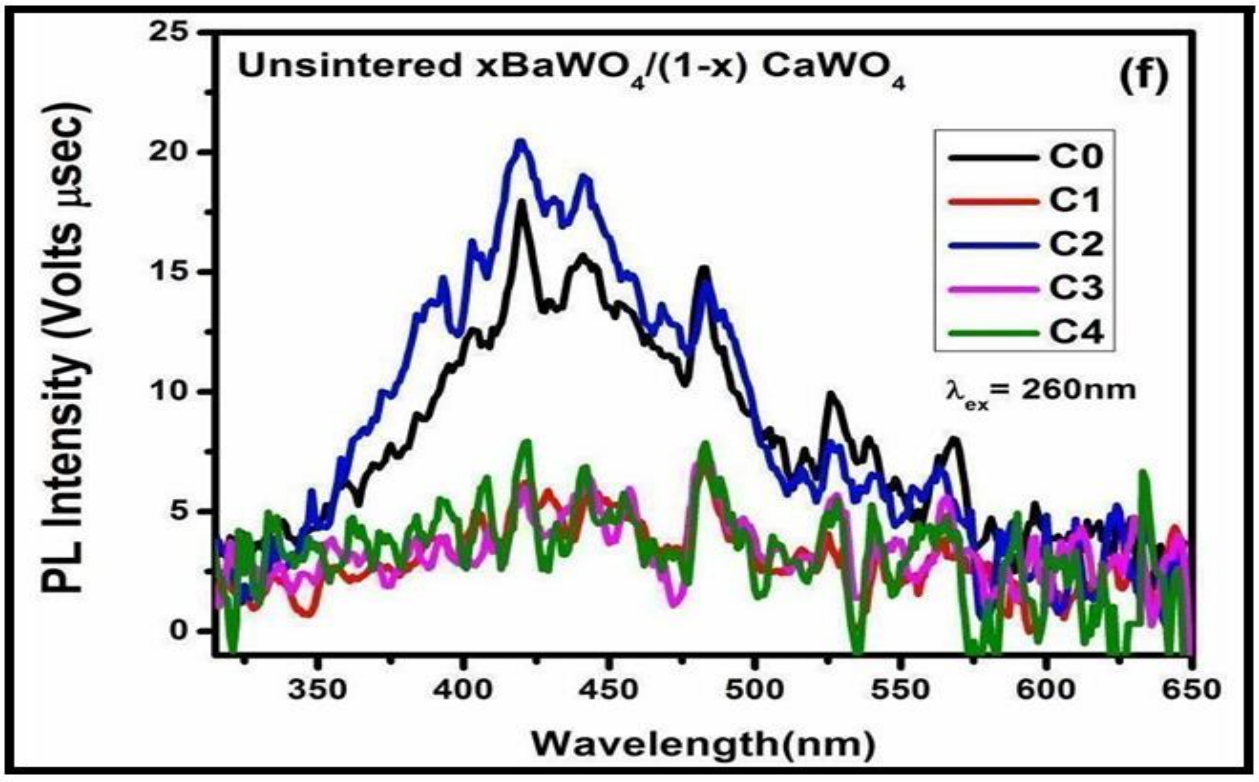
Unsintered xBaWO4/(1-x) CaWO4
(f)
C0
C1
C2
C3
C4
λex= 260nm
PL Intensity (Volts μsec)
Wavelength(nm)
0
5
10
15
20
25
350
400
450
500
550
600
650

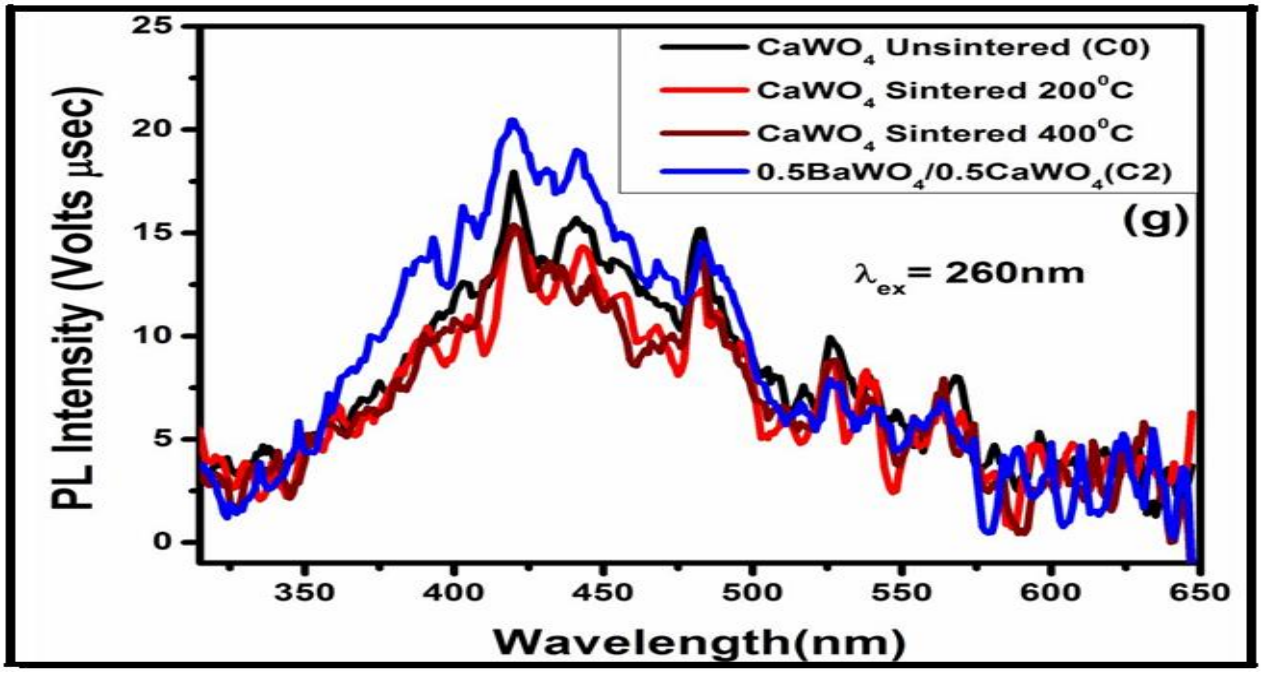

Figure 4.2(d-g):(d) Emission spectra for 260nm excitation of 400^0C sintered nanocomposites. **(e)** Emission spectrafor 260nm excitation of 200^0C sintered nanocomposites. **(f)** Emission spectrafor 260nm excitation of unsintered nanocomposites. (**g)** Emission spectra for 260nm excitation of sintered (400^0C & 200^0C) and unsintered $CaWO_4$ samples along with C2 unsintered nanocomposites.

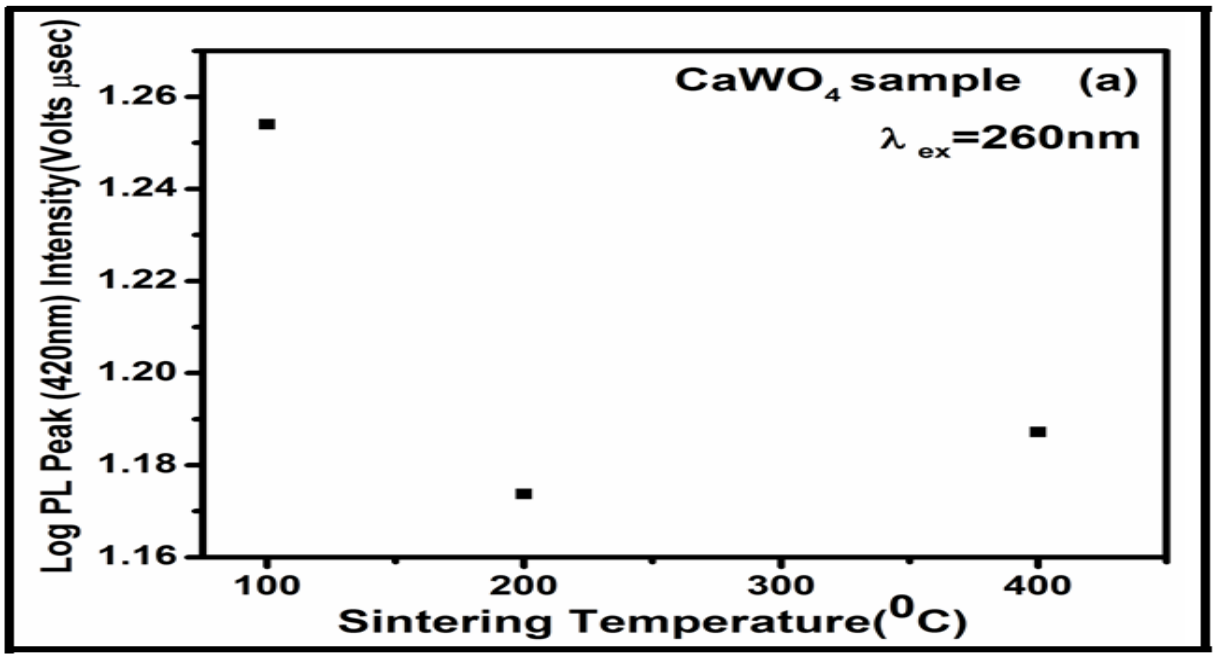

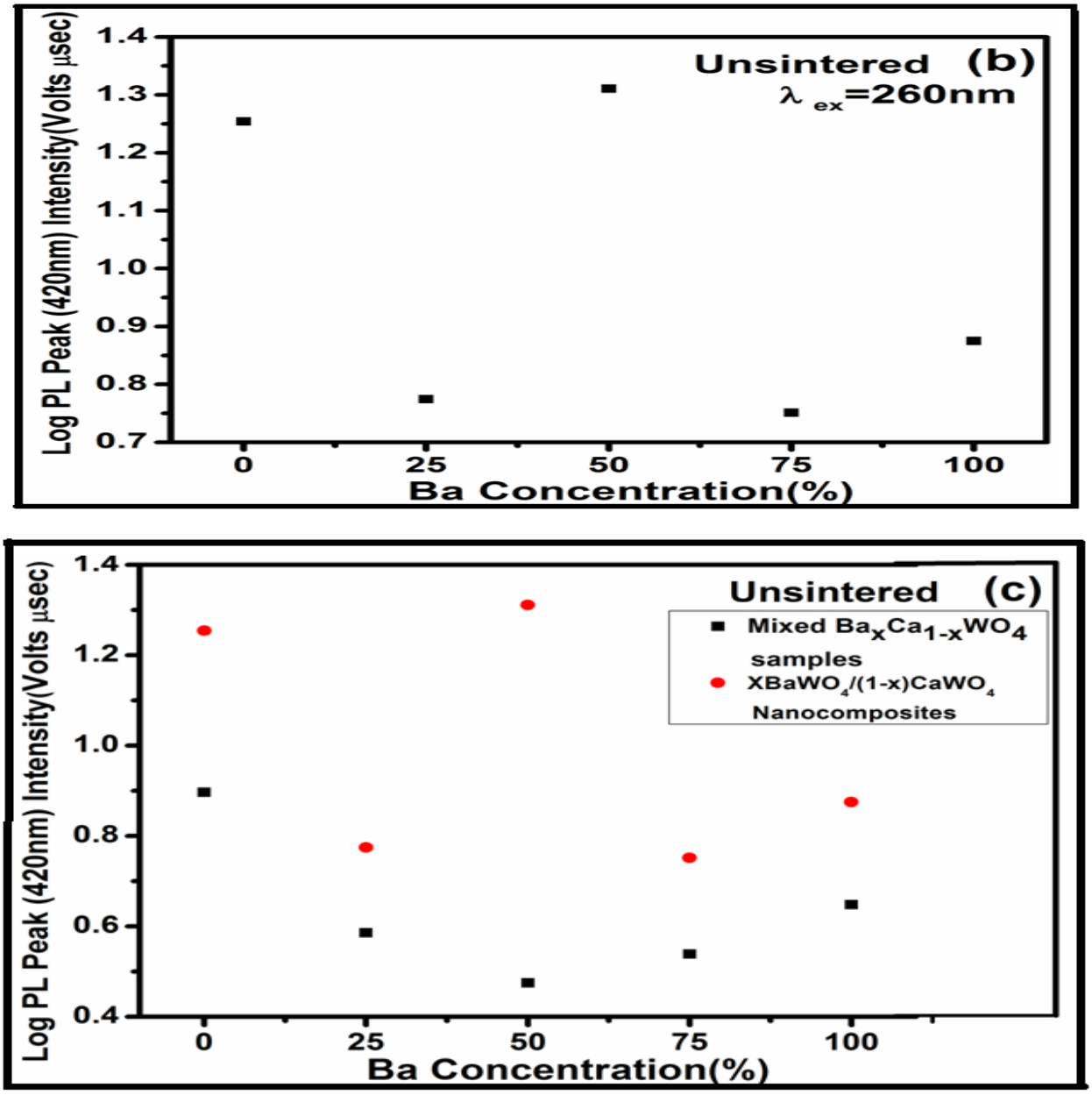

Figure 4.3(a-c): (a) Log PL peak (420nm) intensity versus sintering temperature of $CaWO_4$ nanosamples. **(b)** Log PL peak (420nm) intensity versus % Ba concentration of unsintered nanocomposites samples.**(c)** Log PL peak (420nm) intensity versus % Ba concentration of unsintered Mixed $Ba_xCa_{1-x}WO_4$ nanopowder & nanocomposites samples.

4.2.2.2. Possible mechanism for enhancement of PL intensity

The highest 420nm emission from C2($0.5BaWO_4/0.5CaWO_4$) nanocomposites could be due to the exciton charge transfer of $BaWO_4$ phase to $CaWO_4$ phase because of Type I band

alignment interface occurring between them as shown in **Figure 4.4**. The formation of interface between $BaWO_4$ phase to $CaWO_4$ phase in C2 ($0.5BaWO_4/0.5CaWO_4$) nanocomposites is also confirmed by the HRTEM image given in **Figure 3.7(c)**. The valence band (VB) and conduction band (CB) potentials of $BaWO_4$ and $CaWO_4$ phases for unsintered sample are calculated at the point of zero charge by the following **equation (4.4) and (4.5)[28]**. The band gap values used for $BaWO_4$ and $CaWO_4$ unsintered samples were estimated by us (**Table 4.1)**.

$$\mathbf{E_{CB} = \chi - 0.5E_g - E_e} \qquad \mathbf{(4.4)}$$

$$\mathbf{E_{VB} = E_{CB} + E_g} \qquad \mathbf{(4.5)}$$

Where χ, $\mathbf{E_e}$ and $\mathbf{E_g}$ are the absolute electronegativity of the $CaWO_4$ and $BaWO_4$, energy of free electrons on the hydrogen scale (4.5 eV) and band gap of materials respectively. χ is calculated to be 5.92 eV and 5.79 eV for $CaWO_4$ and $BaWO_4$ respectively. E_{CB} and E_{VB} values of $CaWO_4$ and $BaWO_4$ are estimated to be -0.77eV and 3.60 eV and -1.22eV and 3.80 eV respectively. $BaWO_4$ and $CaWO_4$ phases get excited by 260nm irradiation with formation of excitons. CB-electrons of $BaWO_4$ will be transferred to the CB edge of $CaWO_4$ through the interface. Similarly the valence band (VB) position of $BaWO_4$ is lower than the valence band (VB) positions of $CaWO_4$. Electrons from valence band (VB) of $CaWO_4$ would flow to the valence band (VB) of $BaWO_4$ creating holes in the valence band (VB) of $CaWO_4$. Due to the availability of additional excitons in the $CaWO_4$ phase more recombination processes can occur leading to enhancement of emissions from the $[WO_4]^{2-}$ anions of $CaWO_4$ phase of the sample. Similar results were reported earlier on ZnO/SnO nanocomposites **[7]**. **Figure 4.5** shows emission processes of $[WO_4]^{2-}$anions of $CaWO_4$ phase of the interface C2 ($0.5BaWO_4/0.5CaWO_4$) nanocomposites. Ground state ($^1A_1$) electron configuration (t_1^6) of $[WO_4]^{2-}$ in T_d symmetry done using molecular orbital calculations by **[29]**. Lower excited states are $^1T_2$, $^1T_1$, $^3T_2$, $^3T_1$. Radiative transitions and broad peaks are due to the transition from the $^3T_2$ and $^3T_1$excited states to the $^1A_1$ground state **[30]**. The fundamental absorption edge of $CaWO_4$ is due to $^1A_1 \rightarrow {}^1T_2$, $^1T_1$ transitions. Orbital's of $BaWO_4$ and $CaWO_4$ phases overlap due to interfacing which favors transfer of additional charges from the excited of $BaWO_4$ phase to $[WO_4]^{2-}$ anions of $CaWO_4$ phasein C2 ($0.5BaWO_4/0.5CaWO_4$) nanocomposites giving rise to higher intrinsic emission of $CaWO_4$.

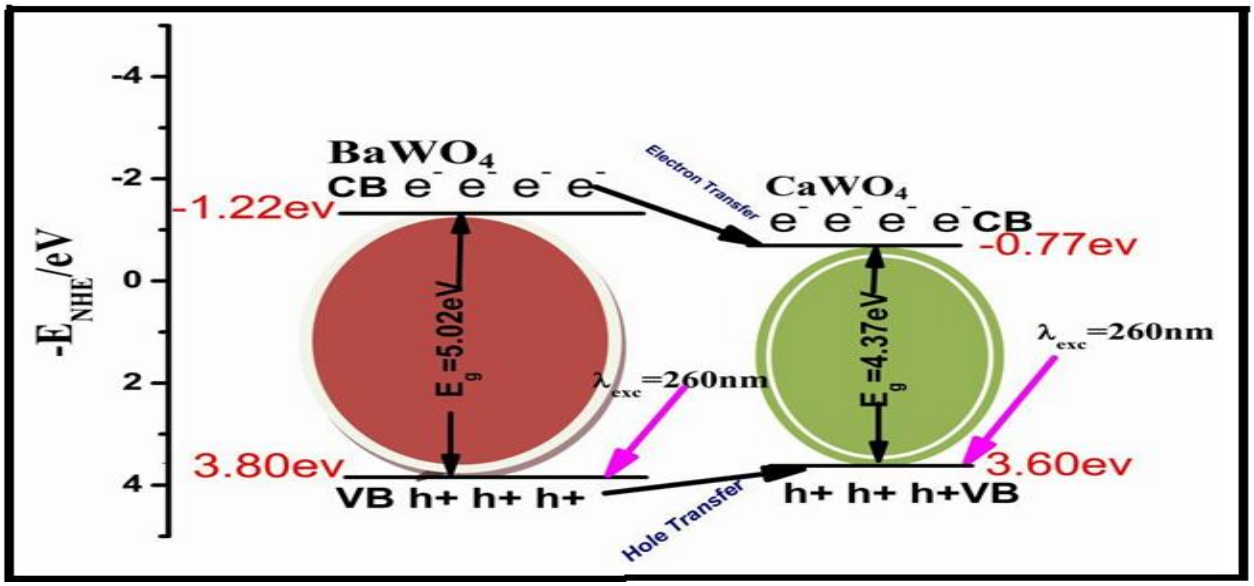

Figure 4.4: Schematic of band position diagram and charge transfer processes of C2 ($0.5BaWO_4/0.5CaWO_4$)unsintered nanocomposites.

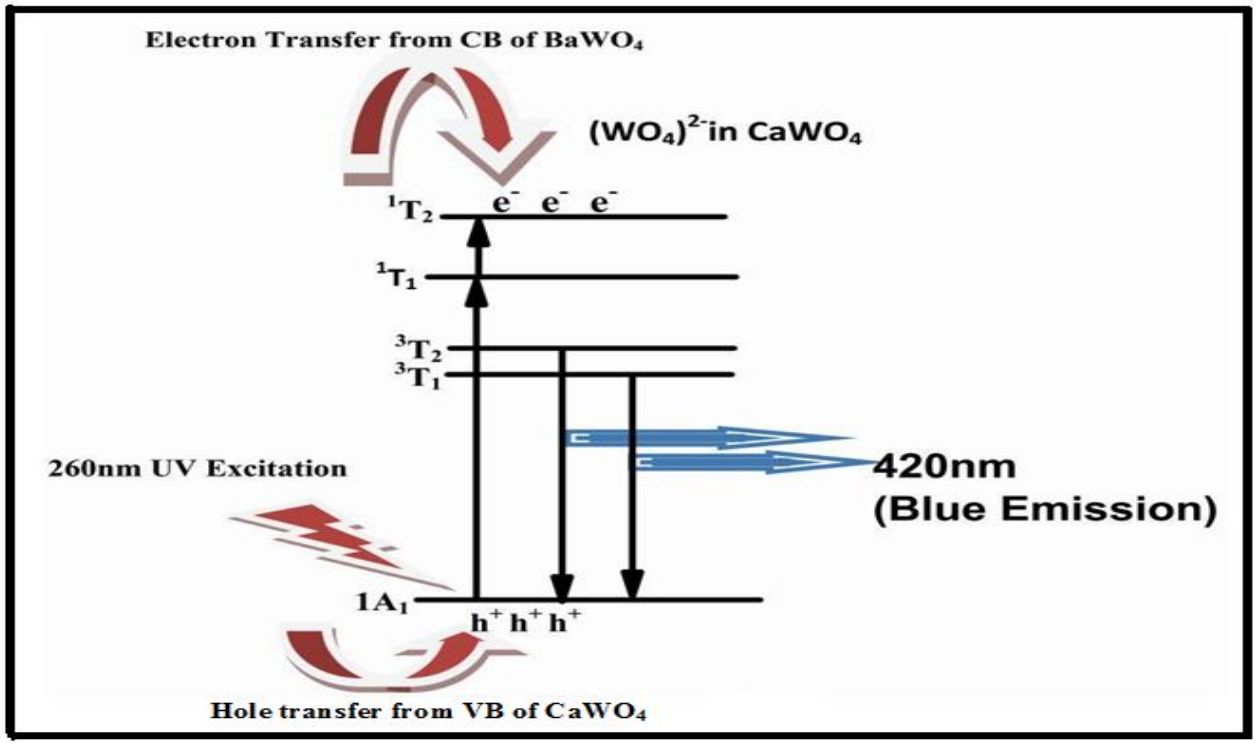

Figure 4.5: Emission processes of $(WO_4)^{2-}$ anion of $CaWO_4$ phase in C2 ($0.5BaWO_4/0.5CaWO_4$**)** unsintered nanocomposites.

4.2.2.3. PL lifetime (τ)

Photoluminescence (PL) lifetime curves for 420 nm emissions due to 260 nm excitations recorded at room temperature (RT) for all the unsintered samples are given in **Figure 4.6(a)**.The lifetime curves follow the single exponential function:

$$I = I_0 + Ae^{-t/\tau} \qquad (4.6)$$

Where I_0, I, A, t and τ are the initial PL intensity, instantaneous photoluminescence (PL) intensity, A is constant, measurement time and lifetime of the photoluminescence (PL) emission respectively **[31]**. The photoluminescence (PL) lifetime (τ) values obtained are given in **Table 4.2**. Obtained photoluminescence (PL) lifetime (τ) values for $CaWO_4$ and $BaWO_4$ nanosamples matches with literature values of nanosamples **[32, 33]**. **Figure 4.6(b)** shows the plot of lifetime versus % Ba concentration of the nanocomposites.It is observed that the lifetime of 420nm photoluminescence (PL) emission decreases almost linearly as the % Ba concentration increases except for C2 ($0.5BaWO_4/0.5CaWO_4$) nanocomposites. The C2($0.5BaWO_4/0.5CaWO_4$) nanocomposites emission has maximum lifetime as compared to other samples which are approximately 13% more than the emission lifetime of C0($CaWO_4$) single phases respectively.This increase in lifetime of the emission from C2($0.5BaWO_4/0.5CaWO_4$) nanocomposites may be due to the recombination through the non-radiative process**[34-36]** introduced to the charge migration from the conduction band (CB) of $BaWO_4$ phase to the conduction band (CB) of $CaWO_4$ phase of the samples as shown in **Figure 4.4**.

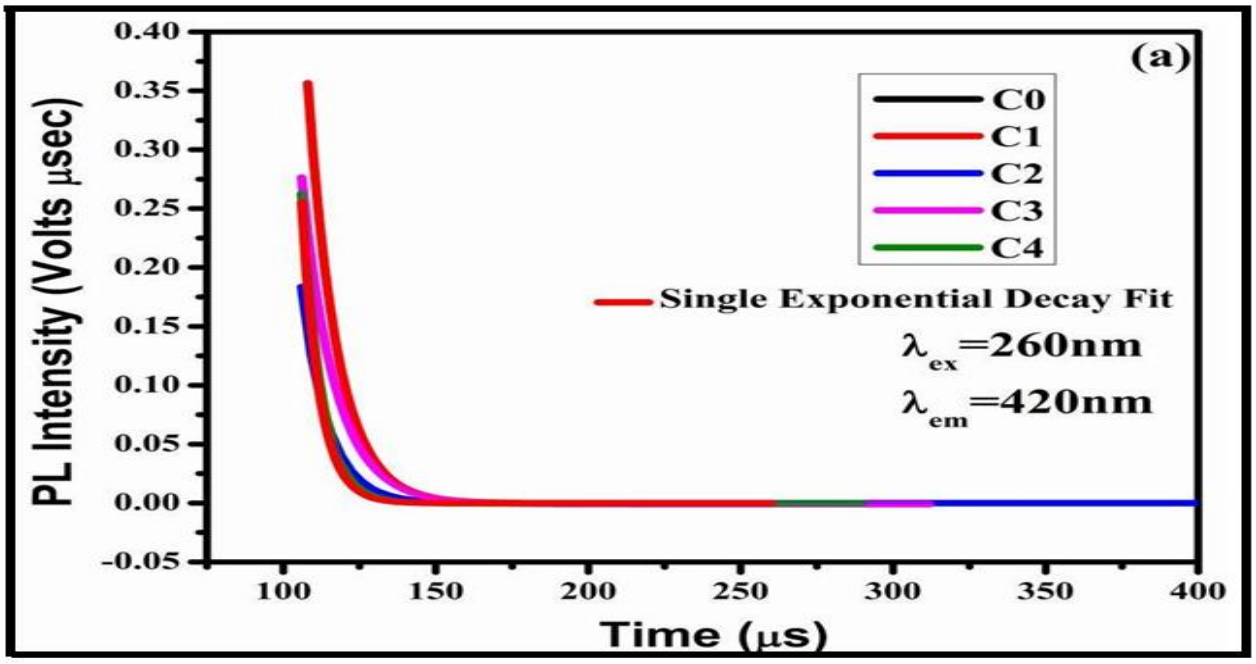

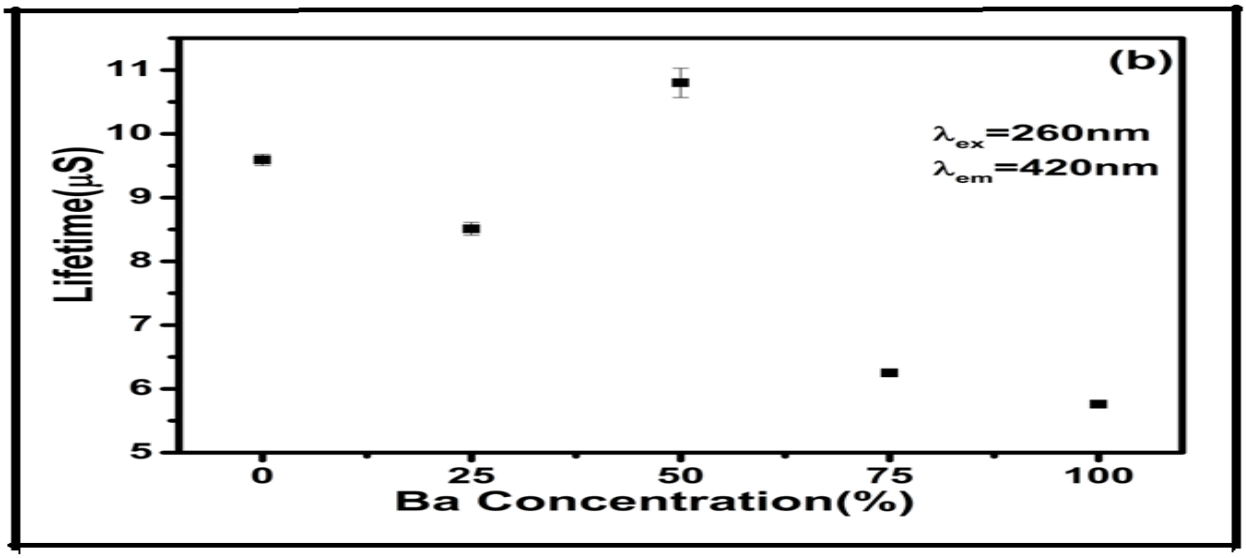

Figure 4.6(a-b): (a) Photoluminescence (PL) lifetime (τ) curves of unsintered nanocomposites. **(b)** Lifetime (τ) versus % Ba concentration of unsintered nanocomposites.

Table 4.2: Photoluminescence (PL) lifetime (τ) of unsintered nanocomposites.

Samples	Lifetime(τ) (μs)	Literature value Lifetime(τ) (μs)
C0	09.59±0.09	4.05 **[32]**
C1	08.51±0.10	
C2	10.80±0.23	
C3	06.25±0.03	
C4	05.76±0.05	8.9 **[33]**

4.2.2.4. CIE color coordinates analysis

The CIE coordinates for the samples C0, C1, C2, C3 and C4 estimated to be (0.23, 0.24), (0.25, 0.25), (0.21, 0.20), (0.28, 0.30) and (0.21, 0.27) respectively are shown in **Figure 4.7**. Under 260nm excitation blue light was observed for all the samples with slight changes for the chromaticity coordinates.CIE color coordinates of the entire samples lie in the blue region.The CIE results shows that nanocomposites can be used in fluorescent lamps, electronic display and other optolectronic applications.

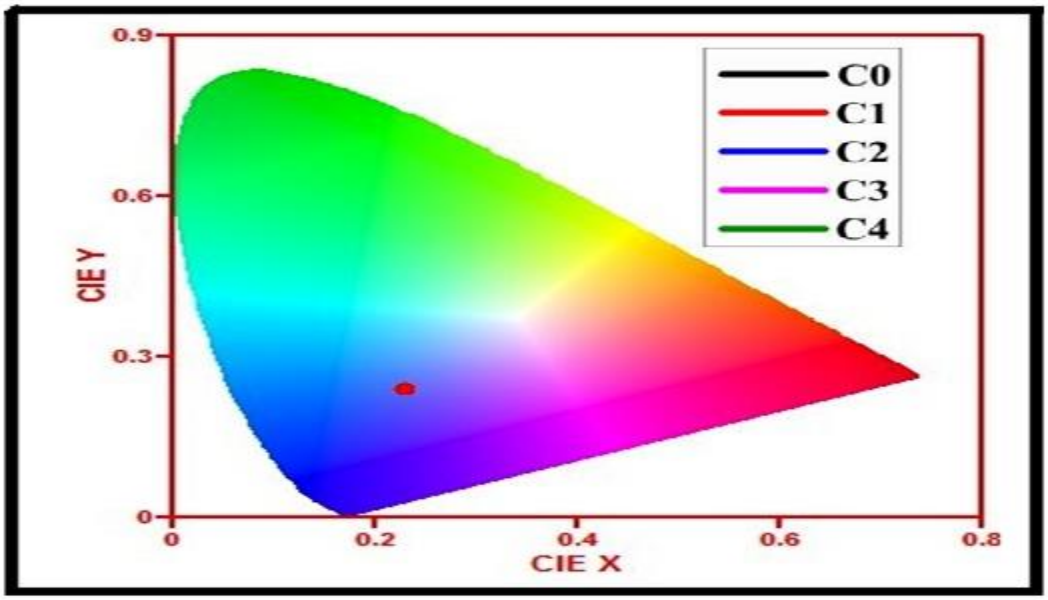

Figure 4.7: CIE diagram of unsintered nanocomposites.

4.3. Conclusion

The bandgap energy increases from increase in % Ba concentration. This is because Eg of $BaWO_4$ is higher than that of $CaWO_4$ sample. Among all the samples (unsintered and sintered), maximum photoluminescence (PL) 420nm intrinsic peak intensity is emitted by C2 ($0.5BaWO_4/0.5CaWO_4$) unsintered nanocomposites.This maximum photoluminescence (PL) 420nm emission intensity of C2($0.5BaWO_4/0.5CaWO_4$) nanocomposites could be due to the excitons charge transfer of $BaWO_4$ phase to $CaWO_4$ phase because of their type I band alignment and interface occurring between them. More excitons in the $CaWO_4$ phase lead to increase to the number of recombination processes which increases emission intensity from the $[WO_4]^{2-}$ anions of $CaWO_4$ phase of the sample. HRTEM image of C2 ($0.5BaWO_4/0.5CaWO_4$) nanocomposites also shows interfacing confirmation with $BaWO_4$ phase and $CaWO_4$ phase. The C2 ($0.5BaWO_4/0.5CaWO_4$) nanocomposites emission has maximum lifetime as compared to other samples which are approximately 13% more than the emission lifetime of C0 ($CaWO_4$) single phases respectively. This may be attributed to the recombination through non-radiative process introduced during the migration of charge from the conduction band (CB) of $BaWO_4$ phase to the conduction band (CB) of $CaWO_4$ phases respectively. Due to the charge transfer mechanism this nanocomposites could be a host material to get enhanced dopant photoluminescence (PL) emissions.These nanocomposites can be considered for producing blue component of emission of

white light emitting diodes (WLEDs), electronic display and other optolectronic applications. Whereas Mixed $Ba_xCa_{1-x}WO_4$ nanopowder samples did not give enhanced 420 nm emission in comparison with $CaWO_4$ emission.

4.4. Supplementary graphs of Mixed $Ba_xCa_{1-x}WO_4$ nanopowder samples

4.4.1 Results and discussion of Mixed $Ba_xCa_{1-x}WO_4$ nanopowder samples

4.4.1.1 Optical absorption study of Mixed $Ba_xCa_{1-x}WO_4$ nanopowder samples

Diffuse reflectance spectra of the samples were measured and converted to the absorption spectra by using Kubelka–Munk equation (K-M equation) **[17]**. Reflectance spectra of Mixed $Ba_xCa_{1-x}WO_4$ nanopowder samples are shown in **Figure 4.8(a)**. Transfer of UV excited electrons from oxygen(O) 2p-states to tungsten(W) 5d-states of $[WO_4]^{2-}$anion gives rise to the observed broad reflectance spectra from 200nm to 330nm and the hole (on the oxygen) and the electron (on the tungsten) due to their strong interactions form an exciton **[18]**. The reflectance spectra peak wavelength shifts from 248nm to 220nm and also the reflectance peak intensity gradually decreases as the % Ba concentration increases. Minimum reflectance peak intensity (maximum absorption) is for $BaWO_4$ sample and maximum reflectance (minimum absorption) peak intensity is for $CaWO_4$ sample. This is because the molecular photon- absorption cross section of $BaWO_4$ is larger than that of $CaWO_4$**[19]**. **Figure 4.8(b)** were used to calculate band gap energies Eg of the Mixed nanopowder samples and are tabulated in **Table 4.3**. Calculated E_g values for $CaWO_4$ and $BaWO_4$ nanosamples match with literature values **[23]**.Variation in band gap energy versus % Ba concentration of the Mixed nanopowder samples is plotted **Figure 4.8(c)**. E_g is enhanced with increase in % Ba concentration except Mixed $Ba_{0.25}Ca_{0.75}WO_4$ nanopowder samples. This increase in Eg is higher in $BaWO_4$ than that of $CaWO_4$ samples due to the larger radius of Ba^{2+} ion (1.42Å) as compared to that of Ca^{2+} ion (1.12Å) **[23]**.The energy of Ca 3p-states in $CaWO_4$ is lower than that of Ba 5p-states in $BaWO_4$. Hybridization between Ca 3p-states and O 2p-states will be there in $CaWO_4$ lowering its band gap. Whereas hybridization between Ba 5p-states and O 2p-states will not be there in $BaWO_4$ making its bandgap higher **[25]**.

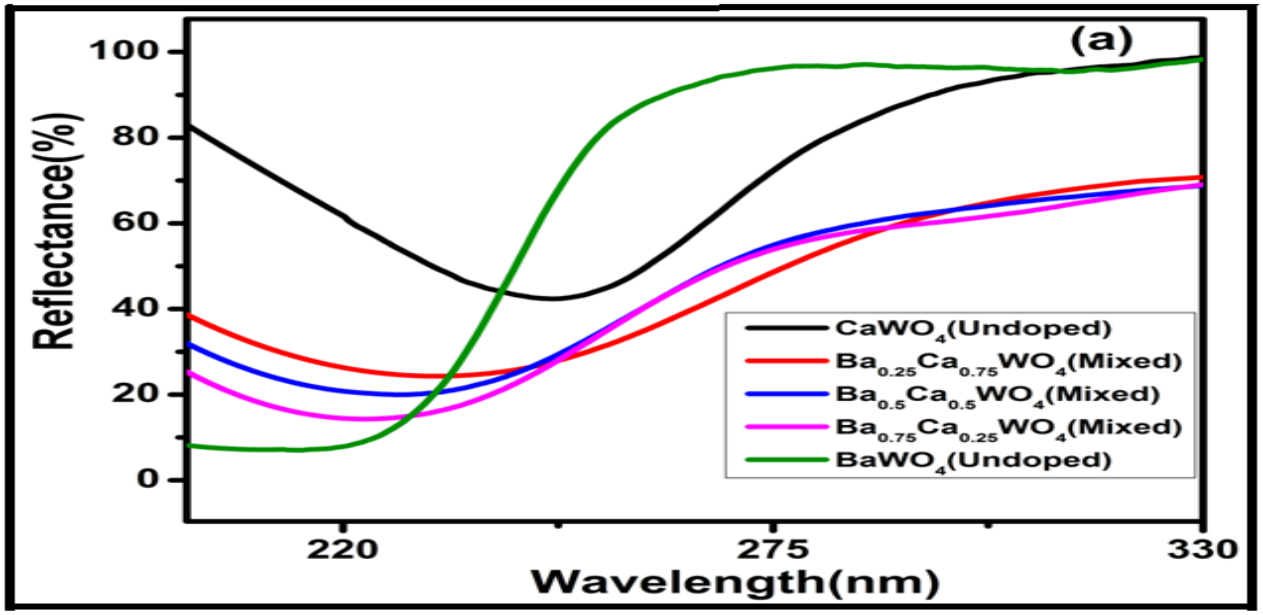
(a)
Reflectance(%)
100
80
60
40
20
0
220
275
330
Wavelength(nm)
CaWO4(Undoped)
Ba0.25Ca0.75WO4(Mixed)
Ba0.5Ca0.5WO4(Mixed)
Ba0.75Ca0.25WO4(Mixed)
BaWO4(Undoped)

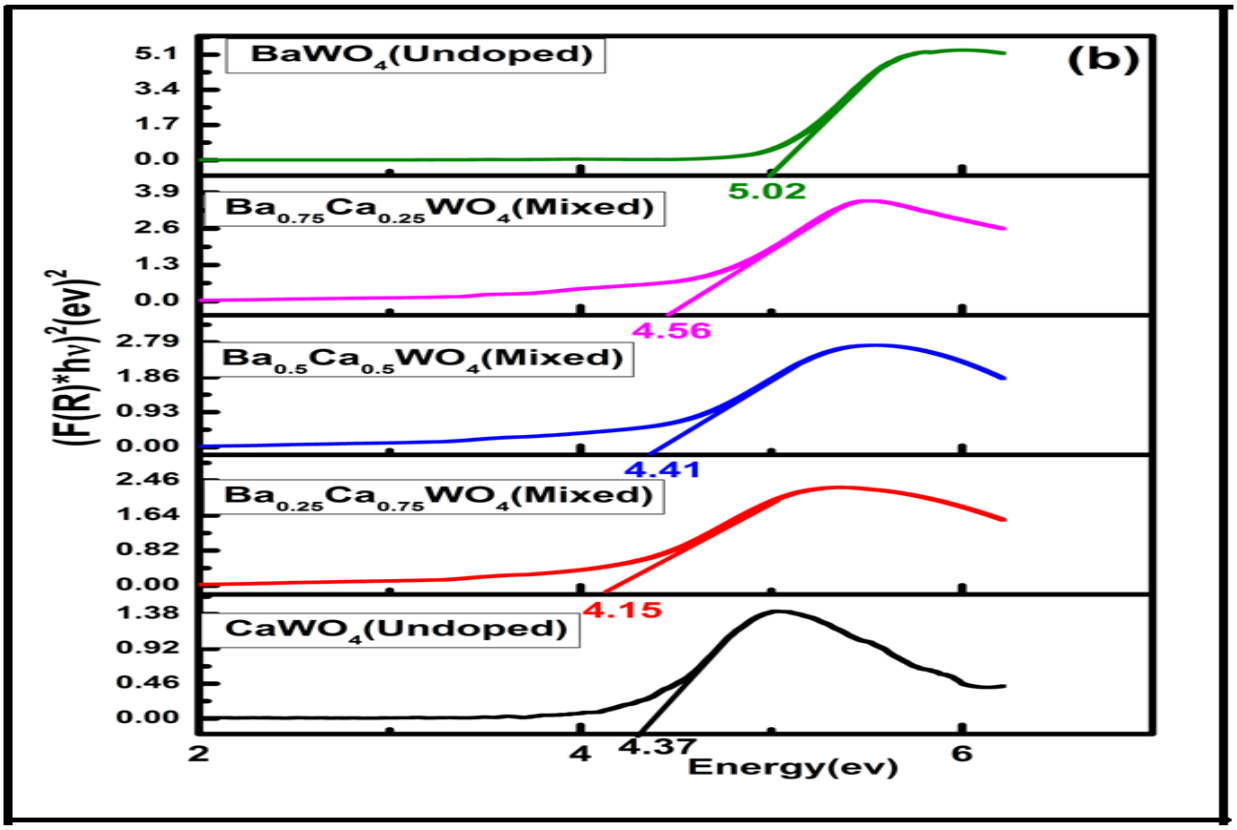
(b)
(F(R)*hν)2(ev)2
BaWO4(Undoped)
5.1
3.4
1.7
0.0
5.02
Ba0.75Ca0.25WO4(Mixed)
3.9
2.6
1.3
0.0
4.56
Ba0.5Ca0.5WO4(Mixed)
2.79
1.86
0.93
0.00
4.41
Ba0.25Ca0.75WO4(Mixed)
2.46
1.64
0.82
0.00
4.15
CaWO4(Undoped)
1.38
0.92
0.46
0.00
2
4
4.37
6
Energy(ev)

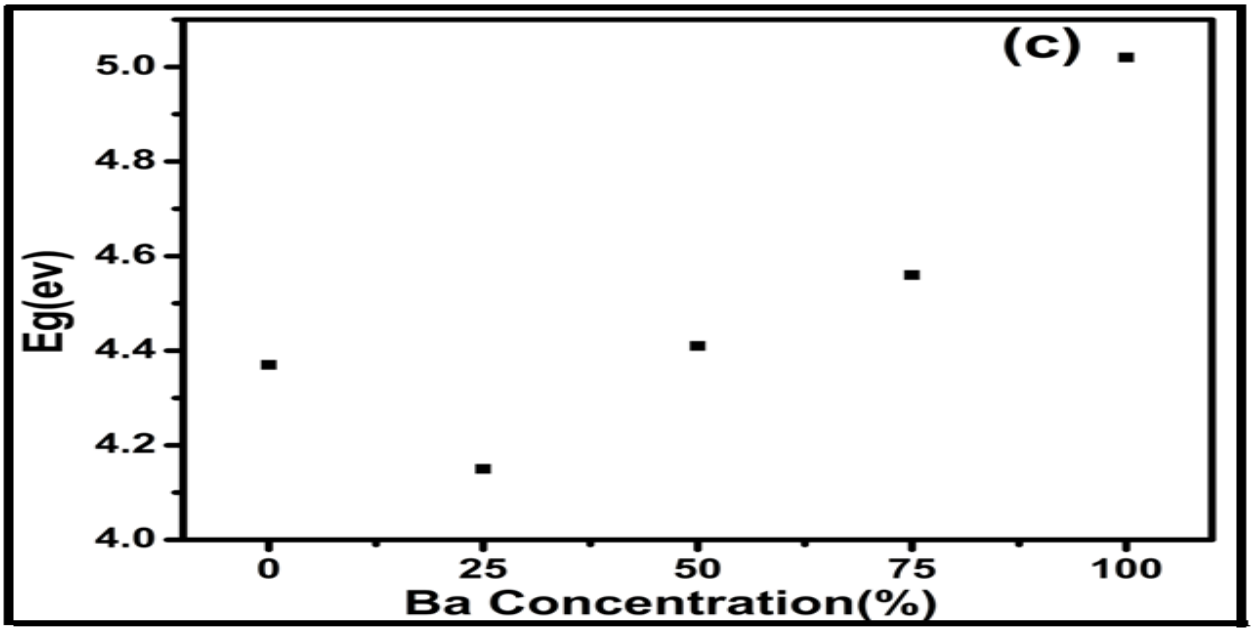

Figure 4.8(a-c): (a) DRS spectra of unsintered Mixed $Ba_xCa_{1-x}WO_4$ nanopowder samples. **(b)** K-M plots of unsintered Mixed $Ba_xCa_{1-x}WO_4$ nanopowder samples. **(c)** Eg versus % Ba concentration of unsintered Mixed $Ba_xCa_{1-x}WO_4$ nanopowder samples.

Table 4.3: Bandgap energy of Mixed $Ba_xCa_{1-x}WO_4$ nanopowder samples.

Samples	K-M Bandgap energy Eg(eV)	Literature value Eg(eV)
C0	4.37±0.00153	4.94 **[23]**
C1	4.15±0.00139	-----
C2	4.41±0.00157	-----
C3	4.56±0.00168	-----
C4	5.02±0.00203	5.26 **[23]**

4.4.1.2. PL spectral analyses of Mixed$Ba_xCa_{1-x}WO_4$ nanopowder samples

Excitation spectra measured for 420 nm emissions of sintered (400^0C & 200^0C) and unsintered Mixed $Ba_xCa_{1-x}WO_4$ nanopowder samples are shown in **Figure 4.9(a-c)**. All the samples exhibit broad peaks centered around 260 nm because of transfer of UV excited electrons from oxygen (O) 2p-states to tungsten (W) 5d-states of $[WO_4]^{2-}$ anion. **Figure 4.9 (d-f)** shows emission spectra for 260nm excitation for sintered (400^0C & 200^0C) and unsintered Mixed $Ba_xCa_{1-x}WO_4$ nanopowder samplesrecorded from 280nm to 650nm. Intrinsic luminescence of

$CaWO_4$ is due to the annihilation of self-trapped excitons forming excited $[WO_4]^{2-}$ anions giving rise to the broad emission spectra peaking around 420nm. For (400^0C & 200^0C) and unsintered Mixed $Ba_xCa_{1-x}WO_4$ nanopowder samples exhibits $CaWO_4$maximum photoluminescence (PL) intensity. In tungstates with Scheelite structure the excited $[WO_4]^{2-}$ ions get relaxed by intrinsic emission due to recombination of self-trapped exciton (STE) **[27]**. Incase of (400^0C & 200^0C) and unsintered Mixed $Ba_xCa_{1-x}WO_4$ nanopowder samples photoluminescence (PL) emission intensity is lower in Mixed $Ba_xCa_{1-x}WO_4$ nanopowder samples due to totally disordered and well crystallized powders present very little emissionin comparison to $CaWO_4$ **[37]**.

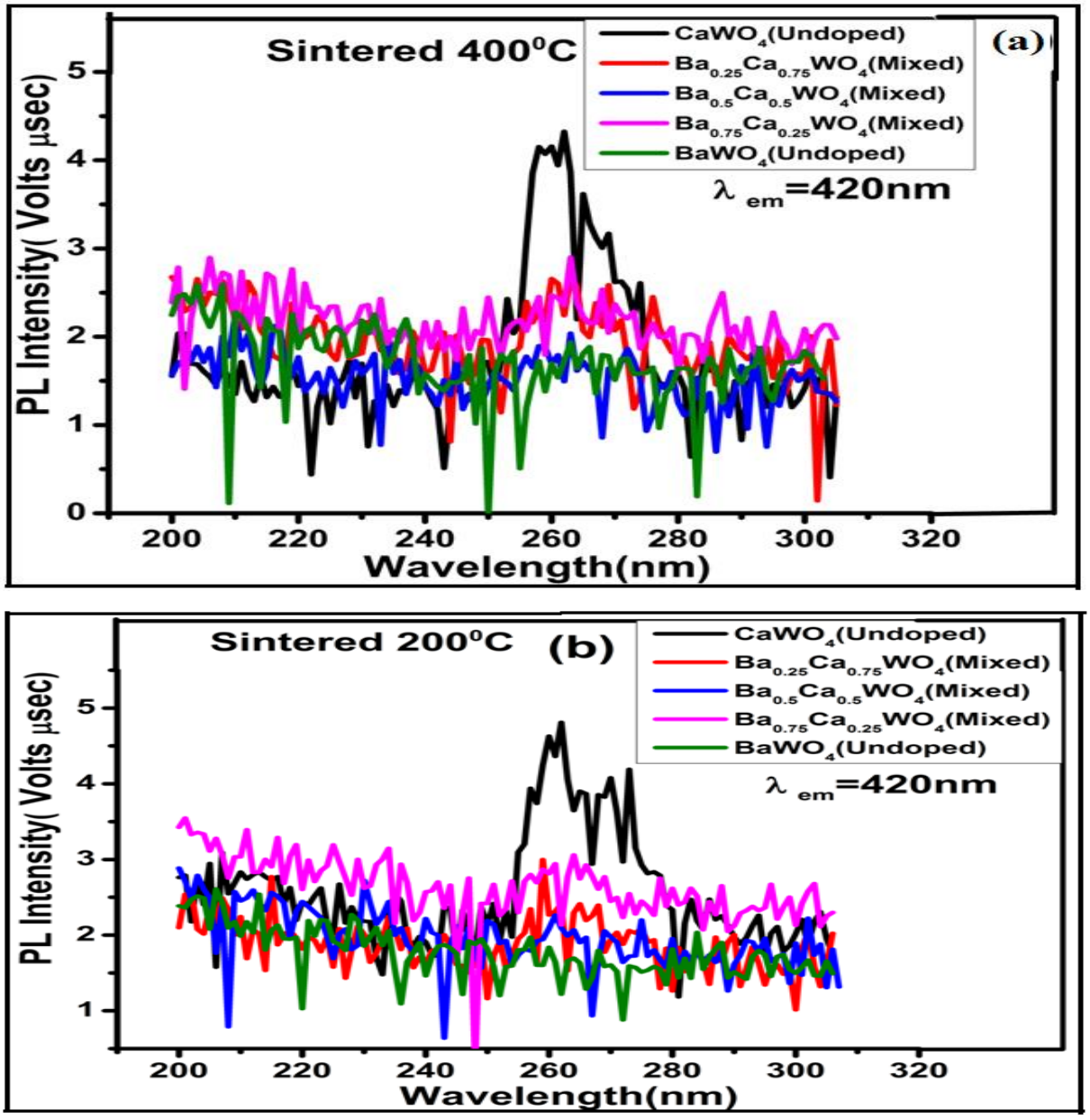

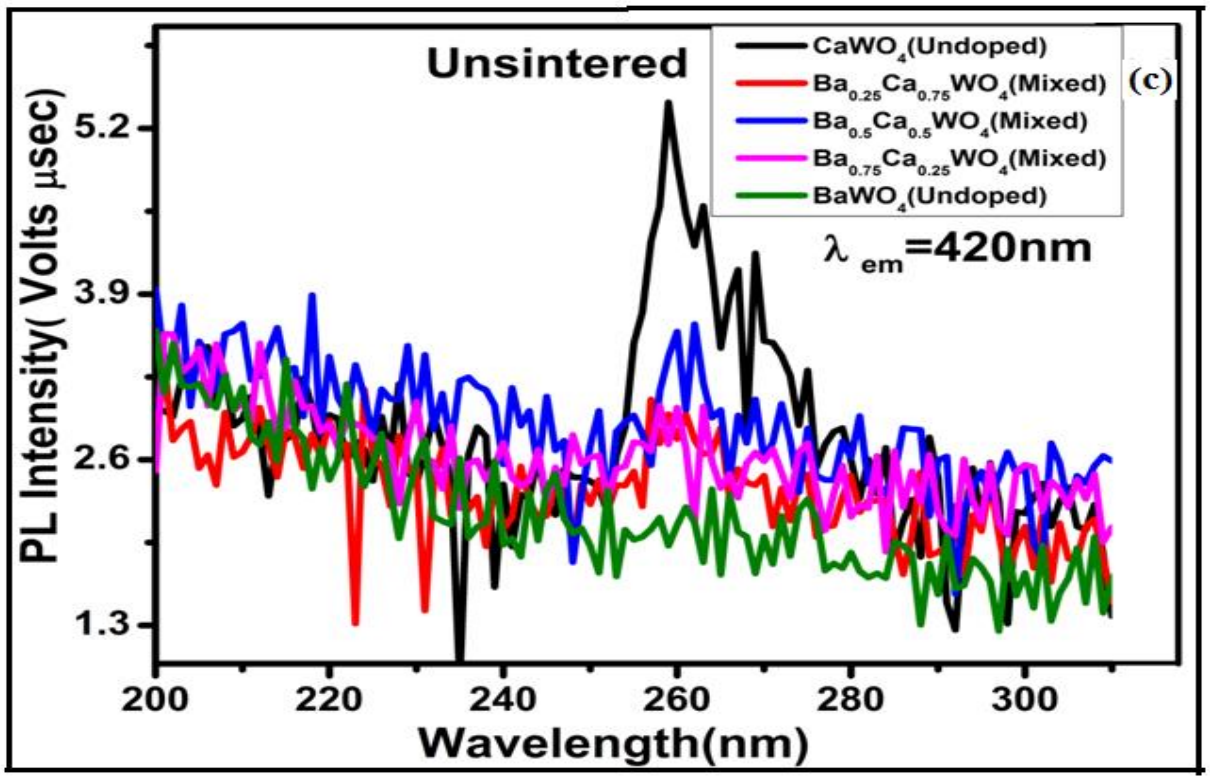

Figure 4.9(a-c): Excitation spectra measured for 420 nm emission for sintered (400^0C & 200^0C) and unsintered Mixed $Ba_xCa_{1-x}WO_4$ nanopowder samples.

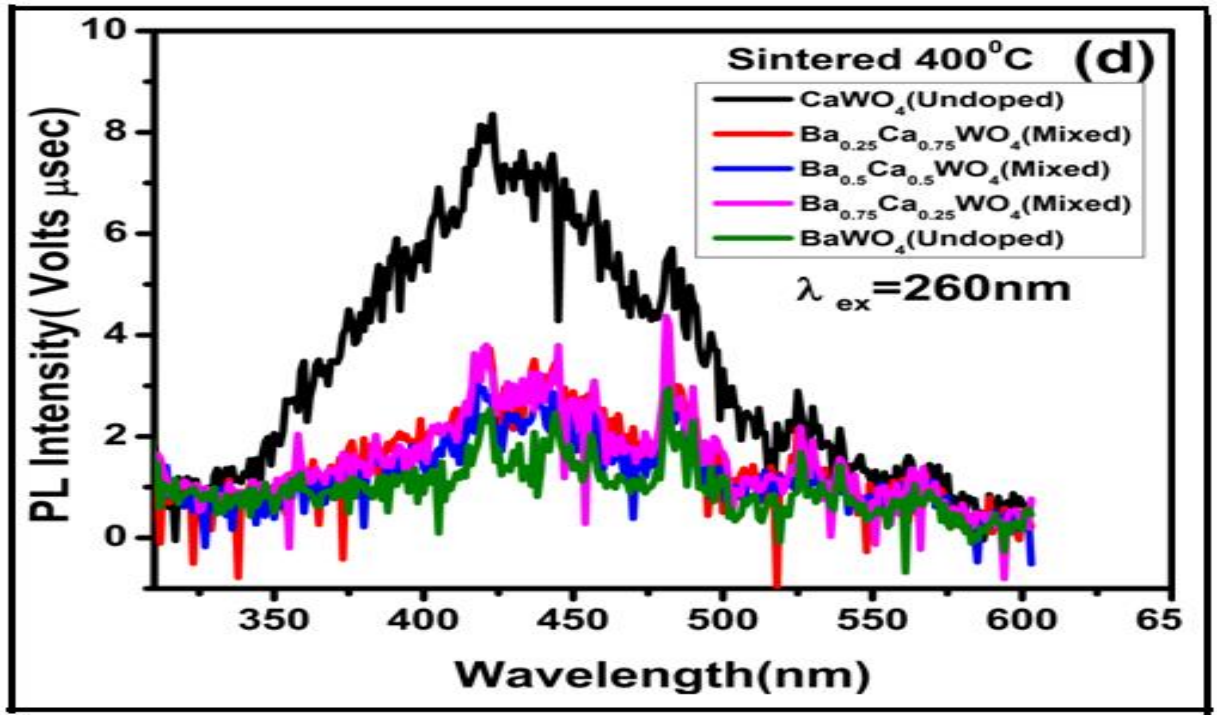

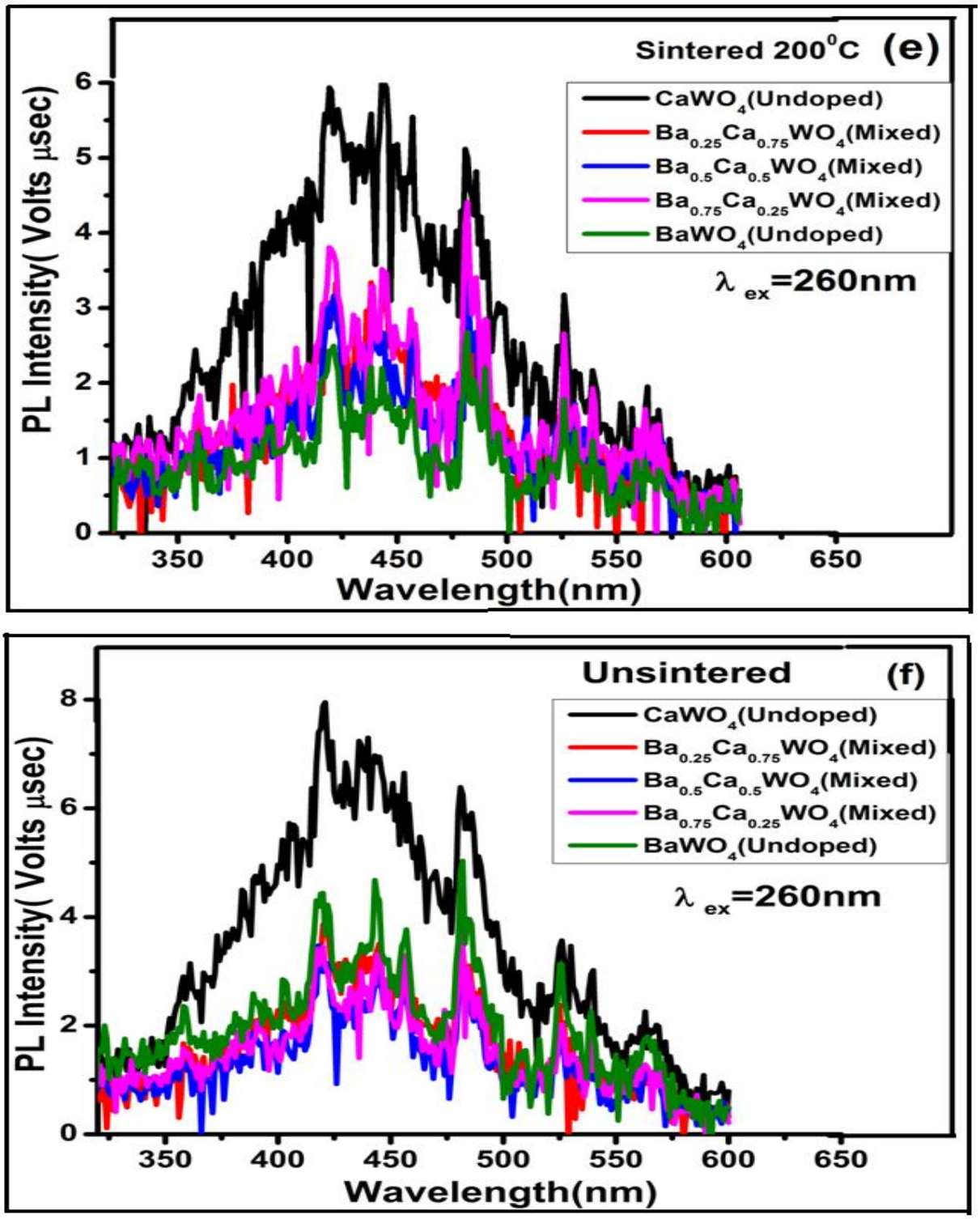

Figure 4.9(d-f):(d-f) Emission spectrameasured for 260nm excitation of sintered (400^0C & 200^0C) and unsintered Mixed $Ba_xCa_{1-x}WO_4$ nanopowder samples.

4.4.1.3. PL peak intensity variation of Mixed $Ba_xCa_{1-x}WO_4$ nanopowder samples

Figure 4.10 (a-c) shows the plot of log photoluminescence (PL) peak (420nm) intensity versus % Ba concentration of unsintered & sintered (200^0C &400^0C) Mixed $Ba_xCa_{1-x}WO_4$ nanopowder samples.In all unsintered & sintered (200^0C &400^0C)Mixed samples maximum photoluminescence (PL) intensity is emitted by $CaWO_4$ sample. Photoluminescence (PL) peak intensity of $CaWO_4$ nanosample is much higher than that of $BaWO_4$nanosample. This is because the radius of Ba^{2+} ions (1.42Å) surrounding the tungstate ions is higher than that of Ca^{2+} ions (1.12Å) and when $BaWO_4$ is excited with ultraviolet (UV) energy Ba^{2+} ions cannot counteract the expansion of $[WO_4]^{2-}$ anions. Then the offset between the excited state parabola and ground state parabola in the configuration coordinates system becomes large resulting in increase in non-radiative transitions, broader optical absorption and emission bands **[26]**.Whereas when $CaWO_4$ is ultraviolet (UV) excited Ca^{2+} ions can counteract the expansion of $[WO_4]^{2-}$ anions resulting in less non-radiative transitions. Therefore it is seen that among all the Mixed $Ba_xCa_{1-x}WO_4$ nanopowder samples (sintered and unsintered), gives maximum photoluminescence (PL) 420nm intrinsic emission of $CaWO_4$.

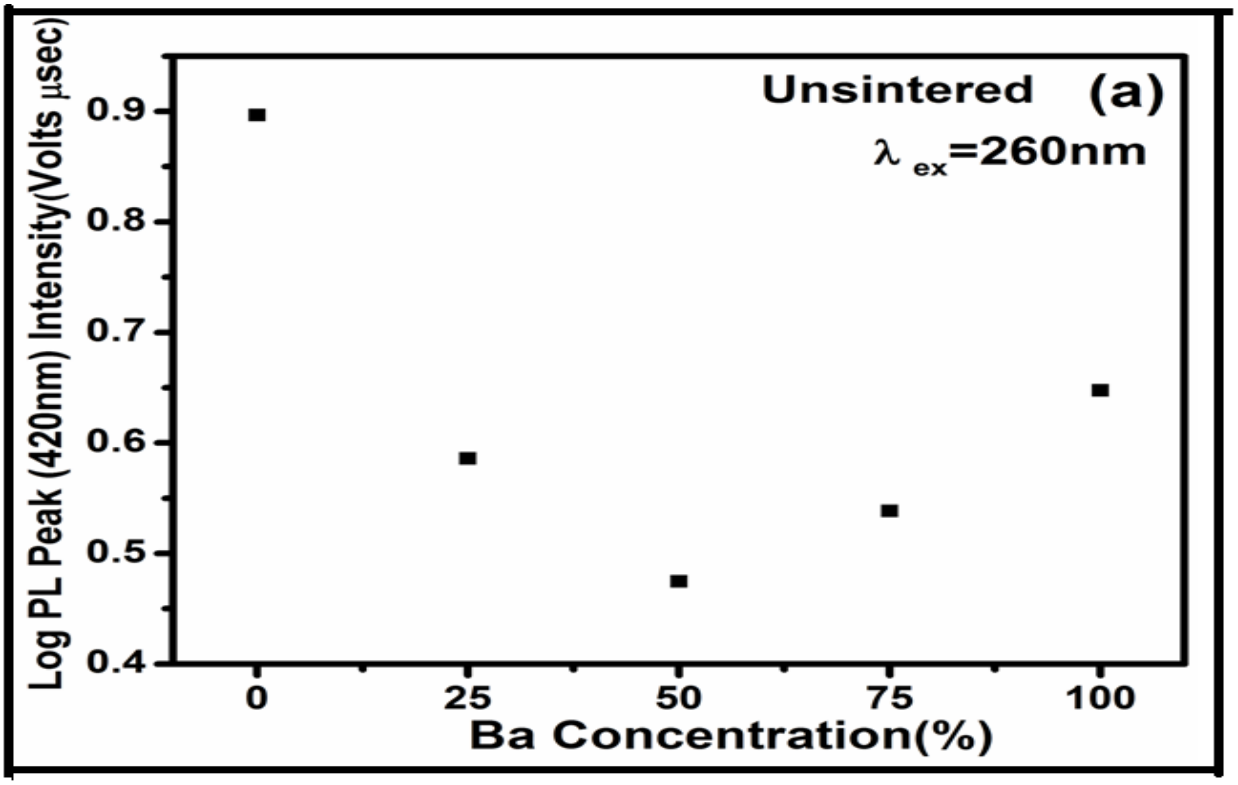

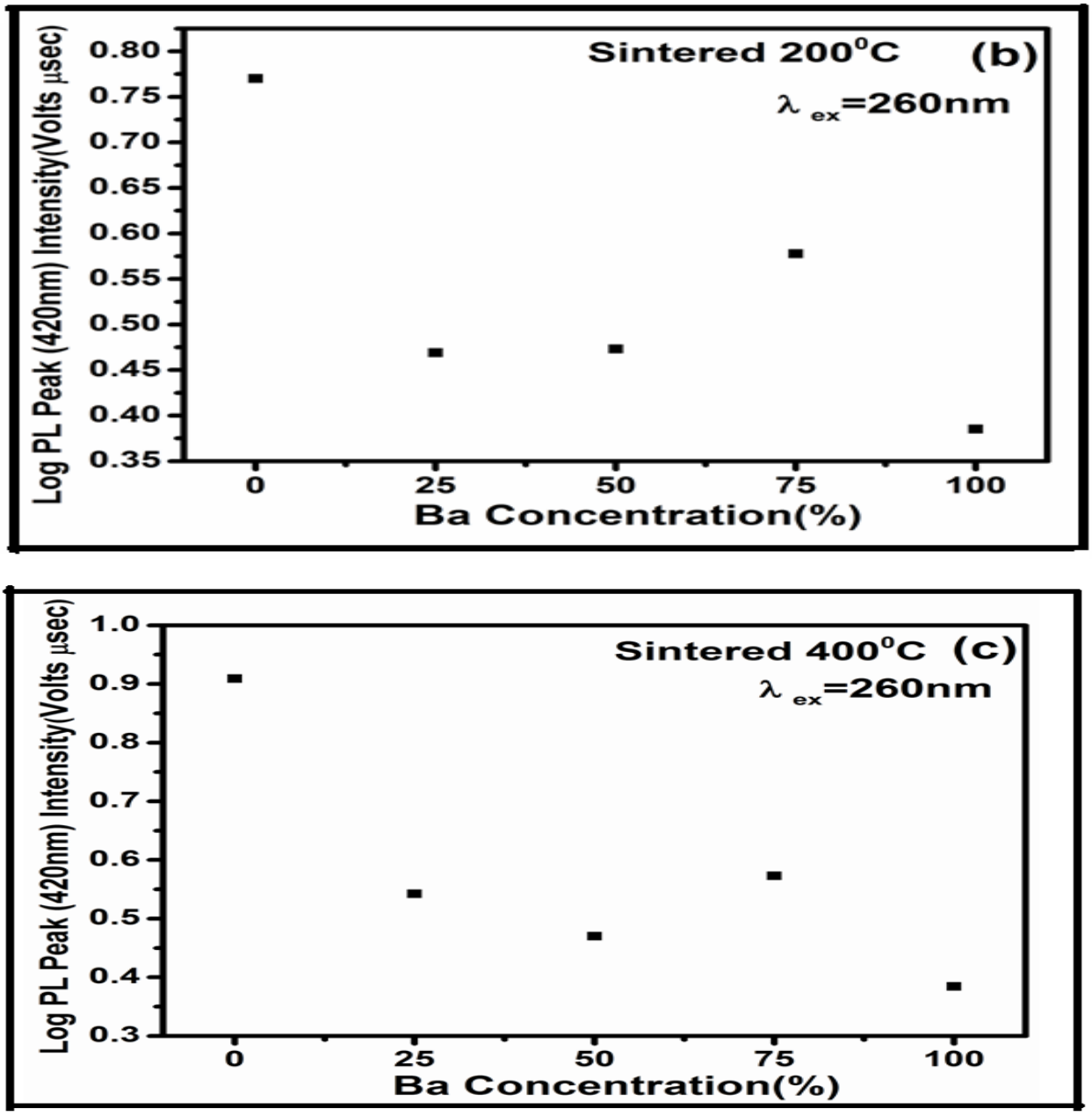

Figure 4.10(a-c): Variation of (420nm) Log PL peak intensity versus % Ba concentration for **(a)** Unsintered **(b)** 200^{0}C sintered **(c)** 400^{0}C sintered Mixed $Ba_xCa_{1-x}WO_4$ nanopowder samples.

4.5. Conclusion

The bandgap energy increases from increase in % Ba concentration except Mixed $Ba_{0.25}Ca_{0.75}WO_4$ nanopowder samples. This is because Eg of $BaWO_4$ is higher than that of $CaWO_4$ sample. Among all the samples (unsintered and sintered), maximum photoluminescence (PL) 420nm intrinsic peak intensity is emitted by sintered 400^{0}C C0 ($CaWO_4$) single phase

samples. This Intrinsic luminescence of $CaWO_4$ is due to the annihilation of self-trapped excitons forming excited $[WO_4]^{2-}$ anions giving rise to the broad emission spectra peaking around 420nm. More excitons in the C0 ($CaWO_4$) single phase lead to increase to number of recombination processes which increases emission intensity from the $[WO_4]^{2-}$ anions of C0 ($CaWO_4$) single phaseof the sample. Whereas Mixed $Ba_xCa_{1-x}WO_4$ nanopowder samples did not give enhanced 420 nm emissions in comparison with C0 ($CaWO_4$) single phase emission.

References

[1] M. Zamkov and C. S. S. R. Kumar, *UV-VIS and Photoluminescence Spectroscopy for Nanomaterials Characterization* (Springer Heidelberg New York Dordrecht London, **2013**).

[2] Y. Keereeta, S. Thongtem, and T. Thongtem, Enhanced photocatalytic degradation of methylene blue by $WO_3/ZnWO_4$ composites synthesized by a combination of microwave-solvothermal method and incipient wetness procedurePowder Technology, **284**:85-94 **(2015)**.

[3]X. Jiang, X. Zhao, L. Duan, H. Shen, H. Liu, T. Hou, F. Wang, Enhanced photoluminescence and photocatalytic activity of ZnO-$ZnWO_4$ nanocomposites synthesized by a precipitation method. Ceram. Int., **42**:15160–15165 **(2016)**.

[4] X. Xu, J. Gao, G. Huang, H. Qiu, Z. Wang, J. Wu, Z. Pan, and F. Xing, Fabrication of $CoWO_4$@$NiWO_4$ nanocomposites with good super capacitive performances,Electrochim. Acta, **174**:837-845 **(2015)**.

[5] Y. Wang, C. Shen, L. Niu, Z. Sun, F. Ruan, M. Xu, S. Shan, C. Li, X. Liu, and Y. Gong,High rate capability of mesoporous $NiWO_4$–$CoWO_4$ nanocomposite as a positive material for hybrid supercapacitor,Mater. Chem. Phys.,**182**:394-401**(2016)**.

[6] Y. V. B.De Santana, J. E. C. Gomes, L. Matos, G. H. Cruvinel, A. Perrin, C. Perrin, J.Andrès, J. A. Varela, and E. Longo, Silver Molybdate and Silver Tungstate Nanocomposites with enhanced photoluminescence, Nanomaterials and Nanotechnology,**4**:22 **(2014)**.

[7] J. M. Lin, C. L. Cheng, H. Y. Lin, and Y. F. Chen, Giant enhancement of band edge emission in ZnO and SnO nanocomposites,Opt.Lett.,**31**(21):3173-3175 **(2006)**.

[8] Y. Guo, G. Zhang, H. Gana, Y. Zhang, Micro/Nano-structured $CaWO_4/Bi_2WO_6$ composite: synthesis,characterization and photo catalytic properties for degradation of organic contaminants, Dalton Transaction,**41**:12697–12703 **(2012)**.

[9]L.S.Cavalcante,F.M. C. Batista, M. A. P. Almeida, A. C. Rabelo, I. C. Nogueira, N. C. Batista, J. A. Varela, M. R. M. C. Santos, E. Longobd and M. Siu Li Structural refinement, growth

process,photoluminescence and photo catalytic properties of (Ba_{1-x} $Pr_{2x/3}$) WO_4 crystals synthesized by the co precipitation method, RSC Advances,**2**:6438–6454 **(2012)**.

[10] Mohammad Eghbali-Arani, Saeid Pourmasoud, Farhad Ahmadi, Mehdi Rahimi-Nasrabadi, Vahid Ameri, Ali Sobhani-Nasab,Optimization and detailed stability study on coupling of $CdMoO_4$ into $BaWO_4$ for enhanced photo degradation and removal of organic contaminant, Arabian Journal of Chemistry, **13**(1):2425-2438**(2020)**.

[11] Jinkyu Han, Coray McBean, Lei Wang, Jessica Hoy, Cherno Jaye, Haiqing Liu, Zhuo-Qun Li, Matthew Y. Sfeir, Daniel A. Fischer, Gordon T. Taylor, James A. Misewich, and Stanislaus S. Wong, Probing Structure-Induced Optical Behavior in a New Class of Self-Activated Luminescent 0D/1D $CaWO_4$ Metal Oxide−CdSe Nanocrystal Composite Heterostructures, Chem. Mater., **27**:778−792 **(2015)**.

[12]H. Y. Lin, Y. Y. Chou, C. L. Cheng, and Y. F. Chen, Giant enhancement of band edge emission based on ZnO/TiO_2 nanocomposites, Optics Express,**15**(21):13832-13837 **(2007)**.

[13] S. Patole, M. Islam, R. C. Aiyer, and S. Mahamuni, Optics study nanojunctions, J. Mater. Sci., **41**:5602-5607 **(2006)**.

[14]Anukorn Phuruangrat, Titipun Thongtem, Somchai Thongtem, Barium molybdate and barium tungstate nanocrystals synthesized by a cyclic microwave irradiation, Journal of Physics and Chemistry of Solids,**70**:955–959 **(2009)**.

[15]L.S.Cavalcante, J. C. Sczancoski, L. F. Lima, Jr, J. W. M. Espinosa, P. S. Pizani, J. A. Varela and E. Longo,Synthesis, Characterization, Anisotropic Growth and Photoluminescence of $BaWO_4$,Crystal Growth Des.,**9**(2):1002-1012 (**2009)**.

[16]L.S.Cavalcante,J.C.Sczancoski,J.W.M.Espinosa,J.A.Varela,P.S.Pizani,E.Longo,Photolumine scent behavior of $BaWO_4$ powders processed in microwave-hydrothermal, Journal of Alloys and Compounds,**474**:195–200**(2009)**.

[17] J. Shen, Y. Li, and J. He, On the Kubelka–Munk absorption coefficient,Dyes and Pigment,**127**:187-188 **(2016)**.

[18] S.M.M. Zawawi, R. Yahya, A. Hassan, H.N.M.E. Mahmud, M.N. Daud, Structural and optical characterization of metal tungstates (MWO_4; M = Ni, Ba, Bi) synthesized by a sucrose templated method, Chem. Cent. J., **7**(80):1–10 **(2013)**.

[19] L.B. Light, J.S. Huebner, R.A. Vergens, How does light absorption intensity depends on molecular size? J. Chem. Educ., **71**(2):105–108 **(1994)**.

[20] P. Kubelka and F. Munk-Aussig, Zeit. F€ ur. Tech. Physik,**12**:593-601 **(1931)**.

[21] A. E. Morales, E. S. Mora and U. Pal, Use of diffuse reflectance spectroscopy for optical characterization of un-supported nanostructures, Rev. Mex. Fis. S,**53**:18–22 **(2007)**.

[22] R. A. Smith, *Semiconductors*, 2nd edition. Cambridge University Press, London, pp. 434 **(1978)**.

[23]R. Lacomba-Perales, J. Ruiz-Fuertes, D. Errandonea, D. Martinez-Garcia and A. Segura, Optical absorption of divalent metal tungstates: Correlation between the band-gap energy and the cation ionic radius,EPL (Europhysics Letters), **83**(3):37002 **(2008)**.

[24]M. Anicete-Santos, F. C. Picon, C. N. Alves, P. S. Pizani, J. A. Varela and E. Longo, The Role of Short-Range Disorder in $BaWO_4$ Crystals in the Intense Green Photoluminescence,J. Phys. Chem. C, **115**:12180-12186 **(2011)**.

[25]I.P. Carvalho, A.F. Lima, M.V. Lalic, Theoretical study of electronic and optical properties of the scheelite MWO_4 (M = Ca, Sr or Ba) compounds by applying the modified Becke-Johnson exchange-correlation potential, Opt. Mater., **92**:187–194**(2019)**.

[26] G. Blasse, B.C. Grabmaier, *Luminescent Materials*, pp. 77–78, (Springer, Berlin, **1994**).

[27]V. Panratova, L. Grigorjevaa, D. Millersa, S. Chernova, A.S. Voloshinovskii, Luminescence center excited state absorption in tungstates. J. Lumin., **94**:427–432 **(2001)**.

[28] H. Huang, S. Wang, N. Tian, Y. Zhang, A one-step hydrothermal preparation strategy for layered BiO_4/Bi_2WO_6 heterojunctions with enhanced visible light photo catalytic activities, RSC Adv., **4**:5561–5567 **(2014)**.

[29]V.B.Mikhailik, H. Kraus,Luminescence of $CaWO_4$, $CaMoO_4$, and $ZnWO_4$ scintillating crystals under different excitations, J. Appl. Phys., **97**:083523 **(2005)**.

[30]Anukorn P, Titipun T, Somchai T: Barium molybdate and barium tungstatenanocrystals synthesized by a cyclic microwave irradiation, J. Phys. Chem.Solids, **70(6)**:955–959**(2009)**.

[31]X.Jiang, X. Zhao, L. Duan, H. Shen, H. Liu, T. Hou, F. Wang, Enhanced photoluminescence andphotocatalytic activity of $ZnO\text{-}ZnWO_4$ nanocomposites synthesized by a precipitation method. Ceram. Int.,**42**:15160–15165 **(2016)**.

[32] L. S. Cavalcante, V. M. Longo, J. C. Sczancoski, M. A. P. Almeida, A. A. Batista, J. A. Varela,M. O. Orlandi,E. Longo,M. Siu Li, Electronic structure, growth mechanism and photoluminescence of $CaWO_4$ crystals, CrystEngComm, **14**:853-868 **(2012)**.

[33]Xiaoyu Sun, Xingang Li, Xiaodan Sun, Jian He, Binsheng Wang, Hydrothermal synthesis, characterization, and luminescence of $BaWO_4$ nanorods, J. Mater. Science: Materials in Electronics,**25**:1647–1651**(2014)**.

[34] Q. Yang, X. Zhou, Yu Takao Nukui, S.I. Saek, A. Tackeuchi, H. Tatsuoka, S. Liang, Time-resolved ultraviolet photoluminescence of $ZnO/ZnGa_2O_4$ composite layer, AIP Adv., **4**:027101 **(2014)**.

[35] Yu Qing Yanga,S.I.Saeki, T. Nukui, A. Tackeuchi, A. Ishida, H. Tatsuoka, Novel ultraviolet photoluminescence of $ZnO/ZnGa_2O_4$ composite layers, Appl. Surf. Sci., **256**:6928–6931 **(2010)**.

[36] B.K. Sharma, N. Khare, D. Haranath, Photoluminescence lifetime of Al-doped ZnO films in visible region, Solid State Communication,**150**:2341–2345 **(2010)**.

[37]V.M.Longo,E.Orhan, L.S. Cavalcante,S.L. Porto, J.W.M. Espinosa, J.A. Varela, E. Longo,Understanding the origin of photoluminescence in disordered $Ca_{0.60}Sr_{0.40}WO_4$:An experimental and first-principles study,Chemical Physics,**334**:180–188**(2007)**.

CHAPTER 5

DC, AC ELECTRICAL CONDUCTIVITY, DIELECTRIC PROPERTIES AND THERMOELECTRIC PROPERTIES OF $xBaWO_4/(1-x)CaWO_4$ NANOCOMPOSITES

5.1. Introduction

In the last two decades, researchers are working on nanocomposites materials for applicationsofelectronic devices because of their multifunctional properties. Dielectric materials have applications for devices such as microwave filters, voltage controlled oscillators, telecommunication technologies and dynamic access memory. In order to improve electrical properties of (AWO_4) Scheelite and Wolframite type materials significant research has been done **[1–3]**. In recent years interfacial contribution to the overall conductivity of electroceramic materials has been rapidly growing for better knowledge, **[4, 5]** and may have reached a peak point in the consideration of nanocrystalline materials. In these materials the conduction behaviour likely becomes interfacially controlled due to the extremely high density of the interface (grain boundary**) [6-9]**.Physical properties of the nanocomposites are determined by properties of the two separate phases and interaction between them **[10-12]**. There are reports available with ceramic-ceramic nanocomposites improving electrical properties **[13, 14]**. Many approaches such as doping [**15-17]**, sintering**[18,19]** and different preparation methods**[20-22]** have been done to revive the conductivity of oxides semiconductors.Researchers have proved one of the mosteffective methods for improving the dielectric properties of materials with fabrication of heterostructure nanocomposites **[23, 24]**.Challenging to have interfacial effects in homostructure metal oxide nanocomposites. The researcher found that nanocompositeswith space charge layer (SCL) formation also raises the electrical conductivity of metal oxides **[11, 25, 26]**. Also many researchers found that thermoelectric power studies in semiconductor and dielectric materials, phonons (quantized lattice vibrations) are the main energy carriers for heat conduction and this is generally true as long as the nanocomposites forms crystalline structures **[27-29]**.

We are reporting elaborate work done on the DC, AC electrical conductivity, Dielectric properties [dielectric constant (**ε´**) and loss tangent (tanδ)] at room temperature (RT) and above room temperature thermoelectric (TE) power properties of the same nanocomposites which were prepared & characterized for the photoluminescence (PL) studies. It is observed that C2 ($0.5BaWO_4/0.5CaWO_4$) nanocomposite which showed maximum photoluminescence (PL) emission was also found to have higher DC,AC electrical conductivity, higher dielectric constant

(ε′) [**ε′=8190**] which is approximately **3 times & 8 times** more than that of C0($CaWO_4$)[**ε′=2630**] & C4($BaWO_4$)[**ε′=970**] single phases respectively measured at room temperature(RT) at lower frequencies(20Hz).We have explained the reason for the enhanced DC, AC electrical conductivity and dielectric properties [dielectric constant (**ε′**)] at room temperature (RT). The inspiration to explore thermoelectric power study above room temperature (RT) is that the crystallite size doesn't change much when C0($CaWO_4$) & C4($BaWO_4$) nanosamples weresintered till 400^0C **[30, 31**]. So there was interest in exploring the thermoelectric power properties of $xBaWO_4/(1-x)\ CaWO_4$ nanocomposites above room temperature (RT). We are also reporting that C3 ($0.75BaWO_4/\ 0.25CaWO_4$) nanocomposites is an efficient thermoelectric power material at higher temperature (408.8K) because of enhanced power factor (PF) of figure of merit(ZT) even though C0 ($CaWO_4$) and C4($BaWO_4$)nanosamples are not good thermoelectric power materials. The reason for the same has been discussed.

5.2. Results and Discussions

5.2.1. Non-linear properties and DC conductivity analyses

J (A/cm^2) – E (V/cm) characteristics & DC conductivity of the nanocomposites were measured by two electrodes method. It is one of the simplest and cost effective methods. For investigation of varistor effect, the current–voltage i.e. (J-E) characteristics is the main proof. Varistor phenomenon is featured by the breakdown voltage, non-linearity coefficient and grain boundary resistance. Different parameters are important in the manufacturing of an ideal varistor such as breakdown voltage and nonlinear coefficient **[32]**. The current density (J)-electric field (E) characteristics of prepared nanocomposites are studied to evaluate theirelectrical properties including breakdown voltage, non-linearity coefficient and grain boundary resistance. The current- voltage i.e. (J-E) characteristics of the nanocomposites were measured by applying different voltages (1-10Volts) to the nanocomposites and recording the current through the nanocomposites. DC conductivity measurements are carried out by recording the current through nanocomposites of a fixed voltage. DC conductivity & non-linearity coefficients (α) of the nanocomposites were calculated by the following **equation (5.1) & (5.2)[33]**.

$$\boldsymbol{\sigma_{dc} = \frac{L}{RA}} \qquad \textbf{(5.1)}$$

Where (L), (R) and (A) is the thickness, resistance and area of the pellets respectively.

$$\boldsymbol{\alpha = \frac{\log(I_2/I_1)}{\log(V_2/V_1)}} \qquad \textbf{(5.2)}$$

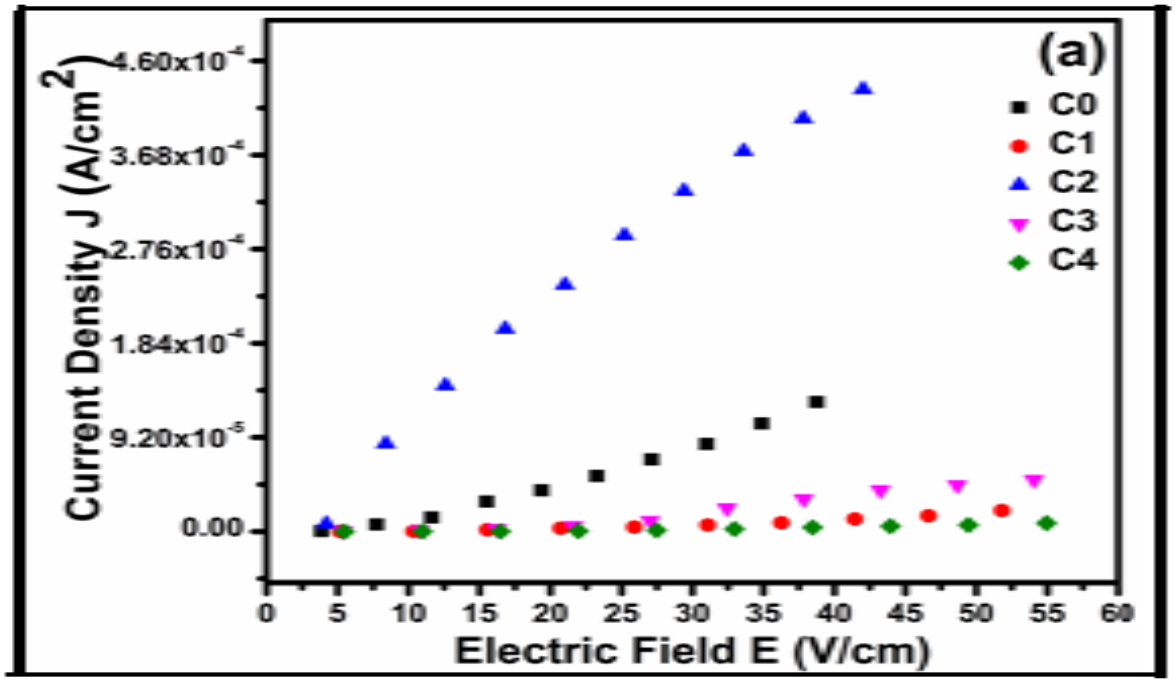
(a)
C0
C1
C2
C3
C4
Current Density J (A/cm^2)
4.60x10^{-4}
3.68x10^{-4}
2.76x10^{-4}
1.84x10^{-4}
9.20x10^{-5}
0.00
0 5 10 15 20 25 30 35 40 45 50 55 60
Electric Field E (V/cm)

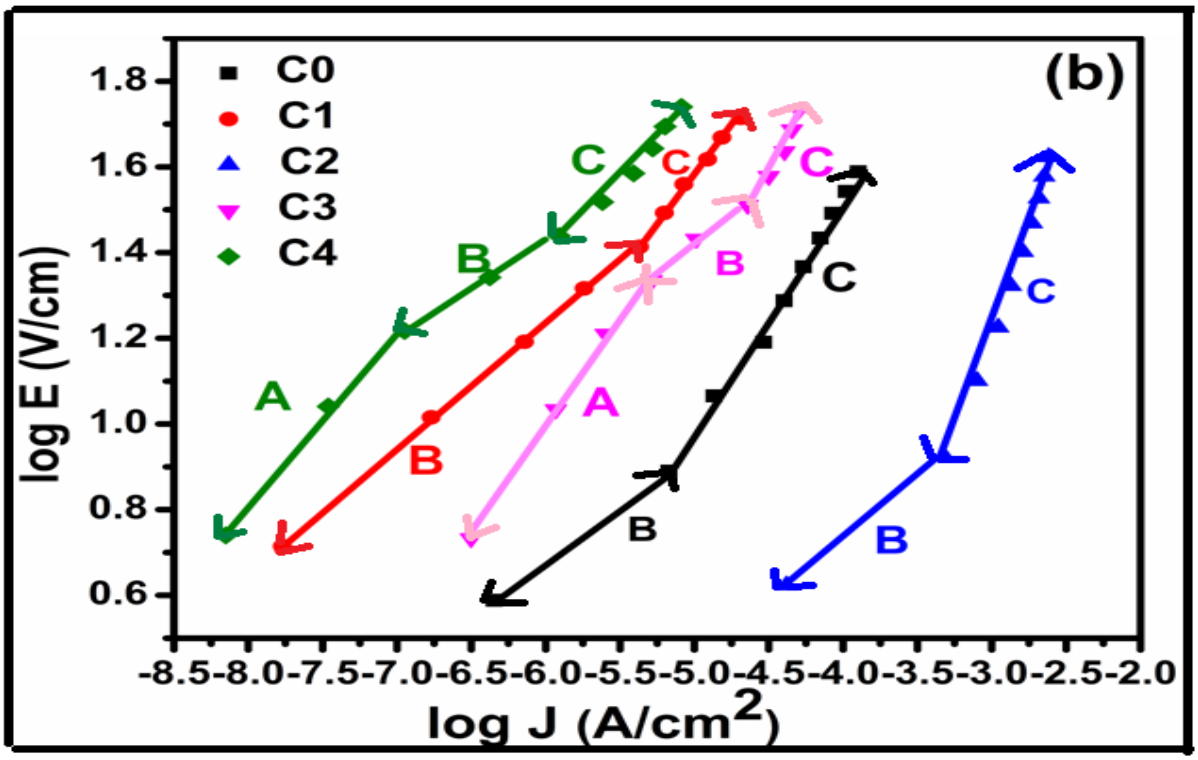
(b)
C0
C1
C2
C3
C4
log E (V/cm)
1.8
1.6
1.4
1.2
1.0
0.8
0.6
A
B
C
-8.5-8.0-7.5-7.0-6.5-6.0-5.5-5.0-4.5-4.0-3.5-3.0-2.5-2.0
log J (A/cm^2)

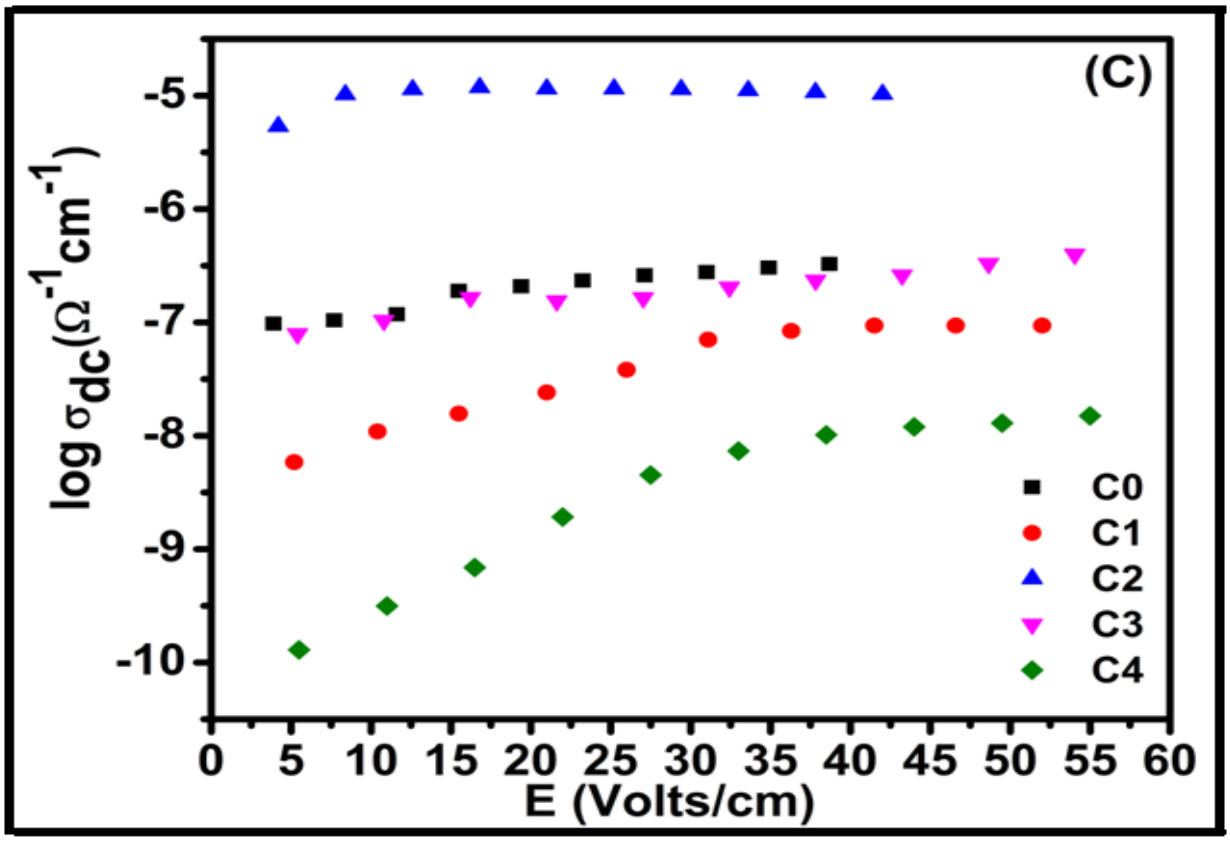
(C)
log σdc(Ω-1cm-1)
-5
-6
-7
-8
-9
-10
0 5 10 15 20 25 30 35 40 45 50 55 60
E (Volts/cm)
C0
C1
C2
C3
C4

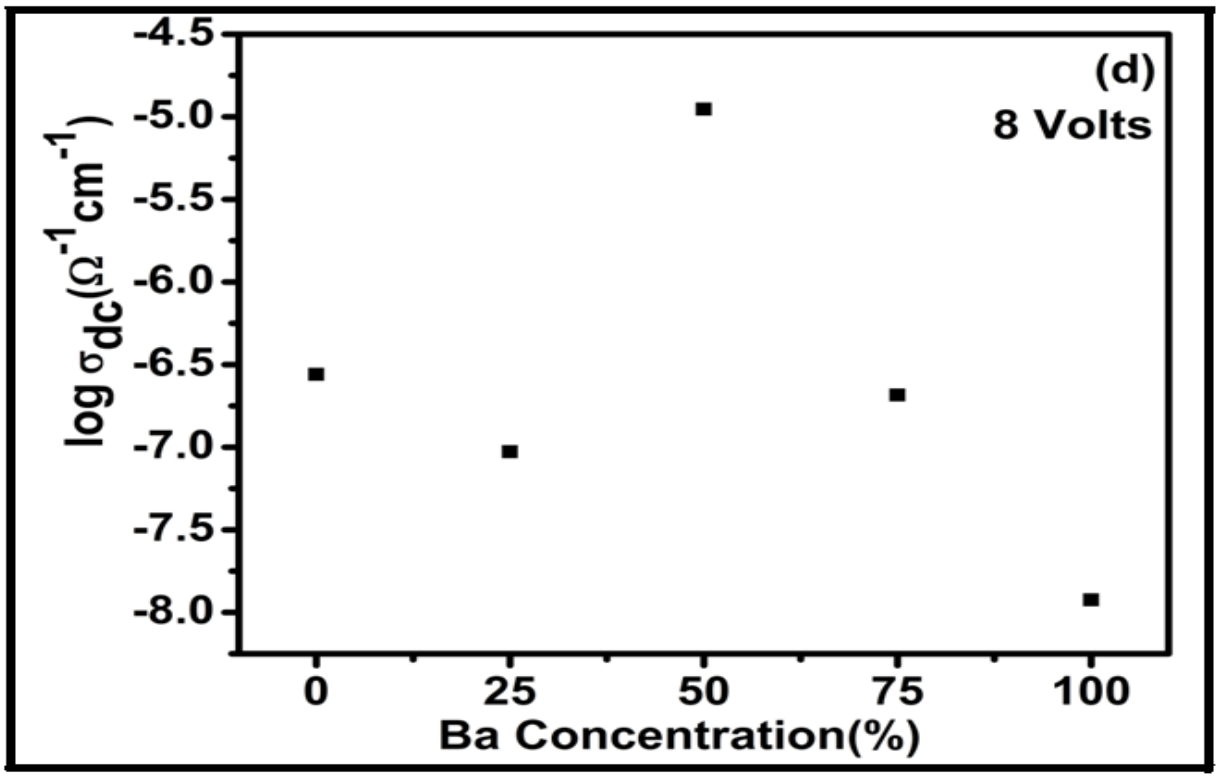
(d)
8 Volts
log σdc(Ω-1cm-1)
-4.5
-5.0
-5.5
-6.0
-6.5
-7.0
-7.5
-8.0
0 25 50 75 100
Ba Concentration(%)

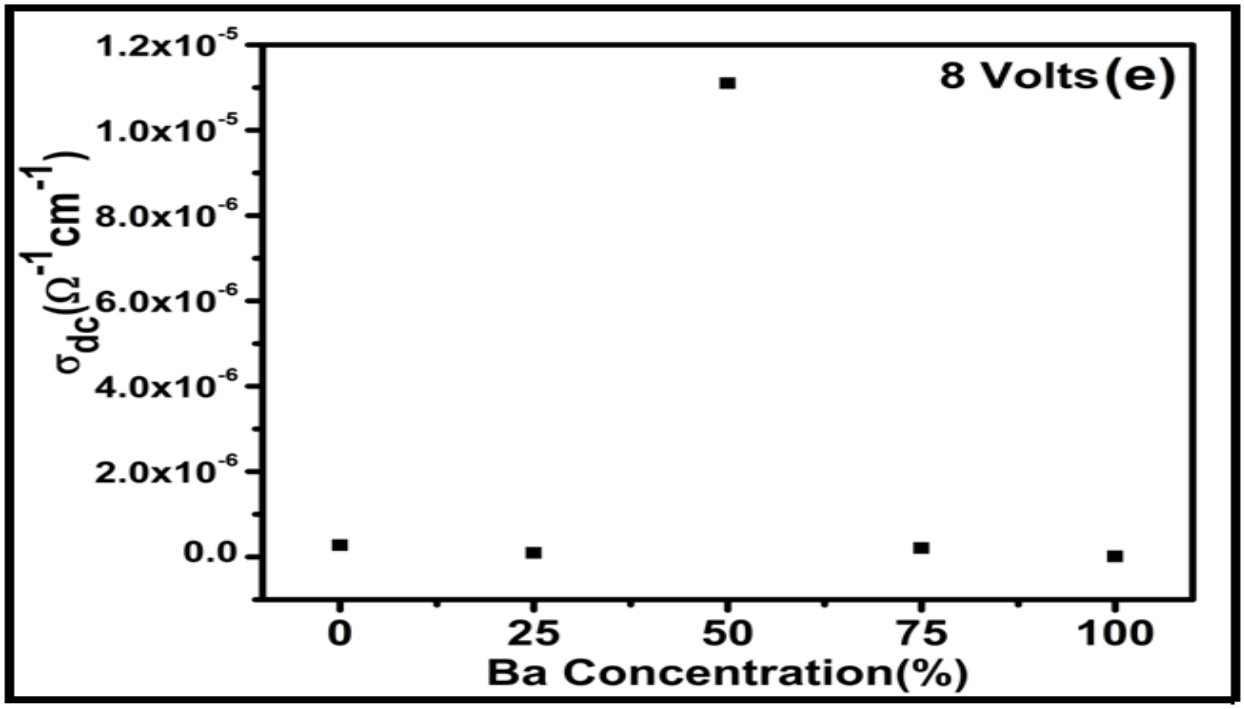

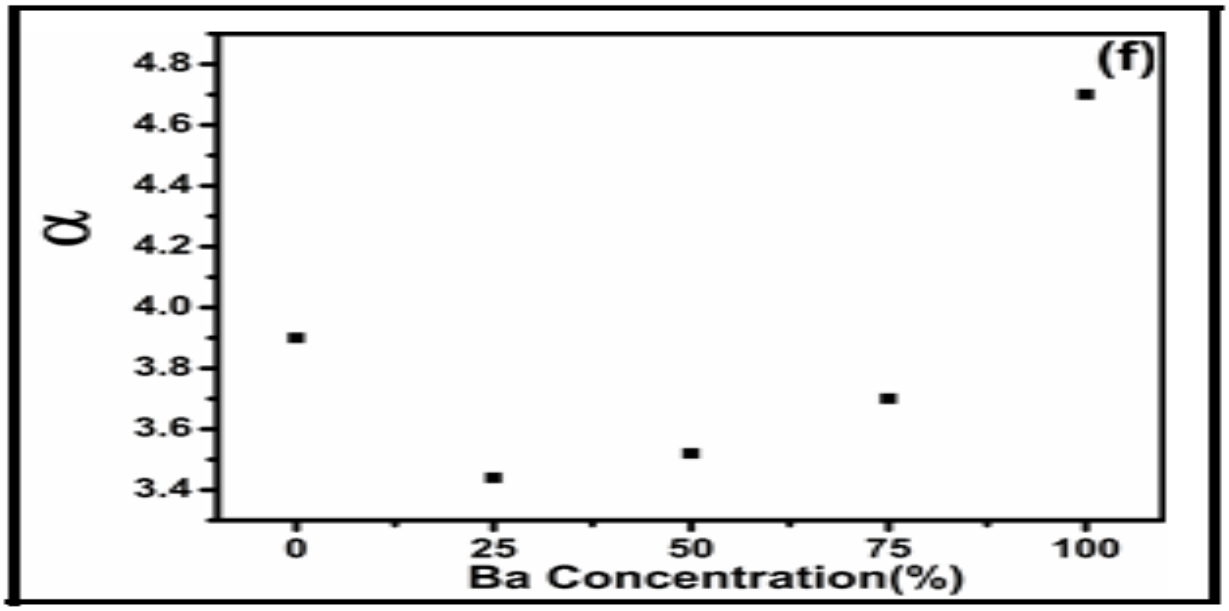

Figure 5(a-f): (a) Current density J (A/cm^2)-E (V/cm) characteristics of nanocomposites at room temperature (RT). **(b)** Log E (V/cm)-log J (A/cm^2) characteristics of nanocomposites at room temperature (RT). **(c)** Log (σ_{dc}) -E (Volts/cm) of nanocomposites at room temperature (RT). **(d)** Log σ_{dc}-%Ba concentration of nanocomposites at room temperature. **(e)** σ_{dc}-%Ba concentration of nanocomposites at room temperature. **(f)** Alpha (α) - % Ba concentration of nanocomposites at room temperature.

Figure 5(a) plot shows the current density J (A/cm^2)-E (V/cm) characteristics of $xBaWO_4/(1-x)CaWO_4$ nanocomposites. From this plot it is observed that the J (A/cm^2) - E (V/cm) characteristics of all nanocomposites show non-ohmic behavior. The non-linearity J (A/cm^2) - E (V/cm) characteristics arises due to grain boundaries segregated with metal oxide additives **[34-36]**. The **Figure 5(b)** plots (logE-logJ) show three distinct regions for C3 and C4 nanocomposites due to the presence of insulating layer between the grain boundaries **[37-39]**. The low current density region which is known as pre-switching or pre-breakdown region (region-A) & physically corresponds to the transport of a very low level leakage current through the varistor below the breakdown or switched region. At higher fields, current density increases very rapidy and particular field called breakdown voltage or switching region(region-B) current density becomes very high.The current density becomes highly non-linear in switching region(region-B), which is generally important for the device fabrications. This region can be expressed in terms of the power law, i.e. $J = kE^{\alpha}$, where (α) is the important parameter in manufacturing of an ideal varistor denoted as non-linearity coefficient, (k) is a constant of proportionality,(J) is the density of current and (E) is electric field **[39]**. Above breakdown voltage or switching region (region-B), the current density is constant & independent of the field.This region is known as up-turn region or high current density region (region-C). All nanocomposites above breakdown voltage or switching region shows very high current region (region-C) & this phenomena known as acoustic-electric saturation.This is a consequence of the piezoelectric effect **[38, 40]**. The values of breakdown and upturn voltages for all the samples are given in **Table 5.1.** It is seen from **Figure 5(b)** that C0 ($CaWO_4$), C1 ($0.25BaWO_4/0.75CaWO_4$) & C2 ($0.5BaWO_4/0.5CaWO_4$) nanocomposites show presence of two regions B & C. While absence of (region-A) is due to the negligible grain boundary resistance. C3($0.75BaWO_4/0.25CaWO_4$) nanocomposites and C4 ($BaWO_4$) single phase show three regions (A, B & C) due to the presenceof non-negligible grain boundary resistance (**Table 5.2)**. The non-linearity coefficient (α) of the nanocomposites from the (J-E) plots were calculated, using **equation (2)**. For the ideal varistor non-linearity coefficient value is ($\alpha = \infty$). The calculated non-linearity coefficient (α) values lies in the range of 3.44 to 4.70(**Table 5.2**) for the nanocomposites.The non-linearity coefficient (α) of C2 ($0.5BaWO_4/ 0.5CaWO_4$) nanocomposites calculated in the region B is 3.52. Due to the observed (**Table 5.1**) higher breakdown voltages (4,3Volts) at room temperature (RT) for samples C3 ($0.75BaWO_4/ 0.25CaWO_4$) & C4 ($BaWO_4$)

respectively they could be considered as promising materials for fabrication of low-voltage varistors. **Figure 5(c)** plot [log (σ_{dc}) - E (V/cm)] shows as electric field increases DC conductivity increases initially and then remains constant for all nanocomposites. **Figure 5(d)** plot shows log conductivity at 8 volts versus % Ba concentration of all nanocomposites and the values are given in **Table 5.3**. DC conductivity is maximum for C2 ($0.5BaWO_4/0.5CaWO_4$) nanocomposites ($\sigma=1.11x10^{-5}\ \Omega^{-1}cm^{-1}$). It is approximately **40 times** greater than that of C0($CaWO_4$)($\sigma=2.76x10^{-7}\ \Omega^{-1}\ cm^{-1}$) and **1008** times greater than that of C4 ($BaWO_4$) [$\sigma=0.11x10^{-7}\Omega^{-1}\ cm^{-1}$] single phase samples.The observed conductivity of C2($0.5BaWO_4/\ 0.5CaWO_4$) nanocomposites is maximum and remains higher than other nanocomposites due to formation of space charge layer (SCL)at the boundaries of two phases in the sample **[11,25,26]**. **Figure 5(e)** plot shows DC conductivity (σ_{dc}) at 8 volts versus % Ba concentration. It is observed that the DC conductivity is significantly maximum for C2 ($0.5BaWO_4/0.5CaWO_4$) nanocomposites. **Figure 5(f)** plot shows alpha (α) versus % Ba concentration of the nanocomposites. It is observed that alpha (**α)** for nanocomposites are less than the single phase C4 ($BaWO_4$) and C0 ($CaWO_4$) samples and is maximum for C4 ($BaWO_4$) sample. This may be because of the possible higher conduction across thegrain boundaries between the two phases $BaWO_4$ and $CaWO_4$ due the (SCL) formation than the condution across the grain boundaries between the similar phases.

Table 5.1: Values of non-linearity coefficient (α)of $xBaWO_4/(1-x)CaWO_4$ nanocomposites

Samples	Breakdown Voltage (V_B) (Volts)	UpturnVoltage (Volts)
C0	-	2
C1	-	5
C2	-	2
C3	4	6
C4	3	5

Table 5.2: Non-linearity coefficient (α) and J-E characteristics parameters of $xBaWO_4/(1-x)CaWO_4$ nanocomposites

Samples	Thickness of sample (D) mm	Average Grain size (d) (nm)	Number of Grain Boundaries (n=D/d)	Grain Boundary Voltage ($V_{gb}=V_B/n$) (Volts)	Breakdown Field ($E_B=V_{gb}/d$) (V/m)	Non-Linear coefficient ($\alpha=\frac{\log(I_2/I_1)}{\log(V_2/V_1)}$)	Grain Boundary Resistance ($R_{gb}=V_{gb}/I$) (Ω)
C0	2.58	63	$0.04x10^6$	-	-	3.90	-
C1	1.93	71	$0.03x10^6$	-	-	3.44	-
C2	2.38	101	$0.02x10^6$	-	-	3.52	-
C3	1.85	111	$0.02x10^6$	$2x10^{-4}$	1797	3.70	$0.14x10^6$
C4	1.82	122	$0.01x10^6$	$3x10^{-4}$	2457	4.70	$6.7x10^6$

Table 5.3: Values of conductivity (σ_{dc}) calculated at 8 volts of $xBaWO_4/(1-x)CaWO_4$ nanocomposites

Samples	σ_{dc} ($\Omega^{-1}cm^{-1}$)	log σ_{dc} ($\Omega^{-1}cm^{-1}$)
C0	$2.76x10^{-7}$	-6.559
C1	$0.93x10^{-7}$	-7.028
C2	$1.11x10^{-5}$	-4.954
C3	$2.06x10^{-7}$	-6.684
C4	$0.11x10^{-7}$	-7.924

5.2.2. Non-linear properties and DC conduction mechanism analyses

When two oxides with similar structures (homophase interface) or different structures (heterophase interface) is formed resulting in a local space charge region in the interface region due to the, redistribution electronic and ionic defects takes place **[11]**. In Scheelite tungstates, major defects are oxygen vacancies and AC, DC electrical conductivity is mainly due to electron charge carriers transfers occurs below 500^0C **[41, 42]**.Since grain size of C0 ($CaWO_4$) single phase is lower than C4 ($BaWO_4$) single phase respectively. In case of all nanocomposites follows this statement denoting grain size is inverse of number of grain boundaries. All nanocomposites show non-linear characteristics behavior due to effective potential barriers (thin or thick insulating layer) at the grain boundaries allowing electrons as a free conduction path which is dependable for the low non-linearity coefficient (α) similar like varistor behavior **[39]**. This effective potential barrier (thin or thick insulating layer) formed in nanocomposites may be due to intra ($BaWO_4$/$CaWO_4$) or inter ($BaWO_4$/$BaWO_4$ and $CaWO_4$/$CaWO_4$) particle blending. All the nanocomposites non-linearity is controlled by effective potential barrier (thin or thick insulating layer) situated within the intra ($BaWO_4$/$CaWO_4$) grains at the grain–grain interface. There is prevention of electrons from crossing into adjacent grains at low applied voltages and all nanocomposites behave as insulating manner, whereas electrons can tunnel into adjacent grains at higher voltages, resulting highly conducting nanocomposites **[43]**. It has been noticed that both thick (1 μm) and thin (<500Å) individual grain boundaries form interfacial layers may show varistor behavior **[44]**. The crystallite size of $CaWO_4$ phase is lower than $BaWO_4$ phase. Also DC conductivity of C0 ($CaWO_4$) single phase is higher due to unit cell volume is lower & its molecular density is higher which signifies higher number of cells per unit volume resulting increase in number of crystallites per unit volume which gives formation of oxygen ion vacancies as a defect center [WO_3] according to the reaction $[WO_4]^{2-} \rightarrow WO_3 + \frac{1}{2} O^{2-} + 2e^-$ showing more number of [WO_3] defects and electrons ($2e^-$) available resulting higher oxygen capturing electron tendency which gives rise to increase in intrinsic charge carriers (electrons) resulting higher conductivity of C0 ($CaWO_4$) single phase in comparison with C4 ($BaWO_4$) single phase,since both belongs to Scheelite structure **[45-47]**. Also DC conductivity of C0 ($CaWO_4$) single phase is higher as compared to C4 ($BaWO_4$) single phase due to band gap (E_g) is lower in C0 ($CaWO_4$) & higher in C4 ($BaWO_4$) single phases respectively **[30]**. Also C0 ($CaWO_4$) single

phase shows small grain size allowing effective potential barrier (thin insulating layer) formed consisting of increase in number of crystallites per unit volume i.e. more n-type charge carriers ($2e^-,\frac{1}{2}O^{2-}$) resulting absence of switching voltage/breakdown voltage(i.e. region A) but small non-linearity coefficient(α) with negligible grain boundary resistance, whereas C4 ($BaWO_4$) single phase shows large grain size allowing effective potential barrier(thick insulating layer) formed resulting less charge carriers($2e^-,\frac{1}{2}O^{2-}$) due to unit cell volume higher & its molecular density is lower resulting decrease in number of crystallites per unit volume showing presence of switching voltage/breakdown voltage (i.e. region A) with higher non-linearity coefficient(α) with non-negligible grain boundary résistance.Similarly C1($0.25BaWO_4/0.75CaWO_4$) nanocomposites shows presence of effective potential barrier (thin insulating layer) formed resulting more number of charge carriers($4e^-,O^{2-}$) due to $CaWO_4$ phase unit cell volume lower and its molecular density higher resulting increase in number of crystallites per unit volume showing absence of switching voltage/breakdown voltage (i.e. region A) but small non-linearity coefficient(α) with negligible grain boundary resistance, whereas C3($0.75BaWO_4/0.25CaWO_4$) nanocomposites show presence of effective potential barriers(thick insulating layer) formed resulting less charge carriers ($4e^-$, O^{2-}) due to $BaWO_4$ phase unit cell volume higher & its molecular density is lower resulting decrease in number of crystallites per unit volume, showing presence of switching voltage/breakdown voltage (i.e. region A) resulting higher non-linearity coefficient(α) with non-negligible grain boundary resistance. Since interface is formed at room temperature (RT) & among all nanocomposites maximum interface occurs for C2 ($0.5BaWO_4/0.5CaWO_4$) nanocomposites which is seen on the surface (nanoparticles are randomly shaped) of the C2 ($0.5BaWO_4/0.5CaWO_4$) nanocomposites along with interface formation which is confirmed from HRTEM image **[30]**. This interface is treated as grain boundaries which gives rise to collection of defects at the interface & maximum defects are collected for C2 ($0.5BaWO_4/0.5CaWO_4$) nanocomposites. So the hopping conduction is reduced, inhibiting decreasing grain boundary resistance/interface in nanocomposites ceramics. This is confirmed from frequency dependence on loss tangents (tan δ) of the nanocomposites measured at room temperature (RT) from **[Figure 6(c)]** which shows loss tangents (tan δ) peaks shifts occur to C2 ($0.5BaWO_4/0.5CaWO_4$) nanocomposites for higher frequency side showing more collection of defects at grain boundaries or interface region**[48]**. On the other hand, more interface states are produced at the

intra ($BaWO_4/CaWO_4$) grains which can be explained by space charge layer (SCL) model. The formation of space charge layer (SCL) model is suitable mechanism for explaining enhanced DC conductivity and non-linearity coefficient (α) existing for C2 ($0.5BaWO_4/0.5CaWO_4$) nanocomposites. In C2 ($0.5BaWO_4/0.5CaWO_4$) nanocomposites, at the interface oxygen vacancies defects get accumulated, generating positive charge core. This is compensated electrostatically by forming an electron and polarons around the positive ions adjacent to the interface forming the space charge layer (SCL) and screening the oxygen vacancies **[11, 25, 26]**. As net effect of the (SCL) formation is that the overall conductivity of the interfacial region of C2 ($0.5BaWO_4/0.5CaWO_4$) nanocomposites increases due to the accumulation of charges forming space charge layer (SCL) and also decrease of the activation energy for charge migration mechanisms **[25]**. Such (SCL) effects of C2 ($0.5BaWO_4/0.5CaWO_4$) nanocomposites resulting an additional interfacial electronic conductivity charge carriers which increases total conductivity by formation of oxygen ion vacancies as a defect center [WO_3] according to the reaction $2[WO_4]^{2-} \rightarrow 2[WO_3] + O^{2-} + 4e^-$ showing maximum number of 2[WO_3] defects and electrons($4e^-$) availableresulting much higher oxygen capturing electron tendency which increases intrinsic charge carriers (electrons i.e.$4e^-$, O^{2-}) tremendously showing higher conductivity of C2 ($0.5BaWO_4/0.5CaWO_4$) nanocomposites and negligible grain boundaries resistance of a several orders of magnitude than C0 ($CaWO_4$) and C4 ($BaWO_4$) single phases respectively**[47]**. Also occurrence of type I band alignment interfacing between them of C2 ($0.5BaWO_4/0.5CaWO_4$) nanocomposites charge transfer of $BaWO_4$ phase to $CaWO_4$ phase take place which shows increase in conduction between intra ($BaWO_4/CaWO_4$) grains resulting maximum conductivity and absence of switching voltage/breakdown voltage but shows small non-linearity coefficient (α) giving negligible grain boundary résistance in C2 ($0.5BaWO_4/0.5CaWO_4$) nanocomposites.

5.2.3. Frequency dependence of the dielectric constant, loss tangent (tanδ) & AC conductivity analyses

5.2.3.1. Frequency dependence of the dielectric constant (ε′)

All thenanocomposites dielectric constant (**ε′**) was calculated using the following **equation (5.3) [49]**.

$$\varepsilon' = \frac{Cd}{A\varepsilon o} \qquad (5.3)$$

Where ε', ε_0, C, A and d are the dielectric constant, permittivity at free space, capacitance, area and thickness of the pellets respectively.

Thedielectric constant (ε′) decreases with increasing frequency which is shown in **Figure 6(a)** and attributed to the Maxwell-Wagner polarization model **[50]**. According to this model, the dielectric materials consist of grains and grain boundaries as shown in **Figure 6(b)**.

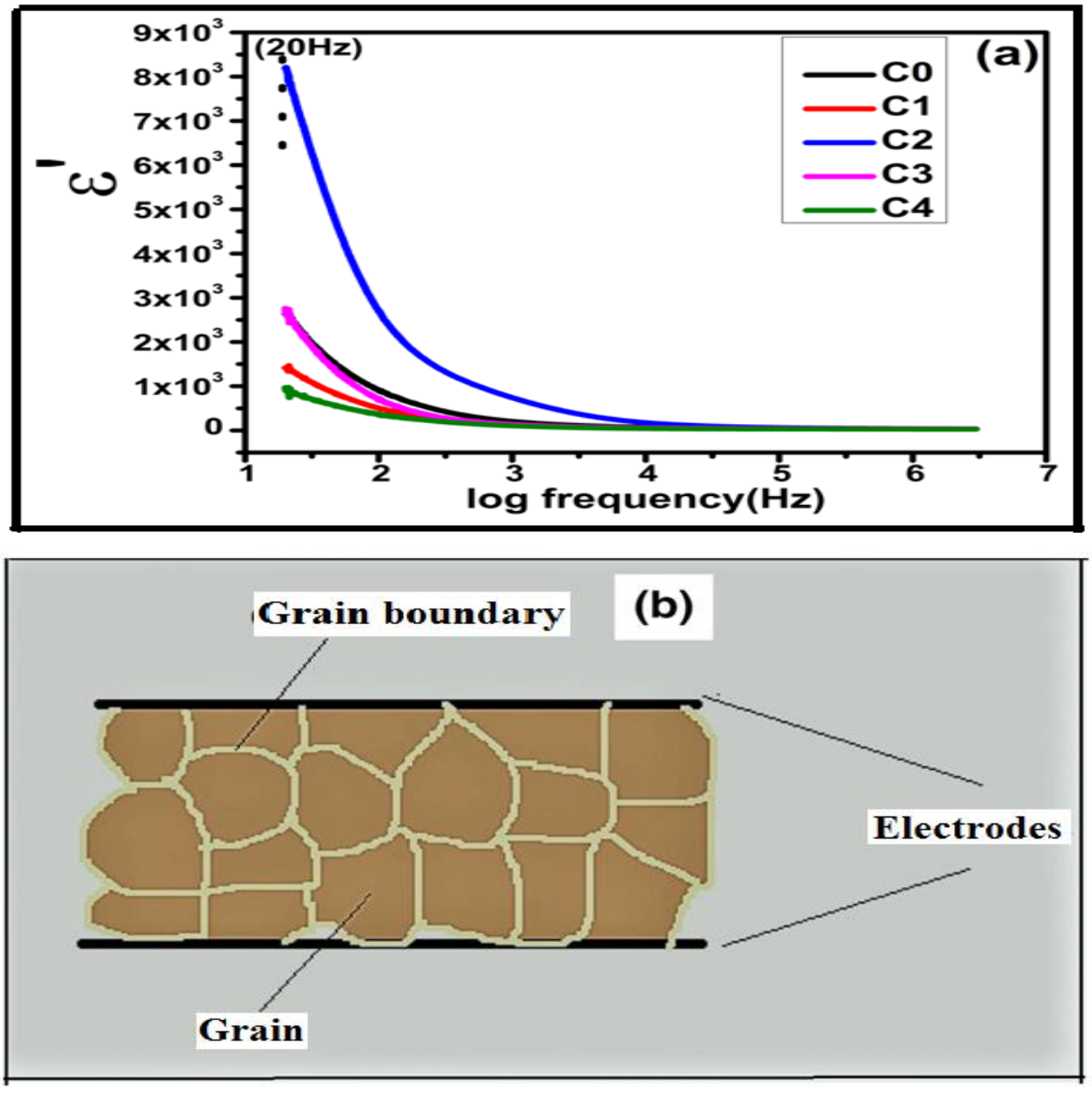

Figure 6(a-b):(a) Frequency dependence on dielectric constant (ε′) of $xBaWO_4/(1-x)CaWO_4$ nanocomposites measured at room temperature (RT). **(b)** Schematic structure of the sample of electrodes.

CHAPTER 5

The enhanced dielectric constant (ε′), i.e., stored energy, at low frequencies (20Hz) are assigned to whichever excellent conductivity, interfacial polarization, electrode polarization(EP) or combination of electronic, ionic and orientation polarization. Electrode polarization (EP) gives rise to both dielectric constant & dielectric loss [(ε′) and (ε″)] owing to occurrence of space charges with the interfaces between the electrode and the sample of examination **[51]**.All nanocomposites were investigated under the same conditions which are having similar constituents. If EP has shown maximum effect on a certain nanocomposites, it supposed to shown in all other nanocomposites as well. Therefore the high value of (ε′) is assigned to conductivity and interfacial polarization. Moreover crystallite size of C0 ($CaWO_4$) single phase is lower than C4 ($BaWO_4$) single phase and plays an important role in dielectric constant (ε′) [**52, 53]**.The dielectric constant (ε′) at lower frequencies (20Hz) is higher for C0 ($CaWO_4$) single phase due to lower unit cell volume and higher molecular density which signifies higher number of cells per unit volume which in turn showing increase in number of crystallites per unit volume and on the surface accumulation of the dipoles increases which gives increased surface charge polarization **[45]**.As a result, significantly there is an increase in dielectric constant (ε′) of the C0 ($CaWO_4$) single phase at low frequencies (20Hz). The reduction in crystallite size in C0 ($CaWO_4$) single phaseincreases surface to volume ratio and an enhancement in over all grain boundaries of the crystallites per unit volume.Thus increase in grain boundary and enrichment of surface charge polarization provide enhancement of dielectric constant at lower frequencies(20Hz) of C0 ($CaWO_4$) single phase as compared to C4 ($BaWO_4$) single phase respectively**[54]**.The frequency dependence dielectric constant **(**ε′=8190) at 20Hz frequency is found to be maximum for C2 ($0.5BaWO_4/0.5CaWO_4$) nanocomposites and it is approximately **3 & 8 times** greater than that of C0 ($CaWO_4$) (ε′=2630) and C4 ($BaWO_4$) (ε′=970) single phases respectively.For increased dielectric constant (ε′) in C2 ($0.5BaWO_4/0.5CaWO_4$) nanocomposite interface plays an important role. Accumulation of dipoles on surface increases due to interface between the two phases of the nanocomposites leads to increased surface charge polarization of the C2 ($0.5BaWO_4/0.5CaWO_4$) nanocomposites and increasing the dielectric constant (ε′)**[55]**.This maximum dielectric constant (ε′) of C2 ($0.5BaWO_4/0.5CaWO_4$) nanocomposites is due to interface occurring owing to type-I band alignment between the two phases. The charge carriers are easily migrated through the grains but get accumulated at grain boundaries which lead to higher interfacial polarization resulting high dielectric constant (ε′) at lower frequencies. Another reason for higher dielectric

constant (ε′) is due to accumulation of unbounded charge carriers at the interfaces, where they do not have enough energy to overcome the potential barrier that restricts them at lower frequencies **[56,57]**.The interfacial polarization decreases and becomes negligible with increasing frequency, only dipolar and electronic polarization contribute to the dielectric constant. Therefore with increasing frequency dielectric constant (ε′) decreases and showing constant value at higher frequencies. Room temperature (RT) measurement of dielectric constant (ε′) observed at 20 Hz of all nanocomposites is listed in **Table 5.4**.

Table 5.4: Dielectric Constant (ε′) at 20Hz of $xBaWO_4$/ (1-x) $CaWO_4$ nanocomposites

Samples	ε′	tan δ	$\sigma_{ac}(\Omega^{-1}cm^{-1})$
C0	2630	1.4530	$4.25x10^{-7}$
C1	1415	1.1100	$1.75x10^{-7}$
C2	8190	0.7150	$7.48X10^{-7}$
C3	2759	1.2990	$3.98x10^{-7}$
C4	970	0.9584	$1.03x10^{-7}$

5.2.3.2. Loss tangent (tanδ) analyses

Figure 6(c) shows the frequency dependence on loss tangents (tanδ) at room temperature (RT) of all nanocomposites. The angle (δ) between the vector for the amplitude of the total current and that for the amplitude of charging current is called the loss angle and is less than 90^o.The loss tangent or dissipation factor or dielectric loss tangent is the tangent of the angle, which signifies dielectric loss factor. The co-relation between dielectric constant (ε′) and dielectric loss (ε″) factor is given by **equation (5.4) [58]**.

$$\tan \delta = \frac{\varepsilon''}{\varepsilon'} \qquad (5.4)$$

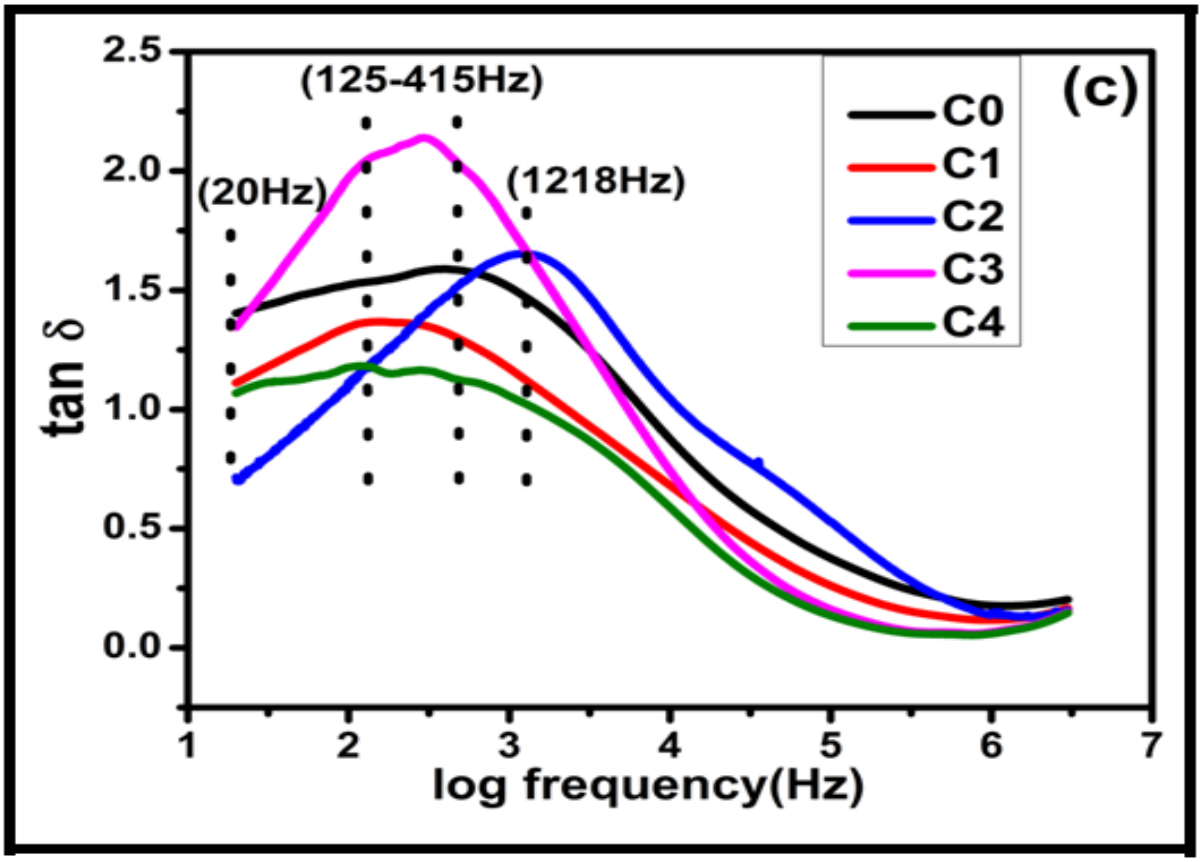

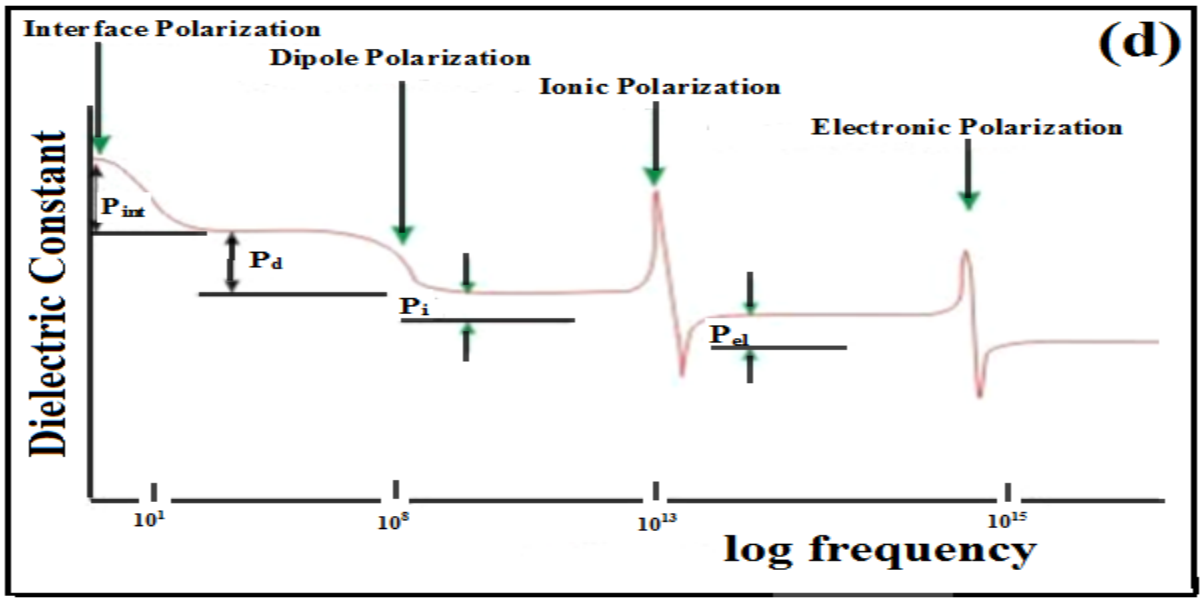

Figure 6(c-d) :(c) Frequency dependence on loss tangents (tan δ) of $xBaWO_4/(1-x)CaWO_4$ nanocomposites measured at room temperature(RT). **(d)**Frequency dependent polarization.

Loss tangent (tan δ) occurs due to (conduction, dipole and vibrational) loss. **Figure 6(c)** shows the frequency dependence of loss tangents (tanδ) of nanocomposites measured at room temperature (RT). At loss tangents (tanδ) peak position dielectric constant (ε') & loss tangents (tanδ) of C0 ($CaWO_4$) single phase is more than that of C4 ($BaWO_4$) due to lower unit cell volume and its molecular higher density. Higher number of cells per unit volume increasesthe number of crystallites per unit volume and therefore buildup of the dipoles on the surface increases which gives increased surface charge polarization and leads to higher dipole loss **[45]**. Similarly loss tangents (tan δ) peak of C2 ($0.5BaWO_4/0.5CaWO_4$) nanocomposites is more than other nanocomposites except that of C3 ($0.75BaWO_4/0.25CaWO_4$) nanocomposites and also occurs at higher frequency. This is due to maximum number of available electronic dipoles giving rise to more dipolar surface charge polarization and result in higher dipole loss and shift in peak frequency for C2 ($0.5BaWO_4/0.5CaWO_4$) nanocomposites as compared to C0 ($CaWO_4$) and C4 ($BaWO_4$) single phases & other nanocomposites except in C3 ($0.75BaWO_4/0.25CaWO_4$) nanocomposites.C3 ($0.75BaWO_4/0.25CaWO_4$) nanocomposites showing maximum dipole peak loss due to dipoles change their directions with applied electric field only when dipole rotation matches with the applied external electric field properly resulting heating is produced in the system giving maximum power transfer and C3 ($0.75BaWO_4/0.25CaWO_4$)nanocomposites absorbs maximum energy because of resonance phenomenon **[59]**. All the nanocomposites exhibit dipolar polarization effect below 10^{10} Hz which is observed in **Figure 6(d)**. The presence of dipolar polarization is significantly important to capacitive and insulating properties applications of the materials at low frequency region. While this dispersion of polarization is known as dipolar polarization which may occur to a wide frequency (10^2-10^{10}Hz) range.It may be seen that in the lower frequency region loss tangents (tan δ) curves of nanocomposites exhibit a peak hump approximately frequencies between 125Hz to 415Hz which may be known as relaxation peak that decreases smoothly with rising % Ba concentration except C2 ($0.5BaWO_4/0.5CaWO_4$) & C3($0.75BaWO_4/0.25CaWO_4$) nanocomposites.When electric field (E=0), then dielectric possesses all motions (rotational/orientation,translational,vibrational) in the absence of field.Whereas (E≠0) alternating electric field is applied the molecules or dipoles changes their directions with respect to the electric field only when frequency of molecule rotation matches with the applied external electric field properly. Resulting heating is produced in

the system giving maximum power transfer of applied field **[60]**.The relaxation time which is the time taken by the electric dipoles to get oriented in the applied electric field direction giving relaxation peaks. When the relaxation time (τ) matches with the applied fieldtime period, the sample absorbs maximum energy from the applied ac field due to resonance phenomenon. According to the condition of the loss tangent (tanδ) peak at the curve of the (tanδ) versus frequency, the relaxation time (τ) can be calculated [$\boldsymbol{\tau = 1/(2\pi f)}$] at the loss tangents (tanδ) peakswhich is listed in **Table 5.5**.The relaxation times (τ) observed to have C0 ($CaWO_4$) & C4 ($BaWO_4$) [$\boldsymbol{\tau}$ **= 410µs, 1340µs**] at loss tangent (tanδ) peak are of single phases respectively. Whereas relaxation time ($\boldsymbol{\tau}$ **=130µs)** observed to be lower at loss tangents (tanδ) peaks of C2 ($0.5BaWO_4/0.5CaWO_4$) nanocomposites. The relaxation time ($\boldsymbol{\tau}$**)** at loss tangents (tanδ) peaks of C2 ($0.5BaWO_4/0.5CaWO_4$) nanocomposites is **3 & 10 times less than** C0 ($CaWO_4$) & C4 ($BaWO_4$) single phases respectively. All the nanocomposites give the signature of single relaxation peak (Debye relaxation peak) whereas relaxation peak shifting to higher frequencyoccurs to C2 ($0.5BaWO_4/0.5CaWO_4$) nanocomposites showing decrease in relaxation time. In the C2 ($0.5BaWO_4/0.5CaWO_4$) nanocomposites relaxation peak location vicinity (1218Hz) frequency which is due to trapping relaxation of certain intrinsic defects (electrons and holes) within the electrical insulating layer of interface. The similar trend of loss tangents (tanδ) occurred to other ceramics which is observed & reported **[48]**.This loss tangents (tanδ) of C2 ($0.5BaWO_4/0.5CaWO_4$) nanocomposites shifted to higher frequency side owing to additional collection of defects & maximum defects is collected at interface of C2 ($0.5BaWO_4/0.5CaWO_4$) nanocomposites.Accumulation of dipoles on surface increases due to interface between the two phases of the nanocomposites which leads to increased surface charge polarization of the C2 ($0.5BaWO_4/0.5CaWO_4$) nanocomposites**[56]**.There is rise in loss tangent (tanδ) at 1218Hz frequency due to the conductivity begins to dominate of C2($0.5BaWO_4/0.5CaWO_4$) nanocomposites. Whereas ac conductivity ($\sigma_{ac}=52.2x10^{-7}\ \Omega^{-1}cm^{-1}$) at loss tangents (tanδ) peaks at particular (1218Hz) frequency of C2 ($0.5BaWO_4/0.5CaWO_4$) nanocomposites is **4 & 19 times** higher than C0 ($CaWO_4$) & C4 ($BaWO_4$) single phases respectively. It is observed that frequency increases loss tangent (tan δ) decreases slowly, exhibiting declining trend similar to the dielectric constant. This process occurs in polar dielectrics molecules which requires small amount of electric energy to overcome the internal forces to orient themselves in the direction of applied electric field. Another reason is that in the presence of applied electric field utilizes fraction of

electric energy which leads to energy loss while rotation of dipole molecules and the movement towards molecules from one site to another site **[60]**. Relaxation time (τ) peak frequency values ofall nanocomposites observed at room temperature (RT) are listed in **Table 5.5**.

Table 5.5: Relaxation Time (τ) Peak frequency values of $xBaWO_4/ (1-x) CaWO_4$ nanocomposites

Samples	ε'	Peak Frequency F_p (Hz)	tanδ at Peak frequency	Relaxation Time (τ) μsecond	σ_{ac} ($\Omega^{-1}cm^{-1}$)
C0	370	388	1.6000	410	$12.6x10^{-7}$
C1	378	158	1.3700	1004	$4.54x10^{-7}$
C2	656	1218	1.6600	130	$52.2x10^{-7}$
C3	295	291	2.1500	547	$10.2x10^{-7}$
C4	336	119	1.1800	1340	$2.67x10^{-7}$

5.2.3.3. AC Conductivity analyses

In order to investigate conduction mechanism of nanocomposites, the frequency dependent AC conductivity σ_{ac} (ω,T). AC conductivity σ_{ac} (ω,T) of the nanocomposites was evaluated using the **equation (5.5) [61]**.

$$\sigma_{ac}(\omega, T) = \varepsilon_0 \varepsilon' \omega \tan\delta \qquad (5.5)$$

Where (σ) is the AC conductivity, (ε_0) is the vacuum dielectric permittivity and its value is $8.854\,187\,817\times 10^{-12}$ F/m, (ε′) is the real part of the dielectric permittivity, (tan δ) is the dielectric loss, (ω) is the angular frequency and (T) is absolute temperature.

5.2.3.4. Frequency dependent AC conductivity analyses

AC conductivity is independent at low frequency implies lack of hopping to charge carrier polarization & identifies as DC conductivity dominates, whereas higher frequencies dispersive region occurs **[62]**.The frequency dependence on the ac conductivity is fitted by "Jonscher's universal power law" by the following **equation (5.6) [63]**.

$$\sigma_\omega = \sigma_o(T) + A\omega^n \qquad (5.6)$$

Where (σ_o) is the DC conductivity (lower frequency independent plateau region), (A) is the pre-exponential factor and (n) is the frequency exponent. The DC conductivity (σ_{dc}), frequency exponent (n) and pre-exponent factor (A) is determined from the Jonscher's universal power law fit.

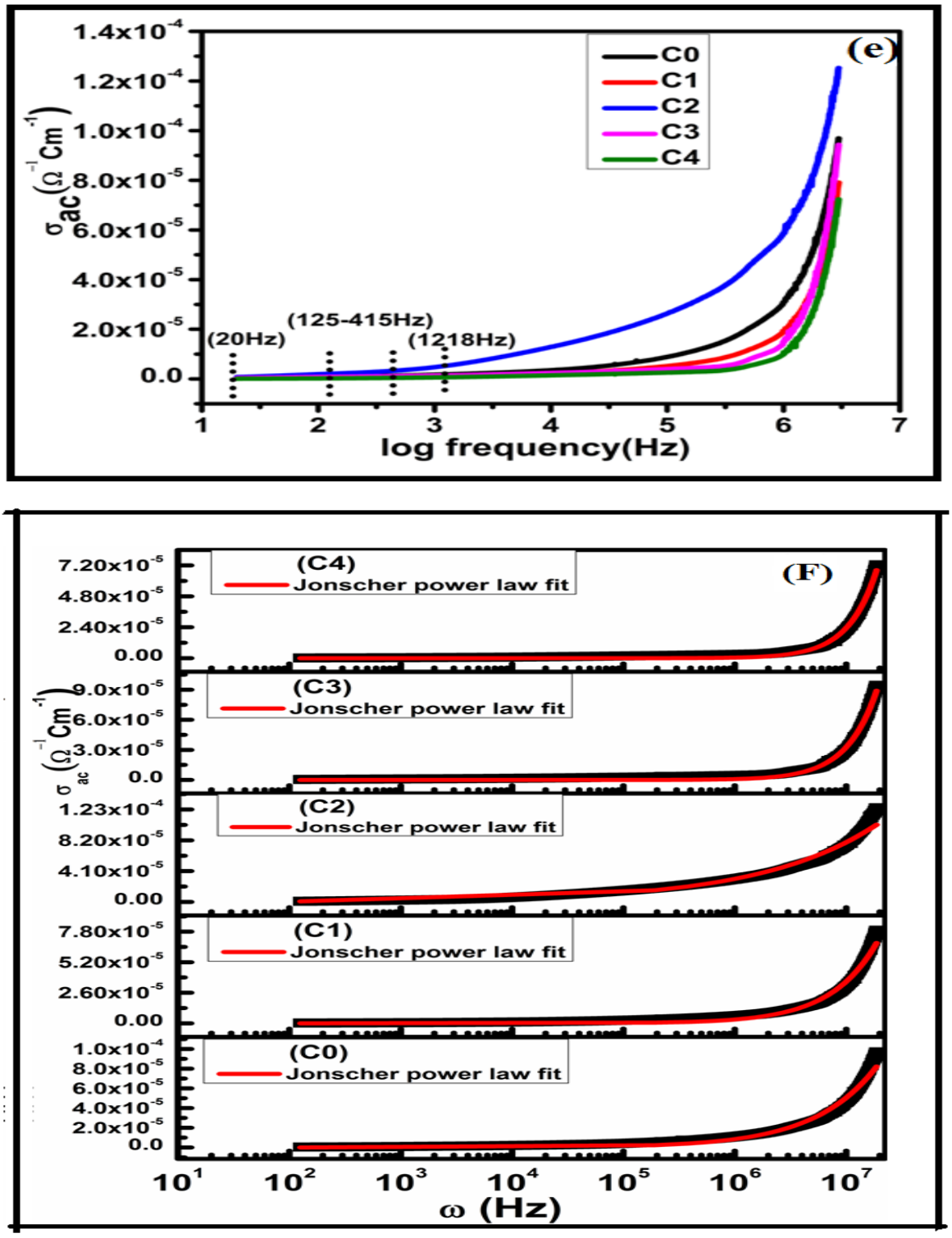

Figure 6 (e-f): (e) Frequency dependent AC conductivity of $xBaWO_4/(1-x)CaWO_4$ nanocomposites measured at room temperature (RT). **(f)** σ_{ac} versus ω of $xBaWO_4/(1-x)CaWO_4$ nanocomposites with Jonscher's universal power law fit.

Figure 6(e) plot shows AC conductivity which is frequency dependent at room temperature (RT) of all nanocomposites. **Figure 6(f)** plot shows σ_{ac} (ω) versus (ω) radial frequencies at room temperature (RT) with Jonscher's universal power law fitting. AC conductivity (σ_{ac}) increases linearly with increasing frequency for all nanocomposites. The conductivity started to increase at particular frequency is called hopping of the charge carriers **[64, 65]**. The (σ_{dc}), (n) and (A) are parameters obtained from fitting of the Jonscher´s universal power law as shown in **Figure 6(e)**.The frequency exponent (n=0.4) has a value of C2 ($0.5BaWO_4/0.5CaWO_4$) nanocomposites which is approximately **2 & 4 times** less than C0 ($CaWO_4$)& C4 ($BaWO_4$) single phases respectively.Whereas frequency exponents(**n**) values are higher for other nanocomposites. When the electrical conduction is frequency independent giving frequency exponents (**n=0**) or denoted as dc conduction occurs and frequency dependent exponents (**n ≤ 1**), denoting as ac conduction occurs **[66]**.According to theory, if frequency exponents (**n**) values lie between 0 and 1 significantly denoting charge carriers and lattice interaction. The observed frequency exponent (**n ≤ 1**) of C0 ($CaWO_4$) single phase and C2 ($0.5BaWO_4/0.5CaWO_4$) nanocomposites indicate conduction is hopping or translational respectively. It is clear about the frequency exponent (**n**) values that C0 ($CaWO_4$) single phase& C2 ($0.5BaWO_4/0.5CaWO_4$) nanocomposites, the conductivity increases as frequency increases, which confirms to small polaron hopping **[67]**. According to Elliot's barrier hopping model, ac conductivity increases to hopping distance **[68]**. Whereas frequency exponents (**n ≥1)** of C1($0.25BaWO_4/0.75CaWO_4$),C3($0.75BaWO_4/0.25CaWO_4$) nanocomposites and C4($BaWO_4$) single phase shows localized motion may be due to the lower site relaxation time than the backward hopping rate of charge carriers. The frequency exponent (**n**) lies in the range of (**n=1.46-1.94**) of C3($0.75BaWO_4/0.25CaWO_4$)nanocomposites & C4($BaWO_4$) single phase samples (i.e. the backward hopping is faster than the site relaxation time), which shows that the hopping motion is localized due to the existence of columbic repulsion between the mobile ions **[69]**.

The pre-exponential factor (A) values are ($1.94x10^{-10}\Omega^{-1}cm^{-1}$second) of C0 ($CaWO_4$) & ($2.80x10^{-17}\Omega^{-1}cm^{-1}$second) of C4 ($BaWO_4$) single phases respectively. The pre-exponential factor (A) values is ($1.02x10^{-7}\Omega^{-1}cm^{-1}$second) of C2 ($0.5BaWO_4/0.5CaWO_4$) nanocomposites. The pre-exponential factor (A) of C2 ($0.5BaWO_4/0.5CaWO_4$) nanocomposites is approximately **500 & $4x10^9$ times** more than C0 ($CaWO_4$) & C4 ($BaWO_4$) single phases respectively. The pre-

exponential factor (A) represents strength of polarization of the nanocomposites and also dependent on temperature called dispersion factor **[64]**.The maximum strength of polarizationshown by C2 ($0.5BaWO_4/0.5CaWO_4$) nanocomposites.

Applying DC conductivity (σ_{dc}) and pre-exponent factor (A) parameters to the hopping frequency (**ω_p)** which can be calculated by using **equation (5.7)** and listed in **Table 5.6[64]**.

$$\omega_p = \left[\frac{\sigma dc}{A}\right]^{1/n} \qquad (5.7)$$

The observed hopping frequency (**ω_p**) to be ($2.41x10^5$Hz) of C0 ($CaWO_4$) & ($2.73x10^5$Hz) of C4 ($BaWO_4$) single phases respectively. The observed hopping frequency (**ω_p**) is ($0.78x10^5$Hz) of C2 ($0.5BaWO_4/0.5CaWO_4$) nanocomposites. The C2 ($0.5BaWO_4/0.5CaWO_4$) nanocomposites hopping frequency (**ω_p**) is approximately **$3.2x10^9$ & $2.8x10^9$** times less than C0 ($CaWO_4$) & C4 ($BaWO_4$) single phases respectively.Whereas C2 ($0.5BaWO_4/0.5CaWO_4$) nanocomposites hopping frequency (**ω_p**) is less than other nanocomposites. Another reason having lower hopping frequency (**ω_p**) of C2 ($0.5BaWO_4/0.5CaWO_4$) nanocomposites is that interface leads to space charge layer (SCL) formation to C2 ($0.5BaWO_4/0.5CaWO_4$) nanocomposites which increasesconductivity of nanocomposites even at lower frequency. Hence in C2 ($0.5BaWO_4/0.5CaWO_4$) nanocomposites hopping frequency is lower than that of the C0 ($CaWO_4$) single phase respectively.

DC conductivity ($\sigma_{dc}=1.07x10^{-5}\Omega^{-1}cm^{-1}$) observed from Jonscher's universal power law fit is the highest for C2 ($0.5BaWO_4/0.5CaWO_4$) nanocomposite and matches ($\sigma_{dc}=1.11x10^{-5}\Omega^{-1}cm^{-1}$) with measurement done for C2 ($0.5BaWO_4/0.5CaWO_4$) nanocomposites by two electrodes method. Enhanced AC conductivity of C2 ($0.5BaWO_4/0.5CaWO_4$) nanocomposites was also observed for C2 ($0.5BaWO_4/0.5CaWO_4$) nanocomposites as compared to other nanocomposites at all the frequencies. In C2 ($0.5BaWO_4/0.5CaWO_4$) nanocomposites, at the interface oxygen vacancies defects get accumulated, generating positive charge core. This is compensated electrostatically by forming an electron and polarons around the positive ions adjacent to the interface forming the space charge layer (SCL) and screening the oxygen vacancies **[11, 25, 26]**. As net effect of the (SCL) formation is that the overall conductivity of the interfacial region of C2 ($0.5BaWO_4/0.5CaWO_4$) nanocomposites increases due to the accumulation of charges and also decrease of the activation energy for charge migration mechanisms **[25]**. Such (SCL) effects of C2 ($0.5BaWO_4/0.5CaWO_4$) nanocomposites resulting an additional interfacial electronic

conductivity which increases total conductivity by formation of oxygen ion vacancies as a defect center [WO_3] according to the reaction $2[WO_4]^{2-} \rightarrow 2[WO_3] + O^{2-} + 4e^-$ showing more number of 2[WO_3] defects and electrons ($4e^-$) available resulting much higher oxygen capturing electron ability which increases intrinsic charge carrier (electrons i.e. $4e^-$,O^{2-}) tremendously showing higher conductivity of C2 ($0.5BaWO_4/0.5CaWO_4$) nanocomposites of a several orders for magnitude than C0 ($CaWO_4$) and C4 ($BaWO_4$) single phases respectively **[59]**. Also Type I band alignment interface occurring between them of C2 ($0.5BaWO_4/0.5CaWO_4$) nanocomposites charge transfer of $BaWO_4$ phase to $CaWO_4$ phase take place which shows increase in conduction between intra ($BaWO_4/CaWO_4$) grains resulting maximum conductivity.

Table 5.6:The parameters obtained from the Jonscher's Power Law fitting of $xBaWO_4/(1-x)CaWO_4$ nanocomposites

Samples	σ_{dc} (Ω^{-1} cm^{-1}) at 300^0K	Frequency Exponent (n)	Pre-Exponential factor (A) ($\Omega^{-1}cm^{-1}$second)	Hopping Frequency (ω_p) Hz
C0	$28.12x10^{-7}$	0.7	$1.943x10^{-10}$	$2.41x10^5$
C1	$11.72x10^{-7}$	1.0	$1.830x10^{-12}$	$3.78x10^5$
C2	$1.07x10^{-5}$	0.4	$1.029x10^{-7}$	$0.78x10^5$
C3	$5.83x10^{-7}$	1.6	$2.259x10^{-16}$	$7.62x10^5$
C4	$0.49x10^{-7}$	1.7	$2.8032x10^{-17}$	$2.73x10^5$

5.2.4. Thermoelectric power properties analyses

Seebeck coefficient (S) of the nanocomposites at a given temperature is determined by the relation of **equation (5.8)[70]**.

$$S = -\frac{\Delta V}{\Delta T} \qquad (5.8)$$

Where measured Seebeck voltage (ΔV) and the temperature difference (ΔT) across the junctions (Hot and Cold).

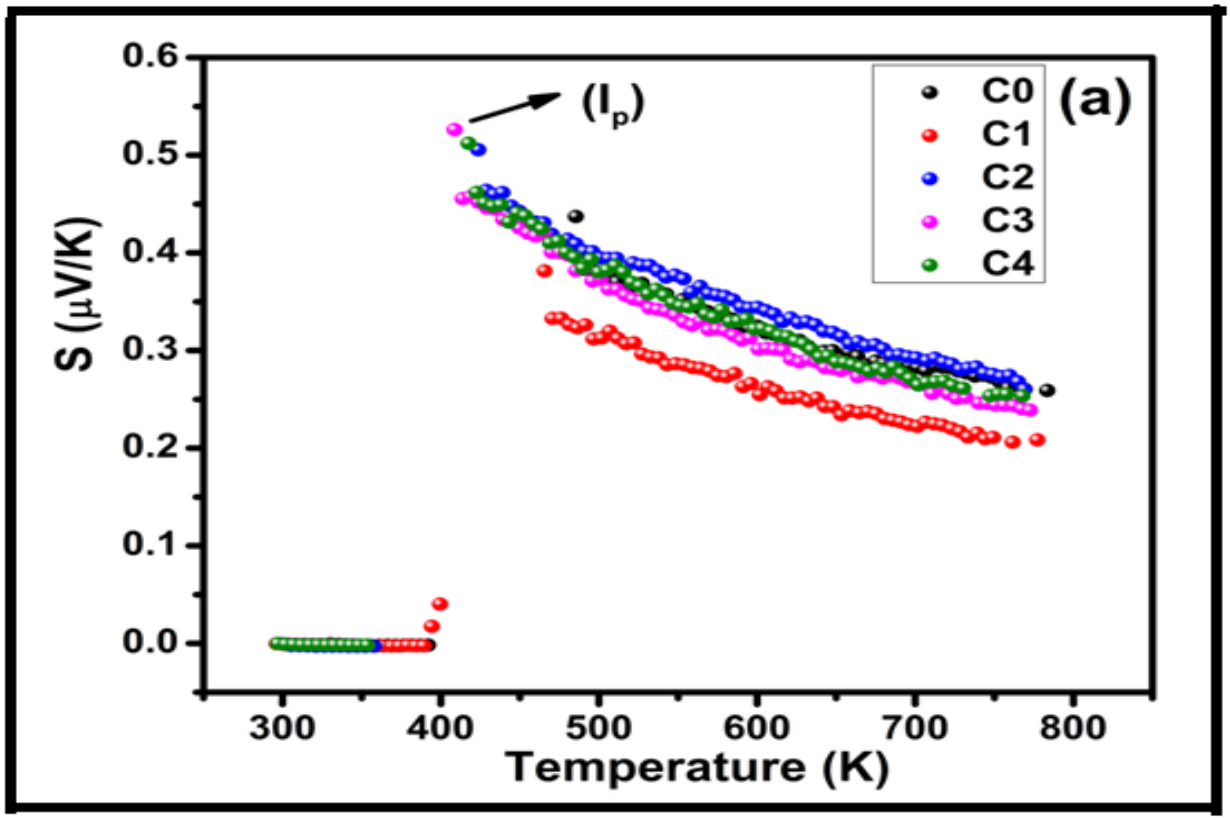
(a)
C0
C1
C2
C3
C4
(I_p)
S (μV/K)
Temperature (K)
0.6
0.5
0.4
0.3
0.2
0.1
0.0
300
400
500
600
700
800

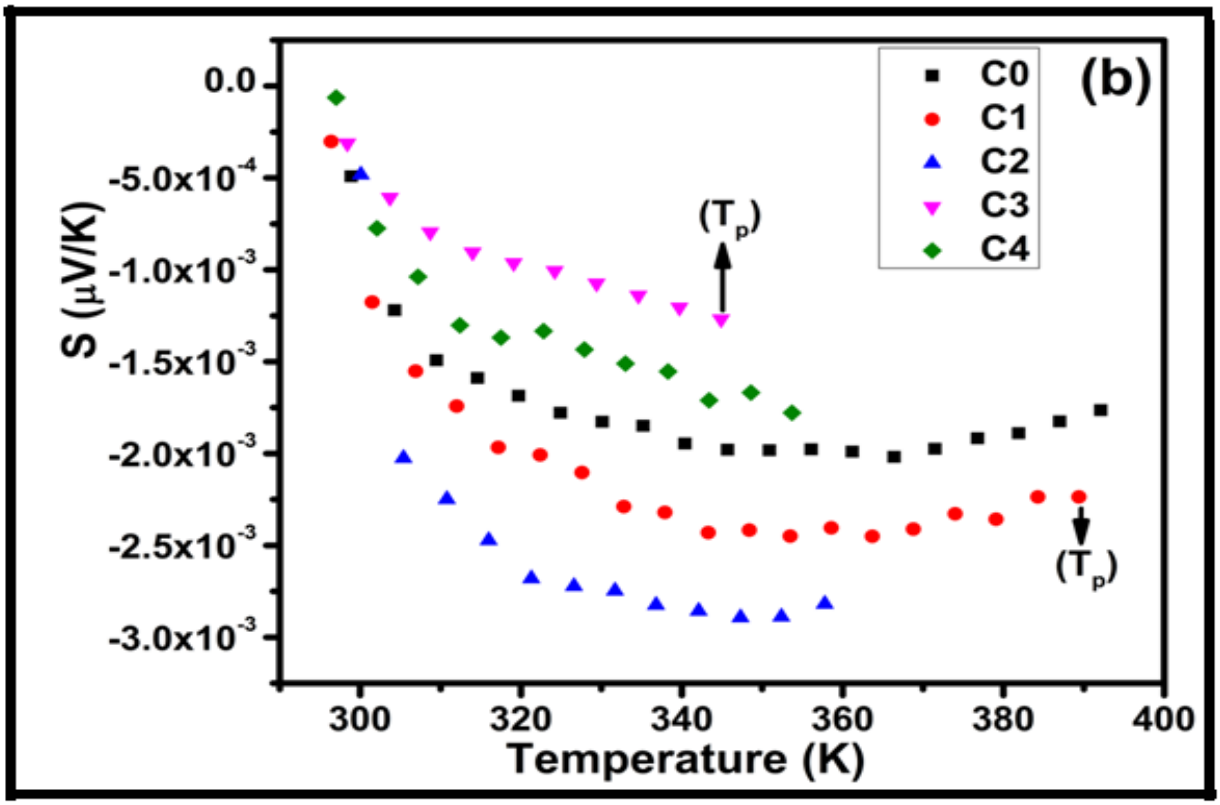
(b)
C0
C1
C2
C3
C4
(T_p)
(T_p)
S (μV/K)
Temperature (K)
0.0
-5.0x10^-4
-1.0x10^-3
-1.5x10^-3
-2.0x10^-3
-2.5x10^-3
-3.0x10^-3
300
320
340
360
380
400

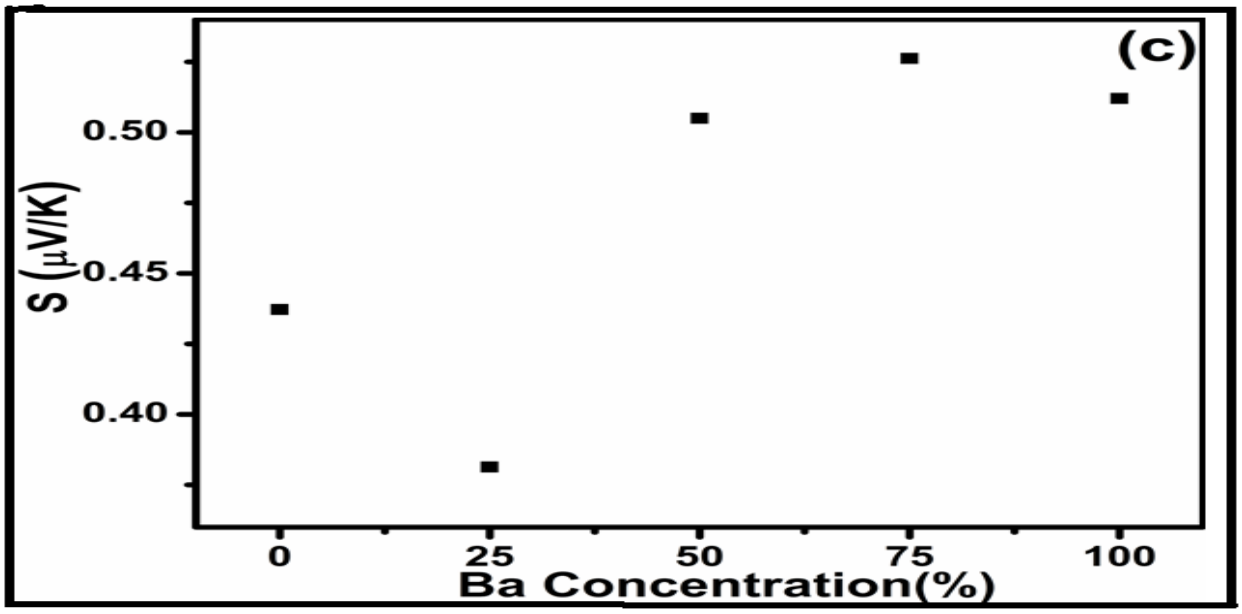

Figure 7(a-c): (a) Temperature dependent Seebeck coefficient(S) of $xBaWO_4/(1-x)CaWO_4$ nanocomposites. **(b)** Variation in temperature dependent Seebeck coefficient (S) up to transition temperature point (T_p) of $xBaWO_4/(1-x)CaWO_4$ nanocomposites.**(c)** Seebeck coefficient(S) versus% Ba concentration of $xBaWO_4/(1-x)CaWO_4$ nanocomposites.

Variation of Seebeck coefficient(S) temperature with temperature for all nanocomposites is shown in **Figure 7(a)**.The measured thermoelectric (TE) power or Seebeck coefficient(S) lies in the temperature range of 300K-773K. It can be observed that the Seebeck coefficient(S) values are negative starting from room temperature (300K) to transition temperature point (T_p) which is shown in **Figure 7(b)**. The absolute value of the Seebeck coefficient(S) increases up to transition temperature point (T_p) & and starts becoming more positive and then suddenly the value becomes positive and high till the inflexion point(I_p). Seebeck coefficient(S) tends to decline with furtherincrease in temperature. It can be seen that all nanocomposites show n-type semiconductor behavior up to transition temperature point (T_p) & p-type semiconductor behavior from T_p to inflexion point peak (I_p) and again n-type semiconductor behavior after I_p. The hot surface becomes positively charged and loses some of the electrons in the case of n-type semiconductor material. The cold surface becomes negatively charged. Conversely the hot surface becomes negative and cold one positive for p-type semiconductor. Therefore given semiconducting material conduction type can be readily determined from the sign of the thermoemf. The polarity sign of the Seebeck coefficient(S) determines from charge carriers (holes or electron) and gives

information about type (p or n-Type) of the material **[71]**. In **Figure 7(c)** plot shows Seebeck coefficient(S) versus % Ba concentration of all nanocomposites. The Seebeck coefficient(S) of C3 ($0.75BaWO_4/0.25CaWO_4$) [0.52 μV/K] is greater than that of all other samples.

5.2.4.1. Conduction mechanism

Seebeck coefficient(S) of all the nanocomposites confirm n-type semiconductors behaviour from room temperature (RT) till the transition temperature point (T_p). Seebeck coefficient(S) from transition temperature point (T_p) to inflexion point peak (I_p) shows p-type conduction behavior **[72]**. The absolute value of Seebeck coefficient (S) increases upto transition temperature point (T_p) due to the conduction of electrons in n-type material(majority charge carriers) and starts becoming more positive due to the conduction of holes (minority charge carriers) in addition to the electrons in an n-type material and suddenly becomes high and positive on further increase in temperature upto the inflexion point (I_p) due to enhanced lattice scattering effect.Then it decreases from inflexion point peak (I_p) as the temperature is further increased on account of intrinsic electrons excitation and conduction**[73, 74]**. The Seebeck coefficient(S) of C0 ($CaWO_4$) nanosample at inflexion point peak (I_p) is lower than that of C4 ($BaWO_4$) due to its smaller grain size resulting in higher thermal conductivity **[75]**. In the present study it is also found that the crystallite sizes of C0 ($CaWO_4$) and C4 ($BaWO_4$) samples do not change much when sintered till 400^0C. Among all nanocomposites C3 ($0.75BaWO_4/0.25CaWO_4$) nanocomposites was observed to have highest Seebeck coefficient(S) at I_p. This could be due to the numerous grain boundaries or interfaces introduced in such a manner to promote more phonon scattering, decrease thermal conductivity and preserve electrical conductivity. This shows C3 ($0.75BaWO_4/0.25CaWO_4$) nanocomposites does'nt have incomplete bonds or strains in the bonds around the grain boundaries and do not interrupt charge carriers. Optimal atomic ratio (Ba/Ca=3) and optimized grain size in C3 ($0.75BaWO_4/0.25CaWO_4$) nanocomposites could be the reason for enhanced phonon scattering while preserving the electrical conductivity simultaneously **[76]**.The mechanism of charge carrier interaction with grain boundaries of C3 ($0.75BaWO_4/0.25CaWO_4$) nanocomposites is given in **Figure 8** below. In general charge carriers are scattered by large/small particles, grain boundaries and interfaces. Lower energy charge carriers (at lower temperature) would be scattered by large particles and vice versa **[77, 78]**. Therefore optimal atomic ratio (Ba/Ca=3), grain size and electrical conductivity significantly

support enhanced power factor (PF) of figure of merit (ZT) of C3 ($0.75BaWO_4/0.25CaWO_4$) nanocomposites.

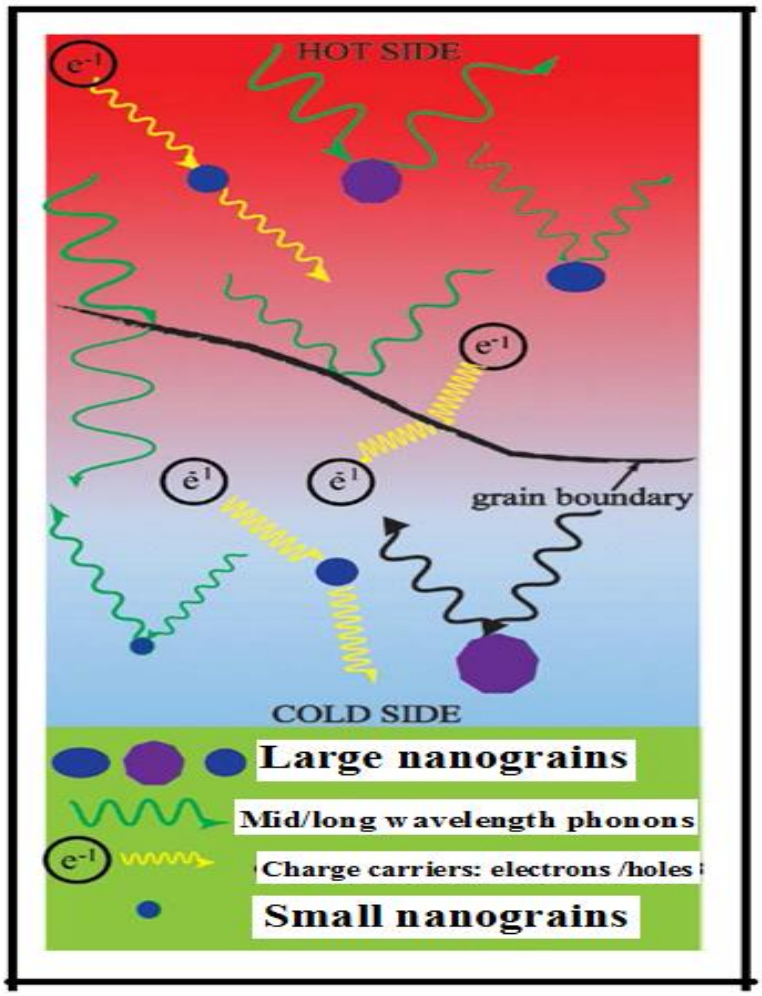

Figure 8: Mechanism of phonon and charge carrier interaction with large nanograins, small nanograins and grain boundaries of C3 ($0.75BaWO_4/0.25CaWO_4$) nanocomposites. [From:https*://uwspace.uwaterloo.ca/bitstream/handle/10012/10442/Nandihalli_Nagaraj.pdf]*.

5.2.4.2. Thermoelectric power factor (PF)

The figure-of-merit (ZT) is dimensionless described asThermoelectric power efficiency of a material, $\mathbf{ZT = S^2\sigma_{dc}T/\kappa}$, where (S) is the Seebeck coefficient, (σ_{dc}) is the electrical conductivity, (T) is the absolute temperature and (κ) is the total thermal conductivity.

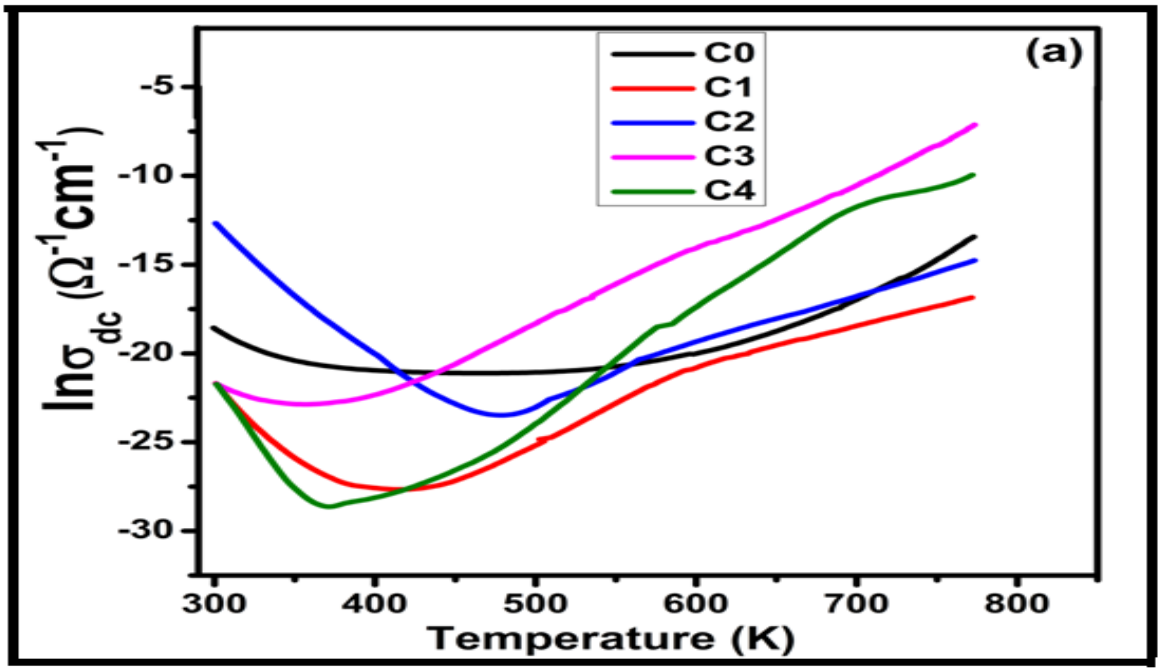
(a)
C0
C1
C2
C3
C4
$\ln\sigma_{dc}$ ($\Omega^{-1}cm^{-1}$)
-5
-10
-15
-20
-25
-30
300
400
500
600
700
800
Temperature (K)

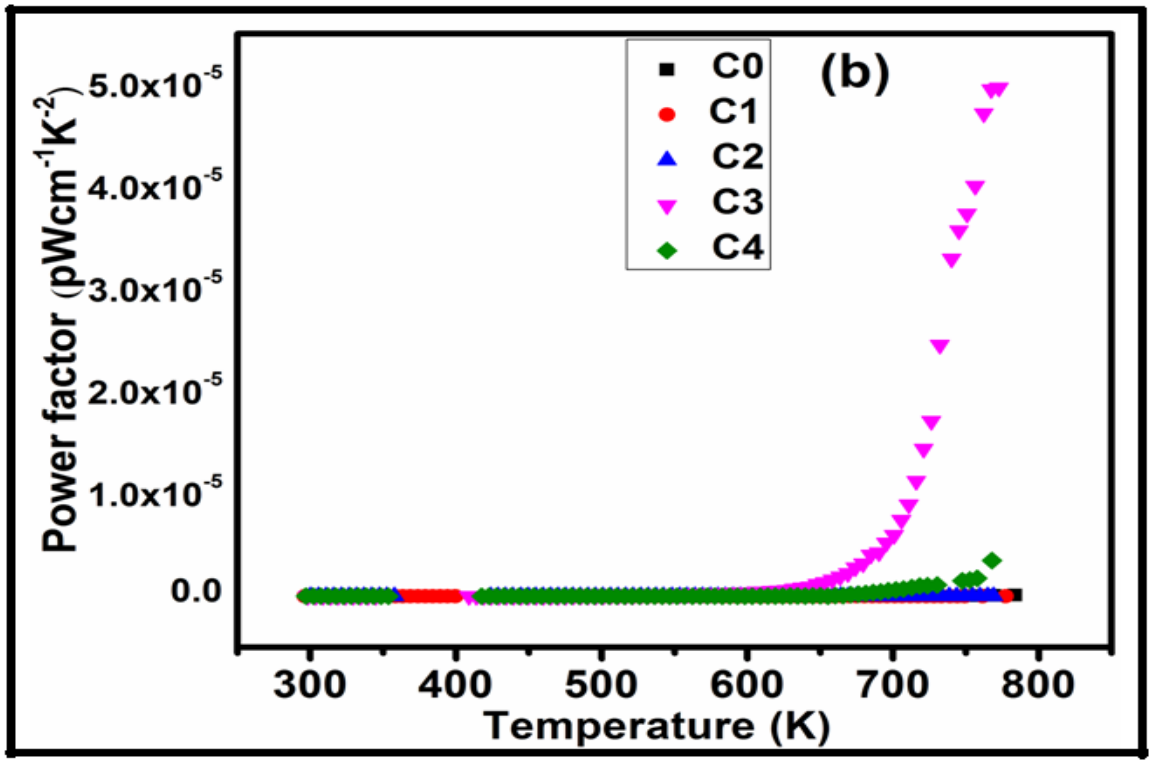
(b)
C0
C1
C2
C3
C4
Power factor (pWcm^{-1}K^{-2})
5.0x10^{-5}
4.0x10^{-5}
3.0x10^{-5}
2.0x10^{-5}
1.0x10^{-5}
0.0
300
400
500
600
700
800
Temperature (K)

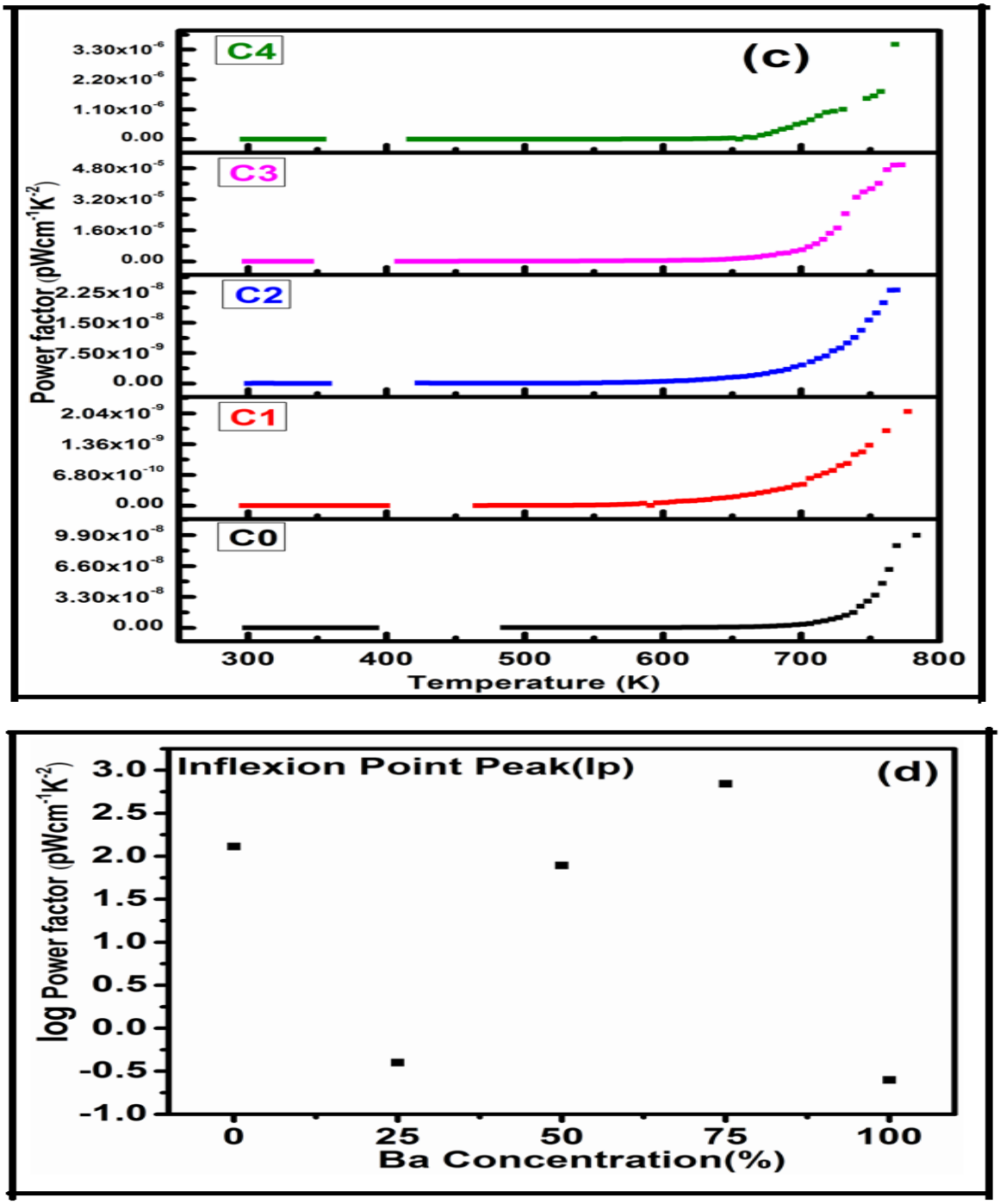

Figure 9(a-d): (a) Temperature dependent DC conductivity of $xBaWO_4/(1-x)CaWO_4$ nanocomposites.**(b)**Temperature dependent power factor of $xBaWO_4/(1-x)CaWO_4$ nanocomposites. **(c)** Stacked Temperature dependent power factor (PF) of $xBaWO_4/(1-x)CaWO_4$ nanocomposites. **(d)** Inflexion point peak (I_p) log power factor (PF) $^{V}/_{S}$ % Ba Concentration of $xBaWO_4/(1-x)CaWO_4$ nanocomposites.

High thermoelectric figure-of-merit (ZT) may be achieved by reducing (κ) and/or by enhancing the thermoelectric power factor (PF) [$PF = S^2\sigma_{dc}$]. Power factor (PF) of the thermoelectric materials play a crucial role in thermoelectric devices **[79]**.The temperature dependence DC conductivity of nanocomposites are given in **Figure 9(a)**.As can be seenfrom **Figure 9(a)**, the conductivity (σ_{dc}) decreases with increasing temperature behaving as metal conduction characteristics, when the temperature is higher than 350K, the descending trend of conductivity (σ_{dc}) is weaken, and there is even a tendency to rise slowly. It is mainly due to the enhancement of carrier scattering caused by lattice vibration as the temperature rises, which leads to a decline in conductivity (σ_{dc}). After reaching a minimum value, the conductivity (σ_{dc}) values increase again owing to the significant intrinsic excitation (electron conduction) **[73]**.The temperature dependence on power factor (PF) of the nanocomposites is shown in **Figure 9(b-c)**. The power factor (PF) at inflexion point peak (I_p) of C3 ($0.75BaWO_4/0.25CaWO_4$) nanocomposites & C0 ($CaWO_4$) single phase at the temperatures 408.8K & 485.5K respectively are found to be maximum. PF of C3 ($0.75BaWO_4/0.25CaWO_4$) nanocomposites is approximately **5 times** (PF=698 $pWcm^{-1}K^{-2}$) greater than that of C0 ($CaWO_4$) [PF=130 $pWcm^{-1}K^{-2}$]. Also power factor (PF) at inflexion point peak (I_p) for C4 ($BaWO_4$) single phase sample at the temperature 417.6K is found to be maximum. PF of C3 ($0.75BaWO_4/0.25CaWO_4$) nanocomposites is approximately **2774 times** (PF=698 $pWcm^{-1}K^{-2}$) greater than that of C4 ($BaWO_4$) [PF=0.251 $pWcm^{-1}K^{-2}$] single phase sample. **Figure 9(d)** plot shows log power factor (PF) at inflexion point (I_p) versus % Ba concentration. Maximum power factor of C3 ($0.75BaWO_4$/ $0.25CaWO_4$) nanocomposites at I_p is due to higher lattice scattering effect resulting from optimal atomic ratio (Ba/Ca=3), grain size which support a good balance between electrical conductivity and Seebeck coefficient(S) **[73, 80]**. The inflexion point peak (I_p) Seebeck coefficient(S) & power factor (PF) values of nanocomposites are tabulated & shown in **Table 5.7**.

Table 5.7 : Inflexion point peak(I_p) Seebeck coefficient(S) & power factor(PF) values of $xBaWO_4/(1-x)CaWO_4$ nanocomposites

Samples	Temperature(K)	Seebeck coefficient(S) (μV/K)	$\sigma_{dc}(\Omega^{-1}cm^{-1})$	Power Factor ($PF= S^2\sigma_{dc}$) ($pWcm^{-1}K^{-2}$)
C0	485.5	0.44	$6.714x10^{-10}$	130
C1	465.7	0.38	$27.70x10^{-13}$	0.40
C2	423.7	0.50	$31.32x10^{-11}$	78.30
C3	408.8	0.52	$25.81x10^{-10}$	698
C4	417.6	0.51	$9.65x10^{-13}$	0.25

5.3. Conclusions

$xBaWO_4/(1-x)CaWO_4$ nanocomposites were prepared by co-precipitation method by first time. Structural characterization was confirmed by XRD, FTIR, SEM, EDS and HRTEM images. HRTEM images confirm the interface formation in C2 ($0.5BaWO_4$/ $0.5CaWO_4$) nanocomposites. Room temperature (RT) study on DC, AC electrical conductivity and above room temperature (RT) thermoelectric power properties of $xBaWO_4/(1-x)CaWO_4$ nanocomposites are reported here first time. The DC conductivity at room temperature (RT) from 8Volts or (27.5 Volts/cm) onwards is found to be maximum for C2($0.5BaWO_4/0.5CaWO_4$) nanocomposites and is approximately **40 times** ($\sigma = 1.11x10^{-5}\ \Omega^{-1}\ cm^{-1}$) greater than that of C0($\sigma = 2.76x10^{-7}\ \Omega^{-1}\ cm^{-1}$) and **1008** times greater than that of C4 ($BaWO_4$) [$\sigma = 0.11x10^{-7}\Omega^{-1}\ cm^{-1}$] single phase samplesrespectively. It is observed that the non linear coefficient alpha (**α)** for nanocomposites are less than the single phase C4($BaWO_4$) and C0($CaWO_4$) samples and is maximum for C4($BaWO_4$) sample.The dielectric constant (ε′) at room temperature (RT) for all measured frequencies is found to be maximum (ε′=8190) for C2($0.5BaWO_4/0.5CaWO_4$) nanocomposites and at 20Hz, it is approximately **3 & 8 times** greater than that of C0 ($CaWO_4$) (ε′=2630) and C4 ($BaWO_4$) (ε′=970) single phase respectively.These enhanced dielectric constant (ε′) properties of C2 ($0.5BaWO_4$/ $0.5CaWO_4$) nanocomposites are due to the space charge layer (SCL) formation at the interface. All the samples give the signature of single relaxation peak (Debye relaxation peak).Loss tangents (tan δ) peak of C2 ($0.5BaWO_4/0.5CaWO_4$) nanocomposites is more than other samples except that of C3 ($0.75BaWO_4/0.25CaWO_4$) nanocomposites and also occurs at higher frequency. Higher tan δ atrelaxation peak and shift towards the higher frequency side for C2 ($0.5BaWO_4/0.5CaWO_4$) nanocomposites shows decrease in relaxation time due to maximum

additional collection of defects (electrons and holes) at the interface. The relaxation time (**τ**)[**τ** =130μsec] at loss tangents (tanδ) peak of C2 ($0.5BaWO_4/0.5CaWO_4$) nanocomposites is **3 & 10 times less than** C0 ($CaWO_4$)[**τ** =410μsecond] & C4($BaWO_4$) [**τ**=1340μsecond] single phases respectively andac conductivity (σ_{ac}=52.2x10^{-7} $\Omega^{-1}cm^{-1}$) at loss tangents (tanδ) peaks at particular (1218Hz) frequency of C2 ($0.5BaWO_4/0.5CaWO_4$) nanocomposites is **4 & 19 times** higher than C0 ($CaWO_4$) & C4 ($BaWO_4$) single phases respectively. Seebeck coefficient(S) gives the confirmation of n-type semiconductors at room temperature (RT).The Seebeck coefficient(S) at inflexion point peak (I_p) of C3 ($0.75BaWO_4/0.25CaWO_4$) [0.52 μV/K] is greater than that of all other samples. Enhanced power factor (PF) (698 $pWcm^{-1}K^{-2}$**)** of C3 ($0.75BaWO_4/0.25CaWO_4$) nanocomposites is due to higher lattice scattering effect resulting from optimal atomic ratio (Ba/Ca=3), grain size which support a good balance between electrical conductivity and Seebeck coefficient(S)

References

[1] Z. Kukua, E. Tomaszewicz, S. Mazur, T. Gro, H. Duda, S. Pawlus, S. M. Kaczmarek, H. Fuks, and T. Mydlarz, Dielectric and magnetic permittivities of three new ceramic tungstates $MPr_2W_2O_{10}$ (M = Cd, Co, Mn) Philos. Mag., **92**:4167-4181 **(2012)**.

[2]Y. Huang, H. J. Seo, and S.H. Doh, Q.Feng,Kyounghyuk Jang,H.-D. Kang Luminescence and electrical properties in Nd^{3+}doped lead-tungstate single crystals, J.Korean Phys. Soc., **46**(5):1198-1202**(2005)**.

[3] S. Takai, K. Sugiura, and T. Esaka, Mater.Ionic conduction properties of $Pb_{1-x}M_xWO_{4+\delta}$ (M = Pr, Tb) Res. Bull., **34**:193-202**(1999)**.

[4] J. Maier, Point Defect Thermodynamics: Macro- vs. Nanocrystals Electrochemistry, **68**:395-402**(2000)**.

[5]H. L. Tuller, Ionic conduction in nanocrystalline materials, Solid State Ionics, **131**(1-2), 143-157 **(2000)**.

[6]N. Sata, K. Eberl, K. Eberman and J. Maier, Mesoscopic fast ion conduction in nanometer-scale planar heterostructures Nature, **408**:946–949 **(2000)**.

[7]Y.M. Chiang, E.B. Lavik, I. Kosacki, H.L. Tuller, J.Y. Ying, Defect and transport properties of nanocrystalline CeO_{2-x} Applied Physics Letters, **69**(2):185-187**(1996)**.

[8] A. Tschope, Grain size-dependent electrical conductivity of polycrystalline cerium oxide II: Space charge model, Solid State Ionics, **139**(3-4), 267-280 **(2001)**.

[9]S. Kim, J. Maier, On the conductivity mechanism in nanocrystalline ceria. J. Electrochem. Soc. **149**(19): J73–J83 **(2002)**.

[10]E. Fabbri, D. Pergolesi, E. Traversa, Ionic conductivity in oxide heterostructures: the role of interfaces, Science and Technology of Advanced Materials, **11** (9pp):054503**(2010)**.

[11]Maier J, Nanoionics: Ion transport and electrochemical storage in confined systems Nature Materials, **4**:805-815,**(2005)**.

[12]Maier Joachim, Defect chemistry and ion transport in nanostructured materials: Part II. Aspects of nanoionics, Solid State Ion., **157**(1-4): 327-334 (**2003)**.

[13]S.A. Salehizadeh, H.M. Chenari, M. Shabani, H.A. Ahangar, R. Zamiri, A. Rebelo, J.S. Kumar, M.P.F. Graça, J.M.F. Ferreira, Structural and impedance spectroscopy characteristics of $BaCO_3/BaSnO_3/SnO_2$ nanocomposite: observation of a non- monotonic relaxation behavior, RSC Adv., **8** :2100–2108**(2018)**.

[14] L. Li, M. Xu, Q. Zhang, P. Chen, N. Wang, D. Xiong, B. Peng, L. Liu, Electrocaloric effect in La-doped BNT-6BT relaxor ferroelectric ceramics, Ceram. Int., **44**:343–350 **(2018)**.

[15]M.A. Ahmed, E. Ateia, S.I. El-Dek, Rare earth doping effect on the structural and electrical properties of Mg-Ti ferrite, Mater. Lett., **57**:4256–4266**(2003)**.

[16]S.Dewan, M.Tomar, R.P. Tandon, V. Gupta, Zn doping induced conductivity transformation in NiO films for realization of p-n homo junction diode, J. Appl. Phys., **121:**215307 **(2017)**.

[17] A.U. Rahman, M.A. Rafiq, M.U. Hasan, M. Khan, S. Karim, S.O. Cho, Enhancement of electrical conductivity and dielectric constant in Sn-doped nanocrystalline $CoFe_2O_4$, J. Nanoparticle Res., **15**:2–7 **(2013)**.

[18]Q.Q. Yang, B. Meng, Z.L. Lin, X.K. Zhu, F. Yang, S. Wu, Effect of sintering temperature on the elemental diffusion and electrical conductivity of $SrTiO_3$/YSZ composite ceramic, Ionics (Kiel) **23**:967–975 **(2017)**.

[19] Y. Jing, N. Luo, S. Wu, K. Han, X. Wang, L. Miao, Y. Wei, Remarkably improved electrical conductivity of ZnO ceramics by cold sintering and post-heat-treatment, Ceram. Int.,**44**:20570–20574 **(2018)**.

[20] R.F. Shimanouchi, T. Tsuji, R. Yagi, Y. Matsumoto, H. Nishizawa, Hydrothermal synthesis and crystal structure of ionic conductive metal tungstates, IOP Conf. Ser. Mater. Sci. Eng., **18**:2–6**(2011)**.

[21] L. Zhang, C. Lu, Y. Wang, Y. Cheng, Hydrothermal synthesis and characterization of $MnWO_4$ nanoplates and their ionic conductivity, Mater. Chem. Phys., **103**:433–436**(2007)**.

[22] R.M. Sebastian, S. Xavier, E.M. Mohammed, Dielectric behavior and AC Conductivity of Mg^{2+} doped zinc ferrite nanoparticles synthesized by sol-gel technique, Ferroelectrics,**481**:48–56 **(2015)**.

[23]A.D. Mani, I.Soibam, Dielectric, magnetic and optical propertiesof (Bi, Gd) FeO_3–$Ni_{0.8}Zn_{0.2}Fe_2O_4$ nanocomposites. Ceram. Int., **44(2)**:2419–2425 **(2018)**.

[24] Z. Wang, T. Wang, C. Wang, Y.J. Xiao, Mechanism of enhanceddielectric performance in $Ba(Fe_{0.5}Ta_{0.5})O_3$/poly(vinylidene fluoride)nanocomposites. Ceram.Int.,**43(1)**, S244–S248 **(2017)**.

[25] S. Kim, J. Fleig, J. Maier, Space charge conduction: simple analytical solutions for ionic and mixed conductors and application to nanocrystalline ceria.Phys.Chem. Chem. Phys., **5**(11):2268–2273 **(2003)**.

[26]Nini Pryds &Vincenzo Esposito, when two become one: An insight into 2D conductive oxideinterfaces, J Electroceram., **38**(1):1-28**(2016)**.

[27]Kittel, C., *Introduction to Solid State Physics*, JohnWiley & Sons, New York **(1986)**.

[28]Chen, G., *Nanoscale Energy Transport and Conversion*, Oxford, New York **(2005)**.

[29]Weixue Tian, and Ronggui Yang, Phonon Transport and Thermal Conductivity Percolation in RandomNanoparticle Composites, CMES, **24**(2):123-141 **(2008)**.

[30]Prasad Narayan Patil, Uma Subramanian, M Jeyakanthan,Enhanced blue emission of $CaWO_4$ in $BaWO_4$/$CaWO_4$ nanocomposite, Journal of Materials Science: Materials in Electronics, **31**(9):7260-7275 **(2020)**.

[31]Chang Sung Lim, Cyclic Microwave Synthesis and Photoluminescence of Barium Tungstate Particles Assisted by a Solid-State Metathetic Reaction, Asian Journal of Chemistry, **25**(1):63-66**(2013)**.

[32]Ali Olad, Sahar Shakoori, Sajedeh Mohammadi Aref, Investigation of non-linear electrical properties of ZnO/PPy nanocomposite and its application as a low-voltage varistor, Physica B: Condensed Matter, **550**:127–135**(2018)**.

[33]R.N.P. Choudhary, Ratnakar Palai, S. Sharma, Structural, dielectric and electrical properties of lead cadmium tungstate ceramics, Materials Science and Engineering B, **77**(3):235–240**(2000)**.

[34]C.W. Nan, D.K. Clarke, Effects of variations in grain sizeand grain boundary barrier heights on the current-voltage characteristics of ZnO varistors, Journal American Ceram. Soc., **79**(12):3185-3192 **(1996)**.

[35]Y.S. Lee, T.Y. Tseng, Phase Identificationand Electrical Properties in ZnO-Class Varistors J. Am. Ceram. Soc., **75**(6):1636-1640 **(1992)**.

[36]T. Asokan, R. Freer, Dependence of ZnO varistor grain boundary resistance on sintering temperature, Journal of Materials Science Letters, **13**:925-926 **(1994)**.

[37]F.Greuter, G.Blatter, Electrical properties of grain boundaries in polycrystalline compound semiconductors, Semiconductor Science and Technology, **5**(2):111-137 **(1990)**.

[38] D.R. Clarke, Varistor ceramics, J. Am. Ceram. Soc., **82**(3):485-502 **(1999)**.

[39]Mateus Gallucci Masteghin, Marcelo Ornaghi Orlandi, Grain-Boundary Resistance and Nonlinear Coefficient Correlation for SnO_2-Based Varistors, Materials Research,**19**(6):1286-1291**(2016)**.

[40]T. Pompe, V. Srikant, D. Clarke, Acoustoelectric current saturation in c-axis fiber-textured polycrystalline zinc oxide films Appl. Phys. Lett., **69**:4065-4067 **(1996)**.

[41]Y. Li, Z. Wang, L. Sun, Z. Wang, S. Wang, X. Liu, and Y. Wang, Investigation of oxygen vacancy and photoluminescence in calcium tungstate nanophosphors with different particle sizes,Mater. Res. Bull., **50**:36-41 **(2014)**.

[42]Nadine Dirany, Edward Mcrae, and Madjid Arab, Morphological and structural investigation of $SrWO_4$ microcrystals in relationship with the electrical impedance properties, CrystEngComm, **19**(34):5008-5021 **(2017)**.

[43]Mahan, G.D, Levinson M. and Phillip, H. R., Theory of conduction in ZnO varistors. J. Appl. Phys., **50:**2799-2812**(1979)**.

[44]Olsson, E., Dunlop, G. and Osterlund, R., Characterization of individual interfacial barriers in a ZnO varistor material. J.Appl.Phys., **66:**3666-3675**(1989)**.

[45]Sung Hun Yoon, Dong-Wan Kim, Seo-Yong Cho, Kug Sun Hong, Investigation of the relations between structure and microwave dielectric properties of divalent metal tungstate compounds, Journal of the European Ceramic Society, **26**:2051–2054 **(2006)**.

[46]Roger A. De Souza, The formation of equilibrium space-charge zones at grain boundaries in the perovskite oxide $SrTiO_3$, Phys. Chem. Chem. Phys., **11**:9939–9969 **(2009).**

[47]A.Ya. Neiman,Cooperative transport in oxides: Diffusion and migration processes involving Mo (VI), W&Q), V (V) and Nb (V),Solid State Ionics **83(3-4)**:263-273**(1996)**.

[48]Mohammad Alim, Admittance frequency response in zinc oxide varistor ceramics, J.Am.Ceram.Soc., **72**(1):28-32 **(1989)**.

[49]E.C. Snelling, *Soft Ferrites*, 2nd Edition, Butterworth, London, pp. 34,**(1988)**.

[50]R. B. Hilborn, Maxwell - Wagner Polarization in Sintered Compacts of Ferric Oxide Journal Appl. Phys.,**36**:1553-1557**(1965)**.

[51]M. Hema, S. Selvasekerapandian, A. Sakunthala, D. Arunkumar, H. Nithya,Structural, vibrational and electrical characterization of PVA–NH_4Br polymer electrolyte systemPhysica B: Condensed matter, **403**(17):2740–2747 **(2008)**.

[52]M. Ashokkumar, S. Muthukumaran, Effect of Ni doping on electrical, photoluminescence and magnetic behavior of Cu dopedZnO nanoparticles. J. Lumin.,**162**:97–103 **(2015)**.

[53]M.M. Hassan, W. Khan, A. Azam, A.H. Naqvi, Influence of Crincorporation on structural, dielectric and optical properties ofZnO nanoparticles. J. Ind. Eng. Chem.,**21**:283–291 **(2015)**.

[54]S.Sagadevan,K.Pal,Z.Z.Chowdhury,M.E.Hoque,Structural,dielectric and optical investigation of chemically synthesized Ag doped ZnO nanoparticles composites. J. Sol-Gel Sci. Technol.,**83**(2): 394–404 **(2018)**.

[55]T. Ahmad, H.L. Irfan, Citrate precursor synthesis and multifunctional properties of $YCrO_3$ nanoparticles. New J. Chem.,**40**:3216–3224 **(2016)**.

[56]I.Tantis,G.C.Psarras, D.Tasis, Functionalized graphene–poly (vinyl alcohol) nanocomposites: Physical and dielectric properties eXPRESS Polymer Letters, **6**(4):283–292 **(2012)**.

[57] S. Amrin, V.D. Deshpande, Dielectric relaxation and ac conductivity behavior of carboxyl functionalized multiwalled carbon nanotubes/poly (vinyl alcohol) composites, Physica E: Low dimensional systems and nanostructures,**87**:317–326 **(2017)**.

[58]W. R. Agami, Effect of neodymium substitution on the electric and dielectric properties of Mn-Ni-Zn ferrite, Physica B: Condensed Matter, **534**:17-21 **(2018).**

[59]R. J. Singh, *Solid State Physics*, Dorling Kindersley (India) **(2012)**.

[60]Kapil Y. Salkar,R. B. Tangsali, R. S. Gad, Asnit Gangwar, N. K. Prasad, Electrical properties of $Zn_{(1-x)}Co_xO$ dilute magnetic semiconductor nanoparticles, Journal of Materials Science: Materials in Electronics, **30**:18374- 18383 **(2019)**.

[61]T. Wang, J. Hu, H. Yang, L. Jin, X. Wei, C. Li, F. Yan, Y. Lin, Dielectric relaxation and Maxwell-Wagner interface polarization in Nb_2O_5 doped $0.65BiFeO_3$- $0.35BaTiO_3$ ceramics, Journal of Applied Physics, **121**(8):084103 **(2017)**.

[62]S.R.Alharbi,M.Alhassan,O.Jalled,S.Wageh,A.Saeed,Structural characterizations and electrical conduction mechanism of $CaBi_2Nb_2O_9$ single phase nanocrystallites synthesized via sucrose-assisted sol-gel combustion method, Journal of Materials Science,**53**(18):11584-11594 **(2018)**.

[63]A.K.Jonscher, The universal dielectric response, Nature, **267**:673-679 **(1977)**.

[64]S. Shanmugapriya, S. Surendran, V.D. Nithya, P. Saravanan, R. Kalai Selvan, Temperature dependent electrical and magnetic properties of $CoWO_4$ nanoparticles synthesized by sonochemical method, Materials Science and Engineering: B, **214**:57–67 **(2016)**.

[65]A. Singh, S. Suri, P. Kumar, B. Kaur, A.K. Thakur, V. Singh, Effect of temperature and frequency on electrical properties of composite multiferroic of lead titanate and strontium hex ferrite ($PbTiO_3SrFe_{12}O_{19}$), Journal of Alloys Compounds, **764**:599-615 **(2018)**.

[66]M.A. El-Hiti, AC electrical conductivity of Ni–Mg ferrites Journal of Physics D: Applied Physics, **29**:501–505 **(1996)**.

[67]N.Aloysius,M.S. Rintu, E. M. Muhammed, T. Varghese, Dielectric studies of nanocrystalline calcium tungstate, Nanosystems: Physics, Chemistry, Mathematics, **7** (4): 599–603**(2016)**.

[68]Elliot S.R., Temperature dependence of a.c. conductivity of chalcogenide glasses. Philosophical Magazine B, **37**(5):553-560 **(1978)**.

[69]M. Vijayakumar, G. Hirankumar, M.S. Bhuvaneshwari, S. Selvasekarapandian, Influence of B_2O_3 doping on conductivity of $LiTiO_2$ electrode material, Journal of Power Sources, **117**(1-2): 143–147 **(2003)**.

[70]Cao, J., Fan, W., Zheng, H. & Wu, J. Thermoelectric effect across the metal-insulator domain walls in VO_2microbeams.Nano Lett., **9**:4001–4006 **(2009)**.

[71] M. Raghasudha, D. Ravinder, P. Veerasomaiah, Thermoelectric power studies of Co–Cr nano ferrites. Journal of Alloys and Compounds,**604**:276–280**(2014)**.

[72]Shubha Gupta, Y.P.Yadav, R.A.Singh, Electrical Transport Properties of Polycrystalline Chromium Vanadate,Z. Naturforsch, **42a**:577-581 **(1987)**.

[73] Zhengang Zhang, Weiwei Zhao, Wanting Zhu, Shifang Ma, Cuncheng Li, Xin Mu, Ping Wei, Xiaolei Nie, Qingjie Zhang, and Wenyu Zhao, Preparation and Thermoelectric Performance of $BaTiO_3/Bi_{0.5}Sb_{1.5}Te_3$ Composite Materials, Journal of Electronic Materials, **49**:2794–2801 **(2020)**.

[74]Karlheinz Seeger,*Semiconductor Physics: An Introduction*, Springer **(2010)**.

[75]Yingguang Liu, Shingbing Zhan, Zhonghe Han, Yujin Zhao, Grain-size-dependent thermal conductivity of nanocrystalline materials. J. Nanopart. Res., **18**(10):296 **(2016)**.

[76]Y. Lan, A.J. Minnich, G. Chen, Z. Ren, Enhancement of Thermoelectric Figure-of-Merit by aBulk Nanostructuring Approach, Adv. Funct. Mater., **20:357**-376**(2010)**.

[77] B. Paul, V. A. Kumar, and P. Banerji, Embedded Ag-rich nanodots in PbTe: Enhancement of thermoelectric properties through energy filtering of the carriers J. Appl. Phys. **108**, 064322 **(2010)**.

[78] J. Martin, L. Wang, L. Chen, and G. S. Nolas, Enhanced Seebeck coefficient through energy-barrier scattering in PbTe nanocomposites Phys. Rev. **B 79**, 115311 **(2009)**.

[79]B.Liu, J.hu, J.Zhou, R.Yang, Thermoelectric Transport in Nanocomposites, Materials, **10**(4):418 **(2017)**.

[80]Isabelle Levesque,Pier-Olivier Bertrand, Nicolas Blouin, Mario Leclerc, Sandro Zecchin, Gianni Zotti, Christopher I. Ratcliffe, Dennis D. Klug, Xing Gao, Faming Gao, and John S. Tse,Synthesis and Thermoelectric Properties of Polycarbazole, Polyindolocarbazole, and Polydiindolocarbazole Derivatives, Chemistry of Materials,**19**(8):2128-2138 **(2007)**.

CHAPTER 6
CONCLUSIONS AND FUTURE SCOPE

6.1. Conclusions

In this chapter the main findings of the research work and discussion about the scope of the future work are summarized for $CaWO_4$ and $xBaWO_4/(1-x)CaWO_4$ nanocomposites. The samples were successfully prepared in an aqueous medium by simple co-precipitation method without using surfactant and characterized. It is observed from (W-H equation) that $CaWO_4$ phase crystallite sizes lie between 18nm to 25nm and that of $BaWO_4$ phase crystallite sizes lie between 40nm to 50nm which matches with that obtained from HRTEM image of C2($0.5BaWO_4/0.5CaWO_4$)nanocomposite.

All the samples showed characteristics photoluminescence (PL) emission of $CaWO_4$ single phase. Among all the samples (unsintered and sintered), maximum intrinsic photoluminescence (PL) 420nm peak intensity was emitted by C2 ($0.5BaWO_4/0.5CaWO_4$) unsintered nanocomposite. This maximum 420nm emission intensity of C2 ($0.5BaWO_4/0.5CaWO_4$) nanocomposite could be due to the excitonic charge transfer of $BaWO_4$ phase to $CaWO_4$ phase because of their Type I band alignment and interface occurring between them. More excitons in the $CaWO_4$ phase lead to increase to number of recombination processes which increases emission intensity from the $[WO_4]^{2-}$ anions of $CaWO_4$ phase of the sample. HRTEM image of C2 ($0.5BaWO_4/0.5CaWO_4$) nanocomposite also shows interfacing with $BaWO_4$ phase and $CaWO_4$ phase respectively. The C2 ($0.5BaWO_4/0.5CaWO_4$) nanocomposite emission has maximum lifetime as compared to other nanocomposites which are approximately 13% more than the emission lifetime of C0 ($CaWO_4$) single phases respectively. This may be attributed to the recombination through non-radiative process introduced into the migration of charge from the conduction band (CB) of $BaWO_4$ phase to the conduction band (CB) of $CaWO_4$ phase of the sample respectively. Due to the charge transfer mechanism this C2 ($0.5BaWO_4/0.5CaWO_4$) nanocomposite could be a host material to get enhanced dopant photoluminescence (PL) emissions. These nanocomposites could be considered for producing blue component of emission from white LED.

In the present study non-linear current density J (A/cm^2)– electric field E (V/cm) characteristics of prepared $xBaWO_4/(1-x)CaWO_4$ nanocomposites were studied to evaluate their

electrical properties including breakdown voltage, non-linearity coefficient and grain boundary resistance for determining varistor properties. This non-linearity of current density J (A/cm^2)– versus electric field E (V/cm) characteristics arise for the $xBaWO_4$/ (1−x) $CaWO_4$ nanocomposites due to the presence of insulating layer between the grain boundaries except C2 ($0.5BaWO_4/0.5CaWO_4$) nanocomposite. The DC conductivity at room temperature (RT) from 8Volts or (27.5 Volts/cm) onwards is found to be maximum for C2 ($0.5BaWO_4$/ $0.5CaWO_4$) nanocomposite and is approximately **40times** ($\sigma = 1.11x10^{-5}\ \Omega^{-1}\ cm^{-1}$) greater than that of C0($\sigma = 2.76x10^{-7}\ \Omega^{-1}\ cm^{-1}$) and **1008** times greater than that of C4 ($BaWO_4$) [$\sigma = 0.11x10^{-7}\Omega^{-1}\ cm^{-1}$] single phase samples respectively.It is observed that the non-linear coefficient alpha (**α)** for nanocomposites are less than the single phase C4($BaWO_4$) and C0($CaWO_4$) samples and is maximum for C4($BaWO_4$) sample.The calculated non-linearity coefficient (α) values lie in the range of 3.44 to 4.70 for the samples.The space charge layer (SCL) formation is suitable mechanism to explain high conductivity and lower non-linearity in the C2 ($0.5BaWO_4/0.5CaWO_4$) nanocomposite.

Dielectric properties of $xBaWO_4/(1-x)CaWO_4$ nanocomposites are reported for the first time. Room temperature (RT) Dielectric properties of $xBaWO_4$/ (1−x) $CaWO_4$ nanocomposites were studied with respect to frequency in the range of 20Hz-3MHz. The dielectric constant (ε′) at room temperature (RT) for all measured frequencies are found to be maximum (ε′=8190) for C2 ($0.5BaWO_4/0.5CaWO_4$) nanocomposite and at 20Hz, it is approximately **3 & 8 times** greater than that of C0 ($CaWO_4$) (ε′=2630) and C4 ($BaWO_4$) (ε′=970) single phase respectively.These enhanced dielectric constant (ε′) properties of C2 ($0.5BaWO_4$/ $0.5CaWO_4$) nanocomposite are due to the space charge layer (SCL) formation at the interface. The peak loss tangent (tanδ)] of C2 ($0.5BaWO_4/0.5CaWO_4$) nanocompositeis more than that of other samples except for C3 ($0.75BaWO_4/0.25CaWO_4$) nanocomposite.Variation of loss tangent (tanδ) with frequency shows that all loss tangents (tanδ) curves have broad peak in the lower frequency region approximately between 125Hz to 415Hz which may be viewed as relaxation peaks except C2($0.5BaWO_4/0.5CaWO_4$) nanocomposite. All the nanocomposites give the signature of single relaxation peak (Debye relaxation peak) whereas relaxation peak of C2 ($0.5BaWO_4/0.5CaWO_4$) nanocomposite shifts towards the higher frequency (1218Hz) side showing decrease in relaxation time.Higher (tanδ) at relaxation peak and decrease in relaxation for C2 ($0.5BaWO_4/0.5CaWO_4$) nanocomposite is due to maximum additional collection of defects (electrons and holes) at the

interface. The relaxation time [**τ**=130μsec] at loss tangents (tanδ) peak of C2 ($0.5BaWO_4/0.5CaWO_4$) nanocomposite is **3 & 10 times less than** C0 ($CaWO_4$) [**τ** =410μsecond] & C4 ($BaWO_4$) [**τ**=1340μsecond] single phases respectively and ac conductivity ($\sigma_{ac}=52.2x10^{-7}$ $\Omega^{-1}cm^{-1}$) at loss tangents (tanδ) peaks at particular (1218Hz) frequency of C2 ($0.5BaWO_4/0.5CaWO_4$) nanocomposite is **4 & 19 times** higher than C0 ($CaWO_4$) & C4 ($BaWO_4$) single phases respectively.The frequency dependence on the ac conductivity is well fitted by "Jonscher's universal power law" and all samples obey the "Jonscher's universal power law" fit. DC conductivity ($\sigma_{dc}=1.07x10^{-5}\Omega^{-1}cm^{-1}$) observed from Jonscher's universal power law fit is the highest for C2 ($0.5BaWO_4/0.5CaWO_4$) nanocomposites and matches ($\sigma_{dc}=1.11x10^{-5}\Omega^{-1}cm^{-1}$) with measurement done for C2 ($0.5BaWO_4/0.5CaWO_4$) nanocomposites by two electrodes method. Enhanced AC conductivity of C2 ($0.5BaWO_4/0.5CaWO_4$) nanocomposites was also observed for C2($0.5BaWO_4/0.5CaWO_4$) nanocomposites as compared to other nanocomposites at all the frequencies.Enhanced DC and AC conductivities for C2($0.5BaWO_4/0.5CaWO_4$) nanocomposites may be due to the space charge layer (SCL) formation at the interface.

Seebeck coefficient(S) of all the nanocomposites confirms n-type semiconductors behaviour from room temperature (RT) till the transition temperature point (T_p). Seebeck coefficient(S) from transition temperature point (T_p) to inflexion point peak (I_p) shows p-type conduction behavior. The absolute value of Seebeck coefficient (S) increases upto transition temperature point (T_p) due to the conduction of electrons in n-type material (majority charge carriers) and starts becoming more positive beyond (T_p) due to the conduction of holes (minority charge carriers) in addition to the electrons in an n-type material and suddenly becomes high and positive on further increase in temperature upto the inflexion point (I_p) due to enhanced lattice scattering effect.Then it decreases from inflexion point peak (I_p) as the temperature is further increased on account of intrinsic electrons excitation and conduction. The inflexion point peak (I_p) for C3($0.75BaWO_4/0.25CaWO_4$), C0($CaWO_4$) and C4($BaWO_4$) samples are at temperatures 408.8K, 485.5K and 417.6K respectively and the power factor at these temperatures for the respective samples are $698pWcm^{-1}K^{-2}$,$130pWcm^{-1}K^{-2}$ and $0.251pWcm^{-1}K^{-2}$. The PF of C3 ($0.75BaWO_4/0.25CaWO_4$) nanocomposites is approximately **5** and **2774** times higher than that of C0 ($CaWO_4$) and C4 ($BaWO_4$) single phases samples respectively. Enhanced power factor (PF) of C3($0.75BaWO_4/0.25CaWO_4$) nanocomposites at inflexion point is due to higher lattice scattering effect resulting from optimal atomic ratio (Ba/Ca=3), grain size which support a good

balance between electrical conductivity and Seebeck coefficient(S). C2($0.5BaWO_4/0.5CaWO_4$) nanocomposites with optimized atomic ratio (Ba/Ca=1) may be considered as an efficient multifunctional material because of its enhanced optical properties (PL emission), electrical properties (DC conductivity, dielectric constant & AC conductivity) at room temperature (RT).C3 ($0.75BaWO_4/0.25CaWO_4$) nanocomposite with optimized atomic ratio (Ba/Ca=3), grain size which support a good balance between electrical conductivity and Seebeck coefficient(S) at higher temperature (408.8K) in comparsion to other nanocomposites.

6.2. Future scope of the work

The results and conclusions of the present research work have the following scope for further investigations:-

- The preparation of $xBaWO_4/(1-x)CaWO_4$ nanocomposites by other methods (than co-precipitation) could be tried.
- Preparation of homostructured nanocomposites with Type I band alignment by the combination of metal tungstates and binary oxides for enhancing luminescence and electrical properties could be explored.
- Preparation of various shaped particles of $CaWO_4$ in $xBaWO_4$/ (1-x) $CaWO_4$ nanocomposites could be carried out and possible theory for shape formation can be predicted for photoluminescent and photocatalytic applications.
- Doping red and green emitting rare earth elements on the $CaWO_4$ and $BaWO_4$ phases in $xBaWO_4$/ (1-x) $CaWO_4$ nanocomposites for enhanced white light emission.
- Other tungstate nanocomposites could be prepared for thermoelectric applications.

APPENDIX

❖ LIST OF JOURNAL PUBLICATIONS

[1] "Enhanced blue emission of $CaWO_4$ in $BaWO_4/CaWO_4$ nanocomposite".

Prasad Narayan Patil, Uma Subramanian, M Jeyakanthan, *Journal of Materials Science: Materials in Electronics, Volume 31, Issue: 9, 7260-7275,* (**2020)**.DOI:https://doi.org/10.1007/s10854-020-03298-7 **Impact Factor: 2.478 (SPRINGER)**

[2]"Enhanced Electrical & Thermoelectric Power properties of $BaWO_4/CaWO_4$ nanocomposites".

Prasad Narayan Patil, Uma Subramanian, Rajeshkumar Shankar Hyam, *Applied Physics A, Volume 127, Issue 09, 731* (**2021)**.DOI:https://doi.org/10.1007/s00339-021-04864-4

Impact Factor: 2.584 (SPRINGER)

❖ PAPER PRESENTED IN CONFERENCES AND SYMPOSIUM

[1]"Synthesis & Characterization of Nanophosphors-Future Luminescent Materials" Prasad Narayan Patil,Uma Subramanian, "*7th International Conference on IT & BUSINESS INTELLIGENCE (ITBI-15)*" On 21-23rd January 2016,IMT Nagpur & Shree Rayeshwar Institute of Engineering & Information Technology (SRIEIT), at Shree Rayeshwar Institute of Engineering & Information Technology (SRIEIT),Shiroda,Goa.

[2]"Production of Metal Nanopowder through Wire Explosion Process"Prasad Narayan Patil,Uma Subramanian, "*7th International Conference on IT & BUSINESS INTELLIGENCE (ITBI-15)*" On 21-23rd January 2016,IMT Nagpur & Shree Rayeshwar Institute of Engineering & Information Technology (SRIEIT), at Shree Rayeshwar Institute of Engineering & Information Technology (SRIEIT),Shiroda,Goa.

[3] "Preparation, Characterization & study of Luminescence properties of rare earth doped $BaWO_4$ nanomaterials"Prasad Narayan Patil,Uma Subramanian, "*National Level symposium on Materials characterization and manufacturing (MCM-2016)*"on 18-19th August 2016,at Department of Physics,Goa University,Taleigao Plateau,Goa.

[4]"**Preparation, Characterization & Study of Luminescence Properties of Chromium Doped $BaWO_4$ Nanomaterials"**<u>**Prasad Narayan Patil**</u>,Uma Subramanian,"*International Conference on Energy, Environment and Advanced Materials for a Sustainable Future (ICEEAMSF-2017)*"on 23-24th May 2017, Kongu Engineering College, Perundurai-Erode, Tamilnadu.

[5]"Preparation, Characterization & Study of Luminescence properties of manganese doped $BaWO_4$ nanomaterials" <u>**Prasad Narayan Patil,**</u> Uma Subramanian, "*National seminar on Advancement in Science and Technology*", organized on 9th February 2019 by Department of Chemistry and Physics, Government college of Arts, Science & Commerce, Khandola, Goa.

[6]"Preparation, Characterization & Optical properties of trivalent doped $BaWO_4$ Nanomaterials" <u>**Prasad Narayan Patil,**</u> Uma Subramanian,"*International Conference on Nano-materials for Environmental Applications (NEA2019)*", organized on 6th-7th March 2019 by Dhempe College of Arts & Science, Miramar, Goa.

[7] "Preparation, Characterization of Cr^{3+} doped $BaWO_4$ Nanomaterials"<u>**Prasad Narayan Patil,**</u>Uma Subramanian,"*National Symposium on recent Trends in Condensed Matter Physics and Materials Science (CMPGoa-2020)*" on 12th-13th March 2020 organized by Goa University & Indian Institute of Technology (IIT), Goa at Department of Physics, Goa University,Taleigao Plateau,Goa.

[8]"Preparation and Characterization of Bi^{3+} doped $BaWO_4$ Nanomaterials"<u>**Prasad Narayan Patil,**</u>Uma Subramanian,"*International E-Conference on Nanoscience and Nanotechnology for Energy,Enviornment and Biomedical Applications*" on 07th-08th October 2021 Jointly organized by Vinayaka Mission's Kirupanada Variyar Arts & Science college(Salem) & Gyeongsang National University (South Korea) at Vinayaka Mission's Kirupanada Variyar Arts & Science college,Periyaseeragapadi,Salem, Tamil Nadu.

❖ <u>WORKSHOPS ATTENDED</u>

[1]Workshop on **"Application of X–Rays & Neutrons in study of Condensed Matter"**, Organized by Indian Association of Physics Teachers Goa Regional Council & Parvatibai Chowgule College of Arts &Science (Automonous) Gogol, Margao, Goa, on 3rd–4th September 2015.

[2]Workshop on **"Scientific Typesetting and Diagram Plotting using LATEX"**, Organized by Department of Mathematics, St. Xavier's College, Mapusa, Goa,on 4th November 2017.